

Optomechanical Inertial Sensors and Feedback Cooling

Thesis by
Timothy Dobson Blasius

In Partial Fulfillment of the Requirements
for the Degree of
Doctor of Philosophy



California Institute of Technology
Pasadena, California

2016
(Submitted January 12th, 2016)

© 2016
Timothy Dobson Blasius
All Rights Reserved

Acknowledgments

Although my name is the only one on the front of this thesis, that certainly does not mean that I did this work alone. I had an entire support group of people helping and guiding me along the way. Without the support of those listed below, this feat would have been much more difficult if not impossible and I am very grateful.

First, I'd like to thank my advisor, Oskar Painter. Oskar's knowledge of the field of optomechanics is unsurpassed. His intuition is second to none and his brilliant insights and suggested courses of action have left an indelible mark on my work and this thesis.

Oskar has always populated his lab with very intelligent and exceptionally hard-working students and post-docs, many of whom have been of great assistance to me during my time at Caltech. Martin Winger was a post-doc in Oskar's group and the first person I worked with extensively and I don't believe I would have completed my PhD if not for him. Caltech can be an intense, intimidating environment for a first year graduate student, especially one joining a lab in a field that is new to him. Martin was a patient and extremely knowledgeable guide for my first year in the group. He turned the lab from a place where a first year student can get lost and have his confidence shaken to a supportive learning environment. He gave me the foundation of lab knowledge and experience upon which I was able to build the rest of my thesis. For several years and several projects, I worked very closely with Alex Krause. He was an excellent partner to have and taught me a lot about optical measurement and experimental setup design. We encouraged each other during long work hours in the lab and outside the lab when things weren't going according to plan. Justin Cohen is a valued friend both inside the lab and out. He was the unofficial cleanroom czar and was always the person to go to when the machines in the cleanroom were misbehaving. In general, he was a great resource off of whom one could bounce crazy new ideas. Sean Meenehan was an invaluable resource when it comes to computer simulation. A lot of my simulation work was based on scripts written by him (and Jasper Chan). I learned a lot about the field of granular physics when working with Carly Donahue, and I thank her for encouraging me to get out of the lab and join her for trivia-night once a week. Michelle Aldecua, our administrative assistant, certainly deserves special thanks. She is one of those great people who truly puts the needs of others above her own. Michelle could always be counted on to order supplies, organize a room for your candidacy/defense, and take

the time to listen to your troubles. I also want to thank our lab manager, Barry Baker, for doing all the behind-the-scenes work necessary to keep our lab up and running. Finally, I'll list all the remaining students and post-docs who had a positive impact on my time at Caltech (I'll especially remember Amigos nights, BBQs, GRC, and the IQIM retreat): Richard Norte, Laura DeLorenzo, Simon Groblacher, Amir Safavi-Naeini, Jeff Hill, Taofiq Paraiso, Ari Weinstein, Chan U Lei, Joe Redford, Mike Martin, Emma Wollman, Johannes Fink, Thiago Alegre, Matt Eichenfield, Jasper Chan, Viva Horowitz, Su-Peng Yu, and Andrew McClung.

Before reaching graduate school I had several professors and teachers who I should thank for helping me get here. My undergraduate research advisors were Professor Gregory Stewart at the University of Florida, Professor Morten Eskildsen at Notre Dame University, and Professors Carl Akerlof and John Monnier at the University of Michigan. I would also like to thank my high school science teacher Mr. Brian Derowski. His requirement that we complete and present an original research project each year set me down the scientific path.

Getting through graduate school required more than just guidance and friendship inside the lab, but outside as well. Dan McNamee's camaraderie was crucial for my survival of graduate school (even if he's a clear second-best at Mario Kart). I want to thank Michael Hosler for always being there for me since we became friends in first grade, even if we live on opposite sides of the country or the globe. I also want to thank Tony Robbert for being a good friend since we roomed together at the University of Michigan.

It goes without saying that my family has played a large role in my ability to make it to this point. I sincerely thank my parents, Tim and Louise Blasius, for supporting me financially throughout my undergraduate education. Without that sacrifice I would not be in the position to write this thesis. More than that, they taught me to place the utmost importance on my education from a young age and always encouraged me to seek out academic challenge. In a similar vein, my grandparents (Robert and June Dobson and Ken and Betty Blasius) and godmother Nana Dot always treated me with love and encouraged me in my endeavors. Additionally, I want to thank my parents-in-law, Cory and Karen Reina, and my siblings-in-law, Lilly, Lucy, Logan, and Lydia. They have really integrated me into the family and been incredibly supportive and interested in me and my work.

Last, and most importantly, I want to thank my wife, Louise. Without her, this work surely would have been impossible. She has been unwaveringly supportive even through more late nights in the lab than either of us can recall. She was at my side for the celebrations and the frustrations. Getting your PhD requires lots of hard work and long hours spent away from those who love you, which means, in some sense, it is a selfish endeavor. I thank Louise from the bottom of my heart for seeing me through this selfish period of my life, and I look forward to spending more time with her in the future.

Abstract

The optomechanical interaction is an extremely powerful tool with which to measure mechanical motion. The displacement resolution of chip-scale optomechanical systems has been measured on the order of $\sim 10^{-16} m/\sqrt{Hz}$ [1, 2], which is a mere 1/10th of a proton radius. So strong is this optomechanical interaction that it has recently been used to remove almost all thermal noise from a mechanical resonator and observe its quantum ground-state of motion starting from cryogenic temperatures [3, 4].

In Chapter 1 of this work, we describe the basic physics of the canonical optomechanical system, optical measurement techniques, and how the optomechanical interaction affects the coupled mechanical resonator. In Chapter 2, we describe our techniques for realizing this canonical optomechanical system in a chip-scale form factor.

In Chapter 3, we describe an experiment where we used radiation pressure feedback to cool a mesoscopic mechanical resonator near its quantum ground-state from room-temperature. We cooled the resonator from a room temperature phonon occupation of $\langle n \rangle = 6.5 \times 10^6$ to an occupation of $\langle n \rangle = 66 \pm 10$, which means the resonator is in its ground state approximately 2% of the time, while being coupled to a room-temperature thermal environment. At the time of this work, this is the closest a mesoscopic mechanical resonator has been to its ground-state of motion at room temperature, and this work begins to open the door to room-temperature quantum control of mechanical objects.

Chapter 4 begins with the realization that the displacement resolutions achieved by optomechanical systems can surpass those of conventional MEMS sensors by an order of magnitude or more. This provides the motivation to develop and calibrate an optomechanical accelerometer with a resolution of approximately $10 \mu g/\sqrt{Hz}$ over a bandwidth of approximately 30 kHz. In Chapter 5, we improve upon the performance and practicality of this sensor by greatly increasing the test mass size, investigating and reducing low-frequency noise, and incorporating more robust optical coupling techniques and capacitive wavelength tuning. Finally, in Chapter 6 we present our progress towards developing another optomechanical inertial sensor – a gyroscope.

Contents

Acknowledgments	iv
Abstract	vi
List of Figures	x
List of Tables	xiii
1 Theoretical Introduction to Optomechanics	1
1.1 Introduction: Fabry-Pérot Cavity Optomechanics	1
1.2 Optical Cavity Reflection and Direct Detection	2
1.3 Homodyne Detection	8
1.4 Mechanical Equations of Motion	11
1.5 Optomechanical Back-Action	14
1.5.1 Dynamical Back-Action	14
1.5.2 Quantum Back-Action	18
2 Chip-Scale Optomechanics	23
2.1 Introduction: Photonic crystals	23
2.1.1 Finding and Designing Photonic Crystal Modes	24
2.2 Coupling to Nano-scale Optical Cavities	29
2.3 High-Stress Silicon Nitride Mechanical Resonator Design	34
2.4 Nanofabrication Techniques	36
2.4.1 Double-sided Lithography	39
3 Optomechanical Feedback Cooling	42
3.1 Introduction	42
3.2 Feedback Cooling Theory	43
3.2.1 Noiseless Feedback Cooling	43
3.2.2 Feedback Cooling with Measurement Noise	45

3.2.3	Optomechanical Feedback Cooling in the Quantum Regime	47
3.3	Experimental Setup and Device Characterization	51
3.4	Results and Discussion	58
3.5	Moving Forward	63
4	Demonstration of an Optomechanical Accelerometer	66
4.1	Introduction	66
4.2	Accelerometer Noise and Design	67
4.2.1	Thermal Brownian motion (a_{th})	68
4.2.2	Detector noise (a_{det})	70
4.2.3	Shot noise (a_{SN})	71
4.2.4	Back-Action Noise (a_{BA})	72
4.3	Experimental Setup and Device Characterization	72
4.3.1	Characterization Continued: Thermo-Opto-Mechanical Cooling	76
4.3.2	Characterization Continued: Tapered Optical Fiber Modes	79
4.4	Calibration: Accelerometer Sensitivity and Resolution	81
4.5	Moving Forward	84
5	Improving the Performance and Practicality of the Optomechanical Accelerometer	86
5.1	V-groove Fiber Coupled Accelerometer	87
5.2	Capacitive Wavelength Tuning	92
5.2.1	Working Principle of Capacitive Wavelength Tuning	92
5.2.2	On-Chip Capacitor Wire Fabrication	93
5.2.3	Silicon Wavelength Tuning	96
5.2.4	Accelerometer Wavelength Tuning	99
5.3	Intel On-Chip Laser Testing	101
5.4	Reduction of Low-Frequency Noise	104
5.4.1	Adsorbed Water Diffusion Model	107
5.4.2	Removing Diffusion Noise Through Surface Treatment	111
5.5	Heavy Mass Accelerometers	115
5.5.1	Testing at Atmospheric Pressure	116
5.5.2	Testing in Vacuum	120
6	Progress Towards an Optomechanical Gyroscope	124
6.1	Introduction	124
6.2	Device Presentation, Fabrication, and Characterization	126

6.3	Vibration Isolation Introduction	133
6.3.1	Passive Mechanical Isolation Working Principle	134
6.3.2	Frame Isolation Results	135
6.4	Conclusions	138
A	Mathematical Definitions	139
B	Publications	141
	Bibliography	142

List of Figures

1.1	Fabry-Pérot Cavity	2
1.2	Optical Cavity Waveguide Coupling	3
1.3	Over/Under-coupled Optical Resonances	6
1.4	Reflected Field Phase response	6
1.5	Optical Resonance Slope versus Detuning	7
1.6	Direct Detection Cartoon	8
1.7	Homodyne Detection	9
1.8	Mechanical Displacement Power Spectra	13
1.9	Standard Quantum Limit	22
2.1	1-D Photonic Crystal	24
2.2	1-D Photonic Crystal Band Diagram	27
2.3	Annotated Photonic Crystal	28
2.4	Bonded Optical Modes	28
2.5	Example Displacement Field	29
2.6	Dimpled Tapered Optical Fiber	30
2.7	Tapered Optical Fiber coupled to Photonic Crystal	30
2.8	Adiabatic Waveguide Coupler	32
2.9	On-chip waveguide “side-coupling”	32
2.10	On-chip waveguide “end-coupling”	33
2.11	V-groove Coupling	33
2.12	Mechanical Energy vs Stress	35
2.13	String Displacement Profile	36
2.14	Nanofabrication Steps	38
2.15	KOH etch geometry	39
2.16	Wet Etch Chip Carrier	40
2.17	Double-Sided Nanofabrication Steps	41
3.1	Noiseless Feedback Cooling Example	45

3.2	Feedback Cooling with Measurement Noise Example	47
3.3	Feedback Cooling Experimental Setup	53
3.4	Homodyne Phase Sweep	54
3.5	Feedback Cooling Device Characterization	56
3.6	Measurement Imprecision	57
3.7	Room-Temperature Laser Cooling	59
3.8	Feedback Circuit Response and Delay Time	60
3.9	Whole System Response and Delay Time	61
3.10	Widespan Noise Laser On-resonance	62
3.11	Widespan Noise Laser Off-resonance	62
3.12	Feedback Cooling Color Density Plot	64
4.1	Canonical Accelerometer	67
4.2	Sensor Displacement Resolution	68
4.3	Optomechanical Accelerometer Design	70
4.4	Experimental Setup	73
4.5	Optical Cavity Transmission Spectrum	73
4.6	Optical Power Spectral Density	74
4.7	Investigation of Mechanical Q-factors	75
4.8	Thermo-opto-mechanical Damping and Cooling	79
4.9	Comparison of the low-frequency on and off resonance response of the accelerometer and the bare fiber taper	80
4.10	Optical noise PSDs for different experimental configurations	82
4.11	Frequency-dependence of sensitivity and resolution	83
4.12	Future Directions; adding mass and nanostrings	85
5.1	V-groove Fiber Coupled Accelerometer	88
5.2	V-groove Fiber Coupled PSD	89
5.3	Damping and Cooling	90
5.4	V-groove Fiber Coupled Optical Scans	91
5.5	Simple Capacitor Geometry	94
5.6	Nano-fabrication process flow with metallization	95
5.7	Wire Bonding Example	96
5.8	Silicon Capacitive Tuning Device	97
5.9	Silicon Capacitive Tuning	98
5.10	Example Power Spectral Density	99
5.11	Voltage-Controlled Dynamical Back-Action	100

5.12	Tunable Accelerometer	101
5.13	Intel On-Chip Laser Coupling	103
5.14	Intel Laser Acceleration Resolution	104
5.15	Roll-up Noise Characterization	105
5.16	Roll-up Noise 2 Laser Cancellation	106
5.17	Optical Mode Gaussian Fit	111
5.18	Compare Roll-Up Noise in Vacuum and Atmospheric Pressure	112
5.19	Adsorbed Water Diffusion Model Fit	113
5.20	SAM Siloxane Crosslinking	113
5.21	SAM Suppression of Low-Frequency Roll-Up	115
5.22	Heavy Mass Accelerometer	117
5.23	Heavy Mass Accelerometer Room Pressure Characterization	119
5.24	Heavy Mass Accelerometer Room Pressure Resolution	121
5.25	Heavy Mass Accelerometer Normalized Driven Response	121
5.26	Heavy Mass Accelerometer Vacuum Characterization	122
5.27	Heavy Mass Accelerometer Vacuum Resolution	123
6.1	Canonical Gyroscope	125
6.2	ARW of Micromachined Gyroscopes	127
6.3	Comsol Simulation of Drive and Sense Modes	127
6.4	Comsol Simulation Stress in Gyro Designs	128
6.5	Prototype Optomechanical Gyroscope	130
6.6	Measured Drive and Sense Mode Quality Factors	131
6.7	Interdigitated Capacitor Geometry	131
6.8	Calibration of Gyroscope Drive Amplitude	132
6.9	Passive Mechanical Isolation Theory	135
6.10	Vibration Isolation Device Optical Image	136
6.11	Vibration Isolation Device Schematic	137
6.12	Vibration Isolation Results	138

List of Tables

2.1	Pseudo-Bosch Plasma Etch Parameters	39
5.1	SAM Procedure	114

Chapter 1

Theoretical Introduction to Optomechanics

In this chapter, we will introduce the theoretical concepts needed to understand the basics of optomechanical detection of mechanical motion. As its name suggests, optomechanics involves the interaction of an electromagnetic mode with a mechanically compliant element in its mode volume. Section 1 introduces the Fabry-Pérot cavity as the canonical optomechanical system. Section 2 describes the “optical” part of optomechanics by deriving the reflection spectrum from an optical cavity and the direct detection technique. Section 3 covers an alternative detection scheme called homodyne detection. Section 4 covers the “mechanical” part of optomechanics, including a description of the thermal power spectral density of a mechanical mode. Finally, section 5 discusses optomechanical “back-action”, which is the change in the mechanical mode properties and occupation due to its interaction with the optical mode.

1.1 Introduction: Fabry-Pérot Cavity Optomechanics

The canonical optomechanical system is the Fabry-Pérot cavity, which is diagrammed in Fig. 1.1. The Fabry-Pérot cavity consists of two mirrors, one with unit reflectivity and the other with sub-unit reflectivity to allow the coupling of laser light into and out of the cavity. Such a system will host a series of optical modes whose wavelengths satisfy the following relation: $\lambda_n = \frac{2L}{n}$. That is, the Fabry-Pérot cavity can support optical modes whose wavelengths are integer divisions of twice the cavity length. The corresponding optical resonance frequencies are given by $\omega_n/2\pi = \frac{cn}{2L}$, where c is the speed of light.

The length of this Fabry-Pérot cavity is not static, but rather one mirror is rigidly fixed in space while the other is mounted on a spring, allowing its position, $x(t)$, to vary in time. This naturally leads to a coupling between the optical resonance frequencies and mechanical motion. We call this

the optomechanical coupling, g_{OM} , and define it in Eq. (1.1).

$$g_{\text{OM}} \equiv \frac{d\omega_n}{dx} . \quad (1.1)$$

For the Fabry-Pérot cavity at hand, we can perform a Taylor expansion for the optical resonance frequency to determine the optomechanical coupling.

$$\omega_n = \omega_{n,o} - \frac{\omega_{n,o}}{L_o} x, \quad (1.2)$$

$$g_{\text{OM}} = \frac{-\omega_{n,o}}{L_o} . \quad (1.3)$$

In Eq. (1.2), L_o is the unperturbed length of the cavity and $\omega_{n,o}$ is the cavity frequency when the length is L_o . For this thesis we assume small displacements, x , relative to L_o and hence the Taylor expansion is truncated at first order and we are studying linear optomechanics. This coupling between the optical resonance frequency and the position of a mechanical resonator allows precise monitoring of mechanical motion, as we shall see in subsequent sections.

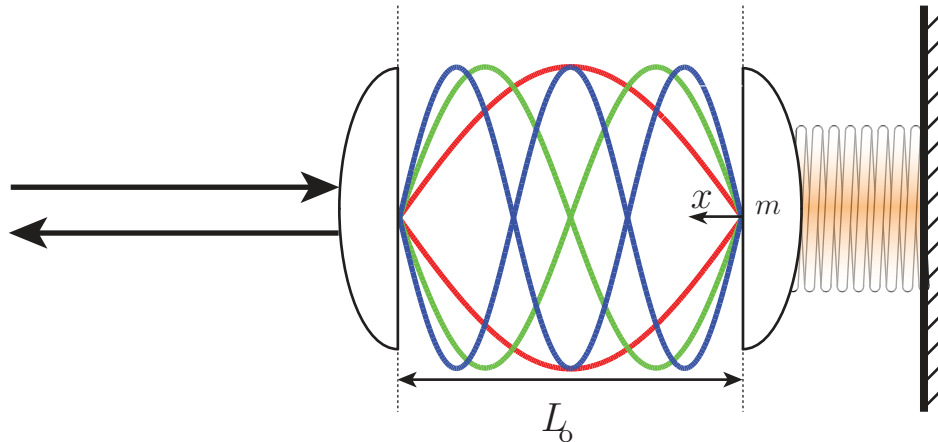


Figure 1.1: **Fabry-Pérot Cavity.** Illustration of a Fabry-Pérot Cavity of length L_o . The wavelengths of the first three optical modes are displayed. The mirror on the left is rigidly fixed in space and has less than perfect reflectivity, allowing laser light to be coupled into and out of the cavity. The mirror on the right is mounted on a spring, which allows its position, x , to fluctuate.

1.2 Optical Cavity Reflection and Direct Detection

So far, we have discussed the canonical optomechanical system and how mechanical motion can imprint itself on the optical resonance frequency through the optomechanical coupling. In order to measure that mechanical motion we must couple it out of the optical cavity into a detection channel. This is accomplished by coupling laser light into and out of the optical cavity via a waveguide placed

in the near-field of the optical mode. In this section, we discuss in depth the optical cavity's response to laser interrogation via a coupling waveguide and how this response can be used to measure the mechanical motion, $x(t)$.

In Fig. 1.2, we provide a diagram of a canonical optical resonator coupled to a waveguide, which acts as a detection channel. As shown in Fig. 1.2, there are two fundamentally different ways for an optical resonator to couple to a waveguide: single-sided and double-sided. In a double-sided coupling scheme, photons inside the cavity are equally likely to couple out and propagate in either direction along the waveguide. Practically, this means an experimenter using such a double-sided configuration can obtain at most 50% of the light inside the cavity. Conversely, in a single-sided coupling scheme, the light inside the cavity can only couple out in one direction down the waveguide. This allows an experimenter, in principle, to collect 100% of the light inside the optical cavity, which is obviously preferable for maximizing detection efficiency. The work in this thesis has utilized both coupling schemes, but in the derivations to follow I will assume the more preferable single-sided coupling scheme (the double-sided case can be treated with trivial changes to the equations that follow).

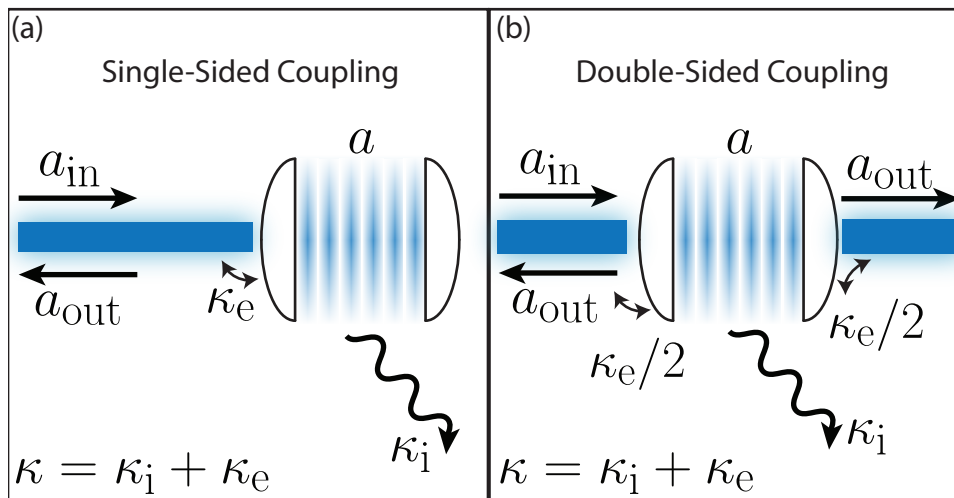


Figure 1.2: **Optical Cavity Waveguide Coupling.** (a) We illustrate a single-sided coupling scheme. The optical cavity is coupled to a single waveguide with strength κ_e . Light is scattered from the cavity into the surrounding environment at a rate κ_i . If $\kappa_e \gg \kappa_i$, all light from the optical cavity can be collected in the reflected field a_{out} . (b) We illustrate a double sided coupling scheme. Note that now that there is a component of the output field that is transmitted and a component that is reflected. Monitoring only one of these output ports will result in a loss of light from the cavity.

The derivations that follow are strongly influenced by work shown in [5]. We start by giving the equation of motion for the optical mode amplitude, a .

$$\dot{a} = i\omega_o a - \frac{\kappa}{2}a + \sqrt{\kappa_e}a_{\text{in}} . \quad (1.4)$$

In Eq. (1.4), dot notation signifies a derivative with respect to time, ω_o is the optical cavity frequency, and κ is the total energy loss rate of the cavity and it has two components κ_e and κ_i such that $\kappa = \kappa_e + \kappa_i$. The energy loss rate into the coupling waveguide is κ_e and κ_i is the intrinsic cavity energy loss rate into the surrounding environment. We will also speak of the optical Q-factor, Q_o , which is defined as $Q_o = \frac{\omega_o}{\kappa}$. Finally, a_{in} is the input laser amplitude from the waveguide. All of these terms are diagrammed in Fig. 1.2. It is important to note that the optical mode amplitude has been normalized to energy such that $|a|^2 = n_c$, where n_c is the number of photons in the optical cavity. Furthermore, the input laser amplitude has been normalized to power such that $|a_{\text{in}}|^2 = \frac{P_{\text{in}}}{\hbar\omega_\ell}$, where P_{in} is the optical power input to the optical cavity and ω_ℓ is the laser frequency. Given these definitions the terms on the right hand side of Eq. (1.4) simply imply the following in order: that the optical mode amplitude oscillates at a characteristic frequency ω_o , the optical mode energy decays at a rate given by κ , and the input laser amplitude from the waveguide, a_{in} , couples into the cavity with a strength $\sqrt{\kappa_e}$.

From a detection and measurement standpoint, we are interested in determining a_{out} , the output optical field reflected from the optical cavity shown in Fig. 1.2. a_{out} can have only two components: one proportional to a_{in} that reflected without entering the cavity mode and one proportional the cavity field, a . Therefore, we require $a_{\text{out}} = \alpha_1 a_{\text{in}} + \alpha_2 a$. These two coefficients can be obtained from a conservation of energy requirement.

$$|a_{\text{in}}|^2 - |a_{\text{out}}|^2 = \frac{d|a|^2}{dt} + \kappa_i |a|^2 . \quad (1.5)$$

Eq. (1.5) simply states that the difference between the input power and the output power must be either in the optical mode or lost to the surrounding environment. By plugging in our ansatz for a_{out} into Eq. (1.5) and solving we arrive at the following result.

$$a_{\text{out}} = -a_{\text{in}} + \sqrt{\kappa_e}a . \quad (1.6)$$

We can further simplify this result by considering the so-called steady state solution. In the steady-state, after transient dynamics have passed, the cavity mode amplitude oscillates at the same frequency as the laser driving the system. This leads to the following equations that hold in the steady state.

$$\dot{a} = i\omega_\ell a = i\omega_o a - \frac{\kappa}{2}a + \sqrt{\kappa_e}a_{\text{in}}, \quad (1.7)$$

$$0 = -\left(i\Delta + \frac{\kappa}{2}\right)a + \sqrt{\kappa_e}a_{\text{in}}, \quad (1.8)$$

$$a = \frac{\sqrt{\kappa_e}a_{\text{in}}}{i\Delta + \frac{\kappa}{2}}, \quad (1.9)$$

$$a_{\text{out}} = a_{\text{in}} \left(\frac{\kappa_e}{i\Delta + \frac{\kappa}{2}} - 1 \right), \quad (1.10)$$

where we have defined the cavity-laser detuning as $\Delta = \omega_\ell - \omega_o$. Using Eq. (1.10), we can now compute the normalized reflection spectrum, $R \equiv \left| \frac{a_{\text{out}}}{a_{\text{in}}} \right|^2$, we expect to see when we couple a laser to such an optical cavity and waveguide system.

$$R = 1 - \frac{\kappa_e \kappa_i}{\Delta^2 + \frac{\kappa^2}{4}}. \quad (1.11)$$

From this equation, we can see that by sweeping the laser-cavity detuning the reflection spectrum will be that of a negative Lorentzian dip. In Fig. 1.3 we plot several example Lorentzians. The plots are split into two cases: undercoupled ($\kappa_e < \kappa$) and overcoupled ($\kappa_e > \kappa$). As one can see, the reflection dip on resonance, $R_D = 1 - \frac{4\kappa_e \kappa_i}{\kappa^2}$, decreases from 1 to 0 as κ_e/κ increases from 0 to 1/2. Then as κ_e/κ increases from 1/2 to 1 the dip disappears and the reflection returns to unity. Intuitively this is because when $\kappa_e/\kappa \ll 1$ no light is coupled into the optical cavity and it is all reflected, when $\kappa_e/\kappa = 1/2$ then $\kappa_e = \kappa_i$ and the optical cavity is said to be critically coupled and all light is coupled into the cavity and lost to the environment, finally when $\kappa_e/\kappa \rightarrow 1$ then all light is coupled into the cavity and back out.

In addition to looking at the normalized reflection spectrum, we can look at the phase response of the reflected field. The phase response is given by the imaginary part of Eq. (1.10) normalized by a_{in} . We will label the phase by Y , and its expression is given below.

$$Y = \frac{\kappa_e \Delta}{\Delta^2 + \frac{\kappa^2}{4}}. \quad (1.12)$$

The phase of the reflected light is plotted in Fig. 1.4. Note that the greatest change in the phase occurs on resonance. Phase sensitive detection schemes, such as homodyne detection (see Section 1.3), can take advantage of these phase shifts to monitor mechanical motion.

Before moving on, we provide one more useful equation for the number of photons in the cavity, n_c . This is obtained by taking the norm-square of Eq. (1.9).

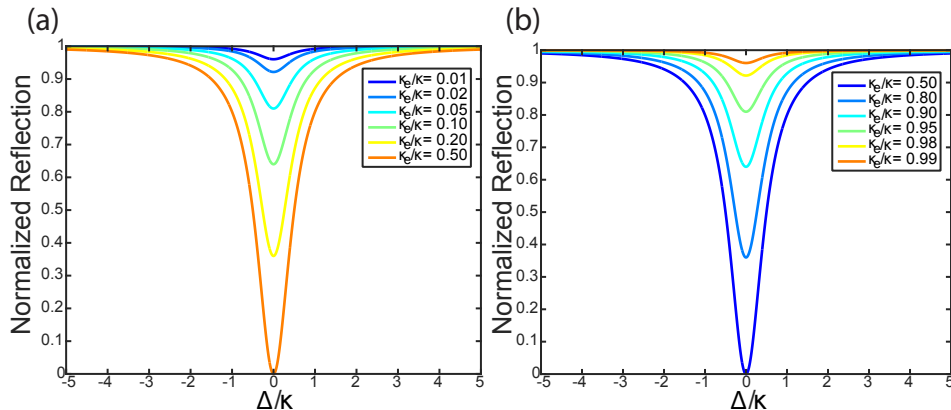


Figure 1.3: **Over/Under-coupled Optical Resonances.** In (a) we show undercoupled optical resonances. Note how the reflection on resonance approaches zero as κ_e/κ approaches $1/2$. This is because when $\kappa_e = \kappa/2$, then $\kappa_e = \kappa_i$ and all light is lost to the surrounding environment. In (b) we plot overcoupled optical resonances. Note that as κ_e/κ approaches 1, the reflection on-resonance approaches unity. This is because as κ_e approaches κ , essentially no light is lost to the surrounding environment via κ_i .

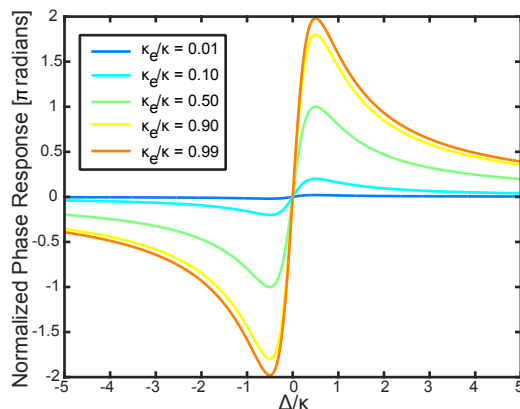


Figure 1.4: **Reflected Field Phase response.** A plot the phase of the reflected light field as a function of detuning for various ratios of κ_e/κ . Note that the greatest rate of change of phase occurs on resonance and the total phase change increases with κ_e/κ .

$$n_c = \frac{\kappa_e}{\Delta^2 + \frac{\kappa^2}{4}} |a_{\text{in}}|^2 = \frac{\kappa_e}{\Delta^2 + \frac{\kappa^2}{4}} \frac{P_{\text{in}}}{\hbar\omega_\ell}. \quad (1.13)$$

Now that we've derived the reflection spectrum, Eq. (1.11), for this optical cavity system we can understand how to get a signal proportional to $x(t)$ in an optomechanical system. In Section 1.1, it was explained that mechanical motion couples to the optics via the optomechanical coupling, $g_{\text{OM}} \equiv \frac{d\omega}{dx}$. That is, mechanical motion shifts the optical resonance frequency. Therefore, by setting the laser at some detuning relative to the cavity frequency any motion of the mechanical mode will

cause a change in the reflected power, which can be easily measured on a photodetector. In fact, we can make the following statement about the optical power modulated by the mechanical motion, P_m .

$$P_m = P_{in} \frac{dR}{dx} \eta x(t) = P_{in} \eta \frac{dR}{d\Delta} \frac{d\Delta}{dx} x(t) = P_{in} \eta \frac{dR}{d\Delta} g_{OM} x(t) , \quad (1.14)$$

where we have included some realistic optical losses from the cavity to the detector, η . Given Eq. (1.14), we can now write the optical power spectral density (PSD) due to mechanical motion.

$$S_{PP} = \left(\frac{dR}{d\Delta} P_{in} \eta g_{OM} \right)^2 S_{xx} , \quad (1.15)$$

where S_{xx} is the mechanical PSD. The mathematical definition of the power spectral density is provided in appendix A. In Fig. 1.5, $\frac{dR}{d\Delta}$ is plotted so that the reader can understand where the quantity is maximal. Note that there is no transduction directly on resonance with the optical cavity. In Fig. 1.6, a cartoon of this detection scheme is presented. For the remainder of the text, this detection scheme will be referred to as “direct detection.”

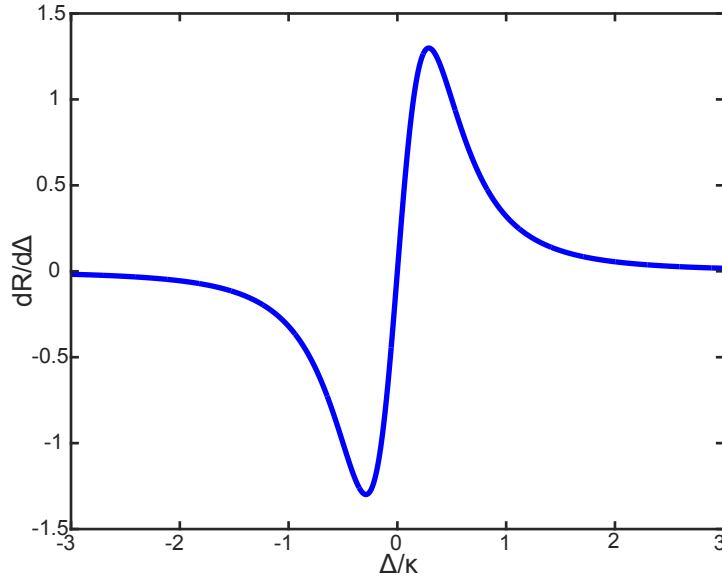


Figure 1.5: **Optical Resonance Slope versus Detuning.** A plot of the derivative of the reflected signal with respect to laser detuning

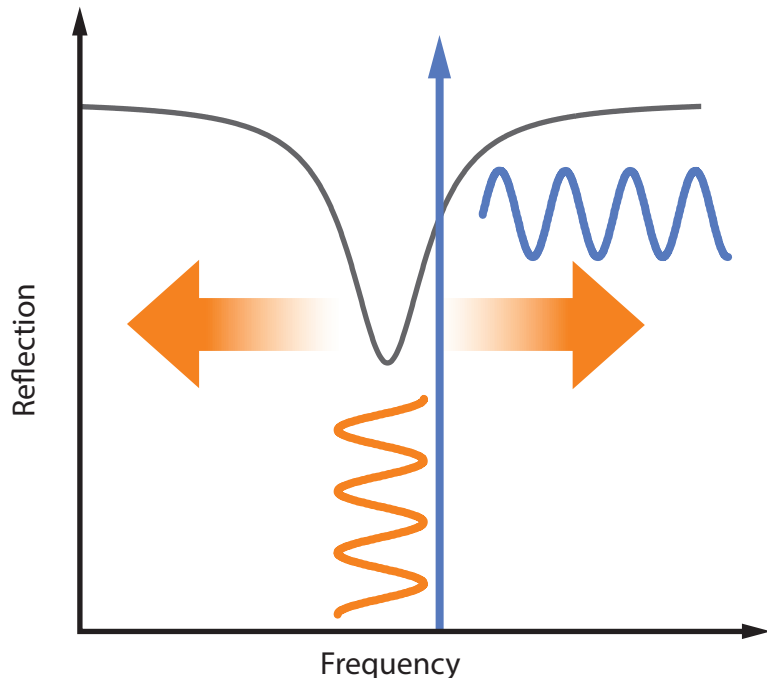


Figure 1.6: **Direct Detection Cartoon.** A cartoon of how the direct detection measurement scheme works. If the laser (blue arrow) is placed at some detuning from the optical resonance, then any fluctuations of the cavity resonance frequency due to mechanical motion (orange), will manifest itself as fluctuations of the reflected power (blue).

1.3 Homodyne Detection

In this section, we discuss an alternative detection method to direct detection called homodyne detection. In this scheme, the laser is placed directly on-resonance with the optical mode and phase fluctuations of the signal beam are sensed instead of amplitude fluctuations. The derivations and discussion to follow lean heavily on discussions in Refs. [6–8]. The homodyne measurement setup is illustrated in Fig. 1.7. It is essentially a Michelson Interferometer with one beam, the “Local Oscillator” (LO), having much larger amplitude than the other, the signal beam (s). We start by writing down the fields for each of these beams.

$$\alpha_s(t) = X_s(t) + iY_s(t) \quad (1.16)$$

$$\alpha_{LO}(t) = (|\alpha_{LO}| + X_{LO}(t) + iY_{LO}(t)) e^{i\theta_H}. \quad (1.17)$$

We have written the LO beam as a mean value amplitude with small modulations about this mean in both the amplitude quadrature, X, and phase quadrature, Y. Note $X_s(t)$, $Y_s(t)$, $X_{LO}(t)$, $Y_{LO}(t)$ are all real valued and $|\alpha_{LO}|^2 = P_{LO}/\hbar\omega_\ell$. Note also that we have included a relative phase difference

between the two arms parameterized by θ_H . From now we will cease to explicitly state the functional dependence on time, t . These two beams are mixed on the beamsplitter and the two outputs are sent to separate photodetectors whose photocurrents are subtracted. The field on each detector is given as follows.

$$\alpha_{D1} = \sqrt{\frac{1}{2}}\alpha_{LO} + \sqrt{\frac{1}{2}}\alpha_s \quad (1.18)$$

$$\alpha_{D2} = \sqrt{\frac{1}{2}}\alpha_{LO} - \sqrt{\frac{1}{2}}\alpha_s . \quad (1.19)$$

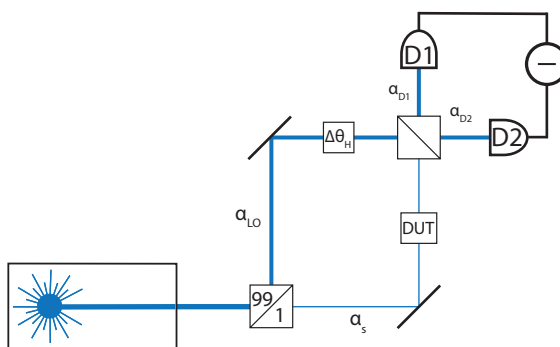


Figure 1.7: **Homodyne Detection.** Illustration of homodyne detection scheme. Laser light is split into two components: α_{LO} and α_s , with α_{LO} having a much larger amplitude (represented, for example, by the 99% port on a 99% – 1% splitter). The relative phase between the two arms is parameterized by a phase shift in the LO arm, θ_H . The signal arm contains the “Device Under Test” (DUT). The two paths are then mixed on a beamsplitter whose outputs are sent to two different photodetectors and the photocurrents are subtracted.

Note that we have included, in accordance with the fresnel equations, that one of the reflections from the beamsplitter is accompanied by a π phase shift. The detected photocurrent at each detector is given $I_{1,2} = |\alpha_{D1,2}|^2$, and subtracting the two photocurrents yields the following:

$$I_- = I_1 - I_2 = \alpha_{LO}\alpha_s^* + \alpha_{LO}^*\alpha_s . \quad (1.20)$$

Plugging in Eqs. (1.16) and (1.17) into Eq. (1.20) and simplifying by using our assumption that $|\alpha_{LO}| \gg |\alpha_s|$ in order to keep terms only terms that are at least linear in $|\alpha_{LO}|$ yields the following:

$$I_- = 2|\alpha_{LO}| (\cos(\theta_H) X_s + \sin(\theta_H) Y_s) . \quad (1.21)$$

There are several remarkable properties about this equation. Firstly, the noise on the difference photocurrent has no contribution from the LO noise, quantum or otherwise. If the signal beam is shot-noise limited, then X_s and Y_s represent vacuum fluctuations and the variance of I_- is simply these vacuum fluctuations scaled by $|\alpha_{LO}|^2$. In other words, the noise of the homodyne signal is the scaled vacuum noise of the signal beam, whose magnitude is equal to the shot noise of the LO beam. This is shown in the equation below for the case of $\theta_H = \pi/2$ and shot noise limited signal beam.

$$Var(I_-) = 4|\alpha_{LO}|^2 Var(Y_s) = |\alpha_{LO}|^2. \quad (1.22)$$

We have used the fact that for a simple harmonic oscillator the total variance is $1/2$ quanta and thus for each quadrature it is $1/4$. Eq. (1.22) is the definition of shot noise for a beam with $|\alpha_{LO}|^2$ photons in it [9].

The other remarkable property of equation Eq. (1.21), is that it allows us to measure either quadrature of the signal beam by setting θ_H . As stated previously, we are interested in using homodyne detection when the laser is placed directly on-resonance with the optical mode. As discussed in Section 1.2, in this configuration all mechanical motion will be encoded on the phase of the reflected light. From here, we will thus assume that $\theta_H = \pi/2$ and we will plug in for Y_s using our reflected cavity field given in Eq. (1.10).

$$\alpha_s = a_{out} = a_{in} \left(1 - \frac{\kappa_e}{\frac{\kappa}{2} - i\Delta} \right) = a_{in} \left(1 - \frac{\kappa_e \kappa}{2(\Delta^2 + \frac{\kappa^2}{4})} + \frac{-i\Delta\kappa_e}{\Delta^2 + \frac{\kappa^2}{4}} \right). \quad (1.23)$$

Now we can pick out the phase quadrature.

$$Y_s = a_{in} \frac{-\Delta\kappa_e}{\Delta^2 + \frac{\kappa^2}{4}}. \quad (1.24)$$

Mechanical motion causes changes in detuning, so we are interested in how this phase quadrature changes with detuning.

$$\frac{dY_s}{d\Delta} = a_{in} \left(\frac{-\kappa_e}{\Delta^2 + \frac{\kappa^2}{4}} + \frac{2\kappa_e\Delta^2}{(\Delta^2 + \frac{\kappa^2}{4})^2} \right). \quad (1.25)$$

In particular, we are interested in the case of on-resonance detection, where $\Delta = 0$.

$$\left. \frac{dY_s}{d\Delta} \right|_{\Delta=0} = a_{\text{in}} \frac{-4\kappa_e}{\kappa^2} \quad (1.26)$$

Now we can plug this into the derivative of the difference photocurrent, I_- , with respect to detuning, which is to what our signal will be proportional.

$$\left. \frac{dI_-}{d\Delta} \right|_{\Delta=0} = 2|\alpha_{\text{LO}}| |a_{\text{in}}| \frac{4\kappa_e}{\kappa^2} \quad (1.27)$$

From now on, everything will be evaluated at $\Delta = 0$ and it will no longer be explicitly stated. Now we will use Eq. (1.13) to substitute in n_c , the number of photons in the cavity, for $|a_{\text{in}}|$.

$$\left. \frac{dI_-}{d\Delta} \right|_{\Delta=0} = 2|\alpha_{\text{LO}}| \sqrt{n_c} \sqrt{\frac{4\kappa_e}{\kappa^2}} \quad (1.28)$$

We can now finally state the theoretical prediction for the optical power spectral density resulting from mechanical motion for a homodyne detection scheme.

$$S_{PP} = \left(\hbar\omega_\ell \left. \frac{dI_-}{dx} \right| \sqrt{\eta}\eta_{qe} \right)^2 S_{xx} = \left(\hbar\omega_\ell \left. \frac{dI_-}{d\Delta} \right| \left. \frac{d\Delta}{dx} \right| \sqrt{\eta}\eta_{qe} \right)^2 S_{xx} = 16 (\hbar\omega_\ell)^2 |\alpha_{\text{LO}}|^2 n_c \frac{\kappa_e}{\kappa^2} g_{\text{OM}}^2 \eta \eta_{qe}^2 S_{xx} , \quad (1.29)$$

where we have introduced η , which represents the optical losses any real system will have from the cavity to the detector in the signal arm, and η_{qe} , which is the quantum efficiency of the detector. Please note that η only affects the signal beam and hence the linear dependence, while η_{qe} affects both the LO and the signal beam and is thus squared.

1.4 Mechanical Equations of Motion

So far we have discussed the optical mode properties of an optomechanical system and how to read-out fluctuations in optical power due to mechanical motion. In this section, we discuss the mechanical equation of motion and motivate the mechanical power spectral density. The mechanical equation of motion is shown in Eq. (1.30).

$$m\ddot{x} + m\gamma\dot{x} + m\omega_{\text{m}}^2 x = F_{\text{th}} . \quad (1.30)$$

In Eq. (1.30) m is the mass of the mechanical element (in the Fabry-Pérot cavity example it is the mass of the movable mirror), x is the position of the mechanical element, γ is the mechanical energy decay rate (a.k.a. the mechanical damping rate), $\omega_m/2\pi$ is the mechanical frequency, and F_{th} is a random force from the surrounding thermal bath that impinges upon the resonator. More extensively, γ is the rate at which energy inside the mechanical resonator couples out into the surrounding thermal bath. The fluctuation-dissipation theorem states that any system with such a dissipative coupling to a thermal bath must be subject to a related fluctuating force from the same bath. If such a force were not present, one would conclude that all of the mechanical energy in the resonator would eventually be dissipated into the bath. The path to the quantum ground-state would be simple – just place the resonator in a dissipative environment. But, alas, this random force does exist because, as the fluctuation-dissipation theorem shows, the same physical couplings and interactions that lead to dissipation of energy from the resonator to the bath, γ , must, in thermal equilibrium, lead to thermal energy and excitations being coupled into the resonator from the surrounding thermal bath. The thermal force is assumed to be incoherent and perfectly random, i.e., its auto-correlation is a delta function ($F_{\text{th}}(t)$ does not help predict $F_{\text{th}}(t')$ for $t' \neq t$). This implies the power spectral density of F_{th} , $S_{\text{FF}}(\omega)$, is white. When proper magnitude set by the fluctuation-dissipation theorem, power spectral density of this thermal force noise is given by the following.

$$S_{\text{FF}}^{th}(\omega) = 4k_{\text{B}}mT\gamma \quad (1.31)$$

In Eq. (1.31), k_{B} is Boltzmann's constant and T is the temperature of the thermal bath with which our resonator is in thermal equilibrium. That Eq. (1.31) represents the correct magnitude of the thermal force noise PSD will be easily verified by computing the mean-squared deviations of x , which, from equipartition theorem, is known to be $\langle x^2 \rangle = \frac{k_{\text{B}}T}{m\omega_m^2}$.

Next, we will compute the power spectral density for mechanical motion, x . Taking Eq. (1.30) and Fourier transforming it (see appendix A), and solving for x yields the following.

$$F_{\text{th}}[\omega] = -m\omega^2x[\omega] + im\omega\gamma x[\omega] + m\omega_m^2x[\omega] \quad (1.32)$$

$$x[\omega] = \frac{F_{\text{th}}[\omega]/m}{\omega_m^2 - \omega^2 + i\omega\omega_m/Q_m} \quad (1.33)$$

$$\chi(\omega) = \frac{1}{\omega_m^2 - \omega^2 + i\omega\omega_m/Q_m} \quad (1.34)$$

In Eq. (1.32), we have introduced our Fourier transform notation, e.g., the Fourier transform of $F_{\text{th}}(t)$ is written $F_{\text{th}}[\omega]$. We have also introduced the mechanical quality factor, Q_m , which is defined as

$Q_m \equiv \omega_m/\gamma$. In Eq. (1.34), $\chi(\omega)$ is called the mechanical susceptibility and physically it represents the mechanical displacement response to a unit acceleration at frequency ω . We are now in a position to calculate the displacement power spectral density, $S_{xx}(\omega)$.

$$S_{xx}^{th}(\omega) = |\chi(\omega)|^2 S_{FF}(\omega)/m^2 \quad (1.35)$$

$$S_{xx}^{th}(\omega) = \frac{4k_B T \omega_m}{m Q_m} \frac{1}{(\omega^2 - \omega_m^2)^2 + \left(\frac{\omega \omega_m}{Q_m}\right)^2} \quad (1.36)$$

To confirm this is indeed the correct displacement power spectral density we calculate $\langle x^2 \rangle$.

$$\langle x^2 \rangle = \int_0^\infty |\chi(\omega)|^2 \frac{S_{FF}(\omega)}{m^2} d\omega = \frac{k_B T}{m \omega_m^2} \quad (1.37)$$

This is indeed what we expect from equipartition theorem. Therefore, when analyzing displacement power spectral densities in later chapters we can look to Eq. (1.36) for the expected form.

Fig. 1.8 shows some example norm-squared susceptibilities, $|\chi(\omega)|^2$, in accordance with Eq. (1.34). This serves to familiarize the reader with how the response of the mechanical resonator scales important parameters. Note that the response on resonance increases like Q_m^2 and the DC (0 Hz) tail decreases like ω_m^4 .

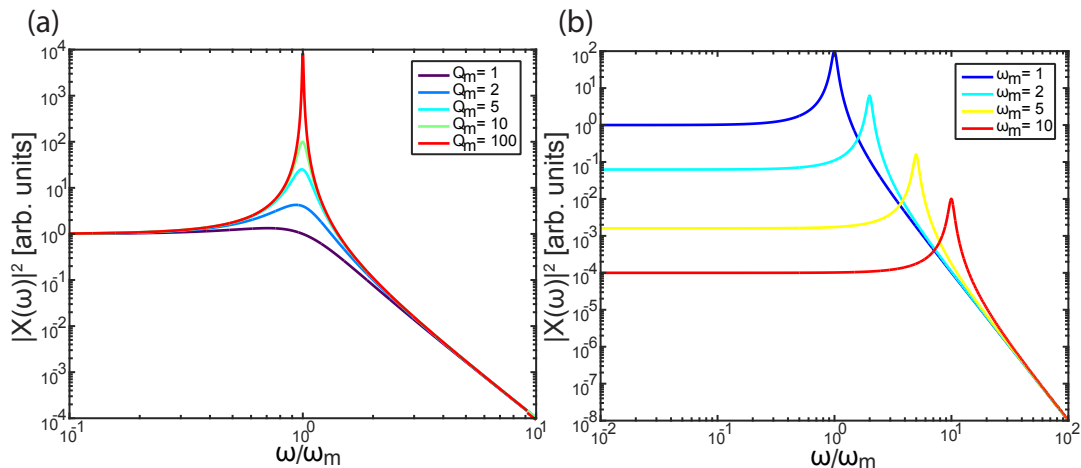


Figure 1.8: Mechanical Displacement Power Spectra. (a) A plot with several norm-squared susceptibilities, $|\chi(\omega)|^2$, with varying Q_m values. Note that the response on resonance increase like Q_m^2 . (b) A plot with several norm-squared susceptibilities, $|\chi(\omega)|^2$, with varying ω_m values. Note that the response at DC (0 Hz) decreases like ω_m^4 .

Before moving on, we will address a technical point for the curious reader. The mechanical equation of motion, Eq. (1.30), looks like it is written for a point-mass of size m . However, the

physical systems we will study in this thesis are certainly not point-masses. Nevertheless, we can still use Eq. (1.30), if we replace the physical mass of the system, m , with the effective mass, m_{eff} for a mechanical eigenmode of the resonator represented by a displacement profile, $u(\mathbf{r})$.

$$m_{\text{eff}} = \frac{\int \rho(\mathbf{r}) u^2(\mathbf{r}) d\mathbf{r}}{\int u^2(\mathbf{r}) d\mathbf{r}} \quad (1.38)$$

In Eq. (1.38), $\rho(\mathbf{r})$ is the density of the material. m_{eff} is thus a weighted average of the mass based on how much each infinitesimal piece is moving. For the rest of the thesis, we will not differentiate between m and m_{eff} . All masses discussed in this thesis are effective masses and will be labeled simply as m .

1.5 Optomechanical Back-Action

Up to this point, we have discussed a canonical optomechanical system, optical modes, mechanical modes, and how mechanical motion can affect the light field. However, there is one more piece to the puzzle. The light inside the cavity also affects the mechanical mode through radiation pressure. This phenomenon is called optomechanical back-action and it is the subject of this section.

1.5.1 Dynamical Back-Action

In Section 1.2 and Section 1.4 we solved the equation of motion for the optical mode and mechanical mode respectively. However, in these solutions we ignored how the light field inside the cavity affects the mechanical motion and vice-versa. In this section, we will derive results for the true coupled system and our derivation is guided by work in references [1, 10]. From Section 1.1, we know that mechanical motion changes the resonance frequency of the optical mode according to $\Delta\omega_o = g_{\text{OM}}x$. The energy inside the optical mode obviously depends on the resonance frequency, $E = \hbar\omega_o|a|^2$, so this frequency shift implies the following interaction hamiltonian.

$$H_{\text{int}} = -\hbar g_{\text{OM}} x |a|^2 \quad (1.39)$$

Eq. (1.39) implies there is a radiation pressure force, F_{rp} , from the light in the optical mode onto the mechanical mode.

$$F_{\text{rp}} = -\frac{\partial}{\partial x} H_{\text{int}} = \hbar g_{\text{OM}} |a|^2 = \hbar g_{\text{OM}} n_c \quad (1.40)$$

Now that these interaction terms are understood, we can write down the coupled equations of motion for the optical and mechanical modes.

$$\dot{a} = - \left(i(\Delta - g_{\text{OM}}x) + \frac{\kappa}{2} \right) a + \sqrt{\kappa_e} a_{\text{in}} \quad (1.41)$$

$$\ddot{x} = -\gamma_i \dot{x} - \omega_{\text{m},i}^2 x - \frac{\hbar |a|^2 g_{\text{OM}}}{m} \quad (1.42)$$

In Eq. (1.42), we have taken special care to denote the intrinsic mechanical damping rate and resonance frequency, γ_i and $\omega_{\text{m},i}$, respectively. This is because, as we'll soon see, the optomechanical interaction will change these mechanical properties. Eqs. (1.41) and (1.42) can be solved together using a perturbative method. That is, we solve these equations in a regime where both a and x have large static values and relatively small fluctuations about that value. We expand to first order as follows:

$$x(t) = x_0 + \varepsilon x_1(t) \quad (1.43)$$

$$a(x, t) = a_0 + \varepsilon a_1(x, t). \quad (1.44)$$

In Eqs. (1.43) and (1.44) ε is an order parameter assumed to be much less than 1. We plug Eqs. (1.43) and (1.44) into Eqs. (1.41) and (1.42), keeping only terms up to first order in ε . The result is two equations (one for each order of ε) per coupled equation, so four in total.

$$0 = - \left(i\Delta' + \frac{\kappa}{2} \right) a_0 + \sqrt{\kappa_e} a_{\text{in}} \quad (1.45)$$

$$\dot{a}_1 = i g_{\text{OM}} a_0 x_1 - \left(i\Delta' + \frac{\kappa}{2} \right) a_1 \quad (1.46)$$

$$0 = -\omega_{\text{m},i}^2 x_0 - \frac{\hbar g_{\text{OM}} |a_0|^2}{m} \quad (1.47)$$

$$\ddot{x}_1 = -\gamma_i \dot{x}_1 - \omega_{\text{m},i}^2 x_1 - \frac{\hbar g_{\text{OM}}}{m} (a_0 a_1^* + a_0^* a_1) \quad (1.48)$$

In Eqs. (1.45) and (1.46), we have introduced for convenience $\Delta' \equiv \Delta - g_{\text{OM}}x_0 = (\omega_\ell - \omega_o) - g_{\text{OM}}x_0$, which is the time averaged detuning. Fourier transforming the remaining differential equations, Eqs. (1.46) and (1.48), will turn them into algebraic ones. The immediate goal will be to plug in the solution for a_1 and a_1^* into Eq. (1.48), so we will Fourier transform Eq. (1.46) and its complex conjugate along with Eq. (1.48).

$$\left(i(\omega + \Delta') + \frac{\kappa}{2}\right) a_1[\omega] = ig_{\text{OM}} a_0 x_1[\omega] \quad (1.49)$$

$$\left(i(\omega - \Delta') + \frac{\kappa}{2}\right) a_1^*[\omega] = -ig_{\text{OM}} a_0^* x_1[\omega] \quad (1.50)$$

$$-\omega^2 x_1[\omega] = -i\gamma_i \omega x_1[\omega] - \omega_{\text{m},i}^2 x_1[\omega] - \frac{\hbar g_{\text{OM}}}{m} (a_0 a_1^*[\omega] + a_0^* a_1[\omega]) \quad (1.51)$$

Plugging the solutions to Eqs. (1.49) and (1.50) into Eq. (1.51) and simplifying yields

$$-\omega^2 x_1[\omega] = -i\gamma_i \omega x_1[\omega] - \omega_{\text{m},i}^2 x_1[\omega] - \frac{2\hbar g_{\text{OM}}^2 \Delta' |a_0|^2 / m}{\frac{\kappa^2}{4} - (\omega^2 - \Delta'^2) + i\kappa\omega} x_1[\omega]. \quad (1.52)$$

From here, we will make a couple simplifying assumptions. Firstly, we assume $x_1(t) = \cos(\omega_{\text{m},i}t)$ and thus $x_1[\omega] = \frac{1}{2}(\delta(\omega_{\text{m},i}) + \delta(-\omega_{\text{m},i}))$. Secondly, we assume the “sideband unresolved” limit, where $\omega_{\text{m},i} \ll \kappa$. After applying these assumptions, the final term in Eq. (1.52) is broken into an imaginary part and a real part which yields the following:

$$-\omega^2 x_1[\omega] = -i\gamma_i \omega x_1[\omega] - \omega_{\text{m},i}^2 x_1[\omega] - i \frac{-2\hbar g_{\text{OM}}^2 \Delta' |a_0|^2 \kappa}{m (\Delta'^2 + \frac{\kappa^2}{4})^2} \omega x_1[\omega] - \frac{2\hbar g_{\text{OM}}^2 \Delta' |a_0|^2}{m (\Delta'^2 + \frac{\kappa^2}{4})} x_1[\omega]. \quad (1.53)$$

Comparing the first two terms on the left hand side of Eq. (1.53) to the second two terms shows that the optomechanical interaction has changed the effective damping rate and frequency of the mechanical mode.

$$\gamma_{\text{eff}} = \gamma_i + \frac{-2\hbar g_{\text{OM}}^2 \Delta' |a_0|^2 \kappa}{m (\Delta'^2 + \frac{\kappa^2}{4})^2} \quad (1.54)$$

$$\omega_{\text{m,eff}}^2 = \omega_{\text{m},i}^2 + \frac{2\hbar g_{\text{OM}}^2 \Delta' |a_0|^2}{m (\Delta'^2 + \frac{\kappa^2}{4})} \quad (1.55)$$

The renormalization of the mechanical frequency is called the optical spring effect and the change in the damping rate is known as optomechanical damping. Collectively, these phenomenon are known as optomechanical dynamical back-action. Interestingly, the effects depend on the probe laser’s detuning from the optical cavity. When the laser is “blue-detuned” (“red-detuned”) from the optical cavity, i.e., $\Delta' > 0$ ($\Delta' < 0$) the mechanical frequency is increased (decreased) and the damping rate is decreased (increased). In other words, the optical field stiffens (softens) the mechanical structure and amplifies (dampens) the motion. Intuitively, the optical spring effect occurs because from Eq. (1.40) the radiation pressure force is proportional to the number of photons

in the optical cavity, from Eq. (1.13) the number of photons in cavity depends on detuning (and, in a perturbative limit, linearly so), and from Eq. (1.2) mechanical motion linearly changes the detuning. Thus, radiation pressure exerts a force linearly proportional to the mechanical displacement, which is a “spring” force. The sign of this spring force depends on the slope of $\frac{dn_c}{d\Delta}$.

The optomechanical damping effect can be intuitively understood by the solution to Eq. (1.49) for the cavity field.

$$a_1[\omega] = \frac{ig_{\text{OM}}a_0}{i(\omega + \Delta') + \frac{\kappa}{2}} x_1[\omega] = \frac{ig_{\text{OM}}a_0}{i(\omega + \Delta') + \frac{\kappa}{2}} \frac{\delta(\omega_{\text{m,i}}) + \delta(-\omega_{\text{m,i}})}{2} \quad (1.56)$$

Now we take this solution to the time domain.

$$a_1(t) = \frac{ia_0g_{\text{OM}}}{2} \left(\frac{e^{i\omega_{\text{m,i}}t}}{i(\Delta' + \omega_{\text{m,i}}) + \frac{\kappa}{2}} + \frac{e^{-i\omega_{\text{m,i}}t}}{i(\Delta' - \omega_{\text{m,i}}) + \frac{\kappa}{2}} \right) \quad (1.57)$$

Note that this result holds even when not in the “sideband unresolved” regime. This result illustrates the stokes/anti-stokes scattering nature of the optomechanical interaction. When the light field interacts with the mechanics, the light field is doppler shifted up and down in frequency by $\omega_{\text{m,i}}$ to different sidebands. However, as shown by Eq. (1.57), the weights on each process are not necessarily equal, but rather the cavity can resonantly enhance one sideband more than the other. In fact, when $\Delta' < 0$, the $\omega_{\text{m,i}}$ or anti-stokes sideband is preferred. Because the cavity field frequency undergoes $\omega_\ell \rightarrow \omega_\ell + \omega_{\text{m,i}}$, the light field gains energy in this process, and, by conservation of energy, the mechanical mode must lose this energy. Thus, when $\Delta' < 0$, mechanical motion is damped and vice-versa.

Before moving on, we emphasize that the amount by which this dynamical optomechanical back-action broadens the mechanical linewidth (Eq. (1.54)) is the same amount by which the effective mechanical mode temperature is reduced (and vice-versa). The broadened mechanical resonance means that the light field represents an additional loss mechanism for mechanical motion. Normally, that is, if this extra loss was into a thermal bath at the same room temperature, the additional loss would be accompanied by an increase in random force fluctuations and the mechanical mode temperature would remain unchanged (as dictated by the fluctuation-dissipation theorem, discussed earlier). However, unlike the thermal bath, the laser is effectively at zero-temperature. The laser does have quantum shot noise, which will induce mechanical motion, but we will neglect this small (but important) correction until the next section. Essentially, that is, until you get to quantum limits, the laser removes energy from the system without injecting noise, which results in a lower effective mode temperature. This can be seen by the following argument. The Fourier transform of the mechanical motion with an effective damping rate and mechanical frequency can be found by

substituting into Eq. (1.33).

$$x[\omega] = \frac{F_{\text{th}}[w]/m}{\omega_{\text{m,eff}}^2 - \omega^2 + i\omega\gamma_{\text{eff}}} \quad (1.58)$$

From equipartition theorem, the effective mode temperature, T_{m} , is given by the following.

$$\frac{1}{2}k_{\text{B}}T_{\text{m}} = \frac{1}{2}m\omega_{\text{m,eff}}^2\langle x^2 \rangle \quad (1.59)$$

$$T_{\text{m}} = \frac{m\omega_{\text{m,eff}}^2\langle x^2 \rangle}{k_{\text{B}}} \quad (1.60)$$

The expectation value of the squared displacement can be obtained from the power spectral density of the displacement as follows.

$$\langle x^2 \rangle = \int_0^\infty S_{xx}(\omega) \frac{d\omega}{2\pi} = \int_0^\infty \frac{S_{\text{FF}}/m^2}{(\omega_{\text{m,eff}}^2 - \omega^2)^2 + (\gamma_{\text{eff}}\omega)^2} \frac{d\omega}{2\pi} = \frac{4\gamma_i k_{\text{B}}T}{m} \frac{1}{4\gamma_{\text{eff}}\omega_{\text{m,eff}}} = \frac{\gamma_i k_{\text{B}}T}{m\gamma_{\text{eff}}\omega_{\text{m,eff}}^2}, \quad (1.61)$$

where we have substituted in Eq. (1.31) and remember that T is the ambient temperature of the thermal bath. Substituting Eq. (1.61) into Eq. (1.60) yields the desired expression for the effective mechanical mode temperature.

$$T_{\text{m}} = T \frac{\gamma_i}{\gamma_{\text{eff}}} \quad (1.62)$$

Thus we see that the important result in Eq. (1.62) is that the optomechanical damping provides a commensurate amount of mechanical mode cooling (ignoring quantum noise limits). This result will be important at various points in this thesis.

1.5.2 Quantum Back-Action

In Section 1.5.1, we discussed dynamical back-action where the optical field renormalizes the mechanical resonator's dynamic properties, i.e. its damping rate and frequency. In this section we discuss quantum back-action, where the quantum shot-noise of the cavity optical field fundamentally limits how precisely one can continuously measure the mechanical resonator's position. A great in-depth discussion of this phenomenon can be found in reference [9].

We will start by discussing the quantum back-action force power spectral density, $S_{\text{ff}}^{\text{ba}}$. We know

the light inside the cavity will obey Poissonian statistics and thus, if there are n_c photons in the cavity, the standard deviation of the photon number will be $\sqrt{n_c}$. Furthermore, from Eq. (1.40), we know the force each photon imparts on the resonator. This allows us to write the quantum back-action radiation pressure force, $F_{\text{rp}}^{\text{ba}}$ [9].

$$F_{\text{rp}}^{\text{ba}} = \hbar g_{\text{OM}} \sqrt{n_c} \quad (1.63)$$

Although shot noise has a white frequency spectrum, this shot noise force will have a bandwidth set by the optical cavity bandwidth of $\frac{\kappa}{4}$ [9]. We can now write the quantum back-action force power spectral density.

$$S_{\text{ff}}^{\text{ba}} = \frac{8(\hbar g_{\text{OM}})^2 n_c}{\kappa} \quad (1.64)$$

The extra factor of 2 comes from our use of the single-sided power spectral density. To better understand the impact of this force, we'd like to calculate the number of phonons (quantum excitations of vibration) this shot noise force puts in the mechanical resonator, $n_{\text{BA,SN}}$. We'll do this by calculating $S_{\text{xx}}^{\text{ba}}$, the mechanical power spectral density caused by the back-action force, and S_{xx}^0 , the mechanical power spectral density at zero temperature.

$$S_{\text{xx}}^{\text{ba}} = \frac{8(\hbar g_{\text{OM}})^2 n_c |\chi(\omega)|^2}{\kappa}, \quad (1.65)$$

where $|\chi(\omega)|^2$ is the mechanical susceptibility defined in Eq. (1.34). To obtain S_{xx}^0 , we revisit Eq. (1.31). In the quantum limit, the more accurate expression replaces $k_{\text{B}}T$ with the quantum expression for the energy in a harmonic oscillator, $\hbar\omega_{\text{m}}(\bar{n} + \frac{1}{2})$, where \bar{n} is the number of phonons in the mechanical mode when it is in thermal equilibrium at a temperature T [11].

$$S_{\text{FF}}(\omega) = 4\hbar\omega_{\text{m}} \left(\bar{n} + \frac{1}{2} \right) m\gamma \quad (1.66)$$

$$\bar{n} = \frac{1}{e^{\frac{\hbar\omega_{\text{m}}}{k_{\text{B}}T}} - 1} \quad (1.67)$$

Thus, when $T = 0$, there is 1/2 phonon in the resonator (the so-called quantum zero-point energy) and we have the following.

$$S_{\text{FF}}^0(\omega) = 2\hbar\omega_{\text{m}}m\gamma \quad (1.68)$$

$$S_{\text{xx}}^0 = 2\hbar\omega_{\text{m}}m\gamma \frac{|\chi(\omega)|^2}{m^2} \quad (1.69)$$

Now to obtain $n_{\text{BA,SN}}$ we take the following ratio [12].

$$\frac{S_{\text{ff}}^{\text{ba}}}{2S_{\text{xx}}^0} = n_{\text{BA,SN}} = \frac{4n_{\text{c}}g_{\text{o}}^2}{\kappa\gamma} \quad (1.70)$$

In Eq. (1.70) we have made use of g_{o} , which is called the bare optomechanical coupling rate and is defined as $g_{\text{o}} = g_{\text{OM}}x_{\text{zpf}}$, where x_{zpf} is the zero-point amplitude of the mechanical motion, $x_{\text{zpf}} = \sqrt{\frac{\hbar}{2m\omega_{\text{m}}}}$. The extra factor of 2 is needed in the denominator of Eq. (1.70) because S_{xx}^0 only represents 1/2 phonon. As one can see, $n_{\text{BA,SN}}$ linearly increases with n_{c} . This means as laser light more strongly probes the mechanical mode, the more strongly it perturbs its motion by injecting noise phonons.

On the other hand, the more light used to measure the mechanical mode the less imprecision one has in the measurement of the intrinsic mechanical motion. This is because the PSD for mechanical motion increases quadratically with optical power, while the noise floor given by shot noise only increases linearly. We will quantify the imprecision the shot noise floor represents as an equivalent phonon number, $n_{\text{imp,SN}}$. $n_{\text{imp,SN}}$ is given by the optical PSD for shot noise divided by the optical PSD caused by 1 phonon of mechanical motion. We will assume on-resonance homodyne detection and, from Section 1.3, the optical PSD caused by 1 phonon of mechanical motion is as follows.

$$S_{pp,1\text{phonon}}(\omega) = 16|\alpha_{\text{LO}}|^2 n_{\text{c}}\hbar\omega_{\ell}g_{\text{OM}}^2\eta_{qe}^2 \frac{\kappa_{\text{e}}}{\kappa^2} (4\hbar\omega_{\text{m}}m\gamma|\chi(\omega)|^2) \quad (1.71)$$

We will evaluate Eq. (1.71) at ω_{m} to consider the on-mechanical-resonance imprecision. The formula for the optical PSD for shot noise when an optical power P hits a detector with quantum efficiency, η_{qe} , is as follows [9].

$$S_{pp}^{\text{sn}}(\omega) = 2\hbar\omega_{\ell}P\eta_{qe} \quad (1.72)$$

Plugging in the appropriate values for homodyne detection yields the following.

$$S_{pp}^{\text{sn}} = 2(\hbar\omega_{\ell})^2 |\alpha_{\text{LO}}|^2 \eta_{qe} \quad (1.73)$$

Now taking Eq. (1.73) and dividing by Eq. (1.71) yields $n_{\text{imp,SN}}$.

$$n_{\text{imp,SN}} = \frac{2(\hbar\omega_\ell)^2 |\alpha_{\text{LO}}|^2 \eta_{qe}}{128 |\alpha_{\text{LO}}|^2 n_c (\hbar\omega_\ell)^2 g_{\text{OM}}^2 \eta \eta_{qe}^2 \frac{\kappa_e}{\kappa^2}} = \frac{\kappa\gamma}{64 n_c g_{\text{O}}^2 \eta \eta_{qe} \kappa_e / \kappa} \quad (1.74)$$

It is useful to define a couple of terms: the single photon cooperativity, C , and the total detection efficiency, η_{tot} .

$$C = \frac{g_{\text{O}}^2}{\kappa\gamma} \quad (1.75)$$

$$\eta_{\text{tot}} = \frac{\kappa_e}{\kappa} \eta \eta_{qe} \quad (1.76)$$

Using Eqs. (1.70) and (1.74) to (1.76), we can write an expression for the minimum total mechanical noise quanta, $n_{\text{imp,SN}} + n_{\text{BA,SN}}$, and the value of n_c at which this minimum total noise is achieved [12].

$$n_{\text{min}} = \frac{1}{2\sqrt{\eta_{\text{tot}}}} \quad (1.77)$$

$$n_c^{\text{SQL}} = \frac{1}{16C\sqrt{\eta_{\text{tot}}}} \quad (1.78)$$

Assuming perfect detection efficiency, $\eta_{\text{tot}} = 1$, then $n_{\text{min}} = 1/2$ and this is known as the standard quantum limit (SQL). For imperfect detection efficiency, $n_{\text{min}} > 1/2$, and the necessary intracavity photon number to reach this minimum noise quanta increases. A plot of the total measurement noise quanta, $n_{\text{imp,SN}} + n_{\text{BA,SN}}$, as a function of n_c , which illustrates these results is shown in Fig. 1.9.

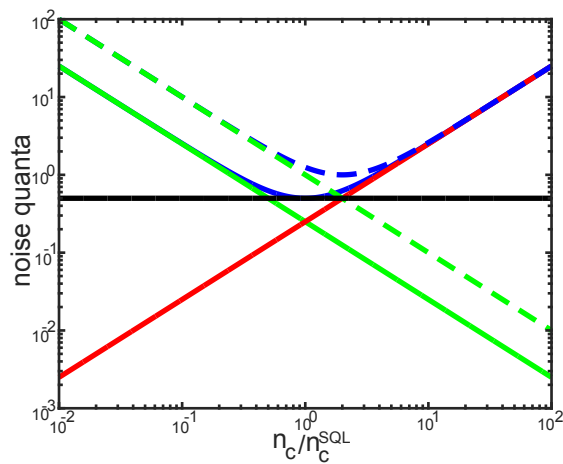


Figure 1.9: **Standard Quantum Limit.** This is a plot of the measurement noise quanta, $n_{\text{imp,SN}} + n_{\text{BA,SN}}$, versus a normalized intracavity photon number, n_c/n_c^{SQL} . The solid red line represents $n_{\text{BA,SN}}$. The solid (dashed) green line represents $n_{\text{imp,SN}}$ with $\eta_{\text{tot}} = 1$ ($\eta_{\text{tot}} = 1/4$). The solid (dashed) blue line represents the total noise quanta, $n_{\text{imp,SN}} + n_{\text{BA,SN}}$, with $\eta_{\text{tot}} = 1$ ($\eta_{\text{tot}} = 1/4$). The solid black line indicates the SQL, 1/2 quanta. Note that, for $\eta_{\text{tot}} = 1/4$, n_{min} has increased from the SQL value and so has the required n_c to reach that minimum.

Chapter 2

Chip-Scale Optomechanics

So far in Chapter 1, we have discussed the fundamentals of optomechanics in reference to the canonical Fabry-Pérot cavity. While this system accurately and intuitively models the physical interactions we will use in our experiments, our optical cavities do not visually resemble the Fabry-Pérot cavity depicted in Fig. 1.1. Rather, we utilized nano-scale photonic crystals patterned on silicon-nitride on silicon microchips. This chapter aims to explain the fundamentals of photonic crystals and their design and fabrication.

2.1 Introduction: Photonic crystals

The optical cavities studied in this work look like the structure shown in Fig. 2.1. This structure is an example of a photonic crystal and, because of its appearance, is called a “zipper” cavity. A photonic crystal is a regular array of dielectric material, often designed to alter the flow of light in interesting ways. Each of the “zipper” beams in Fig. 2.1, is a 1-D array of alternating indices of refraction. The beams are made of silicon nitride with index of refraction, $n = 2$, and the holes are air (or vacuum), $n \cong 1$. By patterning the beams in this way, light of a certain frequency (and polarization) cannot propagate down the length of the beam. Light at these certain frequencies coupled into the beam will undergo reflections and destructive interference causing cancellation. Then locally, in the center of the beams, the lattice constant (the spacing between the holes) is perturbed, allowing that certain frequency of light to exist in the center of each beam, with the ends of the beams acting effectively as mirrors. We call the center region where the lattice constant is perturbed the “defect” region. Then the two beams are moved in close proximity to one another such that the two optical modes are in the evanescent field of one another. This causes the modes to couple and “hybridize” producing “supermodes” that are of even or odd symmetry about the center of the gap. That is, the norm of the electric field has either a node (odd symmetry) or a significant contribution (even symmetry) at the center of the gap.

If one of the beams moves relative to the other, this will change the amount of electric field in

the dielectric, which, according to Eq. (2.1), will change the energy of the electric mode and thereby its frequency [13]. This provides the optomechanical coupling first defined in Section 1.1.

$$U_E = \frac{\epsilon_0}{4} \int d^3\mathbf{r} \epsilon(\mathbf{r}) |\mathbf{E}(\mathbf{r})|^2 \quad (2.1)$$

In Eq. (2.1), ϵ_0 is the permittivity of free space, $\epsilon(\mathbf{r})$ is called the dielectric function, $\mathbf{E}(\mathbf{r})$ is the electric field, and “bold” font indicates a vector.

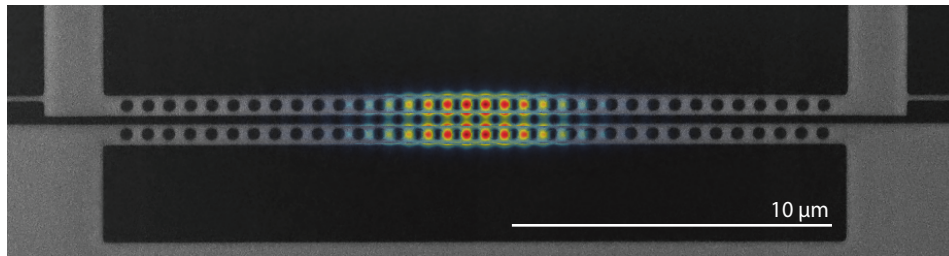


Figure 2.1: **1-D Photonic Crystal**. This figure shows an SEM image of an example “Zipper” 1-D photonic crystal along with an overlay of the norm of the electric field. The grey regions are silicon nitride and the black is vacuum.

2.1.1 Finding and Designing Photonic Crystal Modes

In Section 2.1, we presented an example 1-D photonic crystal. It remains an open question, however, how this mode was designed. An unparalleled introduction to the design of photonic crystals is given by the book “Photonic Crystals: Molding the flow of light” [13]. The derivations and intuitions presented below are presented and discussed much more thoroughly in that resource.

We begin, as most discussions about electromagnetism do, with Maxwell’s equations. We take the assumptions that there are no free charges or currents, the dielectric function, $\epsilon(\mathbf{r})$, is independent of time and frequency, and the magnetic permeability is equal to the vacuum permeability, μ_0 . Under these assumptions the Maxwell equations are as follows [13].

$$\begin{aligned} \nabla \cdot \mathbf{H}(\mathbf{r}, t) &= 0 & \nabla \times \mathbf{E}(\mathbf{r}, t) + \mu_0 \frac{\partial \mathbf{H}(\mathbf{r}, t)}{\partial t} &= 0 \\ \nabla \cdot [\epsilon(\mathbf{r}) \mathbf{E}(\mathbf{r}, t)] &= 0 & \nabla \times \mathbf{H}(\mathbf{r}, t) - \epsilon_0 \epsilon(\mathbf{r}) \frac{\partial \mathbf{E}(\mathbf{r}, t)}{\partial t} &= 0 \end{aligned} \quad (2.2)$$

In Eq. (2.2), $\mathbf{H}(\mathbf{r}, t)$ is the magnetic field, $\mathbf{E}(\mathbf{r}, t)$ is the electric field, and ϵ_0 is the permittivity of free space. Without loss of generality, we will look for harmonic solutions to the Maxwell equations, that is, we look for solutions of the following form.

$$\mathbf{H}(\mathbf{r}, t) = \mathbf{H}(\mathbf{r}) e^{-i\omega t} \quad (2.3)$$

$$\mathbf{E}(\mathbf{r}, t) = \mathbf{E}(\mathbf{r}) e^{-i\omega t} \quad (2.4)$$

Plugging in Eqs. (2.3) and (2.4) into Eq. (2.2) yields the following set of equations.

$$\begin{aligned} \nabla \cdot \mathbf{H}(\mathbf{r}) &= 0 & \nabla \cdot [\epsilon(\mathbf{r}) \mathbf{E}(\mathbf{r})] &= 0 \\ \nabla \times \mathbf{E}(\mathbf{r}) - i\omega\mu_0 \mathbf{H}(\mathbf{r}) &= 0 & \nabla \times \mathbf{H}(\mathbf{r}) + i\omega\epsilon_0 \epsilon(\mathbf{r}) \mathbf{E}(\mathbf{r}) &= 0 \end{aligned} \quad (2.5)$$

By taking the equation for the curl of $\mathbf{E}(\mathbf{r})$ and substituting it into the equation for the curl of $\mathbf{H}(\mathbf{r})$ we arrive at the eigenvalue equation for photonic crystals.

$$\nabla \times \left(\frac{1}{\epsilon(\mathbf{r})} \nabla \times \mathbf{H}(\mathbf{r}) \right) = \left(\frac{\omega}{c} \right)^2 \mathbf{H}(\mathbf{r}) \quad (2.6)$$

We have used $c = \sqrt{\frac{1}{\epsilon_0\mu_0}}$, which is the speed of light. Note that $\mathbf{H}(\mathbf{r})$ must still satisfy the divergence equation in Eq. (2.5). Also note, that once we have $\mathbf{H}(\mathbf{r})$, $\mathbf{E}(\mathbf{r})$ can be found by taking $\nabla \times \mathbf{H}(\mathbf{r})$ and using Eq. (2.5). This eigenvalue problem in Eq. (2.6) can be discretized and solved numerically. To solve for the eigenmodes of our full nano-structures, defect region and all, we use a finite-element analysis software called COMSOL [14]. However, trying to “fly-blind” and find an optical mode with high quality factor starting from Eq. (2.6) alone would be exceedingly difficult. We can gain the requisite intuition and knowledge about our system by fully utilizing the symmetry of the geometry.

Consider a dielectric geometry that has a 1-dimensional symmetry, such as the “zipper” device shown in Fig. 2.1, ignoring the defect region and the finite length of the beams. That is, the geometry is unchanged by translation by a vector $\mathbf{R} = n\mathbf{a}$, where n is an integer and \mathbf{a} is the lattice constant (spacing between the holes). Each unit of symmetry, in this case a length of \mathbf{a} , is called a unit cell. The magnetic field must be nearly identical from cell to cell. The only possible change from cell to cell can be a constant phase shift. Otherwise, one would be able to discern different parts of the identical crystal, which should be impossible [13]. This allows us to write the magnetic field as follows.

$$H(x) = e^{ikx} u_k(x) \quad (2.7)$$

In Eq. (2.7), x is the 1-D coordinate and \mathbf{k} is called the wave-vector, and $u(x)$ is periodic function of x (of period a). This formalism is discussed at length and with much more rigor in Ref. [13]. Note that \mathbf{k} is only defined modulo $\frac{2\pi}{a}$, $e^{i(k+n\pi/a)a} = e^{ika}$. This means that without loss of generality we can restrict $-\frac{\pi}{a} < k < \frac{\pi}{a}$, which is the so-called Brillouin zone.

Extending this argument to three dimensions leads to the Bloch formalism [13].

$$\mathbf{H}_{\mathbf{k}}(\mathbf{r}) = e^{i\mathbf{k} \cdot \mathbf{r}} \mathbf{u}_{\mathbf{k}}(\mathbf{r}) \quad (2.8)$$

Plugging this form into our eigenvalue equation yields the following eigenvalue problem.

$$(i\mathbf{k} + \nabla) \times \frac{1}{\epsilon(\mathbf{r})} (i\mathbf{k} + \nabla) \times \mathbf{u}_{\mathbf{k}}(\mathbf{r}) = \left(\frac{\omega(\mathbf{k})}{c} \right)^2 \mathbf{u}_{\mathbf{k}}(\mathbf{r}) \quad (2.9)$$

For each value of \mathbf{k} in the Brillouin zone, this equation can be solved numerically by discretizing one unit cell. We solve the 1-D version of this eigenproblem using MIT Photonic-Bands (MPB) [15]. This amounts to solving for the frequency, ω , as a function of the wave-vector, k . Plotting ω vs k is known as a band diagram. The band structure for a “zipper” structure very similar to the one shown in Fig. 2.1 is shown in Fig. 2.2a [16]. Note that instead of frequency ω in Fig. 2.2a, the lattice-normalized frequency $\omega_{\text{norm}} = \omega a / 2\pi c$ is shown, and k_{\parallel} is used to illustrate that the wave-vector is parallel to the length of the beams. Also note that the simulation was run for square holes and Fig. 2.1 has circular holes but this is a cosmetic difference that doesn’t impair our ability to learn everything we need from Fig. 2.2.

Note in Fig. 2.2, there is a black line denoting $\omega_{\text{norm}} = k_{\parallel}$. This is called the light line and the grey shaded region above it is called the light cone. The light cone represents the continuum of modes that are not confined to the beams, but rather extend in the air out to infinity. As the modes extend far beyond the beams, they resemble the free space plane wave solution [13]. For free space plane waves $\omega = c|\mathbf{k}| = c\sqrt{k_{\parallel}^2 + k_{\perp}^2}$ [13]. Since there is no restriction on k_{\perp} , $\omega > ck_{\parallel}$ can take on any value and hence the continuum of frequency states.

The most important bands of Fig. 2.2a are the first (lowest frequency) blue and red bands. The corresponding electric field energy density for the first blue (red) band at the band-edge is shown in Fig. 2.2b (Fig. 2.2c). The color of these bands signifies their symmetry. The blue bands are called “bonded” and they have significant electric field energy density in the gap between the two beams (as can be seen in Fig. 2.2b). Red bands are called “anti-bonded” and they have a node in the electric field energy density at the center of the gap (as can be seen in Fig. 2.2d). Note that there is not a complete band gap in Fig. 2.2a. Firstly, as previously mentioned, there are radiating modes at all frequencies inside the light cone. Coupling into these modes does not prevent radiation-limited

optical Q's reaching 1 million. Secondly, there is not a gap between the first bonded band and the first anti-bonded band. However, they are of different symmetry and thus coupling between them does not severely limit optical Q.

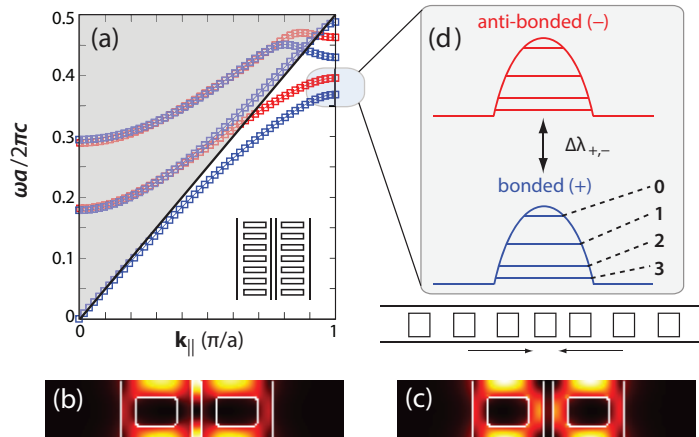


Figure 2.2: **1-D Photonic Crystal Band Diagram.** This figure is adapted from Ref. [16]. (a) shows the band diagram for the representative 1-D photonic crystal shown in the inset. The modes represented by the blue bands are called bonded and have different symmetry than the modes represented by the red bands, which are called anti-bonded. The electric field energy density at the band-edge for the bonded (anti-bonded) band is shown in (b) ((c)). Note how the bonded mode has significant energy density confined to the slot between the two beams, while the anti-bonded mode has a node there. (d) shows the frequency of the band-edges as the lattice constant is quadratically shortened. The most tightly bound, fundamental, modes are of the highest frequency.

As previously mentioned in Section 2.1, localized optical modes are created from this band diagram by locally perturbing the lattice constant in the center region of the “zipper” beams. Typical parameters used in this thesis are 16 mirror holes on each side and 17 defect holes in the center. The shortest defect lattice constant is $\sim 88 - 90\%$ the length of the mirror lattice constant, a_o . The transition into this shortest defect lattice constant is made gradual to avoid radiation loss by changing the lattice constant quadratically in the defect region [16]. These properties are plotted in Fig. 2.3. The result of shortening the lattice constant is to quadratically pull up the band-edge; see Fig. 2.2d. There will be a series of modes confined to this defect, and those of highest frequency are those that are most confined to the center defect region and hence the lowest order; again see Fig. 2.2d. The electric field energy density of these defect modes can be numerically simulated using Comsol and the first first three bonded modes are shown in Fig. 2.4 [16].

Once one has computed the optical modes shown in Fig. 2.4, one can use comsol to compute the optomechanical coupling [14]. For the structures presented in this thesis, the dominant source of optomechanical coupling is the moving dielectric boundaries. That is, mechanical motion of the optical beams in Fig. 2.4 will cause dielectric to move into and out of regions with electric fields. This will cause the electric mode energy to change and thereby also its frequency. These moving

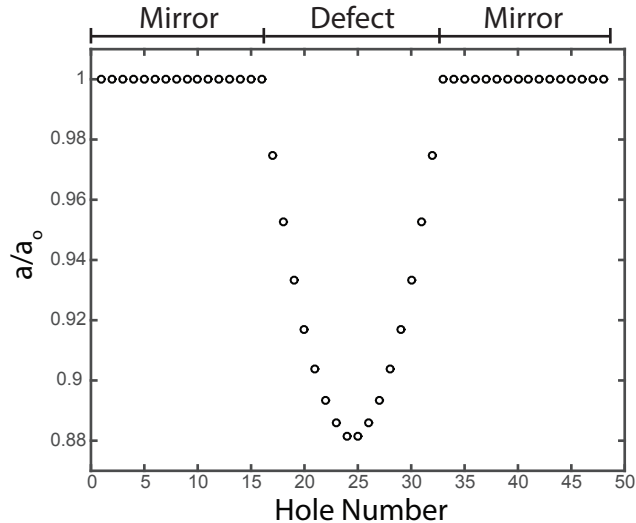


Figure 2.3: **Annotated Photonic Crystal.** This figure shows how the lattice constant varies over the length of the optical beam. The mirror and defect regions are labeled at the top of the figure. Typical designs have 16 holes in each mirror region and 17 holes in the defect region and vary the lattice constant quadratically to a minimum value of $\sim 88 - 90\%$ the length of the mirror region lattice constant, a_o .

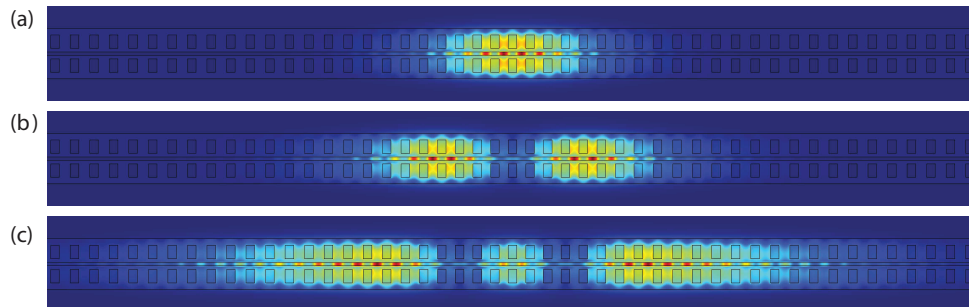


Figure 2.4: **Bonded Optical Modes.** (a),(b),(c) show the electric field energy density for the fundamental, second order, and third order bonded modes, respectively. Figure is adapted from Ref. [16].

boundary effects are not necessarily the only significant contribution to the optomechanical coupling, although they are in this work. The photoelastic effect where mechanical motion causes stress which changes the index of refraction and hence the optical cavity frequency can, in certain systems, be very important [17]. The optomechanical coupling due to the moving dielectric boundaries caused by mechanical motion is given by the following [18, 19].

$$g_{\text{OM}} = \frac{1}{2} \frac{\int dA (\mathbf{Q} \cdot \mathbf{n}) \left[\Delta\epsilon |\mathbf{E}_{\parallel}|^2 - \Delta(\epsilon^{-1}) |\mathbf{D}_{\perp}|^2 \right]}{\int dV \epsilon |\mathbf{E}|^2} \quad (2.10)$$

In Eq. (2.10), the top integral is performed over every moving surface and the bottom integral is done over the entire volume. \mathbf{Q} is the unitless displacement profile normalized so that the maximum displacement is 1. An example displacement profile is shown in Fig. 2.5. \mathbf{n} is the surface normal, $\Delta\epsilon = \epsilon_1 - \epsilon_2$, where ϵ_1 is the dielectric constant of the beams and ϵ_2 is the dielectric constant of air, $\Delta\epsilon^{-1} = \epsilon_1^{-1} - \epsilon_2^{-1}$. \mathbf{E}_{\parallel} is the component of the electric field parallel to the surface. $\mathbf{D} \equiv \epsilon\mathbf{E}$ is electric displacement and thus \mathbf{D}_{\perp} is the electric displacement component perpendicular to the surface.

As previously mentioned, Comsol also returns the radiation-limited optical Q-values for the modes. That is, the optical Q as given by the optical mode’s coupling to the continuum of modes inside the light cone. Taken together, Comsol is a tool that allows one to optimize a photonic crystal structure for highest g_{OM} and radiation-limited optical Q-factor, Q_o . Using Comsol’s Matlab interface and Matlab’s “fminsearch” algorithm, a wide range of parameter space can be opened up in order to optimize the structure (see, for example, Ref. [20]). Many of the photonic crystals used in this thesis are the result of an optimization procedure that allowed the holes to be elliptical and the defect to be formed by both shrinking the lattice constant quadratically and shrinking the hole size linearly in the defect region.

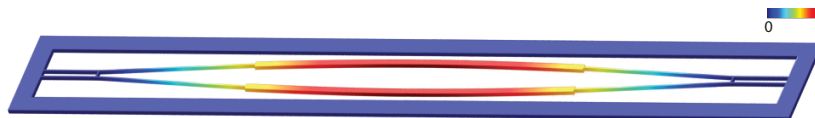


Figure 2.5: **Example Displacement Field.** This figure shows the displacement field for the fundamental in-plane differential mechanical mode of a zipper cavity. When properly normalized, dark red (dark blue) represents unit (zero) displacement.

2.2 Coupling to Nano-scale Optical Cavities

In Section 2.1.1, we described how we design the optical modes of our photonic crystals. The question remains, however, of how do we couple laser light into and out of these optical cavities. In other words, how do we actually implement the coupling waveguide cartoon illustrated in Fig. 1.2. The work in this thesis has utilized several different coupling techniques, which are outlined below.

The most common tool we use to get light into and out of our structures is a dimpled, tapered optical fiber [21]. A tapered optical fiber is made by locally heating the center of a length of standard optical fiber and slowly pulling the ends. This causes the width of the optical fiber to decrease until its final diameter is $1 - 2 \mu\text{m}$. At these thinned diameters, light is no longer totally internally reflected as it travels down the fiber. Instead, the light evanescently extends outside of the tapered

fiber. A dimple is added to the tapered region to allow testing of individual devices on a planar microchip array, see Fig. 2.6 [21]. If the evanescent field of the tapered fiber is placed in the near field of one of our photonic crystal optical modes, a two sided coupling scheme (as described in Fig. 1.2) results, see Fig. 2.7. The strength of the coupling to the waveguide, κ_e , is determined by the distance between the tapered fiber and the optical cavity. By carefully moving the fiber taper using attocube nano-positioners, we can choose κ_e , which is a definite advantage of this coupling scheme. Note, however, that this coupling scheme is double-sided. Light from the optical cavity is just as likely to couple forwards or backwards into the tapered fiber. In principle, one could collect both the reflected and transmitted light and combine them to obtain all the light from the cavity. In practice, doing so in a phase-coherent way is extremely difficult, and not done in this thesis. Therefore, this double-sided coupling technique involves a necessary efficiency hit.

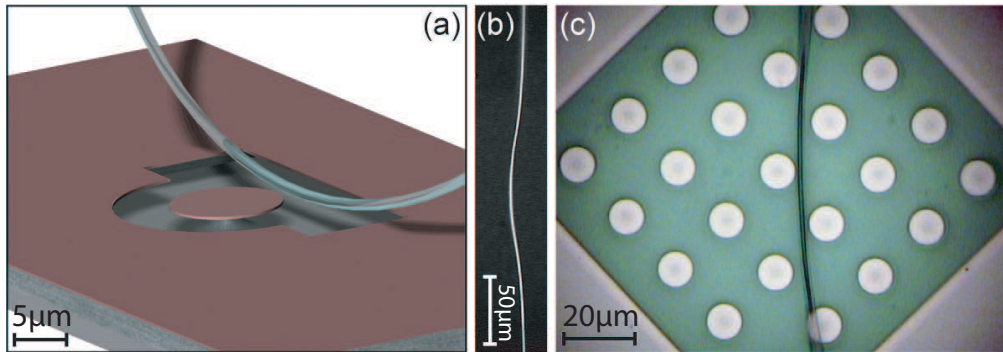


Figure 2.6: **Dimpled Tapered Optical Fiber.** This figure is taken from Ref. [21]. (a) Shows a cartoon of a dimpled, tapered optical fiber coupling to a microdisk resonator. (b) Shows an optical microscope image of a dimpled tapered fiber. (c) An optical microscope image showing a dimpled, tapered optical fiber in the midst of an array of optical resonators, demonstrating its advantage of being able to rapidly test several devices on a planar chip.

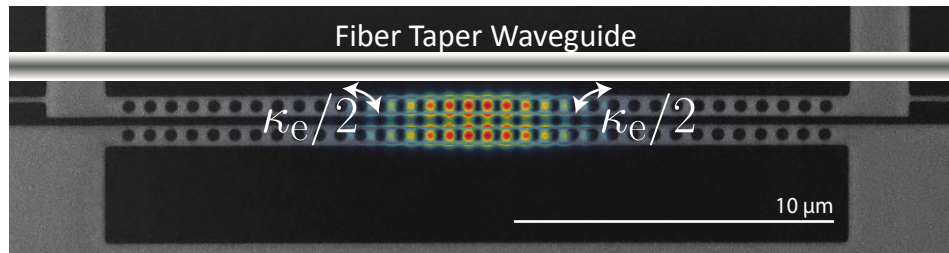


Figure 2.7: **Tapered Optical Fiber coupled to Photonic Crystal.** This figure illustrates a dimpled, tapered optical fiber placed in the near field of the photonic crystal cavity mode. This allows light to be coupled into and out of the cavity via the tapered fiber. Note, however, that this coupling scheme is inherently double-sided.

The work in this thesis also employs single-sided coupling techniques. One single-sided coupling method involves placing the dimpled, tapered optical fiber onto an on-chip waveguide with adia-

batically changing width, which routes the light to the optical cavity and back on reflection. The development of this coupling scheme is discussed in Ref. [22] and is described in Fig. 2.8, which is a figure taken from that paper.

The working principle behind the adiabatic coupler is as follows. The tapered fiber has a fundamental optical mode with an effective index, $n_{\text{eff,taper}}$, see Fig. 2.8a. The fundamental optical mode of the on-chip waveguide has an effective index that is dependent on its width, w , $n_{\text{wg}}(w)$. When the optical fiber is placed on top of the on-chip waveguide, a series of combined super-modes are formed. When the effective index of the fiber is much larger than the effective index of the on-chip waveguide, the super-mode of the fundamental modes looks like the bare optical mode (see Fig. 2.8a-b). When the converse is true, the fundamental super-mode looks like the bare waveguide mode. If the transition between these two regimes is made slowly enough, i.e. adiabatically, nearly 100% of the optical energy in the tapered fiber mode can be converted to the on-chip waveguide mode and vice-versa. The adiabatic condition is $\lambda_o \frac{dn_{\text{wg}}}{dy} \ll 2\pi |\Delta n_{\text{eff}}|^2$, where λ_o is the free-space wavelength of light, y is the spatial coordinate along the length of the waveguide, and Δn_{eff} is the effective index difference between two super-modes. In other words, the change in the effective index of the waveguide in the span of one wavelength must be much less than the square of the index difference between two super-modes [22]. Note that Fig. 2.8 was made for a coupler fabricated in silicon. However, nearly identical results are obtained in silicon nitride if the on-chip waveguide width is scaled by roughly the ratio of the refractive indices, $n_{\text{Si}}/n_{\text{SiN}}$, so that its effective index can match that of the optical fiber.

Once light is coupled into this adiabatic waveguide, there are two methods used in this thesis to couple that light into the photonic crystal cavity. The first option is called “side-coupling”, where the waveguide enters the near-field of the photonic crystal from the side. The coupling between the optical cavity and this side waveguide, κ_e , is set lithographically by the lateral distance between the waveguide and the cavity. The waveguide is terminated in a photonic crystal mirror section, sending all light back out on reflection through the tapered fiber. This scheme is shown in Fig. 2.9.

The other method is called “end-coupling”, where the waveguide terminates into one of the photonic crystal beams itself. In this case we must, again, adiabatically transition from the waveguide to the cavity to avoid scattering and losses into spurious modes. This is accomplished by slowly tapering-up the hole sizes on the input side of the photonic crystal. In this geometry, κ_e is set by the number of mirror holes placed on the input side of the photonic crystal (usually one or zero). This “end-coupling” method is shown in Fig. 2.10.

There is one final optical waveguide coupling technique used in this thesis that does not employ the dimpled, tapered optical fiber at all. This technique is called “V-groove” coupling [12]. We fabricate a V-groove in the thick silicon layer below the silicon nitride device layer (how this is done will be discussed in Section 2.4). A cleaved optical fiber is then glued into place in this V-groove.

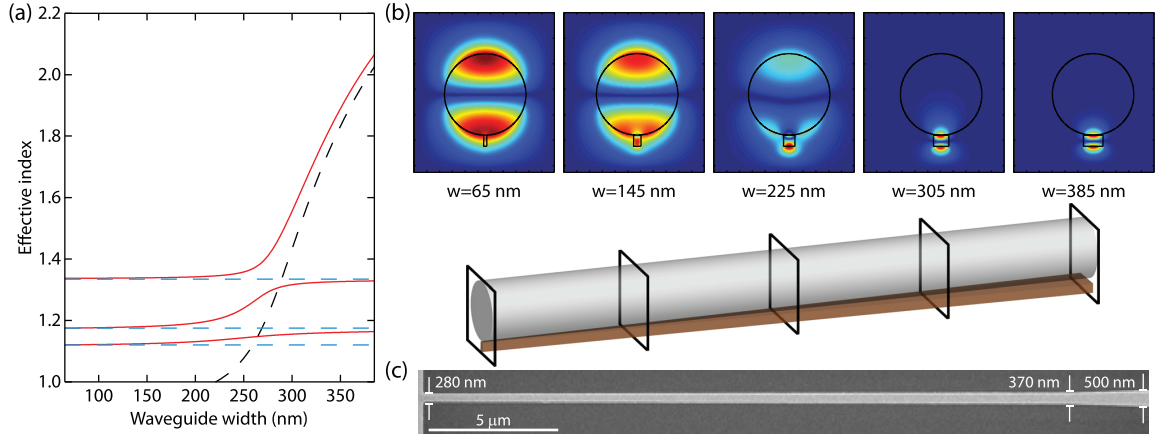


Figure 2.8: **Adiabatic Waveguide Coupler**. This figure is taken from Ref. [22]. (a) The blue dashed lines represent the optical modes of the bare optical fiber. The mode with highest effective index, n_{eff} , being the fundamental. The black dashed line shows the effective index of the fundamental on-chip waveguide mode as a function of its width. The solid red curves show the super-modes of the combined optical fiber, on-chip waveguide system. Note especially the top red band, which shows the effective index of the super-mode of the fundamental optical fiber mode and fundamental waveguide mode, which starts off nearly identical to the fiber mode at small waveguide widths and ends nearly identical to the waveguide mode at large waveguide widths. (b) (top) shows the optical mode profile for various on-chip waveguide widths. (bottom) Three dimensional illustration of a tapered optical fiber sitting on a waveguide whose width is adiabatically increasing. (c) SEM image of the on-chip adiabatic coupler. Note that the device in this figure was made in silicon; however, the same results can be achieved in silicon nitride by scaling the waveguide widths roughly by the ratio of the refractive indices, $n_{\text{Si}}/n_{\text{SiN}}$.

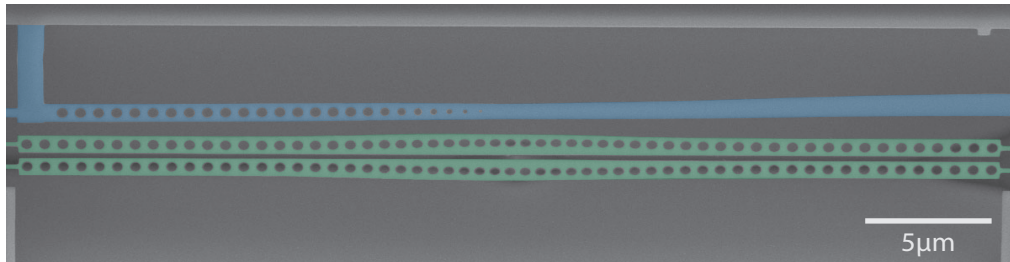


Figure 2.9: **On-chip waveguide “side-coupling”**. This figure shows an example of a side-coupled photonic crystal cavity used in this thesis. The photonic crystal cavity is highlighted in green and the side-coupling waveguide is highlighted in blue. Note how the side-coupling waveguide is terminated in a series of mirror holes so that all light can be reflected and collected in a single detection channel. Also note how these mirror holes in the blue beam start off small and adiabatically taper up in size. This prevents scattering into spurious modes.

In the ~ 400 nm thick silicon nitride layer, a rectangular cross-section waveguide is defined and suspended over the V-groove, see Fig. 2.11. By adiabatically tapering the width of this on-chip waveguide, its mode profile is made to evanescently extend beyond the waveguide and match the profile of the optical mode emitted by the cleaved fiber. Mode overlaps of 95% are possible, which

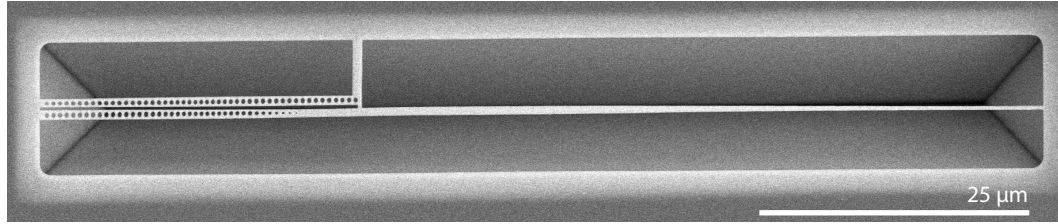


Figure 2.10: **On-chip waveguide “end-coupling”**. This figure shows an example end-coupled photonic crystal cavity used in this thesis. The “input” side of the photonic crystal is the right hand side of the bottom beam. Note how the holes here start off much smaller and slowly taper up in size. This adiabatic change prevents scattering into spurious modes. Also note that the number of mirror holes on the input coupler side is much smaller, which enables light to escape out the end of this beam.

allows for efficient coupling [12]. Once light is coupled into the on-chip waveguide it is routed to the photonic crystal cavity and coupled back out on reflection. This coupling is very useful for sensing applications because the fiber is rigidly glued in place in the v-groove, which is much more robust than dimpled, tapered fiber testing.

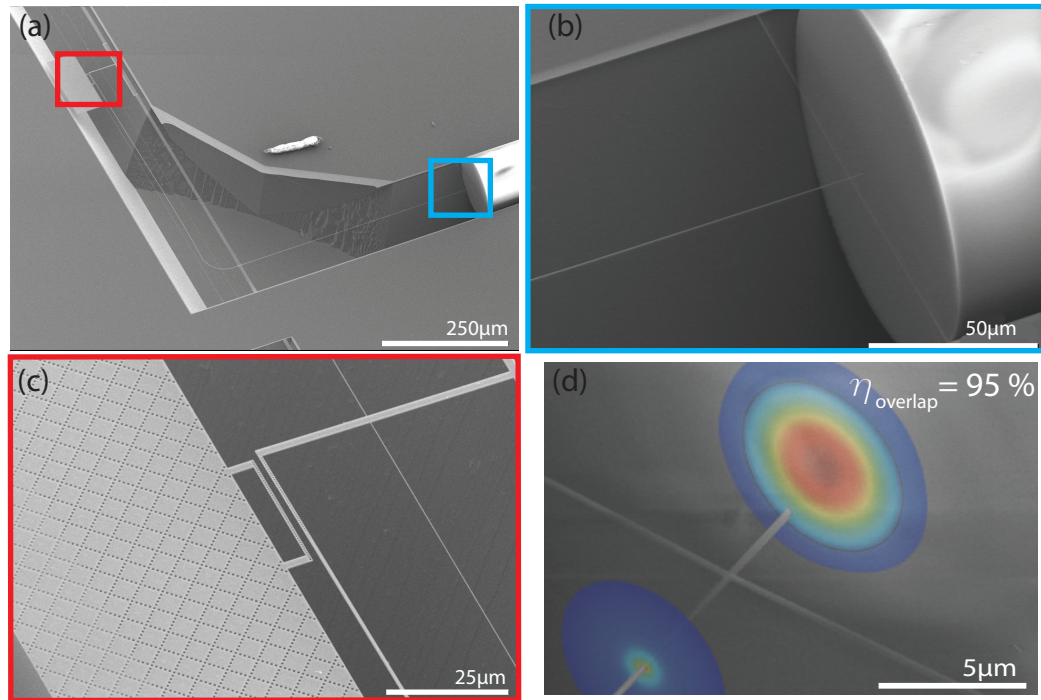


Figure 2.11: **V-groove Coupling**. (a) shows one of our accelerometer devices coupled to a tapered on-chip waveguide, which, in turn, is coupled to a cleaved optical fiber that has been glued into a V-groove in the silicon layer. (b) shows a close-up of the tapered on-chip waveguide nearly butted up against the cleaved face of the optical fiber. (c) shows the end-coupled optical cavity. (d) shows the overlap between the tapered waveguide mode and the optical fiber mode. Figure (d) is taken from Ref. [12].

2.3 High-Stress Silicon Nitride Mechanical Resonator Design

The mechanical modes used and studied in this thesis are made of high stress silicon nitride nano-strings that are 100's of nm wide, 400 nm thick, and 100's of microns long. See Fig. 2.5 for an example. We call the mechanical modes nano-strings because their mechanical frequencies are given by the same equation as for a taught string on a violin [23].

$$f_i = \frac{i}{2L} \sqrt{\frac{\sigma}{\rho A}} \quad (2.11)$$

In Eq. (2.11), i is the mode number, L is the length of the string, σ is the in-plane stress, ρ is the density of the material, and A is the cross-sectional area.

We use silicon nitride (SiN) to make the nano-string resonators (see Fig. 2.5) because of its well-known very high mechanical Q's at room temperature [23–27]. We use ~ 400 nm thick, high in-plane stress ($\sigma = 800$ MPa), silicon nitride layers that are low pressure chemical vapor deposited (lpcvd) onto silicon handle wafers purchased from Silicon Valley Microelectronics. During the high temperature deposition process Si-H and N-H bonds are dissociated, causing a decrease in hydrogen concentration and an associated shrinkage of the film size. This shrinkage is the source of the tensile stress in the films [28].

Highly stressed silicon nitride is an unusual material. Its structure is glassy (a.k.a. disordered, amorphous, or non-crystalline), yet its mechanical Q's can be three orders of magnitude higher than that of other glassy materials, and even an order of magnitude larger than some single-crystal silicon resonators at room temperature [24]. If the stress of the mechanical element is relieved, e.g. by looking at a cantilever instead of a stressed string mode, the mechanical Q drops by orders of magnitude [23, 24]. This clearly indicates that high stress is the cause of the high mechanical Q, but why?

The quality factors of these resonators can be well-modeled by assuming a small imaginary part to the material's young's modulus, which will cause energy dissipation as mechanical motion induces material strain [25]. This strain variation has two components; one due to stress-induced elongation of the string, and one due to local bending of the string. The bending contribution to the energy loss is completely dominant [25]. At the same time, the energy stored in the mechanical mode increases greatly with added stress (see Fig. 2.12 taken from Ref. [25]). Taken together, this means adding stress greatly increases the mechanical energy while basically leaving the dissipation unchanged. Thus, adding stress greatly increases the mechanical quality factor.

Continuing this line of reasoning, we can make the argument that the mechanical Q of the string, Q_{string} , is given by the ratio of the tension energy to the bending energy multiplied by the bending loss limited Q, Q_{bending} [27].

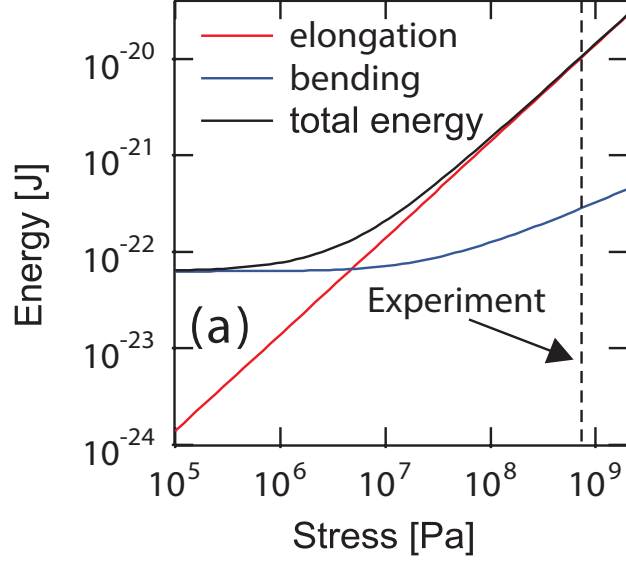


Figure 2.12: **Mechanical Energy vs Stress.** This figure demonstrates that, at the film stress levels used in this work, the relatively lossless elongation energy of the nano-string dominates over the lossy bending energy. Figure taken from Ref. [25]

$$Q_{\text{string}} \approx \frac{E_{\text{tension}}}{E_{\text{bending}}} Q_{\text{bending}} \quad (2.12)$$

$$\approx \frac{\frac{1}{2} \sigma A \int_0^L \left[\frac{\partial}{\partial x} u(x) \right]^2 dx}{\frac{1}{2} EI \int_0^L \left[\frac{\partial^2}{\partial x^2} u(x) \right]^2 dx} Q_{\text{bending}} \quad (2.13)$$

In Eq. (2.13), σ is the in-plane tensile stress, A is the cross-sectional area, L is the length of the string, E is the young's modulus, I is the geometrical moment of inertia, and $u(x)$ is the displacement of the string. A plot of $u(x)$ is shown in Fig. 2.13, adapted from reference [27]. Note that the ideal displacement profile would be a sine wave, but this does not satisfy the boundary conditions that both the displacement and slope must disappear at the clamp points. The result is the kink at the ends of the string for the actual displacement profile. The result of carrying out the math in Eq. (2.13) yields the following [27].

$$Q_{\text{string}} \approx \left[\frac{n^2 \pi^2 E}{12 \sigma} \left(\frac{h}{L} \right)^2 + 1.0887 \sqrt{\frac{E h}{\sigma L}} \right]^{-1} Q_{\text{bending}} \quad (2.14)$$

In Eq. (2.14), n is the mode number and h is the width of the string in the direction of motion. The second term in the bracket is due to bending at the clamp points, and the first term is due to bending of the string at all other points. The result shows that strings should be made as long and

as thin as possible to maximize Q_{string} . This makes sense because, as the string is made longer, all bends of the string are made smaller and more gradual. Also of note is that for long strings, $L \gg h$, Q_{string} is limited by bending losses near the clamp points.

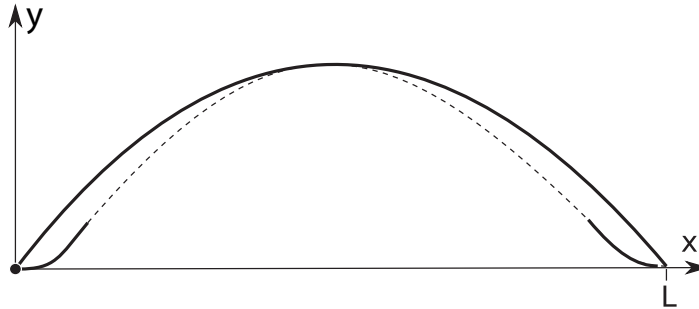


Figure 2.13: **String Displacement Profile.** This figure shows the displacement profile, $u(x)$, for a stressed string. The solid black line shows the “ideal” sinusoidal displacement. The dashed black line shows the actual displacement. Note that the ends of the dashed lines have been made solid to emphasize the kinks near the clamp points. Figure adapted from Ref. [27]

A question remains about the source of the bending losses. This is still a topic of some discussion in the literature. Although, it appears likely that the losses are the result of some localized two-level defect states whose energy spectra couple to the local strain field [25, 26]. Reasonable candidates for such a two-level systems are atomic configurational changes of the glassy, amorphous material and hydrogen defects inherent to the lpcvd deposition process [26].

2.4 Nanofabrication Techniques

In this section, we discuss the general nanofabrication techniques used to actually create the devices studied in this thesis. Fig. 2.14 shows the general outline of our single lithography fabrication process. We start with $1\text{ cm} \times 1\text{ cm}$ chips consisting of a 200 or 500 micron thick silicon layer with $\sim 400\text{ nm}$ high stress silicon nitride layers on top and bottom, Fig. 2.14a. Next, $\sim 500\text{ nm}$ of Zeon Chemicals’ electron beam resist, ZEP-520a, is spun onto the top surface of the chip (Fig. 2.14b). This is accomplished by putting the chip on a vacuum chuck, then placing a couple drops of ZEP-520a on the surface, and then spinning the chuck at $\sim 2000\text{ rpm}$ using a Headway Research Inc. model PWM32 spinner.

The electron beam resist undergoes a physical change when exposed to high energy electrons, which allows one to write a pattern in it using a finely focused electron beam, Fig. 2.14c. We used the Leica Microsystems EBPG-5000+ electron beam pattern generator (EBPG) in the Kavli Nanoscience Institute at Caltech. After the pattern is written by the EBPG, the chip is lightly

shaken in Zeon Chemicals' ZEP-520a developer named ZED-N50 for 2.5 minutes and then rinsed in methyl isobutyl ketone for 0.5 minutes, Fig. 2.14d. This dissolves the regions of the electron resist that were exposed to the electron beam, thereby revealing the written pattern in the resist.

However, having our pattern written in the highly specialized resist material is not of particular interest. We need a method to transfer that pattern into the silicon nitride layer that we're interested in. This is accomplished by inductively coupled plasma - reactive ion etching, ICP-RIE (also referred to as dry etching), using an Oxford Instruments Plasmalab 100 System ICPRIE 180, Fig. 2.14e. Our chip is placed on a silicon carrier wafer in a vacuum chamber and then a flow of C_4F_8 and SF_6 gases are introduced for a so-called pseudo-bosch etch [29, 30]. The gas is ionized into a plasma by excitation from an radio-frequency electromagnetic field and a DC bias is formed between the plasma and the device surface, which causes ions to slam into the surface of the chip. An excellent description of the pseudo-bosch etch process can be found in Refs. [29, 31]. The SF_6 gas molecules are responsible for the etching of the silicon nitride. Upon ionization these molecules split into SF_x and F_y which etch by physically milling the surface due to the bias voltage. This process produces an ideal vertical sidewall etch. Additionally, however, the F_y ions also chemically etch the silicon nitride isotropically. This is why the C_4F_8 gas is also used. Upon ionization C_4F_8 splits into CF_2 and C_2, C_3 . The CF_2 cross-links to form long teflon-like polymer chains, which protect the sidewalls of the etch from chemical reaction. Thus when used in conjunction properly SF_6 and C_4F_8 can produce a smooth vertical sidewall etch. Typical plasma etch parameters for our Oxford ICPRIE can be found in table 2.1.

After the dry etch, the remaining e-beam resist is removed in a "piranha" solution (Fig. 2.14f). The piranha solution is a 4:1 mixture of sulfuric acid and hydrogen peroxide. It is a powerful oxidizer that completely removes organics from the surface of the chip [32, 33].

Next the chip is rinsed in de-ionized (DI) water and placed in a potassium-hydroxide (KOH) and water solution that is 30% KOH by weight and at a temperature of approximately $80^\circ C$, Fig. 2.14g. Importantly, KOH etches different crystal planes of silicon at drastically different rates [34-36]. Specifically, KOH can etch the $\langle 100 \rangle$ plane of silicon up to a factor of 200 times faster than the $\langle 111 \rangle$ plane [37]. If the KOH etch is sufficiently long, a V-groove will form in the silicon layer with the sloped walls of the V-groove set by the $\langle 111 \rangle$ planes; see Fig. 2.15.

Finally the chip is rinsed in DI water, cleaned in another piranha bath, rinsed again, transferred to an isopropyl alcohol (IPA) bath, and then dried in a critical point dryer (CPD), Fig. 2.14h-i. What results is a device with free-standing regions of silicon nitride. Often our structures are at low-frequency and therefore floppy and fragile. If water is allowed to dry on the chip, the devices will collapse due to surface tension and become useless. Therefore, we use a Leica EM CPD300 critical point drying machine to dry our chips while avoiding destructive surface tension. The CPD replaces the IPA bath with liquid CO_2 (LCO_2), and the CPD chamber is then subjected to a temperature

and pressure regimen that navigates around the critical point of CO_2 . Thus, the transition is made from liquid to gas without a phase transition and surface tension is avoided.

Of final note, care must be taken after introducing samples to a wet etchants. During all wet etches and rinses, the sample must not be lifted out of the liquid or else the air-liquid interface surface tension can destroy devices. Also, while in the liquid, quick movement can cause viscous forces that can destroy devices. To avoid these forces, we transfer our devices from liquid to liquid using a holder that carries some of the liquid along with it, shown in Fig. 2.16. This method is described in great detail in Ref [38].

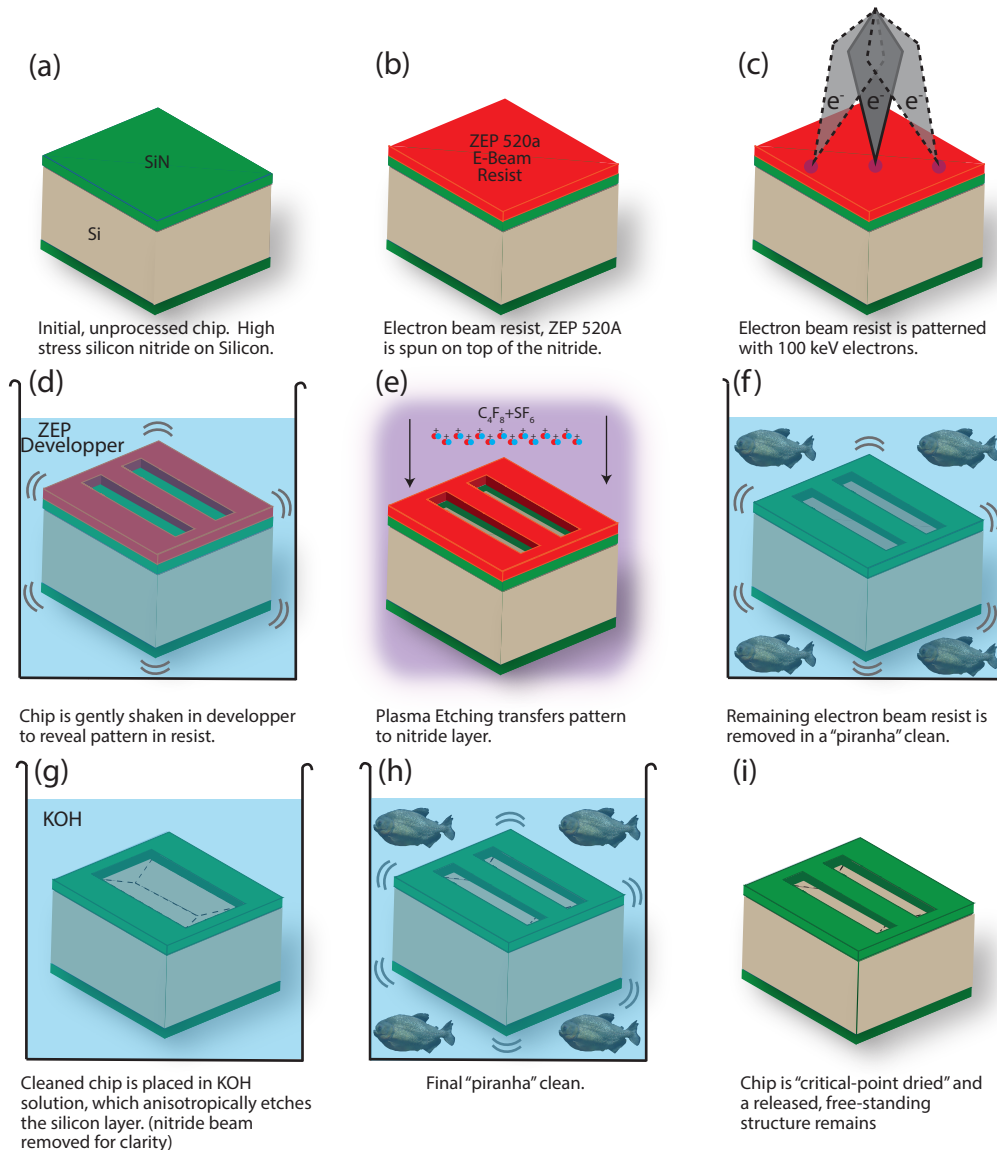


Figure 2.14: **Nanofabrication Steps.** The processes are described in greater detail in the main text. Piranha photo was taken by Greg Hume.

Parameter	Measured Value
C_4F_8 Flow [sccm]	29.0
SF_6 Flow [sccm]	12.0
RF Power [W]	27 (6)
ICP Power [W]	969 (2)
DC Bias [V]	81
Table Temperature [°C]	20
Chamber Pressure [mTorr]	14.4
Helium Backing Pressure [Torr]	10
Helium Flow [sccm]	5.6
Etch Time [min:sec]	6:35

Table 2.1: **Pseudo-Bosch Plasma Etch Parameters.** These are typical etch parameters to produce a near-vertical sidewall pseudo-Bosch etch in our 400 nm thick, high-stress, silicon nitride layers in our Oxford Instruments PlasmaLab System 100 ICPRIE 180. The RF power accelerates the ions towards the sample and is thus responsible for the physical milling of the chip. The DC bias is the voltage between the sample surface and the plasma and is largely determined by the RF power. The ICP (inductively coupled plasma) power strikes the plasma and largely sets the ion density. The numbers in parentheses for both the ICP and RF powers are the measured reflected powers. The helium backing pressure provides a good thermal link between the etch wafer and the table for repeatable etch temperatures. The helium flow is the flow required to maintain the specified helium backing pressure. All of these etch parameters are discussed in much more detail in Ref. [31].

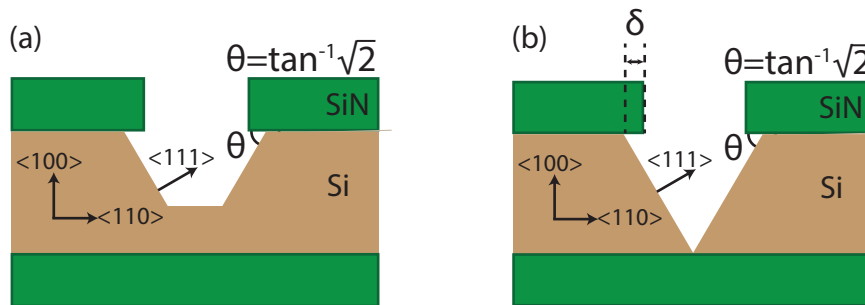


Figure 2.15: **KOH etch geometry.** This figure illustrates how KOH etches silicon. The $\langle 100 \rangle$ and $\langle 110 \rangle$ crystallographic planes are readily etched, while the $\langle 111 \rangle$ planes are hardly etched at all. If the KOH etch time is insufficient to fully define the V-groove the etch profile is as shown in (a). Otherwise, a V-groove results as shown in (b). The angle of the V-groove is given by $\tan^{-1}(\sqrt{2})$. The undercut distance is defined as δ . It is set by the finite etch rate of $\langle 111 \rangle$ crystal plane and how deep into the silicon the dry-etch of the silicon nitride layer penetrated. This figure is adapted from Ref. [39].

2.4.1 Double-sided Lithography

Using the single-lithography nanofabrication methods detailed in Section 2.4, we can obtain free-standing structures in the silicon nitride layer. For some devices in this thesis, we wish to increase the mass by suspending regions of the entire chip (silicon layer and all). This can be accomplished by adding a few fabrication steps as outlined in Fig. 2.17.

For double-sided lithography we use a 200 micron silicon layer. During the first electron-beam

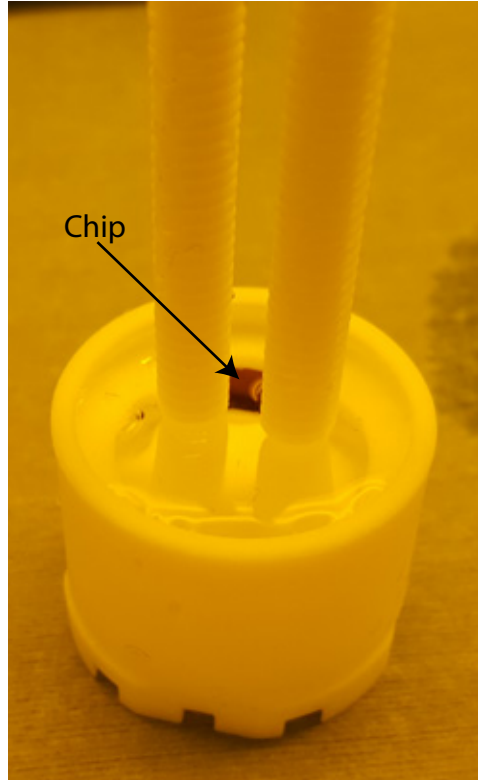


Figure 2.16: **Wet Etch Chip Carrier.** This is the teflon holder used to transport transport chips while submerged in liquid. It is made of teflon so that it does not react with various etchants we use. The chip is held vertically in a groove in the base of the piece. Two teflon screws in the center prevent liquid from flowing out of holes in the bottom piece. When this holder is submerged in a new liquid rinse or etchant, the screws are removed, allowing the old liquid to drain and the new liquid to enter.

lithography step on the bottom side of the chip, alignment markers are included (Fig. 2.17c). After the pattern is dry-etched into the silicon nitride layer, the chip is flipped and Shipley's S1813 photoresist is spun on. Using the Kavli Nanoscience Institute's Karl-Suss optical lithography tool, the bottom side of the chip is imaged and a topside photolithography mask with the same alignment markers is aligned to the bottom set (Fig. 2.17e). After ultraviolet light (UV) exposure, the topside alignment markers are developed and dry-etched into the topside silicon nitride, Fig. 2.17f-g. Zep 520a is then spun on the topside, note that the alignment marks remain visible through the resist. This allows using the EBPG to write a pattern on the topside that is aligned to the pattern on the bottom-side, Fig. 2.17h. From here, the subsequent fabrication steps are the same as in Section 2.4. The one exception is that isopropyl alcohol (IPA) is added to the KOH solution to prevent significant etching of convex corners [36, 37]. The new KOH solution is 20% KOH, 64% water, and 16% IPA by weight heated to approximately 79°C . If the openings written in the silicon nitride layer are large enough, KOH can etch all the way through the silicon layer before stopping at the V-shape. The

result is a device where entire sections of the chip have been suspended (Fig. 2.17).

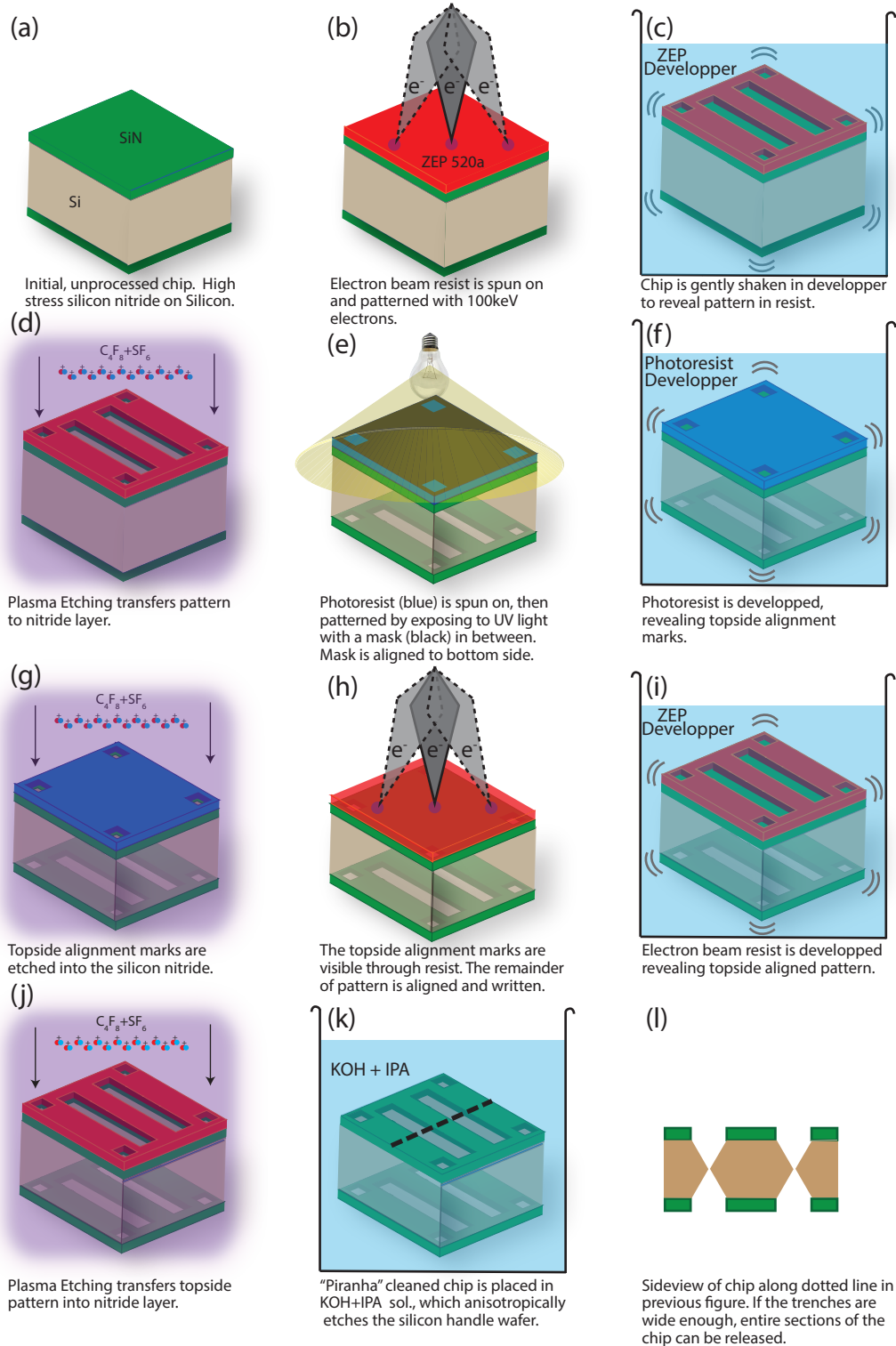


Figure 2.17: **Double-Sided Nanofabrication Steps.** The processes are described in greater detail in the main text.

Chapter 3

Optomechanical Feedback Cooling [2]

3.1 Introduction

In this chapter optical measurement of the motion of a 940 kHz mechanical resonance of a silicon nitride nanostring resonator is demonstrated with read-out noise imprecision reaching 37 dB below that of its zero-point fluctuations. Via intensity modulation of the optical probe laser, radiation pressure feedback is used to cool and damp the mechanical mode from an initial room temperature occupancy of $\bar{n} = 6.5 \times 10^6$ ($T = 295$ K) down to a phonon occupation of $\langle n \rangle = 66 \pm 10$, representing a mode temperature of $T_m \approx 3$ mK. The five decades of cooling is enabled by the system's large single-photon cooperativity ($C_1 = 4$) and high quantum efficiency of optical detection ($\eta_{tot} = 0.27$). This chip-scale microresonator, operating in a room temperature environment, yet close to its quantum ground state of motion, has a thermal-noise-limited force sensitivity of $125 \text{ aN}/\sqrt{\text{Hz}}$ and a bandwidth of 190 kHz.

Resolved-sideband radiation pressure cooling has recently been demonstrated as an effective means to cool a targeted mechanical resonance of a structure close to its mechanical ground-state of motion [3, 4]. This technique, sharing similar physics to the resolved-sideband cooling of trapped ions [40], requires spectral filtering of the upper (anti-Stokes) motional sideband from the lower (Stokes) motional sideband by a high-Q-cavity in which the cavity linewidth (κ) is narrower than the mechanical resonance frequency (ω_m). To date, experiments involving resolved-sideband cooling of mesoscopic mechanical objects to their quantum ground-state have relied on cryogenic pre-cooling using conventional refrigeration means. Bath temperatures $\lesssim 100$ mK are utilized for microwave devices [4] to enable high-Q superconducting cavities, whereas in the optical domain [3] more modest bath temperatures of ~ 10 K in a helium cryostat have been employed to, among other things, reduce intrinsic mechanical damping.

An alternative method of radiation pressure cooling, one which is more amenable to lower

frequency mechanical resonators, relies on low noise optical read-out of mechanical displacement combined with active feedback of the optical probe intensity [41–43]. Previous optomechanical feedback cooling experiments [44–51] have demonstrated the ability to cool a wide range of mechanical resonators, from suspended large scale kilogram mass mirrors [48] to optically levitated microspheres [46, 47]. Although these experiments have realized substantial cooling, reaching the quantum mechanical ground-state of motion using active feedback cooling remains an illusive goal due to the stringent requirements on the measurement imprecision and the mechanical resonator Q-factor. Cooling to the ground-state requires a displacement measurement capable of resolving motion at the level of the quantum zero-point fluctuations of the mechanical resonator within its thermal decoherence time, or equivalently achieving a measurement rate greater than the thermal decoherence rate, and with a back-action close to the Heisenberg limit [4, 9, 52, 53]. This regime has recently been approached in several cavity-optomechanical systems at liquid helium temperatures [53–55], with feedback cooling of a MHz-frequency nanostring resonator being demonstrated in Ref. [53] down to an occupancy of 5 phonons. Here we set out to explore the limits of feedback cooling of a photonic crystal nanostring structure in a room temperature environment suitable for a broad range of sensing applications, and achieve a room-temperature phonon occupation for a mesoscopic mechanical resonator lower than any other previously demonstrated result (to the best knowledge of the author).

3.2 Feedback Cooling Theory

In this section we will discuss the mathematical formalism and basic results of feedback cooling. We start in Section 3.2.1 with the conceptually easiest case – feedback cooling without measurement noise. In reality, of course, there will always be measurement noise that will enter your feedback signal and, accordingly, we analyze feedback cooling with noise in Section 3.2.2. Finally, in Section 3.2.3, we discuss the specific case of optomechanical feedback cooling adopting a quantum picture. Note that for the experimental results presented in this chapter, the measurement noise floor is not significant and, therefore, a lot of the appropriate intuition can be obtained from Section 3.2.1.

3.2.1 Noiseless Feedback Cooling

We begin this section on feedback cooling in the absence of measurement noise by considering the mechanical equation of motion. This was discussed in Section 1.4 and given in Eq. (1.30), and is repeated below for convenience.

$$m\ddot{x} + m\gamma\dot{x} + m\omega_m^2 x = F_{\text{th}}. \quad (3.1)$$

In Eq. (3.1) x is the generalized position coordinate of the mechanical resonator, m is the effective mass of the resonator (see Eq. (1.38)), $\gamma_i = \frac{\omega_m}{Q_{m,i}}$ is the intrinsic mechanical damping rate, ω_m is the mechanical frequency, $Q_{m,i}$ is the intrinsic mechanical quality factor, and F_{th} is the random thermal force. We are taking extra care to denote the intrinsic properties of the system because feedback cooling will cause these parameters to change. To Eq. (3.1) we add a feedback cooling term proportional to the velocity.

$$m\ddot{x} + m\gamma_i\dot{x} + m\omega_m^2x = F_{\text{th}} - gm\gamma_i\dot{x}. \quad (3.2)$$

In Eq. (3.2), g is a positive unitless gain term. Taking Eq. (3.2) into the Fourier domain and then solving for the Fourier transform of x , $x[\omega]$, yields the following.

$$m\omega^2x[\omega] + im\gamma_i\omega x[\omega] + m\omega_m^2x[\omega] = F_{\text{th}}[\omega] - igm\gamma_i\omega x[\omega]. \quad (3.3)$$

$$x[\omega] = \frac{F_{\text{th}}[\omega]/m}{(\omega_m^2 - \omega^2) + i(1+g)\omega\omega_m/Q_{m,i}} \quad (3.4)$$

When we compare this to the case without feedback (Eq. (1.33)), we can see the quality factor has been decreased by a factor of $(1+g)$, or, equivalently, the damping rate has been increased by a factor of $(1+g)$, as shown in Eqs. (3.5) and (3.6).

$$Q_m = \frac{Q_{m,i}}{1+g} \quad (3.5)$$

$$\gamma = \gamma_i(1+g) \quad (3.6)$$

Using the same method as that used at the end of Section 1.5.1, we can show that this increase of the mechanical damping rate without changing the coupling to the thermal bath results in a decreased mechanical mode temperature.

$$T_m = \frac{T}{1+g} \quad (3.7)$$

Eqs. (3.5) to (3.7) are the hallmarks of feedback cooling: simultaneous cooling and broadening of the mechanical mode. Example cooled mechanical spectrum are plotted in Fig. 3.1. Because measurement noise does not significantly affect our mechanical mode in the cooling results presented in this chapter, these equations will provide a very good approximation.

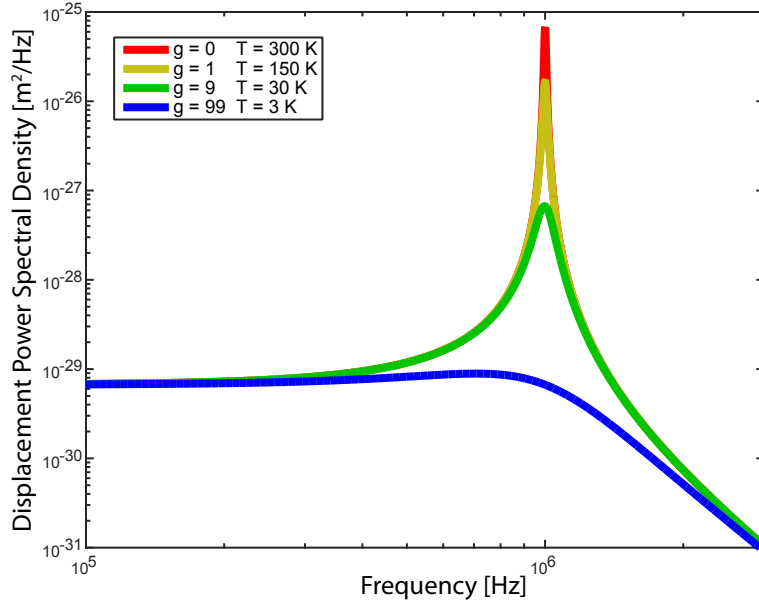


Figure 3.1: **Noiseless Feedback Cooling Example.** This plot shows a series of cooled mechanical spectra for different feedback gains, g , in the absence of measurement noise. The example mechanical resonator was chosen to have a starting temperature of $T = 300$ K, $Q_{m,i} = 100$, $\omega_m/2\pi = 1$ MHz, and an effective mass of $m = 100$ fkg.

3.2.2 Feedback Cooling with Measurement Noise

In this section, we analyze feedback cooling when there is significant measurement noise. Our analysis here largely follows work in Ref. [51]. The new version of Eq. (3.2), including the effects of measurement noise, is as follows.

$$m\ddot{x} + m\gamma_i\dot{x} + m\omega_m^2x = F_{\text{th}} - gm\gamma_i(\dot{x} + \dot{x}_n). \quad (3.8)$$

$x_n(t)$ is the measurement displacement noise. Following the same method used in the previous section, we Fourier transform this equation and solve for $x[\omega]$.

$$x[\omega] = \frac{1/m}{(\omega_m^2 - \omega^2) + i(1+g)\omega\omega_m/Q_{m,i}} F_{\text{th}}[\omega] + \frac{-ig\omega\omega_m/Q_{m,i}}{(\omega_m^2 - \omega^2) + i(1+g)\omega\omega_m/Q_{m,i}} x_n[\omega] \quad (3.9)$$

Making the very reasonable assumption that the thermal bath noise and the measurement noise are uncorrelated, we can obtain the resonator's displacement power spectral density from Eq. (3.9).

$$S_{xx}(\omega) = \frac{1/m^2}{(\omega_m^2 - \omega^2)^2 + (1+g)^2 \omega^2 \omega_m^2 / Q_{m,i}^2} S_{\text{FF}}^{\text{th}} + \frac{g^2 \omega^2 \omega_m^2 / Q_{m,i}^2}{(\omega_m^2 - \omega^2)^2 + (1+g)^2 \omega^2 \omega_m^2 / Q_{m,i}^2} S_{x_n x_n} \quad (3.10)$$

This is the displacement noise for the actual motion of the resonator, x . This, however, will not be what we measure on a spectrum analyzer in an actual experiment. We will measure, of course, the addition of the actual resonator resonator motion and the measurement noise, $y = x + x_n$. We can find the Fourier transform of y , $y[\omega]$, by adding x_n to both sides of Eq. (3.9) and simplifying.

$$y[\omega] = x[\omega] + x_n[\omega] = \frac{1/m}{(\omega_m^2 - \omega^2) + i(1+g)\omega\omega_m/Q_{m,i}} F_{\text{th}}[\omega] + \frac{(\omega_m^2 - \omega^2) + i\omega\omega_m/Q_{m,i}}{(\omega_m^2 - \omega^2) + i(1+g)\omega\omega_m/Q_{m,i}} x_n[\omega] \quad (3.11)$$

Once again, given Eq. (3.11) we can easily calculate the power spectral density for the measured displacement.

$$S_{yy}(\omega) = \frac{1/m^2}{(\omega_m^2 - \omega^2)^2 + (1+g)^2 \omega^2 \omega_m^2 / Q_{m,i}^2} S_{\text{FF}}^{\text{th}} + \frac{(\omega_m^2 - \omega^2)^2 + \omega^2 \omega_m^2 / Q_{m,i}^2}{(\omega_m^2 - \omega^2)^2 + (1+g)^2 \omega^2 \omega_m^2 / Q_{m,i}^2} S_{x_n x_n} \quad (3.12)$$

Fig. 3.2 illustrates the consequences of Eqs. (3.10) and (3.12). The example displacement spectral densities assume the same mechanical parameters as Fig. 3.1, for easy comparison. That is, $T = 300$ K, $Q_{m,i} = 100$, $\omega_m/2\pi = 1$ MHz, and $m = 100$ fkg. Additionally, we have assumed a white displacement noise of $S_{x_n x_n} = 1 \times 10^{-28} \frac{m^2}{\text{Hz}}$. Perhaps the most interesting result is the plot of the measured displacement PSD, $S_{yy}(\omega)$, shown in Fig. 3.2a, where we see the mechanical noise invert at high enough gain, g . Naively, one might assume this means we have somehow cooled the mode to a negative, or perhaps even imaginary, effective temperature. We know, of course, that this can not be the case. Looking at the resonator's actual displacement PSD, $S_{xx}(\omega)$, in Fig. 3.2b, we see that while the mode continues to broaden at these high gains, the mode area (and hence the mode temperature) actually begins to increase. This phenomenon is called noise squashing. Once the mechanical motion becomes comparable to the noise floor, the feedback starts significantly driving the mechanical mode with random measurement noise. This can not lead to cancellation of the resonator's actual motion and, rather, causes an increase in its amplitude. However, by forcing the resonator with measurement noise, we can drive the resonator in such a way that it cancels out measurement noise on the detection channel and, hence, the dip at large gain in Fig. 3.2a. The lesson to be learned here is that the measurement noise floor sets the ultimate cooling limit in a feedback cooling scheme. The effective mechanical mode temperature as a function of gain, g , assuming a

white (frequency independent) measurement noise, $S_{x_n x_n}$, is shown in Eq. (3.13) [51]. It can be determined using the same method as used at the end of Section 1.5.1.

$$T_m = \frac{T}{1+g} + \frac{m\omega_m^3}{4k_B Q_{m,i}} \frac{g^2}{1+g} S_{x_n x_n} \quad (3.13)$$

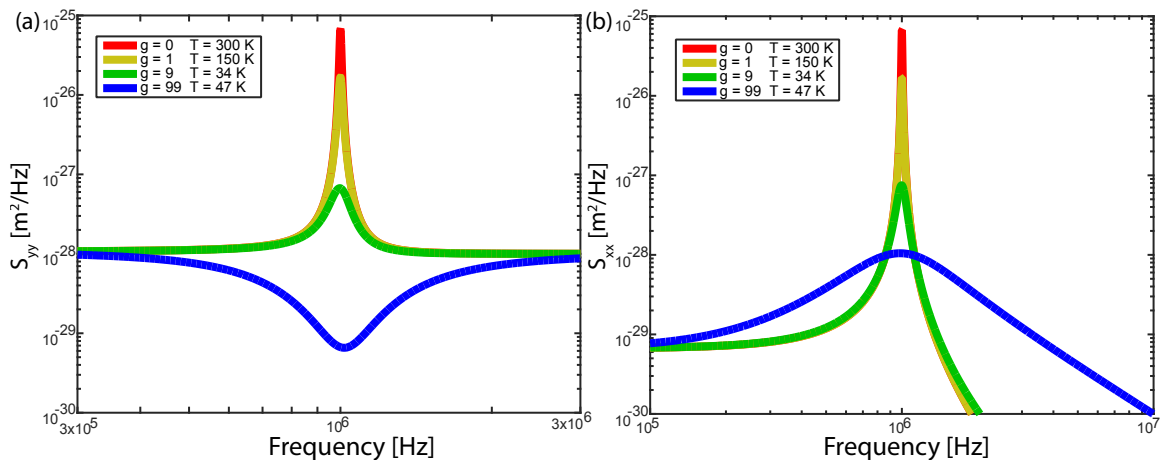


Figure 3.2: **Feedback Cooling with Measurement Noise Example.** These plots show feedback cooling results for a mechanical resonator with the same parameters as in Fig. 3.1, except we have added in a white displacement measurement noise of $S_{x_n x_n} = 1 \times 10^{-28} \frac{m^2}{Hz}$. (a) Plot of the PSD of the measured mechanical displacement. Notice that, at high gain, the resonator is driven in such a way as to cancel out the measurement noise. (b) Plot of the PSD of the actual mechanical displacement. At high gain, the mode continues to broaden, but its area (and hence its temperature) begins to increase.

3.2.3 Optomechanical Feedback Cooling in the Quantum Regime

In this section, we describe optomechanical feedback cooling using a quantum noise limited laser on-resonance with the optical mode (as in the homodyne measurement scheme in Section 1.3). Before discussing the results in detail, we provide the definition of several important terms most of which were defined and discussed in detail in Chapter 1, and are compiled below for the reader's convenience.

$$x_{\text{zpf}} = \sqrt{\frac{\hbar}{2m\omega_{\text{m}}}} \quad (3.14)$$

$$\bar{n} = \frac{1}{e^{\frac{\hbar\omega_{\text{m}}}{k_{\text{B}}T}} - 1} \quad (3.15)$$

$$g_{\text{o}} = g_{\text{OM}}x_{\text{zpf}} \quad (3.16)$$

$$G = g_{\text{o}}\sqrt{n_{\text{c}}} \quad (3.17)$$

$$\eta_{\text{tot}} = \frac{\kappa_{\text{e}}}{\kappa}\eta_{\text{qe}}\eta \quad (3.18)$$

$$n_{\text{imp,SN}} = \frac{\kappa\gamma_{\text{i}}}{64G^2\eta_{\text{tot}}} \quad (3.19)$$

$$n_{\text{BA,SN}} = \frac{4G^2}{\kappa\gamma_{\text{i}}} \quad (3.20)$$

$$g = \frac{4g_{\text{cd}}G\omega_{\text{m}}}{\kappa\gamma_{\text{i}}} \quad (3.21)$$

x_{zpf} is the zero-point fluctuations of the mechanical mode, \bar{n} is the average phonon occupation of the mechanical mode at temperature T , g_{o} is the bare optomechanical coupling rate, G is the parametrically-enhanced optomechanical coupling rate, n_{c} is the average intracavity photon number of the probe laser (defined in Eq. (1.13)), η_{tot} is the total detection efficiency of the experimental setup, η_{qe} is the quantum efficiency of the detector, η is the detection efficiency between the optical cavity and the detector, $n_{\text{imp,SN}}$ is the shot-noise limited imprecision in units of phonon number, $n_{\text{BA,SN}}$ is the quantum back-action of the shot noise in units of phonon number, g is a normalized unitless feedback strength, and g_{cd} is a unitless gain term accounting for the feedback response.

The feedback response is taken to be a standard derivative high-pass derivative filter with a cut-off frequency ω_{fb} , which in the Fourier domain is given by $F[\omega] = -i\omega g_{\text{cd}}/(1 - i\omega/\omega_{\text{fb}})$. With this assumed feedback response, Ref. [42] derives the variances of the two quadratures of the mechanical mode (under certain assumptions valid in this work).

$$\langle \delta q^2 \rangle = \frac{\left[g^2 n_{\text{imp,SN}} + \left(\bar{n} + \frac{1}{2} + n_{\text{BA,SN}} \right) \left(1 + \frac{\omega_{\text{m}}^2}{\omega_{\text{fb}}^2} \right) \right]}{\left(1 + g + \frac{\omega_{\text{m}}^2}{\omega_{\text{fb}}^2} \right)} \quad (3.22)$$

$$\langle \delta p^2 \rangle = \frac{\left[g^2 n_{\text{imp,SN}} \left(1 + \frac{g\gamma_{\text{i}}\omega_{\text{fb}}}{\omega_{\text{m}}^2} \right) + \left(\bar{n} + \frac{1}{2} + n_{\text{BA,SN}} \right) \left(1 + \frac{\omega_{\text{m}}^2}{\omega_{\text{fb}}^2} + \frac{g\gamma_{\text{i}}}{\omega_{\text{fb}}} \right) \right]}{\left(1 + g + \frac{\omega_{\text{m}}^2}{\omega_{\text{fb}}^2} \right)} \quad (3.23)$$

To determine the fundamental cooling limits from these equations we take the limit of large feedback bandwidth $(\omega_{\text{m}}/\omega_{\text{fb}})^2 \ll 1$ and large feedback strength $g \gg 1$, which makes some terms negligible

and greatly simplifies the formula for position fluctuations.

$$\langle \delta q^2 \rangle = gn_{\text{imp,SN}} + \frac{n_{\text{BA,SN}}}{g} + \frac{\bar{n} + 1/2}{g} \quad (3.24)$$

Taking the same limits for the momentum variance we obtain the following.

$$\langle \delta p^2 \rangle = \left[gn_{\text{imp,SN}} + \frac{n_{\text{BA,SN}}}{g} + \frac{\bar{n} + 1/2}{g} \right] + \gamma_i \left[\frac{g^2 n_{\text{imp,SN}} \omega_{\text{fb}}}{\omega_{\text{m}}^2} + \frac{1}{\omega_{\text{fb}}} (\bar{n} + n_{\text{BA,SN}}) \right] \quad (3.25)$$

We note that the first bracketed term on the RHS of Eq. (3.25) is the exact same as the position variance in Eq. (3.24). We will now assume that the second bracketed term on the RHS of Eq. (3.25) is negligible. We will revisit this assumption later and determine in what regime this assumption is valid. Explicitly stated, our working assumption is as follows.

$$\gamma_i \left[\frac{g^2 n_{\text{imp,SN}} \omega_{\text{fb}}}{\omega_{\text{m}}^2} + \frac{1}{\omega_{\text{fb}}} (\bar{n} + n_{\text{BA,SN}}) \right] \ll 1 \quad (3.26)$$

Now we have a simplified (and approximated) form of the momentum variance under optical feedback cooling.

$$\langle \delta p^2 \rangle = gn_{\text{imp,SN}} + \frac{n_{\text{BA,SN}}}{g} + \frac{\bar{n} + 1/2}{g} \quad (3.27)$$

In order to relate these variances to a phonon occupation number, we equate the total energy of the oscillator to the sum of its variances.

$$E = \frac{\hbar\omega_{\text{m}}}{2} [\langle \delta q^2 \rangle + \langle \delta p^2 \rangle] = \hbar\omega_{\text{m}} \left(\langle n \rangle + \frac{1}{2} \right) \quad (3.28)$$

This yields the following for the average mode occupation, $\langle n \rangle$.

$$\langle n \rangle + \frac{1}{2} = \frac{1}{2} [\langle \delta q^2 \rangle + \langle \delta p^2 \rangle] \quad (3.29)$$

Into Eq. (3.29) we plug in the simplified expressions for the quadrature variances, Eqs. (3.24) and (3.27), and arrive at the following.

$$\langle n \rangle + \frac{1}{2} = gn_{\text{imp,SN}} + \frac{n_{\text{BA,SN}}}{g} + \frac{\bar{n} + 1/2}{g} \quad (3.30)$$

Eq. (3.30) gives us much the same intuition that we developed in Section 3.2.2, just now stated in a quantum picture. Feedback cooling acts to reduce the actual motion of the resonator (in this picture given by $n_{\text{BA,SN}}$ and $\bar{n} + \frac{1}{2}$), by a factor of the gain, g , but also drives the resonator with the measurement imprecision noise, $gn_{\text{imp,SN}}$. Looking at Eq. (3.30), one can see there must be an optimal gain, g_{opt} , which minimizes the mechanical mode's phonon occupation. That optimal gain is given in the next equation (ignoring the completely negligible $1/2$ in $(\bar{n} + 1/2)$).

$$g_{\text{opt}} = \left[(\bar{n} + n_{\text{BA,SN}}) n_{\text{imp,SN}}^{-1} \right]^{1/2} \quad (3.31)$$

Substituting this optimal gain into Eq. (3.30) yields the following.

$$\langle n \rangle_{\text{min}} + \frac{1}{2} = 2\sqrt{n_{\text{imp,SN}} (\bar{n} + n_{\text{BA,SN}})} = 2\sqrt{n_{\text{imp,SN}} \bar{n} + \frac{1}{16\eta_{\text{tot}}}} \quad (3.32)$$

To obtain the second equality in Eq. (3.32), we used the quantum limited relation from Eqs. (3.19) and (3.20) that $n_{\text{imp,SN}} n_{\text{BA,SN}} = 1/16\eta_{\text{tot}}$. From Eq. (3.32), we can establish two requirements for reaching the ground state, $\langle n \rangle < 1$.

$$\eta_{\text{tot}} > \frac{1}{9} \quad (3.33)$$

$$n_{\text{imp,SN}} < \frac{1}{16\bar{n}} \left(9 - \frac{1}{\eta_{\text{tot}}} \right) \quad (3.34)$$

That is, if the experimental detection efficiency is any worse than $1/9$, reaching the ground state will be impossible. The most stringent condition is, of course, on the imprecision noise floor. As discussed in Section 3.2.2, the noise floor (imprecision) sets the ultimate feedback cooling limits. Here we find that $n_{\text{imp,SN}} \lesssim \frac{1}{2\bar{n}}$ for $\eta_{\text{tot}} \approx 1$. Of course other technical limitations may come into play, such as excess back-action, excess imprecision, or instabilities which limit the optical power and thus the feedback gain. Furthermore, we must be in a parameter regime that satisfies the assumption in Eq. (3.26). If we substitute Eq. (3.31) into Eq. (3.26) we obtain the following relation.

$$Q_{m,i} > (\bar{n} + n_{\text{BA,SN}}) \left(\frac{\omega_{\text{fb}}}{\omega_m} \right) \quad (3.35)$$

To arrive at Eq. (3.35), we have again used the large feedback bandwidth assumption, $(\omega_m/\omega_{\text{fb}})^2 \ll 1$. Eq. (3.35) can be further simplified by saturating the inequality in Eq. (3.34) and relating $n_{\text{imp,SN}}$ to $n_{\text{BA,SN}}$.

$$Q_{m,i} > \left(\bar{n} + \frac{\bar{n}}{9\eta_{\text{tot}} - 1} \right) \left(\frac{\omega_{\text{fb}}}{\omega_m} \right) \quad (3.36)$$

If we further assume the best case scenario of ideal detection efficiency ($\eta_{\text{tot}} = 1$) and take the feedback bandwidth to be $\omega_{fb,opt} \approx 3\omega_m$, a value numerically found to be the optimal feedback bandwidth in most cases [42], we arrive at the following simple requirement for $Q_{m,i}$ in order for the ground state to be reachable.

$$Q_{m,i} \gtrsim 3\bar{n} \quad (3.37)$$

Thus, we have developed an important intuitive understanding of how to maximize feedback cooling. The total detection efficiency must be made as close to unity as possible, and measurement imprecision must be made as small as possible, and the intrinsic mechanical quality factor ($Q_{m,i}$) must be made as large as possible. In particular, in order to reach the ground state level of cooling, $\langle n \rangle < 1$, Eqs. (3.33), (3.34) and (3.37) must be satisfied.

3.3 Experimental Setup and Device Characterization

The feedback cooling experimental setup used in this work is shown in Fig. 3.3. From Section 3.2, we know for feedback cooling we will need to apply a force proportional to the derivative of the mechanical resonator's motion, \dot{x} . Generally speaking, we accomplish this by using optomechanical detection to obtain a signal proportional to the position, x , then we take the derivative of that signal electronically, and then we use that derivative signal to modulate the optical power input to the optical cavity. This necessarily modulates the radiation pressure force (Eq. (1.40)) inside the cavity and provides the feedback force proportional to \dot{x} .

The measurement technique employed is homodyne detection, the principles of which were discussed in Section 1.3. The laser is placed directly on-resonance with the optical mode and mechanical motion is detected by monitoring the phase quadrature of the homodyne signal. The tunable laser

(New Focus Velocity series) is split into the requisite local oscillator (LO) and signal arms with both arms going through separate variable optical attenuators (VOA) to set the optical power. The LO arm then passes through a fiber stretcher (FS), which is used to set the homodyne phase, θ_H (see Section 1.3), and then a fiber polarization controller (FPC). The FPC sets the LO polarization so that the LO and signal arms appropriately mix on the variable coupler (VC) before reaching the balanced homodyne detector (BHD). After its VOA, the signal arm passes through an intensity modulator (IM), then a FPC which sets the appropriate polarization for the optical mode, and then an optical circulator (OC). After the circulator, the optical fiber of the signal arm enters a vacuum chamber at a pressure of 2.5×10^{-5} mbar, sufficient to eliminate the effects of gas-damping of the mechanics. Light is coupled into the structure using a dimpled, tapered optical fiber and an adiabatic on-chip waveguide in side-coupling configuration as discussed in Section 2.2. After reflection from the optical cavity, the signal arm exits the circulator and continues to the VC before hitting the BHD. The BHD signal is sent to bias tee with the low-pass filtered signal (< 200 kHz) sent to a proportional-integral-differentiator (PID) circuit, whose output is sent to the FS to lock the LO phase, θ_H , to the phase quadrature. The high frequency port of the bias tee is further filtered to make a band-pass filter (bandwidth $0.2 - 1.9$ MHz). This signal is sent to an electronic spectrum analyzer (ESA) to measure mechanical noise spectrum. In the case of optical feedback, the band-pass filtered signal is also sent to an analog differentiator circuit (Toptica mFALC110), whose output is sent through a variable phase shifter, $\Delta\phi$, and finally onto an electro-optic intensity modulator (IM), which closes the feedback loop and modulates the signal beam intensity.

Before moving on to discuss device characterization, we wish to discuss the homodyne phase, θ_H , and its lock in more detail. Once again, the laser is placed on-resonance with the optical cavity, which means mechanical motion (to first order) will only imprint itself on the phase of the reflected laser light (see Section 1.2). This means we will need to set the homodyne phase to $\theta_H = \pi/2$ to measure the phase quadrature (see Section 1.3). However, the phase angle is set by the relative path lengths of the LO and signal arms, and slow thermal drifts or acoustic noise can cause changes in the relative path length and, thus, θ_H and the measured homodyne quadrature. In order to maintain a consistent θ_H we will need active stabilization. To this end, the low frequency component of the BHD signal ($f < 200$ kHz) is fed to a digital feedback system (Toptica DigiLock, labeled PID in Fig. 3.3) that has a high-voltage output panel ($V_{\text{out}} \leq 150$ V), which drives a voltage-controlled fiber stretcher (Optiphase PZ1, labeled FS in Fig. 3.3). This fiber stretcher consists of a long distance of optical fiber (~ 10 m) wrapped around a bulk piezo element. The low frequency component of the BHD signal is used so that the lock does not interfere with/cancel out the mechanical motion we wish to observe at 1 MHz. Fig. 3.4 shows the BHD output (blue) while linearly driving the FS for optical probing on-resonance. The voltage sweep (green) modulates the interference of the LO and the reflected light, which we detect as a DC signal with sinusoidally modulated voltage

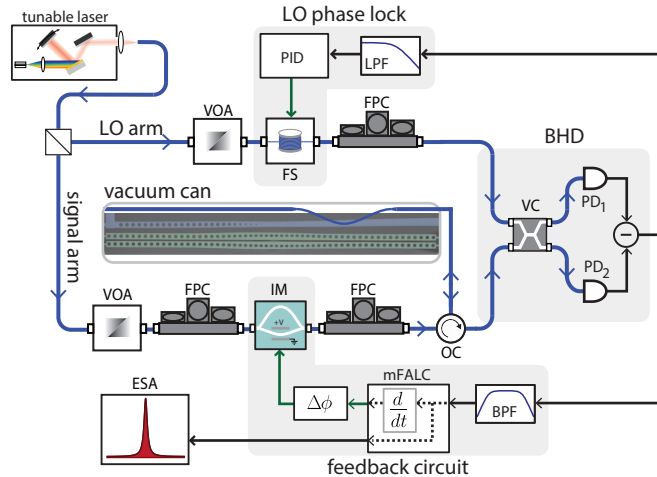


Figure 3.3: **Feedback Cooling Experimental Setup.** This is a schematic of the optical and electrical set-up used to characterize and feedback-cool the mechanical resonator. A tunable external cavity semiconductor diode laser (New Focus Velocity series) is used to provide both the signal beam on-resonance with the zipper cavity and the local oscillator beam (LO) for homodyne detection. Laser light is efficiently coupled into and out of the zipper cavity using a tapered fiber and adiabatic waveguide coupler in side-coupling configuration as discussed in Section 2.2. The device is mounted inside a vacuum chamber reaching a pressure of 2.5×10^{-5} mbar, sufficient to eliminate the effects of gas-damping. The reflected optical signal from the zipper cavity is separated using an optical circulator and sent through a variable coupler (VC) to a balanced homodyne detector (BHD). A low-pass filtered (LPF; bandwidth < 200 kHz) version of the BHD signal is sent to a proportional-integral-differentiator control circuit (PID), which drives a fiber stretcher (FS) to lock the relative phase (θ_H) between the LO and the reflected signal beam, and sets the phase quadrature of the homodyne detected signal. A band-pass filtered (BPF; bandwidth $0.2 - 1.9$ MHz) version of the BHD signal is sent to an electronic spectrum analyzer (ESA) to measure the mechanical noise spectrum. In the case of optical feedback, the BPF signal is also sent to an analog differentiator circuit (Toptica mFalc), whose output is sent through a variable phase shifter, $\Delta\phi$, and finally onto an electro-optic intensity modulator (IM), which closes the feedback loop and modulates the signal beam intensity.

output proportional to $\cos(\theta_H)$. The thermal Brownian motion of the strongly coupled mechanical mode is evident in the blue curve as increased noise on the signal. This noise decreases rapidly at the maximum and minimum points of the curve, which correspond to the read-out of the intensity quadrature of the reflected optical signal. Read-out of the phase quadrature occurs at the average voltage between the peak and trough of this curve (indicated by the grey dashed line), which is the desired lock-point in our measurements. If the laser is detuned from the optical resonance, mechanical transduction is observed at the top and bottom of the fringes. This is one metric we use to determine if the laser is on-resonance with the optical cavity. The homodyne fringe and lock-point are checked before each cooling measurement.

In Fig. 3.5, we show a characterization of the device used for feedback cooling in this work. Fig. 3.5a-b shows false-color SEM images of a device as used in this experiment. The device consists of a zipper photonic crystal cavity (see Section 2.1.1) suspended on $115 \mu\text{m}$ long nanotethers of

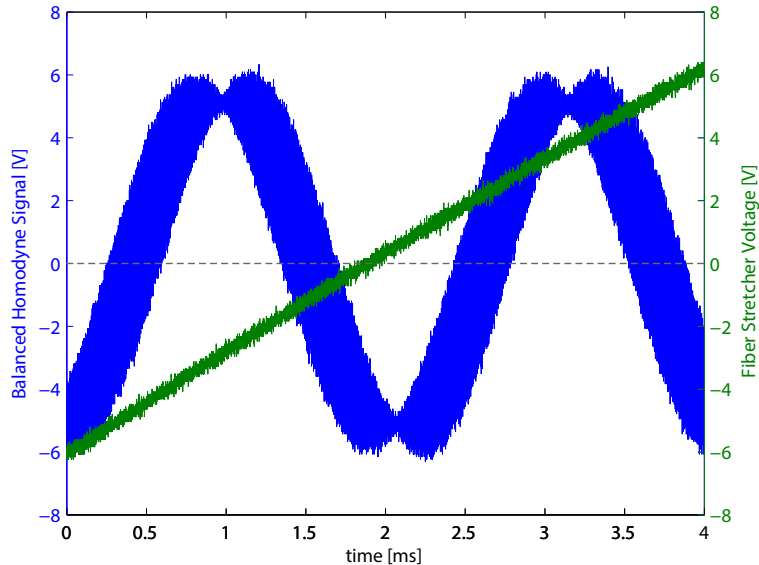


Figure 3.4: **Homodyne Phase Sweep.** Plot of a balanced homodyne signal (blue) as the fiber stretcher voltage is swept (green), with the laser on-resonance with the optical cavity.

width 130 nm. The structure is fabricated using our chips consisting of a ~ 400 nm high-stress silicon nitride layer on silicon (see Section 2.3) and our standard nanofabrication techniques (see Fig. 2.14). The optical cavity design was simulated and optimized using the Comsol finite-element method mode solver (see Section 2.1.1). The optical mode of interest is naturally the fundamental bonded mode (see Section 2.1.1), with electric field polarization primarily in the plane of the silicon nitride film. The central modification of the hole shape and location (shown in Fig. 3.5b) strongly confines the electromagnetic energy to the 150 nm gap between the two optical beams (shown in Fig. 3.5c). Light is coupled into and out of the device on reflection using the dimpled, tapered optical fiber and on-chip adiabatic waveguide in side-coupling configuration technique (discussed at length in Section 2.2 and a close-up SEM image of it is shown here in Fig. 3.5b). In Fig. 3.5e, we plot the reflected optical power normalized by the input power at the device as the laser frequency is scanned across the fundamental bonded optical resonance of the zipper cavity. The measured linewidth of the resonance is $\kappa/2\pi = 77$ GHz, corresponding to a loaded optical Q-factor of $Q_o = 2.5 \times 10^3$. From the depth of the Fano-like shape of the response dip, the coupling rate of the cavity to the on-chip waveguide is fit to be $\kappa_e/2\pi = 49$ GHz, yielding a slightly overcoupled system with $\kappa_e/\kappa = 0.63$. The background level of the normalized reflection plot, $\eta_r = 0.43$, determines the overall detection efficiency of light emitted into the detection channel. It includes the single-pass coupling loss between the on-chip waveguide and optical fiber taper ($\eta_c = 0.72$), optical loss between the fiber taper and the BHD ($\eta_f = 0.69$), and the quantum efficiency of the BHD ($\eta_{qe} = 0.88$). The total detection efficiency (see Eq. (1.76) and Section 1.5.2) is thus $\eta_{tot} = \eta_r (\kappa_e/\kappa) = 0.27$.

As can be seen in Fig. 3.5a, the nanostrings supporting each side of the zipper cavity are pinned together. This couples the strings together creating common and differential mechanical modes. This was done to decrease the energy radiated into the bulk by the tuning-fork-like differential mode. This did not have an apparent effect on Q_m , however, which is consistent with the idea that the mechanical quality factors of high-stress silicon nitride structures are set by localized defect states (see Section 2.3), and at these string lengths the tuning-fork design does not further increase Q_m [56]. The mechanical mode of interest is the fundamental in-plane differential mode depicted in Fig. 3.5d, due to its high optomechanical coupling. The mechanical resonance frequency is $\omega_m/2\pi = 940$ kHz, the simulated effective mass is $m = 90 \times 10^{-15}$ kg, which result in a zero-point fluctuation amplitude of $x_{zpf} = 9.7$ fm. An example electronic power spectral density of the mechanical motion is shown in Fig. 3.5f. The intrinsic mechanical quality factor is determined at low optical power (where dynamical back-action effects, see Section 1.5.1, are negligible) using an autocorrelation method that is discussed in greater detail in Section 4.3. Because the system is driven by a Gaussian thermal noise process, the autocorrelation of the amplitude $\langle x(t)x(t+\tau) \rangle$ can be shown to decay as $e^{-t/\tau}$, from which the quality factor can be obtained as $Q_m = \tau\omega_m$ [57, 58]. The slowly-varying envelope of $\langle x(t) \rangle$ is obtained from the magnitude channel of a lock-in amplifier tuned to the mechanical resonance frequency with a bandwidth (≈ 100 Hz) much larger than than the linewidth. The autocorrelation and its exponential fit are shown in Fig. 3.5g and yield an intrinsic mechanical damping rate of $\gamma_i/2\pi = 1.76$ Hz and a corresponding intrinsic mechanical quality factor of $Q_{m,i} = 5.3 \times 10^5$. This intrinsic mechanical quality factor measured with the autocorrelation method agrees very well with the value obtained from simply fitting the power spectral density to a lorentzian as shown in the inset of Fig. 3.7.

The optomechanical coupling is measured by observing the optomechanical spring shift and using Eq. (1.55). The shift of the mechanical frequency versus laser detuning from the optical resonance for fixed input laser power is shown in Fig. 3.5h. The red line is a fit to data using Eq. (1.55) with the result $g_{OM}/2\pi = 36$ GHz/nm. This is in good agreement with the simulated value from Comsol of 41 GHz/nm. This measured g_{OM} along with x_{zpf} yield a bare optomechanical coupling rate of $g_o = g_{OM}x_{zpf} = 2\pi \times 358$ kHz.

Fig. 3.6 shows the measurement imprecision for the device in Fig. 3.5 using the experimental setup shown in Fig. 3.3 with the laser on-resonance with the optical cavity and $\theta_H = \pi/2$ (and the feedback off). Fig. 3.6a shows a wideband spectrum of the mechanical electronic power spectral density taken at an optical power near the standard quantum limit (SQL, see Section 1.5.2) for this device, $n_c = 0.17$ (blue curve). Measurement of the noise level with the signal arm blocked corresponds very closely to the signal vacuum-noise level (electronic detector noise is 12.9 dB below the measured noise level). Firstly, the reader should notice how incredibly clean the spectrum is. The only other feature in the spectrum is the much more weakly transduced fundamental in-plane common motion

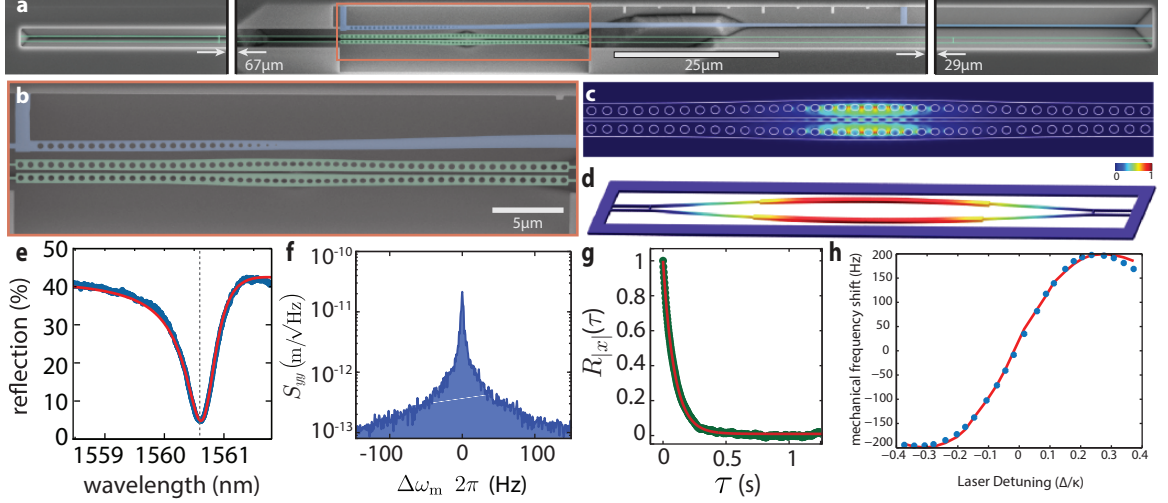


Figure 3.5: **Feedback Cooling Device Characterization.** (a) False color SEM image of a device as used in the experiment, made from highly stressed silicon nitride released from a silicon wafer (see Section 2.3). The green overlay indicates the photonic crystal cavity and nanostring tethers. The blue overlay indicates the coupling waveguide. The optical design utilizes the on-chip adiabatic waveguide side-coupling technique discussed in Section 2.2. Due to the extreme aspect ratio of this device, only the ends of the tether region are shown, with the extent of the missing gaps on either side of the center of the device indicated. (b) Zoomed-in SEM image of the photonic crystal section (green) and the adiabatically tapered on-chip coupling waveguide (blue). (c) FEM-simulated electromagnetic energy density of the fundamental bonded optical resonance, with the outline of the silicon nitride beam shown in white. (d) FEM Comsol simulation of the first-order in-plane differential mechanical resonance of a dual-nanobeam structure, indicating the normalized displacement of the beams. For clarity, the tethers in the simulated structure are shorter than those of the actual device. In (c) the color scalebar indicates large (red) and small (blue) optical energy density, whereas in (d) the scalebar indicates large (red) and small (blue) displacement amplitude. (e) Plot of the laser reflection spectrum when scanned across the optical mode used in the experiment (blue) and fit (red). Dashed grey line indicates on-resonance laser position during measurements. The measured loaded optical Q-factor is $Q_o = 2.5 \times 10^3$, with a waveguide loading to total cavity loss rate ratio of $\kappa_e/\kappa = 0.63$. (f) Example power spectral density (PSD) of the mechanical resonator's thermal noise near 940 kHz, transduced using the setup in Fig. 3.3 with the laser on-resonance, $\Delta = 0$, and at low power, $n_c \lesssim 1$. (g) Autocorrelation of the slowly varying amplitude of the transduced mechanical thermal noise, $R_{|x|}(\tau) = \langle x(t)x(t+\tau) \rangle$. An exponential fit (red curve) to the measured data (green circles) yields an intrinsic mechanical damping rate $\gamma_i/2\pi = 1.76$ Hz and quality factor $Q_{m,i} = 5.3 \times 10^5$. (h) A plot of the mechanical frequency shift versus laser detuning for fixed input optical power to the cavity. The red line is a fit to Eq. (1.55), which allows us to back out the optomechanical coupling, $g_{oM}/2\pi = 36$ GHz/nm.

of the two optical beams. We have plotted the PSD in units of phonons (mechanical quanta) by assuming a room-temperature ($T = 295$ K) occupation of the mechanical mode, $\bar{n} = 6.5 \times 10^6$ (see Eq. (3.15) for a definition of \bar{n}). Fig. 3.6b shows a plot of the measurement imprecision as a function of intracavity photon number. The imprecision in units of quanta (phonons) is determined by dividing the quantity $(\langle n \rangle + 1/2)$ by the signal to noise ratio of the resolved mechanical peak to the noise floor [12]. Intuitively, this means that an imprecision of 1 corresponds to the noise level

one phonon in the mechanical mode would produce at the mechanical resonance. To this end at the lower optical powers, two noise spectra are combined: one broadband spectrum to accurately obtain the noise floor, and one narrow scan to accurately resolve the mechanical peak height. In fact, this is how Fig. 3.6a was generated. At higher optical powers, thermo-opto-mechanical back-action causes fluctuations in the mechanical linewidth. Slight “jitter” of the optical cavity frequency due to, for example, room temperature thermal motion of the mechanical mode will result in significant heating/cooling. At these powers, we simply observe the noise floor relative to vacuum noise and place the inferred imprecision appropriately on the plot.

The solid lines in Fig. 3.6b, are no-fit theory lines for $n_{\text{imp,SN}}$ assuming a total detection efficiency of $\eta_{\text{tot}} = 0.27$ (blue), $n_{\text{BA,SN}}$ (red), and total added quanta $n_{\text{imp,SN}} + n_{\text{BA,SN}}$ (green). The dashed blue line is $n_{\text{imp,SN}}$ for the case of perfect detection efficiency ($\eta_{\text{tot}} = 1$). These theoretical predictions were discussed in detail in Section 1.5.2. That our data lies directly on top of the no-fit theory line for $n_{\text{imp,SN}}$ confirms our measured value of the total detection efficiency. The minimum total added measurement noise occurs at a signal power corresponding to $n_c = 0.12$, and represents the standard quantum limit (SQL) for our measurement set-up, $n_{\text{SQL}} = 1 / (2\sqrt{\eta_{\text{tot}}}) = 0.96$ [12]. The imprecision is vacuum noise limited for all but the highest powers ($n_c \gtrsim 500$), reaching a value 34 dB below the SQL imprecision for an ideal detector ($= 1/4$ quanta [11]).

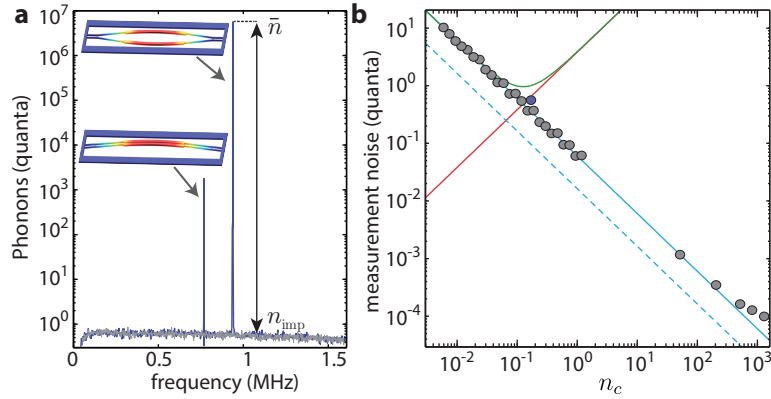


Figure 3.6: **Measurement Imprecision.** Measured wideband electronic PSD plotted in units of phonon quanta of the dominant mechanical mode at 940 kHz for $n_c = 0.17$ (blue) and signal beam blocked ($n_c = 0$; grey curve). The insets of (a) are simulated mechanical mode displacement profiles for the two mechanical resonances visible in the spectrum. The mode at 940 kHz is the fundamental in-plane differential mode while the mode at 740 kHz is the poorly transduced in-plane common motion of the zipper beams. Frequencies below 200 kHz are attenuated by a high-pass filter and the small slope of the background noise level is a result of the frequency-dependent gain of the balanced photodetectors. (b) Plot of the measured imprecision noise in units of phonon quanta (n_{imp} ; grey filled circles). Also plotted are the theoretical vacuum-noise-limited imprecision ($n_{\text{imp,SN}}$; solid cyan curve), theoretical quantum back-action noise ($n_{\text{BA,SN}}$; solid red curve), and theoretical quantum-limited measurement noise ($n_{\text{imp,SN}} + n_{\text{BA,SN}}$; solid green curve), assuming the measured $\eta_{\text{tot}} = 0.27$ and no fit parameters. The dashed curve is the measurement imprecision for an ideal continuous position measurement with $\eta_{\text{tot}} = 1$.

3.4 Results and Discussion

Fig. 3.7a shows the results of feedback cooling the fundamental in-plane mechanical mode. Once again, the laser is placed on resonance with the optical cavity ($\Delta = 0$) and the LO phase is locked to ($\theta_H = \pi/2$). The derivative feedback is switched on and the electronic gain is held constant at a value found to maximize cooling at the highest value of n_c (734). The laser probe power is increased from low to high, increasing the total loop gain, and thereby increasing the observed cooling and damping. The feedback gain was set in this way because, in our experimental setup, the optical attenuation was much easier to finely control than electrical gain.

At each measured optical power in Fig. 3.7a, the mechanical spectra are fit with a Lorentzian curve (black solid lines) from which an area and linewidth of the spectrum are determined. The phonon occupancy of the mechanical resonance, plotted as blue circles in Fig. 3.7b, is proportional to the transduced area under the mechanical spectrum normalized by n_c , whereas the damped mechanical Q-factor is determined from the linewidth. Absolute calibration of the phonon occupancy for each of the optical powers is found by comparing to the measured area under the mechanical spectrum at the lowest power point ($n_c = 0.36$) with the feedback off. At this power, and in open loop, dynamic back-action effects are negligible and the mechanical resonance is at room temperature thermal occupancy ($T = 295$ K, $\langle n \rangle = 6.5 \times 10^6$). Of crucial importance to the interpretation of the data presented in Fig. 3.7 is the fact that the change in the mechanical quality factor (green dots) follows the change in the measured occupation (see inset), which is a hallmark of feedback cooling.

The lowest phonon occupation achieved here is $\langle n \rangle = 66 \pm 10$. At this cooling point the linewidth of the mechanical resonance at $\omega_m/2\pi = 940$ kHz has been broadened to 190 kHz. Further cooling of the mechanical resonance is limited primarily by the combination of two sources. An excess delay time of 1 μs in our feedback loop modifies the broadband phase response of the system away from the ideal value, leading to amplification, rather than damping, of mechanical motion for frequencies outside an approximate 250 kHz bandwidth around the mechanical resonance (this will be discussed in more detail shortly). Additionally, at the highest optical cooling power of $n_c = 734$ we are nearing an optical-absorption-induced, thermo-optic bistability of the optical cavity response.

Here we present and discuss the system response and delay times of our feedback circuit used to apply radiation pressure feedback. In Fig. 3.8, we present the measured amplitude, phase response, and time delay of the analog circuit, mFALC110, used as part of the feedback loop to perform the derivative feedback. The cyan dashed line in Fig. 3.8a indicates the amplitude response for purely derivative feedback, which is proportional to ω . Over the frequency range used for this experiment (0.8 – 1.2 MHz), the amplitude response deviates from the ideal slope by ≈ 0.5 dB and the phase changes by $\approx 5^\circ$. The time delay from the mFALC110 circuit, shown in Fig. 3.8b, is negligible, when compared to the mechanical period (grey dashed line).

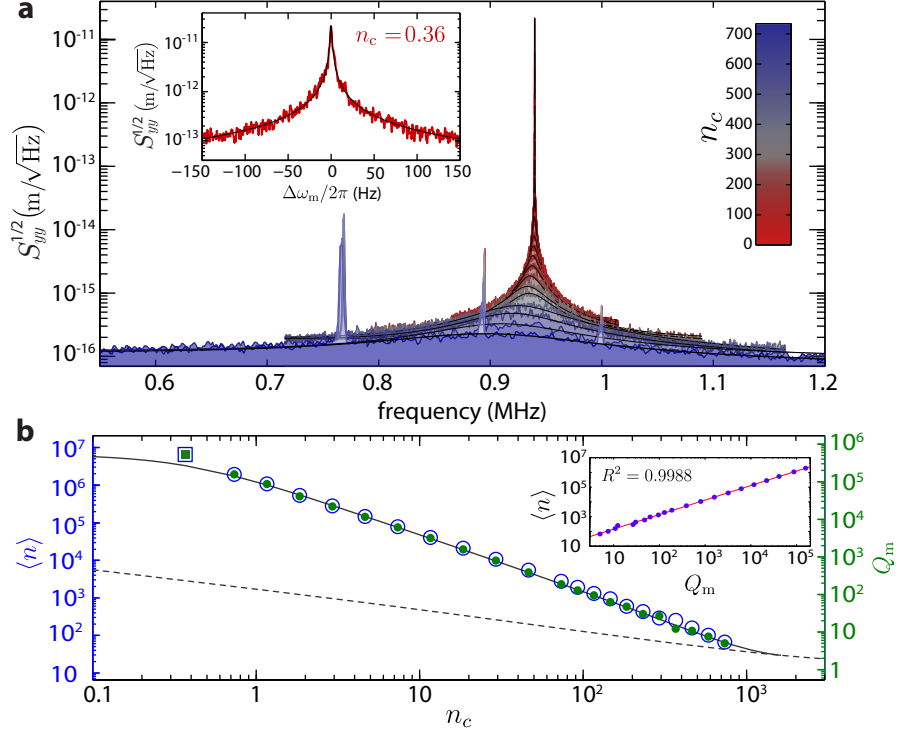


Figure 3.7: **Room-Temperature Laser Cooling.** (a) Plots of the transduced mechanical spectra with the optical feedback engaged for increasing n_c , showing the damping and cooling of the dominant mechanical mode. Color scale indicates photon number of each mechanical spectrum. The black curves are the fits to the measured spectra used to extract the damped mechanical Q-factor (Q_m) and phonon occupation ($\langle n \rangle$). Spectral peaks at 710 kHz and 910 kHz are weakly transduced mechanical modes, white that at 1 MHz is extraneous electronic noise. Inset: room-temperature mechanical spectra taken with the feedback off for calibration. (b) Plot of the inferred $\langle n \rangle$ (blue circles; left axis) and Q_m (green solid circles; right axis) extracted from the fits to spectra shown in (a). The first data point (square), at lowest n_c , is taken from the data in the inset of (a) with the feedback off and is used as a room-temperature calibration. The y-axes scales are normalized such that ideal cold-damping would result in the blue and green data points lying directly on top of each other. The solid black curve is the theoretical prediction of cooling with no fit parameters and the dashed line is the minimum possible cooling for our system if the circuit gain were optimized at each n_c . The uncertainty in the inferred $\langle n \rangle$ of $\pm 15\%$ is smaller than the data points and is dominated by the 95% confidence interval of the fits to each mechanical spectra. Inset shows the measured phonon occupation versus mechanical quality factor during the cooling run (blue points). A linear fit to the data is shown as a red curve with R-squared value of 0.9988.

In Fig. 3.9, we present the amplitude and phase response of the entire feedback loop, including the optical part. It is important to note that this data was taken off-resonance from the optical cavity ($\Delta/\kappa \gg 1$) so that the mechanical motion would not dominate the response; however, a trace of the mechanical response is still visible in the noise of the curve near the mechanical resonance frequency (vertical grey dashed line). The BHD phase θ_H was set to be sensitive to phase fluctuations of the reflected light, as in the experiment. Since the intensity modulator changes amplitude, at this homodyne phase the detected amplitude response is attenuated and should be considered in

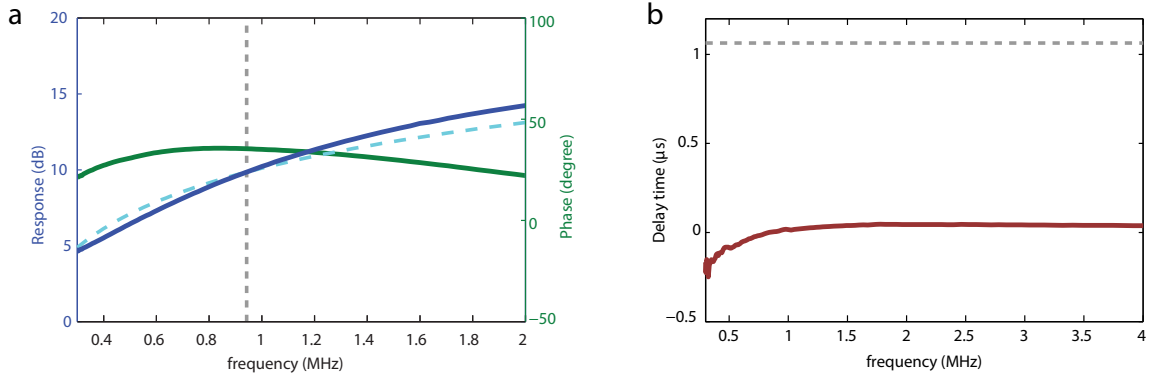


Figure 3.8: **Feedback Circuit Response and Delay Time.** (a) Magnitude (blue) and phase (green) response of the Toptica mFALC110 for the settings used in the cooling experiment. Vertical grey dashed line indicates the mechanical frequency and the cyan dashed line indicates the amplitude response for ideal derivative feedback, proportional to ω . (b) Total time delay (red) as measured on a network analyzer. Horizontal grey dashed line indicates one mechanical period.

arbitrary units. Nonetheless, in the frequency range of interest (0.8 – 1.2 MHz) the amplitude response is qualitatively similar to the response of the mFALC110. Of notable difference, however, is that the overall delay time is now comparable to the mechanical period (see horizontal grey dashed line in Fig. 3.9b). This delay time was measured to have the following components; 200 ns from the optical detector, 400 ns from the band pass filtering of the feedback circuit, 180 ns from the phase-shifter, and the remainder is dominated by the total signal path length. The non-negligible delay in the rest of the feedback loop requires the inclusion of a phase shifter, which allows us to apply a feedback force that purely damps. A consequence of this nearly constant time delay is that the phase of the feedback signal varies linearly with frequency. This becomes important when considering the wideband feedback loop noise.

Next we discuss the wideband excess noise (above vacuum noise) observed in our measurement setup at high optical power and how the time delay in the feedback loop manifests itself as excess noise in the PSD at high power. Fig. 3.10 shows a wide span of the electronic PSD of our device with the feedback engaged, the probe laser on-resonance with the optical cavity ($\Delta = 0$), and the homodyne phase set to the phase quadrature ($\theta_H = \pi/2$). At low optical signal power ($n_c \lesssim 100$), the noise floor is set by the vacuum noise of the signal arm and the Lorentzian mechanical response dominates the signal. At higher signal powers ($n_c = 734$, green) there is a ~ 3 dB additional broadband noise above vacuum noise, which drops off with increasing frequency, but the mechanical response near 940 kHz still dominates. This broadband noise is also seen in the open loop measurements of Fig. 3.10b. A separate measurement indicates that this background noise is not laser intensity noise. Additionally, by measuring the same broadband noise off resonance from the optical cavity ($\Delta/\kappa \gg 1$) we have eliminated the cavity (through thermo-refractive type effects) as the source of

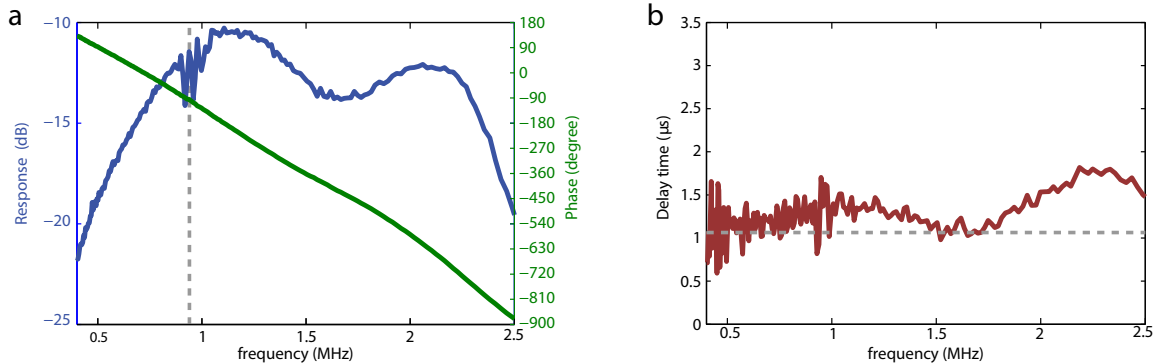


Figure 3.9: **Whole System Response and Delay Time.** (a) Magnitude (blue) and phase (green) response of the entire feedback system including electronics and optical train, with the laser off resonance from the optical cavity. The grey dashed line indicates the mechanical frequency. The noisy signal centered at the mechanical frequency is simply a result of residual mechanical transduction and is not indicative of a rapidly changing response of the circuit. (b) total time delay as measured on a network analyzer (red). A single mechanical period is indicated by the horizontal grey dashed line.

this excess broadband noise. The noise is, therefore, likely due to residual optical phase fluctuations in our set-up, possibly due to intrinsic phase noise of the laser or acoustic noise pick up. Note that in principle homodyne detection is insensitive to frequency fluctuations of the laser since the laser is interfered with itself; however, in practice, the two arms of the interferometer are never exactly the same length and interference is between light emitted by the laser at different times resulting in conversion of frequency noise to intensity noise, which is detected. Currently, this broadband noise limits our imprecision to approximately, $n_{\text{imp}} = 10^{-4}$ quanta.

In the experiment presented in Fig. 3.7 it is not, however, the broadband excess imprecision noise which ends up limiting the attainable cooling. As can be seen in Fig. 3.10a, at increased laser power ($n_c = 925$; red curve) there is a broad noise peak centered near ~ 800 kHz, which grows and prevents further cooling (or accurate determination of the mode occupancy for that matter). In order to investigate this further, we measure the electronic PSD with the laser off-resonance ($\Delta/\kappa \gg 1$) and the feedback lock engaged in Fig. 3.11. Note that because the data was taken off-resonance there is very little intracavity power. For direct comparison then, we have taken the data at $n_c^{\text{eff}} = 500$, which is the number of photons that would be in the cavity for the same reflected optical power as with the laser directly on resonance ($\Delta = 0$). The feedback loop produces excess noise “humps” at approximately 800 kHz, 1.5 MHz, and 2.2 MHz frequencies. The “humps” in Fig. 3.11, correspond in frequency to where the phase of the entire feedback loop (see Fig. 3.9a) is between 0° and 180° modulo 360° , which corresponds to the regions where the feedback loop has positive gain, amplifying the measured noise rather than damping it. This limits the bandwidth over which we can effectively damp and cool the mechanical motion to about 250 kHz, which for the present device limits the

attainable cooling level.

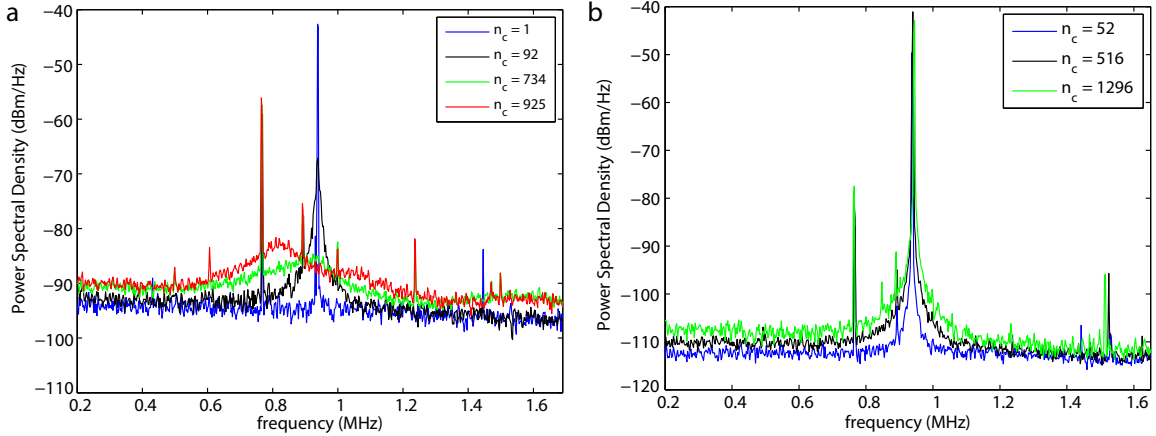


Figure 3.10: **Widespan Noise Laser On-resonance.** (a) The wide-span noise spectra for a series of experimental powers with the feedback loop engaged (closed loop) and the laser tuned on-resonance with the optical cavity ($\Delta = 0, \theta_H = \pi/2$). (b) The wide-span noise spectra for a series of experimental powers with the feedback loop disengaged (open loop) and the laser tuned on-resonance with the optical cavity ($\Delta = 0, \theta_H = \pi/2$). Note that the discrepancy between the absolute noise levels between the two plots is because the data were taken at different detector gain and local oscillator powers.

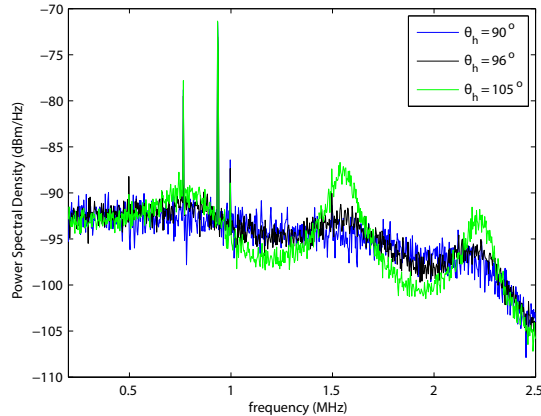


Figure 3.11: **Widespan Noise Laser Off-resonance.** Wide-span noise spectrum for the feedback loop engaged (closed loop) and the laser far detuned from the laser cavity ($\Delta/\kappa \gg 1$). Here we plot the spectrum for a series of different homodyne detector phases around $\theta_H = \pi/2$. Measurements were taken at $n_c^{\text{eff}} = 500$, which corresponds to the number of photons that would be in the cavity to yield the same reflected power at the detector if the laser were on-resonance ($\Delta = 0$).

3.5 Moving Forward

Cooling to the quantum ground-state from room temperature remains an achievable goal, but requires improvement in several key device properties. As discussed in Ref. [42], one cannot increase the feedback bandwidth without limit as eventually the amount of imprecision noise (white vacuum noise in the ideal case) fed back onto the mechanical resonator is enough to heat it out of the ground-state. As discussed in Section 3.2.3 and argued for in Ref. [42], the optimal feedback bandwidth is $\omega_{\text{fb}} \approx 3\omega_{\text{m}}$ and a consequence of this cooling scheme is that $Q_{\text{m}} \gtrsim 3\bar{n}$ in order to reach the ground-state. Silicon nitride structures have been fabricated with $Q_{\text{m}} = \bar{n}$ using membranes [59] and high frequency (~ 30 MHz) tuning-fork designs [56]. Further progress will need to be made by further reducing bending energy losses (especially at clamp points) and perhaps utilizing nitride with fewer bulk defects and higher stress, as discussed in Section 2.3. Even with an increase in the mechanical Q-factor to say, 20×10^6 , however, reaching the ground-state with the optomechanical coupling strength of the devices in this work would still require a prohibitively large intra-cavity photon number of $n_{\text{c}} \approx 5 \times 10^4$. By increasing the optomechanical coupling and optical Q-factor to levels previously demonstrated in similar devices ($g_{\text{OM}}/2\pi = 200$ GHz/nm, $Q_{\text{o}} = 6 \times 10^4$ [60]), and increasing the total detection efficiency to $\eta_{\text{tot}} = 0.7$, this can be lowered to a value as small as $n_{\text{c}} \approx 60$ (this is shown in Fig. 3.12). These theoretical results assume ideal vacuum noise limited imprecision and ideal shot-noise back-action, so we must also satisfy these conditions. As shown in Fig. 3.6, at our highest experimental powers, we were starting to deviate from the theoretical line for vacuum-noise limited imprecision. However, the optical power required to obtain $n_{\text{c}} = 60$ in an optical resonator with $Q_{\text{o}} = 6 \times 10^4$ would obtain $n_{\text{c}} = 2.5$ in our measured optical resonance with $Q_{\text{o}} = 2.5 \times 10^3$. At this value of n_{c} , we have shown our experimental setup to be vacuum noise limited, and thus this is not a concern. Our device does experience some classical back-action due to adsorption heating. As mentioned previously, at the highest optical cooling powers used, $n_{\text{c}} = 734$, we are nearing a thermo-optic bistability. Calibration of the absorption heating via the thermo-optic tuning of the optical cavity indicates only a $\Delta T \approx 10$ K, which is insignificant for the cooling results presented, but will impact the current device's ability to reach the ground-state. Expressing this parasitic absorption back-action in quanta yields $n_{\text{BA,abs}} \approx 300n_{\text{c}}$. The fundamental shot noise back-action for our measured system is $n_{\text{BA,SN}} = 4n_{\text{c}}$, and hence our parasitic back-action is larger than $n_{\text{BA,SN}}$. However, for the new improved parameters given above $n_{\text{BA,SN}}$ will be increased by a factor of $(g_{\text{OM,new}}/g_{\text{OM,old}})^2 (Q_{\text{o,new}}/Q_{\text{o,old}}) (Q_{\text{m,new}}/Q_{\text{m,old}}) \cong 3 \times 10^4$, and thus will completely dominate $n_{\text{BA,abs}}$. Therefore, with these new parameters, all conditions will be met to allow feedback cooling to obtain the quantum ground-state.

Additionally, we can gain some more intuition from our results in Section 3.2.3. We found that in order for the ground-state to be reached $n_{\text{imp,SN}} \lesssim (2\bar{n})^{-1}$. Substituting in for $n_{\text{imp,SN}}$

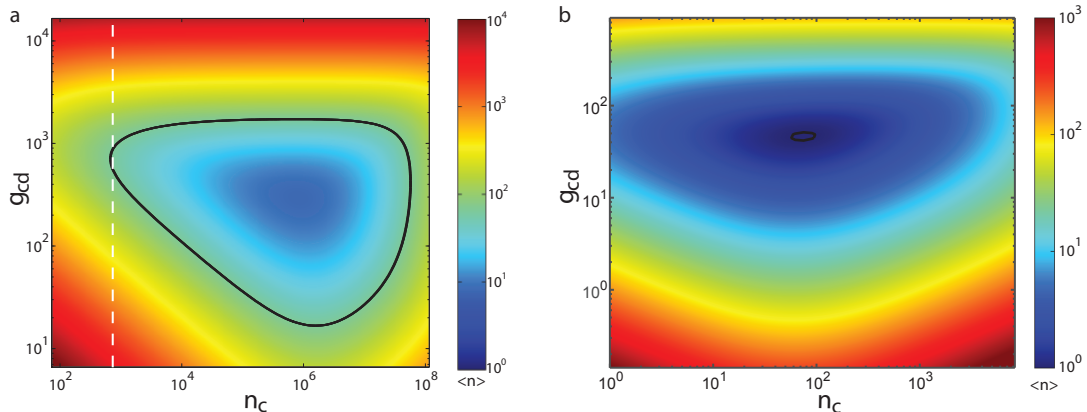


Figure 3.12: **Feedback Cooling Color Density Plot.** (a) Color density plot for the final cooled phonon occupation, $\langle n \rangle$, for ideal radiation-pressure derivative feedback cooling using the same device parameters as the device studied in Fig. 3.7, versus normalized gain and photon number. The black line is a contour at $\langle n \rangle = 66$, the minimum phonon number achieved in Fig. 3.7. The white dashed line denotes $n_c = 734$, which is the maximum number of photons used in Fig. 3.7. The global minimum at ideal power and gain is $\langle n_{min} \rangle = 8$. (b) Same plot as in (a) except now we have set $g_{OM}/2\pi = 200$ GHz/nm, $Q_o = 6 \times 10^4$, which have been demonstrated in similar zipper optomechanical cavity devices [60], and we increased the total detection efficiency to $\eta_{tot} = 0.7$ and the mechanical quality factor to $Q_m = 20 \times 10^6$. The black contour encircles the ground-state, $\langle n \rangle < 1$. As can be seen, the ground-state can now be achieved with $n_c \approx 60$.

using Eq. (3.19) and rearranging yields $4\eta_{tot}n_c g_o^2/\kappa \gtrsim \bar{n}\gamma_i/8$. Viewed from the perspective of a continuous position measurement, attaining ground-state cooling requires (approximately) that the rate at which measurement information is gained about the mechanical motion, $\Gamma_{meas} = 4\eta_{tot}n_c g_o^2/\kappa$ be greater than the rate at which the mechanical resonator is disturbed by coupling to its thermal bath $\Gamma_{th} = \gamma_i(\bar{n} + 1)$, and approach the back-action decoherence rate, $\Gamma_\phi = \gamma_i n_{BA}$ (note that in the shot-noise limit $\Gamma_{\phi,SN} = 4n_c g_o^2/\kappa$) [9, 53, 61]. More generally, then, the photonic crystal optomechanical devices studied here could enable quantum measurement and control protocols [62–68] for the preparation of mechanical objects in highly non-classical quantum states of motion. Specifically speaking, feedback damping can be used to achieve an unconditionally squeezed resonator state from a conditionally squeezed state, which results from a two-tone measurement [65]. Also, feedback cooling can be used as the first preparation step in a quantum superposition-state generation protocol based on homodyne x^2 measurement [66, 69]. With the device improvements mentioned above, these protocols could be implemented without additional cryogenic cooling, and in a room temperature environment where they may be employed for a variety of precision sensing applications. In a similar vein, feedback control is commonly employed in MEMS sensors of forces and fields [70, 71] to change their frequency, bandwidth, and dynamic range of the sensor. In this work the bandwidth of the resonator’s on-resonance response is increased from 1.7 Hz to 190 kHz and the on-resonance dynamic range is increased by 50 dB, all while preserving the undamped thermal noise

force sensitivity of $125 \text{ aN}/\sqrt{\text{Hz}}$. When applied to the field of atomic force microscopy, for example, such an optomechanical sensor [72] might be used to improve imaging resolution by reducing thermal motion of the sensor tip [73], or in the case of measurements of molecular motion, to resolve dynamics at microsecond time scales [74].

Chapter 4

Demonstration of an Optomechanical Accelerometer [75]

4.1 Introduction

The optomechanical interaction described in this text, enables precise measurement of mechanical motion. Perhaps the most powerful and well-known example of this is LIGO - the Laser Interferometer Gravitational-wave Observatory. LIGO features kg scale mirrors separated by km distances and stored optical powers on the order of 10 kW (advanced LIGO may approach 1 MW [76]). From a private communication with LIGO physicist Rana Adhikari, the current stored optical powers in LIGO's optical cavities at the time of submission of this thesis is 100 kW. LIGO has been able to achieve a displacement resolution of $\sim 10^{-19} \frac{m}{\sqrt{Hz}}$ and advanced LIGO has a roadmap to $\sim 10^{-20} \frac{m}{\sqrt{Hz}}$ [76, 77]. Again, from a private communication with LIGO physicist Rana Adhikari, the current displacement resolution of LIGO at the time of submission of this thesis is $3 \times 10^{-20} \frac{m}{\sqrt{Hz}}$. Such fantastically small numbers require context to be better understood. The typical inter-atomic spacing of atoms in a solid is on the order of 1 angstrom, $10^{-10} m$. The charge radius of a proton is approximately 1 fm, $10^{-15} m$. This means that if one of LIGO's mirrors moves relative to the other like $A \cdot \sin(\omega t)$, with amplitude, A, 4 orders of magnitude smaller than a proton radius, LIGO could sense that after 1 second of averaging. This is truly remarkable performance.

The nano-scale zipper cavities studied in this thesis and described in Section 2.1.1 are not quite capable of the same level of performance, but they can achieve a displacement resolution on the order of $10^{-16} \frac{m}{\sqrt{Hz}}$, or 1/10 of a proton radius (see Fig. 3.7 and Ref. [1]). With this resolution, one is naturally led to consider the practical applications of such a sensor. The most straightforward application that comes to mind is acceleration sensing. Typical accelerometers operate by monitoring the displacement of a flexibly mounted test mass, see Fig. 4.1.

Due to the rapid development of silicon micromachining technology, microelectromechanical systems (MEMS) accelerometers have become exceedingly popular over the past two decades [78]. The

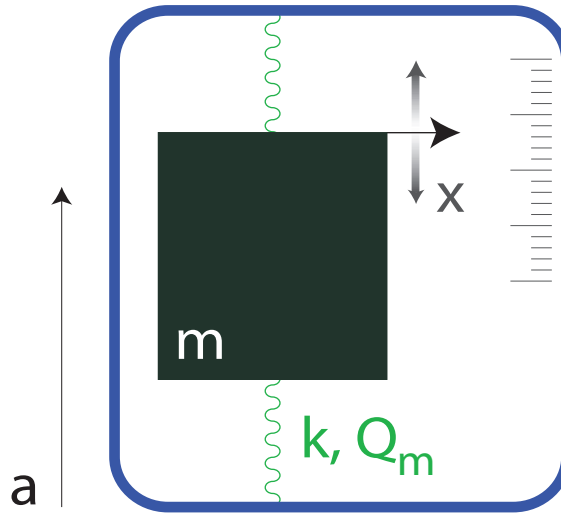


Figure 4.1: **Canonical Accelerometer.** This figure is a cartoon of a canonical accelerometer. The test mass (dark square) is flexibly mounted via springs (green) with stiffness k and quality factor Q_m to a rigid frame (blue rectangle). If the frame undergoes an acceleration, a , the test mass will move an amount x , which can be read-out.

monitoring of acceleration is essential for a variety of applications ranging from inertial navigation to consumer electronics [78, 79]. Different technological applications for MEMS accelerometers have diverse requirements for their performance. For example, sensors for inertial navigation require low noise and bias stability [80], but large bandwidth is crucial for sensors in acoustics and vibrometry applications [81]. The read-out of test-mass motion can be accomplished using capacitive [82, 83], piezo-electric [84], piezo-resistive [85], tunnel-current [86], or optical methods [87–90]. Optical detection has some added benefits in that it provides resilience to electromagnetic interference and allows for long-range readout [91]. Fig. 4.2 shows a plot of displacement resolution versus bandwidth for various examples of these detection schemes. As can be seen in Fig. 4.2, our optomechanical detection scheme can provide superior displacement resolution. We therefore set out to make an optomechanical accelerometer.

4.2 Accelerometer Noise and Design

While displacement resolution is certainly an important figure of merit for accelerometer performance, it is far from the only one. In this section, we’ll discuss the various sources of acceleration noise relevant for our optomechanical accelerometer. This will also serve to motivate the design of our sensor.

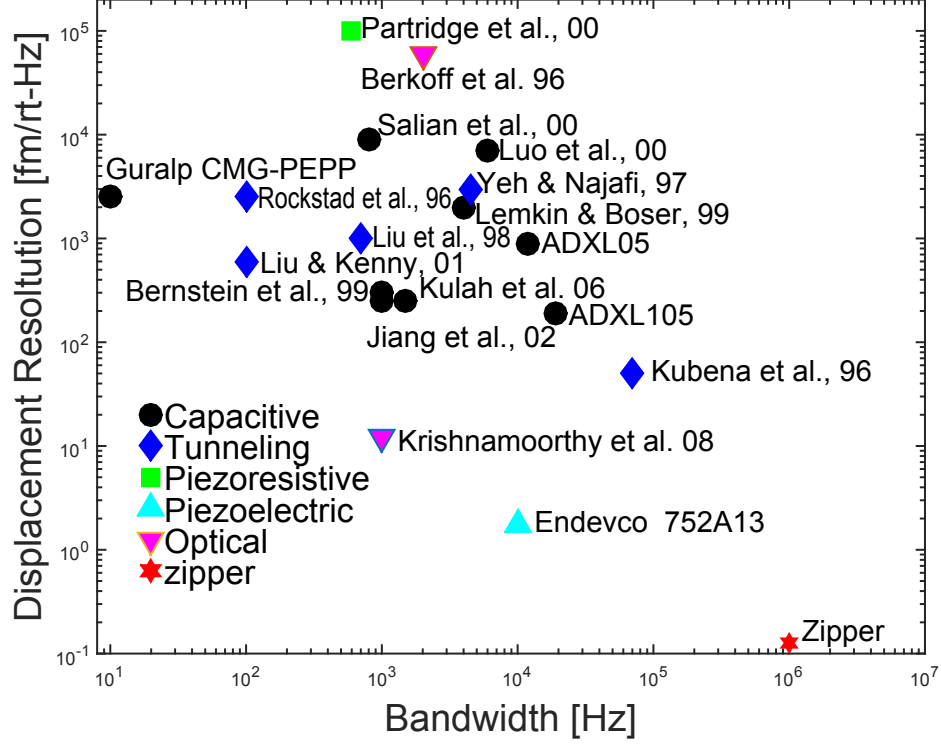


Figure 4.2: **Sensor Displacement Resolution.** This figure plots displacement resolution versus bandwidth for various sensors and is adapted from Ref. [92]. “Partridge et al., 00” is Ref. [85]. “Berkoff et al., 96” is Ref. [90]. “Salian et al., 00” is Ref. [93]. “Luo et al., 00” is Ref. [94]. “Yeh & Najafi, 97” is Ref. [95]. “Rockstad et al., 96” is Ref. [96]. “Guralp CMG-PEPP” is Ref. [97]. “Lemkin & Boser, 99” is Ref. [98]. “Liu et al., 98” is Ref. [86]. “ADXL05” is Ref. [99]. “Liu & Kenny, 01” is Ref. [100]. “Bernstein et al., 99” is Ref. [101]. “ADXL105” is Ref. [102]. “Kulah et al., 06” is Ref. [83]. “Jiang et al., 02” is Ref. [92]. “Kubena et al., 96” is Ref. [103]. “Krishnamoorthy et al 08” is Ref. [87]. “Endevco 752A13” is Ref. [104]. “Zipper” is work based off our zipper photonic crystals and is from Fig. 3.7a and Ref. [2].

4.2.1 Thermal Brownian motion (a_{th})

As discussed in Section 1.4, the mechanical resonator that comprises the accelerometer will undergo thermal fluctuations. Specifically, the displacement power spectral density (PSD) due to thermal noise is given in Eq. (1.36) and is repeated below.

$$S_{xx}^{th}(\omega) = \frac{4k_B T \omega_m}{mQ_m} \frac{1}{(\omega^2 - \omega_m^2)^2 + \left(\frac{\omega\omega_m}{Q_m}\right)^2} = \frac{4k_B T \omega_m}{mQ_m} |\chi(\omega)|^2 \quad (4.1)$$

In Eq. (4.1), we have used the definition for the mechanical susceptibility, $\chi(\omega)$, in Eq. (1.34). These fluctuations will be indistinguishable from displacements due to signals we wish to detect, and hence they represent an important and fundamental noise floor.

We now wish to obtain an expression for the acceleration PSD due to thermal noise of the test mass, $S_{aa}^{\text{th}}(\omega)$. Recall that Eq. (4.1) was obtained in Section 1.4 using the fundamental fluctuating thermal force Eq. (1.31), $S_{FF}(\omega) = 4k_B T m \gamma$. From Newton's law, $a = F/m$, and thus we have the following.

$$S_{aa}^{\text{th}} = \frac{4k_B T \omega_m}{m Q_m} \quad (4.2)$$

$$a_{\text{th}} = \sqrt{\frac{4k_B T \omega_m}{m Q_m}} \quad (4.3)$$

We have defined thermal acceleration noise, $a_{\text{th}} = \sqrt{S_{aa}^{\text{th}}}$. Note that a_{th} is independent of frequency. This is simply a consequence of the white thermal force noise and that the resonator's susceptibility to thermal forces is the same as that for applied external forces.

Naturally, we wish to minimize a_{th} as much as possible. For the original zipper devices [1], a_{th} is actually quite large. The mechanical parameters were $\omega_m = 2\pi \times 8$ MHz, $m = 40 \times 10^{-15}$ kg, $Q_m = 1.6 \times 10^4$ (in vacuum). This leads to $a_{\text{th}} \cong 4 \frac{mg}{\sqrt{\text{Hz}}}$. We have introduced a new acceleration unit here, $g = 9.81 \frac{m}{s^2}$, which is the acceleration due to gravity at the earth's surface.

Looking at the equation for a_{th} , it's easy to pick out which parameters are under our control. k_B is Boltzmann's constant, an immutable constant of the universe, which leaves us with little control over it. T , for practical accelerometers, is set by room temperature, 295 k, and thus we won't change it. ω_m is set by the bandwidth needed for the application. The vast majority of accelerometer applications are at acoustic frequencies or less [87]. Therefore, we leave ω_m on the order of 10 kHz, and don't treat it as an optimization parameter. This leaves us simply with mass, m , and quality factor, Q , as optimization parameters. To minimize a_{th} , we want to make both as large as possible.

The final design for our first demonstration of an optomechanical acceleration is shown in Fig. 4.3. The effective mass was increased to 10×10^{-12} kg by simply adding a large rectangle of silicon nitride to one of the optical beams, see Fig. 4.3a. The mechanical quality factor of the structure was optimized using the intuition developed in Section 2.3. The nanostrings connecting the test mass to the bulk of the chip were made as long and as thin as feasible given our fabrication techniques. The nanostring dimensions are $150 \text{ nm} \times 560 \text{ } \mu\text{m} \times 400 \text{ nm}$, and the measured mechanical Q of this structure in vacuum is, $Q_m = 1.4$ million [75] (how this Q_m is measured is discussed in Section 4.3). The high stress in the nanostrings leads to a frequency of the fundamental in-plane mechanical mode of $\omega_m = 2\pi \times 27.5$ kHz. A Comsol finite-element simulation [14] of the in-plane mechanical mode is shown in Fig. 4.3c (not to scale). Taken together, these parameters imply $a_{\text{th}} \cong 1.4 \frac{\mu g}{\sqrt{\text{Hz}}}$, a very significant improvement from the original zippers.

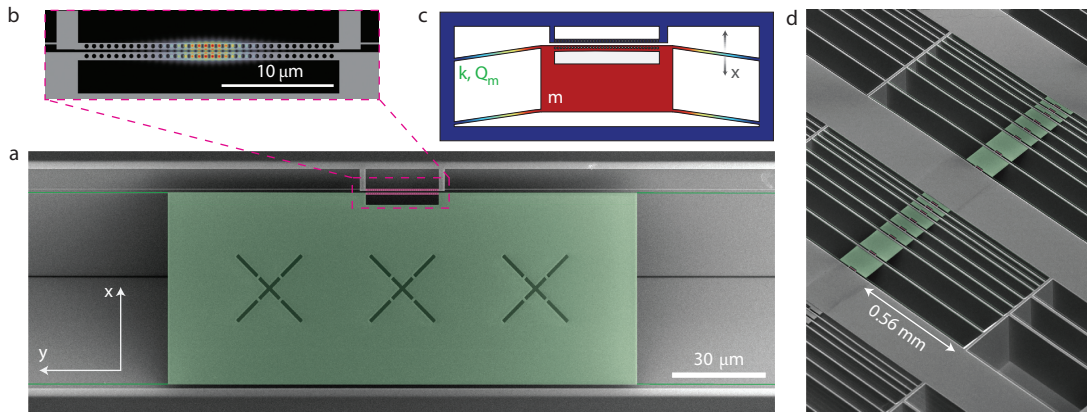


Figure 4.3: **Optomechanical Accelerometer Design.** (a) False-colored SEM image of an optomechanical accelerometer. Highlighted in green is the test mass and the nanostrings. The test mass is a rectangle of suspended silicon nitride of dimensions $150 \mu\text{m} \times 60 \mu\text{m} \times 400 \text{nm}$. The cross pattern is simply a fabrication technique to allow KOH to get underneath the test mass and more efficiently release it from the underlying silicon. The nanostrings are highly stressed silicon nitride of dimension $150 \text{nm} \times 560 \mu\text{m} \times 400 \text{nm}$. These dimensions serve to maximize the mechanical quality factor. The photonic crystal cavity where mechanical motion is sensed, is highlighted in pink. (b) Zoom-in of the optical cavity region showing the magnitude of the electric field, $|\mathbf{E}(\mathbf{r})|$, for the fundamental bonded mode of the zipper cavity. The top beam is rigidly connected to the bulk of the chip and can be considered effectively motionless relative to the chip. The bottom beam is connected to the flexible test mass. (c) Illustration of the displacement profile (not to scale) of the fundamental in-plane mechanical mode used for acceleration sensing. (d) SEM image of an array of devices with different test mass sizes.

4.2.2 Detector noise (a_{det})

An additional source of noise for our optomechanical accelerometer will be the electronic noise of the photodetector used to detect the laser light. This electronic noise is usually quantified by its noise-equivalent-optical-power (NEP). For the Newport 2117 detector and the transimpedance gain setting used in this chapter we have $NEP = \sqrt{S_{PP}^{NEP}} = 2.8 \text{ pW}/\sqrt{\text{Hz}}$. In this chapter, we utilize direct detection so we can use Eq. (1.15) to convert from the optical power spectral density for NEP to an effective displacement PSD. Furthermore, we can use Eq. (1.33), which slightly rewritten states, $x[\omega] = \chi(\omega) a[\omega]$, to convert the displacement PSD to an acceleration PSD. Taken all together yields the following results.

$$S_{\text{PP}}^{\text{NEP}} = NEP^2 \quad (4.4)$$

$$S_{\text{XX}}^{\text{NEP}} = \frac{NEP^2}{\left(\frac{dR}{d\Delta} P_{\text{in}} \eta g_{\text{OM}}\right)^2} \quad (4.5)$$

$$S_{\text{aa}}^{\text{NEP}} = \frac{NEP^2}{\left(\frac{dR}{d\Delta} P_{\text{in}} \eta g_{\text{OM}}\right)^2 |\chi(\omega)|^2} \quad (4.6)$$

$$a_{\text{NEP}} = \sqrt{S_{\text{aa}}^{\text{NEP}}} = \frac{NEP}{\left(\frac{dR}{d\Delta} P_{\text{in}} \eta g_{\text{OM}}\right) |\chi(\omega)|} \quad (4.7)$$

For the parameters used in the experiment of this chapter, including the laser being half an optical linewidth red-detuned from the optical resonance, $a_{\text{NEP}} = 4.1 \mu\text{g}/\sqrt{\text{Hz}}$, at frequencies much lower than ω_{m} .

4.2.3 Shot noise (a_{SN})

As discussed in Section 1.5.2, the laser light field will have quantum shot noise. This shot noise obeys poissonian statistics and, accordingly, the variance of the detected photon number will simply be, n_{det} , which is the number of photons hitting the detector. This leads to the optical power spectral density for shot noise.

$$S_{\text{PP}}^{\text{SN}} = 2 (\hbar\omega_{\ell})^2 n_{\text{det}} \eta_{qe} = 2\hbar\omega_{\ell} P_{\text{det}} \eta_{qe} \quad (4.8)$$

We have included a factor of 2 for using the single-sided power spectral density. P_{det} is the optical power at the detector and η_{qe} is the quantum efficiency of the detector. From here we can use the steps as in the previous section, Section 4.2.2, to derive the effective shot noise displacement PSD and acceleration PSD.

$$S_{\text{XX}}^{\text{SN}} = \frac{2\hbar\omega_{\ell} P_{\text{det}} \eta_{qe}}{\left(\frac{dR}{d\Delta} P_{\text{in}} \eta g_{\text{OM}}\right)^2} \quad (4.9)$$

$$S_{\text{aa}}^{\text{SN}} = \frac{2\hbar\omega_{\ell} P_{\text{det}} \eta_{qe}}{\left(\frac{dR}{d\Delta} P_{\text{in}} \eta g_{\text{OM}}\right)^2 |\chi(\omega)|^2} \quad (4.10)$$

$$a_{\text{SN}} = \sqrt{S_{\text{aa}}^{\text{SN}}} = \frac{\sqrt{2\hbar\omega_{\ell} P_{\text{det}} \eta_{qe}}}{\left(\frac{dR}{d\Delta} P_{\text{in}} \eta g_{\text{OM}}\right) |\chi(\omega)|} \quad (4.11)$$

For the parameters of the experiment to be described in this chapter, $a_{\text{SN}} = 8.9 \mu\text{g}/\sqrt{\text{Hz}}$, near DC (low frequency).

Additional note: to make sure extra classical laser noise was not limiting this experiment, we

split the laser into two paths with one arm entering the accelerometer optical cavity and the other bypassing it and equal power reaching the detector from both arms. The two paths were detected on a balanced photodetector, which subtracted the two signals. This leaves the accelerometer signal unchanged, but any classical laser noise suppressed. The shot noise in such a scheme is due to the total optical power hitting the detector, or twice the optical power in any one arm. The experimental setup is discussed in greater detail in Section 4.3.

4.2.4 Back-Action Noise (a_{BA})

As discussed in Section 1.5.2, the shot noise of the light field will impart a force on and cause motion of the mechanical resonator. Adapting Eq. (1.64), we can obtain the acceleration PSD due to back-action.

$$S_{\text{aa}}^{\text{ba}} = \frac{8(\hbar g_{\text{OM}})^2 n_c}{m^2 \kappa} \quad (4.12)$$

The resulting noise-equivalent acceleration is for the parameters used in this experiment is $a_{\text{ba}} = \sqrt{S_{\text{aa}}^{\text{ba}}} = 5.6 \text{ ng}/\sqrt{\text{Hz}}$. This is much smaller than all other noise sources and can effectively be ignored.

4.3 Experimental Setup and Device Characterization

Testing and characterization of the accelerometer shown in Fig. 4.3, was done using the experimental setup shown in Fig. 4.4. We used a New Focus velocity laser, which is a narrow-bandwidth ($< 300 \text{ kHz}$), 1500 nm telecom band, tunable external cavity diode laser. The laser light is split with a beamsplitter; the signal arm is sent through a fiber polarization controller (FPC) and a fiber taper coupled to the optical cavity, while the other arm is sent directly to a balanced photodetector (BPD). Variable optical attenuators (VOA) in each arm balance the powers. The optomechanical accelerometer chip along with commercial accelerometers are placed on top of a “shake table” composed of a shear piezo. By applying tones from a signal generator to the shear piezo, controlled accelerations can be applied and calibrated using the commercial accelerometers. Transduced accelerations are measured using either an electronic spectrum analyzer (ESA) or a lock-in amplifier.

As shown in Fig. 4.4, laser light is coupled into the cavity using a dimpled, tapered optical fiber. This double-sided coupling scheme was described in Section 2.2 and illustrated in Fig. 2.7. By scanning the laser frequency across the telecom band, we obtained the transmission spectrum of the fundamental bonded mode of the optical cavity, shown in Fig. 4.5. The measured optical resonance was at a wavelength of $\lambda_o = 1537 \text{ nm}$ and had a quality factor of $Q_o = 9500$.

After characterizing the optical mode, the laser is locked using a proportion-integral, PI, con-

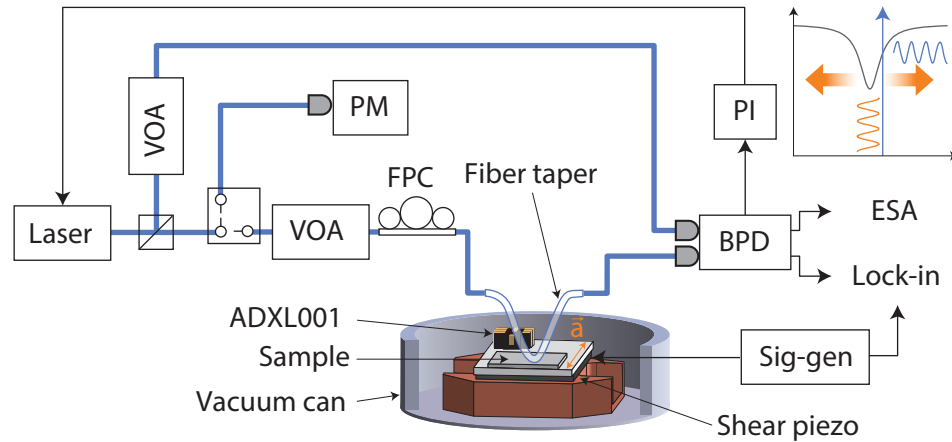


Figure 4.4: **Experimental Setup.** Laser light used to probe the zipper cavity motion is split with a beamsplitter; the signal arm is sent through a fiber polarization controller (FPC) and a fiber taper coupled to the optical cavity, while the other arm is sent directly to a balanced photodetector (BPD). Variable optical attenuators (VOA) in each arm balance the powers, and a power meter (PM) is used to calibrate the probe power. The BPD signal is sent to a proportional-integral controller (PI) locking the laser half a linewidth red-detuned from the optical resonance (lock frequency < 10 Hz). The sample is mounted on a shake table comprised of a shear piezo. Transduced accelerations are measured using either an electronic spectrum analyzer (ESA) or a lock-in amplifier.

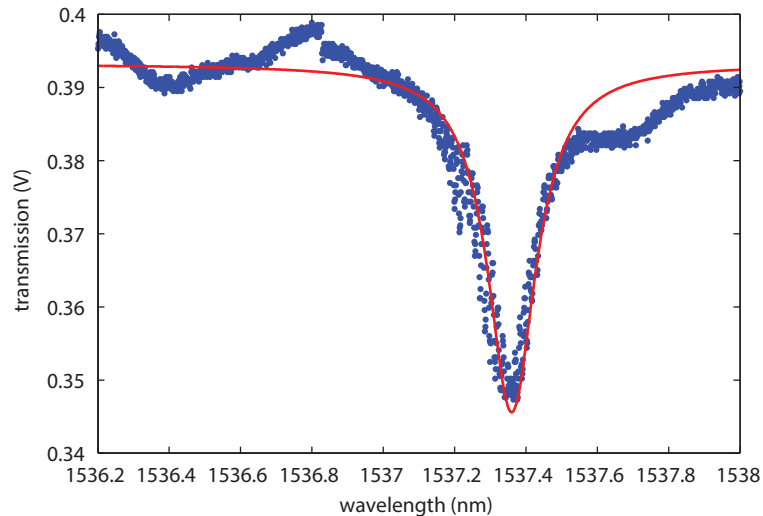


Figure 4.5: **Optical Cavity Transmission Spectrum.** This figure plots the unnormalized optical transmission spectrum of the fundamental bonded optical mode of the accelerometer's zipper cavity.

troller, see Fig. 4.4, half a linewidth red-detuned (i.e. longer wavelength) from the optical mode. This is the point of greatest slope on the laser transmission curve and allows us to transduce mechanical motion, as described in Section 1.2. Note that the PI lock only has a bandwidth of < 10 Hz. If the bandwidth were not limited, the lock would cancel out signals that we're interested as well

as the slow drifts. We employ a balanced detection scheme, which allows for efficient rejection of classical laser amplitude noise, yielding shot noise limited detection for frequencies above ~ 1 kHz. The power spectrum of the output of our balanced photodetector with a laser power incident at the optical cavity of, $P_{in} = 116\mu W$, half a linewidth red-detuned from the optical resonance is shown in Fig. 4.6.

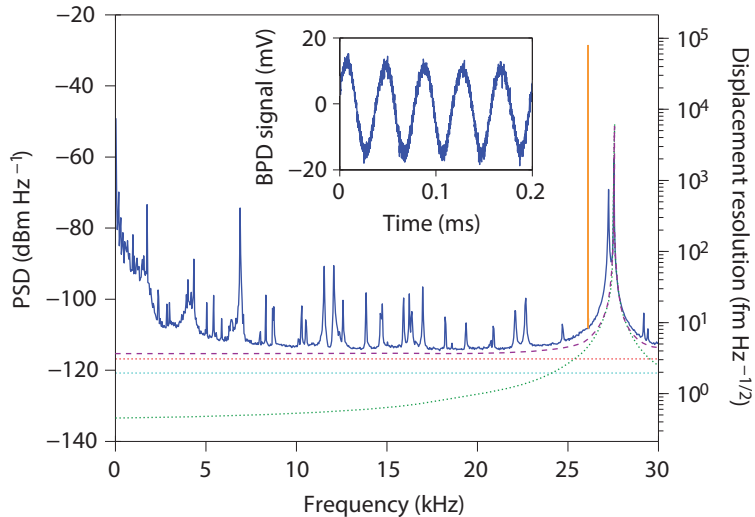


Figure 4.6: **Optical Power Spectral Density.** Left, axis: optical PSD of the BPD signal showing the fundamental in-plane mechanical mode at 27.5 kHz. Right axis: equivalent displacement noise. The tone at 26 kHz (orange) is transduction of a tone applied to the shear piezo corresponding to an rms acceleration of 38.9 mg. The dashed and dotted lines are theoretical noise levels for shot noise (red), detector noise (cyan), thermal noise (green), and total of all noise contributions (purple). Inset: time trace of the transduction of an applied acceleration of 35.6 mg at 25 kHz.

The fundamental in-plane mechanical mode (illustrated in Fig. 4.3) is the best transduced feature at $\omega_m = 2\pi \times 27.5$ kHz, see Fig. 4.6. This is in good agreement with finite-element method simulations in Comsol, from which we also extracted the effective mass, $m = 10 \times 10^{-12}$ kg. In principle, the mechanical quality factor can be determined by fitting the PSD to the form of Eq. (4.1) and extracting the Q_m fit parameter. In practice, the sub-Hz linewidths of our mechanical modes make establishing the quality factor from the PSD measured on a spectrum analyzer infeasible because it requires a fractional stability of the mechanical frequency much greater than $1/Q_m \approx 5 \times 10^{-7}$ over a time period much longer than the decay time $Q_m/\omega_m > 10$ s. However, since the system is driven by a Gaussian thermal noise process, the autocorrelation of the amplitude $\langle x(t)x(t+\tau) \rangle$ can be shown to decay as $e^{-t/\tau}$, from which the quality factor can be obtained as $Q_m = \tau\omega_m$ [57, 58]. The slowly-varying envelope of $\langle x(t) \rangle$ is obtained from the magnitude channel of a lock-in amplifier tuned to the mechanical resonance frequency with a bandwidth (≈ 100 Hz) much larger than than the linewidth, which ensures that small frequency diffusion does not affect the measurement of the

envelope. To obtain the bare mechanical Q-factors the measurement is made at an optical power low enough to ensure there is no back-action. The autocorrelation is numerically computed and the decay is fit to an exponential curve with a constant (noise) offset. In Fig. 4.7a we show an autocorrelation trace of the devices presented in the main text calculated from ≈ 3000 s of data sampled at 100 Hz and fit to find $\tau = 7.85$ s and for $\omega_m = 2\pi \times 27.5$ kHz that yields $Q_m = 1.4 \times 10^6$. For lower-Q structures, it was confirmed that this technique agrees with a direct measurement of the linewidth from a spectrum analyzer.

Since gas damping severely limits the mechanical Q-factor of our oscillator, measurements were carried out in vacuum. Fig. 4.7b, shows pressure-dependent mechanical Q-factors using a device of equal mass to the device shown in Fig. 4.3, but with 70 nanostring tethers, resulting in an eigenfrequency of $\omega_m = 2\pi \times 110$ kHz. We find that the device exhibits a Q-factor of 53 at ambient pressure, which strongly increases when reducing the pressure in the vacuum chamber. In particular, for pressures below 10^{-3} mbar – the regime in which we carried out our acceleration resolution measurements ($\lesssim 2 \times 10^{-5}$ mbar) – we observe Q-factors above 10^6 .

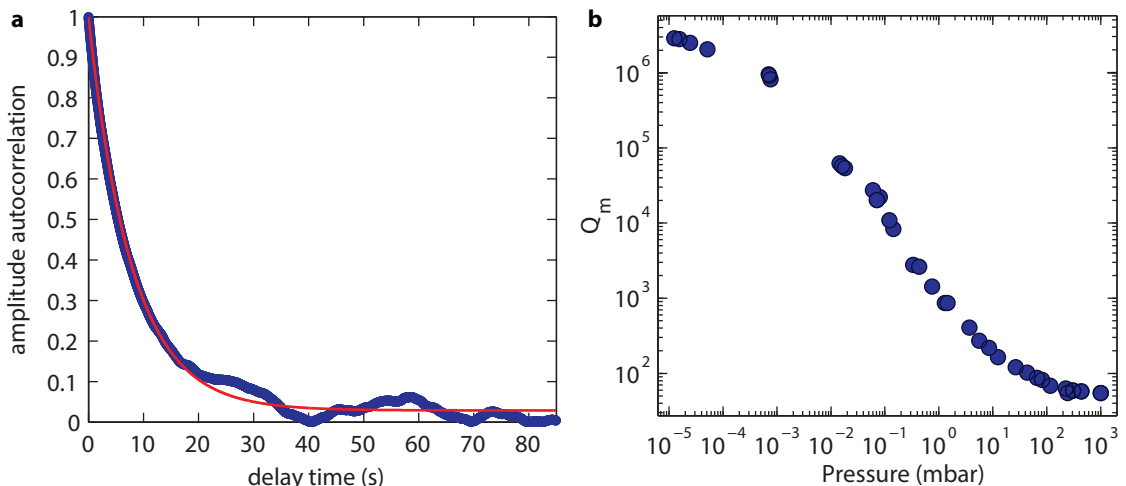


Figure 4.7: **Investigation of Mechanical Q-factors.** (a) Autocorrelation trace of the thermal noise driven mechanical amplitude. The signal was obtained from computing the autocorrelation of the slowly varying magnitude of the mechanical motion returned from a lock-in amplifier, using the experimental setup of Fig. 4.4. Fitting the trace with an exponential decay yields the time constant and thereby the mechanical Q-factor of the mode ($Q_m = 1.4 \times 10^6$). (b) Pressure-dependence of the mechanical Q-factor of a control device with $m = 10^{-11}$ kg and 70 nanostring tethers, showing an increase from $Q_m \approx 53$ to $Q_m \approx 2.5 \times 10^6$ in high vacuum.

Careful calibration of our optical mode parameters, input power, optical losses from the cavity to the detector, $\eta = 0.57$, and mechanical mode parameters allow us to calibrate our value of g_{OM} . We use the direct detection analysis of Section 1.2 (cosmetically altered because we are working on transmission), and assume our mechanical mode is thermally driven according to Eq. (1.36)

(this assumption will be validated later). Furthermore, for the g_{OM} calibration, we use low optical powers where back-action effects are negligible, and therefore the mechanical mode's effective temperature is room temperature. Under these experimental conditions, fitting the optical PSD in the vicinity of the mechanical resonance at $\omega_{\text{m}} = 27.5$ kHz yields the optomechanical coupling constant, $g_{\text{OM}} = 2\pi \times 5.5$ GHz/nm. From electromagnetic finite-element simulations in Comsol using zipper cavity dimensions determined by scanning electron microscopy (SEM), we calculate $g_{\text{OM}} = 2\pi \times 13.5$ GHz/nm, in relatively good agreement with the measured value.

4.3.1 Characterization Continued: Thermo-Opto-Mechanical Cooling

The PSD in Fig. 4.6 was taken with the laser half a linewidth red-detuned from the optical cavity with an incident optical power of, $P_{\text{in}} = 116$ μW , or equivalently, an intracavity photon number, $n_{\text{c}} \approx 430$. At this optical power, the observed linewidth of the mechanical mode is ≈ 2 Hz, approximately 100 times larger than the low-power linewidth. This can be modeled as radiation pressure dynamical back-action, enhanced by slow thermo-optical tuning of the cavity, which provides the necessary phase lag for efficient velocity damping [75]. The case of bare optomechanical dynamical back-action without thermal effects was discussed in Section 1.5.1. Adding in the thermal component was done in supplemental information of Ref [1], and is repeated later in this section. Damping of the mechanical resonance of accelerometers is typically used to reduce the ringing transient response of the sensor when subjected to shock input [105]. Similar to active feedback damping, this optomechanical back-action also cools the mechanical resonator [42] (also see Section 1.5.1), in contrast to, for example, gas damping [106]. The measured effective temperature of the fundamental in-plane mode of the test mass, as determined from the area under the 27.5 kHz resonance, see Fig. 4.6, is $T_{\text{eff}} \approx 3$ K. This combination of damping and cooling keeps the ratio of $T_{\text{eff}}/Q_{\text{m}}$ fixed, and does not degrade the thermally limited acceleration resolution of the sensor.

For the remainder of this subsection, we outline the derivation of thermo-opto-mechanical cooling. The supplementary information of Ref [1] gives a detailed derivation and we follow that derivation here. This outline of the derivation can also be found in the supplementary information of Ref [75]. The methods used to solve the coupled differential equations in this section, are the same as the methods used to solve the bare optomechanical case shown in Section 1.5.1.

The system of differential equations that describes the time evolution of the intra-cavity field a , the oscillator position x , and the cavity temperature shift ΔT is given by

$$\dot{a} = -[i\Delta - (g_{\text{OM}}x + g_{\text{th}}\Delta T)]a - \frac{\kappa}{2}a + \sqrt{\frac{\kappa_{\text{e}}}{2}}a_{\text{in}} \quad (4.13)$$

$$\ddot{x} = -\gamma_{\text{i}}\dot{x} - \omega_{\text{m,i}}^2x - \frac{\hbar g_{\text{OM}}}{m}|a|^2 \quad (4.14)$$

$$\dot{\Delta T} = -\gamma_{\text{th}}\Delta T + \kappa_{\text{abs}}c_{\text{th}}\hbar\omega_{\text{c}}|a|^2, \quad (4.15)$$

where $g_{\text{th}} = -(dn/dT)(\omega_c/n)$ is the thermo-optical tuning coefficient, dn/dT is the thermo-optic coefficient of the material, κ_{abs} is the optical loss rate due to material absorption, c_{th} is the thermal heat capacity, and γ_{th} is the decay rate of the temperature. Linearizing these equations yields the static solutions

$$a_0 = \sqrt{\frac{\kappa_e}{2}} \frac{1}{i\Delta' + \kappa/2}, \quad x_0 = \frac{\hbar g_{\text{OM}}}{m\omega_{\text{m},i}^2} |a_0|^2, \quad \Delta T_0 = \frac{\kappa_{\text{abs}}}{\gamma_{\text{th}}} c_{\text{th}} \hbar \omega_c |a_0|^2 \quad (4.16)$$

with the renormalized detuning $\Delta' = \Delta - g_{\text{OM}}x_0 - g_{\text{th}}\Delta T_0$ arising from the static optomechanical and thermo-optical shift. Using a perturbation ansatz $x(t) = x_0 + \epsilon \cos(\omega_{\text{m},i}t)$ one arrives, after some algebraic manipulation, at a modified harmonic oscillator equation for x with a renormalized frequency $\omega_{\text{m,eff}}$ and damping rate γ_{eff} given by

$$\omega_{\text{m,eff}}^2 = \omega_{\text{m},i}^2 - \frac{\hbar \omega_c n_{\text{cav}} g_{\text{OM}}^2}{\omega_c m} \text{Im}[g(\omega_{\text{m},i})], \quad (4.17)$$

$$\gamma_{\text{eff}} = \gamma_i + \frac{\hbar \omega_c n_{\text{cav}} g_{\text{OM}}^2}{\omega_{\text{m},i} \omega_c m} \text{Re}[g(\omega_{\text{m},i})], \quad (4.18)$$

where the transfer function $g(\omega)$ is defined as

$$g(\omega) = f \frac{1 + f'^* f^*}{|1 + f' f|^2} \quad (4.19)$$

with

$$f(\omega) = \frac{1}{i(\omega + \Delta') + \kappa/2} - \frac{1}{i(\omega - \Delta') + \kappa/2} \quad (4.20)$$

and

$$f'(\omega) = -i \frac{\Delta_{\text{th}} \gamma_{\text{th}}}{i\omega + \gamma_{\text{th}}}, \quad (4.21)$$

and $\Delta_{\text{th}} = g_{\text{th}}\Delta T_0$ is the static thermo-optical shift of the cavity resonance frequency. In the sideband unresolved regime where $\omega_{\text{m},i} \ll \kappa$ and for thermal decay rates γ_{th} smaller than the mechanical frequency, an approximation of $g(\omega)$ yields

$$\omega_{\text{m,eff}}^2 = \omega_{\text{m},i}^2 + \frac{2\hbar n_{\text{cav}} g_{\text{OM}}^2}{m} \frac{\Delta'}{\Delta'^2 + \kappa^2/4} \left[\frac{1+W}{1+s} \right], \quad (4.22)$$

$$\gamma_{\text{eff}} = \gamma_i + \frac{2\hbar n_{\text{cav}} g_{\text{OM}}^2}{m} \frac{\kappa \Delta'}{(\Delta'^2 + \kappa^2/4)^2} \left[\frac{1+V}{1+s} \right], \quad (4.23)$$

with the correction factors

$$W = -\left(\frac{2\Delta_{\text{th}}}{\kappa}\right)\left(\frac{\gamma_{\text{th}}}{\omega_{\text{m},i}}\right)^2\left(\frac{\kappa\Delta'}{\Delta'^2 + \kappa^2/4}\right), \quad (4.24)$$

$$V = \left(\frac{2\Delta_{\text{th}}}{\kappa}\right)\left(\frac{\gamma_{\text{th}}}{\omega_{\text{m},i}}\right)^2\left(\frac{\Delta'}{\gamma_{\text{th}}}\right) \quad (4.25)$$

$$(4.26)$$

and the saturation parameter

$$s = \left(\frac{2\gamma_{\text{th}}\Delta_{\text{th}}\hbar\omega_c n_{\text{cav}}}{\omega_{\text{m},i}} \frac{\Delta'}{\Delta'^2 + \kappa^2/4}\right)^2 \left(1 + \frac{1}{\Delta_{\text{th}}} \left(\frac{\Delta'^2 + \kappa^2/4}{\Delta'^2} - \frac{\omega_{\text{m},i}^2 \kappa}{\Delta' \gamma_{\text{th}}}\right)\right) \quad (4.27)$$

In the parameter regime of our devices, purely optomechanical back-action is a relatively weak effect due to the low optical Q -factor. For the parameters given above and for a pump laser with an incident power of $P_{\text{in}} = 116 \mu\text{W}$ half a linewidth red-detuned from the cavity resonance, optomechanical back-action alone predicts a frequency shift of merely $\omega_{\text{m,eff}} - \omega_{\text{m},i} = -2\pi \times 35.9 \text{ Hz}$ and a damping factor of $\gamma_{\text{eff}}/\gamma_i = 1.01$.

In order to study the influence of thermo-optical back-action, we measured the Q -factor of the mechanical mode as function of the optical power launched into the cavity, shown as the green bullets in Fig. 4.8. When increasing the optical power to $P_{\text{in}} \approx 300 \mu\text{W}$, which corresponds to an intracavity photon number of $n_{\text{cav}} \approx 1,100$, the Q -factor shows strong damping and is reduced by a factor of ≈ 200 . Similarly, we measure the area of the mechanical resonance peak from the optically transduced thermal noise PSD for a series of optical powers, and plot the inferred effective mode temperature as blue bullets in Fig. 4.8. Clear in Fig. 4.8 is that the effective mode temperature is dropping with the measured mechanical Q -factor.

The observed mechanical damping is much larger than the value predicted by pure optomechanical back-action and can be explained when including thermo-optical tuning. The green line in Fig. 4.8 was obtained by calculating the modified Q -factor $Q_{\text{m,eff}} = \omega_{\text{m},i}/\gamma_{\text{eff}}$ using eq. (4.18) with $\Delta_{\text{th}} = -0.05\kappa$ and $\gamma_{\text{th}} = 2\pi \times 9.2 \text{ kHz}$. The latter value is in good agreement with the one from Ref. [1] ($\gamma_{\text{th}} = 2\pi \times 10 \text{ kHz}$), which suggests that the time constant of thermo-optical tuning is dominated by heat-flow from the zipper cavity region to the reservoir formed by the test-mass (or the bulk in the case of Ref. [1]).

The obtained values for Δ_{th} and γ_{th} result in correction factors of $V = 12,400$, $W = -0.011$, and a saturation parameter of $s \approx 3 \times 10^{-36}$. Accordingly, we expect a significant thermo-optical correction to damping, as observed, but only a minor modification of the optomechanical spring: $\omega_{\text{m,eff}} - \omega_{\text{m},i} = 2\pi \times 36.2 \text{ Hz}$ for the pump power used in the experiment. Indeed, we observed a frequency shift of 101 Hz, in reasonable agreement with the theoretical value.

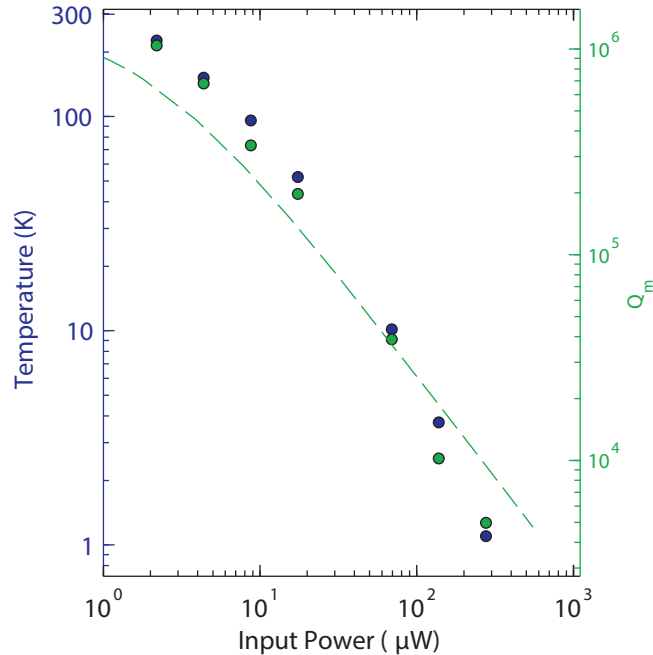


Figure 4.8: **Thermo-opto-mechanical Damping and Cooling.** The green bullets show measured Q-factors of the mechanical mode as a function of the optical power, yielding thermo-optomechanical damping by a factor of ≈ 280 . The blue bullets show the corresponding optical power in the sideband generated by mechanical motion, proportional to the effective mode temperature. We observe cooling to $T_{\text{eff}} \approx 1\text{K}$. The dashed green curve corresponds to a theoretical model that includes optomechanical and thermo-optical back-action.

4.3.2 Characterization Continued: Tapered Optical Fiber Modes

The optical PSD in Fig. 4.6, plots the standard noise sources of shot noise, detector noise, and thermal noise of the main mechanical mode. In addition to these noise sources, we find a series of extra noise features in the optical PSD. These are primarily manifested in a series of sharp resonances as well as an increase of the noise background for frequencies below ≈ 3 kHz. One sharp resonance, closest to the fundamental in-plane mechanical mode at 27.5 kHz, is the fundamental out-of-plane mechanical mode, determined by Comsol simulations of the structure. In order to identify the source of many of these extra noise features as arising from the fiber taper, we measured the response of the fiber taper transmission to acceleration applied via the shake table with the laser far-detuned (2 nm) from the optical resonance. This detuning eliminates pick-up from the zipper cavity. The green curve in Fig. 4.9 shows the sensitivity, i.e. the detected volts at the BPD as measured by the lock-in amplifier per applied g of acceleration by the shaker table as calibrated by the commercial accelerometers. Clearly, the bare fiber taper exhibits a substantial response to applied accelerations, which we attribute to optical losses into the substrate that are modulated by the mechanical motion of the taper. This response contains both a series of sharp resonances and a low-frequency feature

that follows a ω^{-2} dependence like the response of a low-lying mechanical resonance. The sensitivity of the accelerometer with the laser locked half a linewidth red-detuned from the optical cavity is shown in Fig. 4.9 as the blue line for comparison. It follows the frequency-dependence of the fiber taper for low frequencies, yet exhibits a sensitivity increase by roughly a factor of two with respect to the bare taper response. We attribute this increase by an optomechanical coupling between the motion of the taper and the optical cavity resonance.

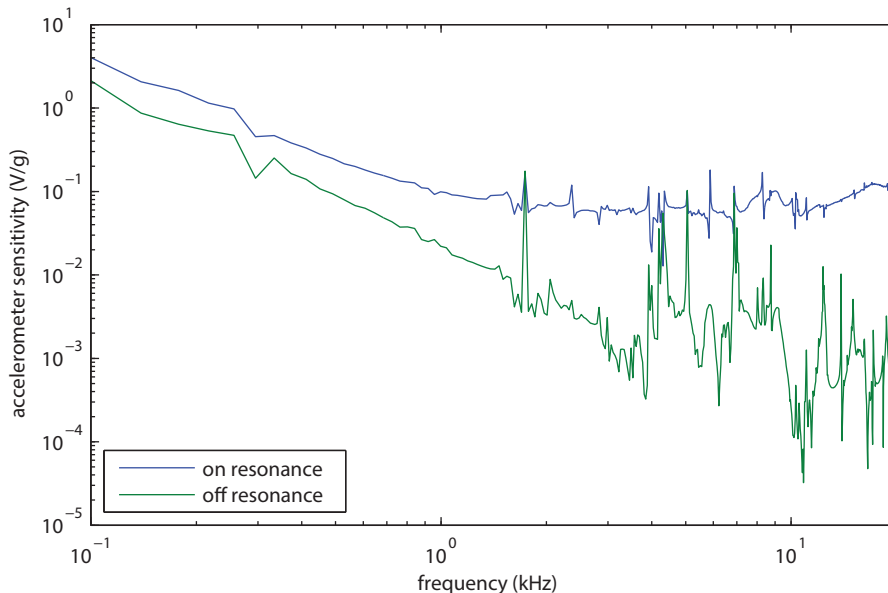


Figure 4.9: **Comparison of the low-frequency on and off resonance response of the accelerometer and the bare fiber taper.** The green curve was obtained by detuning the laser far from the optical resonance and thus excludes any transduction from the optical mode. This curve shows a pronounced ω^{-2} dependence, thus suggesting that the response is dominated by a low-frequency mechanical mode of the taper. The blue curve is taken with the laser locked half a linewidth red-detuned from the optical resonance frequency.

In order to gain further insight into the influence of the fiber taper on the noise performance of our device, we compare noise power spectral densities for different arrangements of the fiber taper waveguide with respect to the zipper cavity, as shown in Fig. 4.10. The blue curve in Fig. 4.10a shows the inherent noise background of our measurement system, obtained by recording the balanced photodiode signal when bypassing the fiber taper. The gray curve for comparison shows the electronic noise background of the detector in the absence of optical signals. The detector exhibits characteristic $1/f$ -noise and creating a noise background well below the optical signal. From the blue curve it can be seen that while for frequencies above ~ 5 kHz the signal is dominated by photon shot noise, there are two prominent noise features at 1 kHz and 4 kHz that arise from acoustic noise in the laboratory transduced by elements in the optical train such as the fiber beamsplitter and the laser head. This identification was established by employing a tunable frequency sound generator while observing

the magnitude of the corresponding modulation tone in the optical PSD. We found substantial enhancement of this acoustic pick-up when the sound frequency was resonant with the features in Fig. 4.10, and in particular when the speaker was placed close to the fiber beamsplitter and laser head.

The green curve in Fig. 4.10b shows a PSD with the taper in the optical path, yet hovering several 100 μm above the sample. In this situation, we observe a qualitatively similar spectrum to the one before, yet with a slightly enhanced response at low frequencies. We note that the power at the detector was different in these four experiments, explaining the difference in background noise levels. The red curve in Fig. 4.10c shows a PSD with the taper touched down near our device at ambient pressure with the laser off-resonance from the cavity mode. Here, we notice a strong increase of noise below ~ 1.5 kHz. We interpret this increase as an enhancement due to the $1/\omega^2$ response of the taper discussed above that arises when the taper is evanescently coupled to the substrate. Finally, the cyan curve in Fig. 4.10d shows a noise spectrum obtained under almost the same conditions as the data in Fig. 4.6, i.e. with the taper touched down near the device in vacuum, yet the laser detuned from the cavity resonance. Here, we observe the emergence of a series of sharp resonances, leading us to conclude that the same features observed in the data in Fig. 4.6 are of mechanical origin, and their appearance in vacuum is caused by an increase of their quality factors.

Test measurements monitoring the output of the commercial accelerometers confirm that these sharp resonances do not arise from the shake table. Also, the extra noise in vacuum does not arise from the vacuum pump, because we use an ion-getter pump with no moving parts. Moreover, we found that different ways of touching the fiber taper on the device shifts both the amplitude and frequency of these extra noise modes. In combination, these observations strongly support the existence of extra noise channels introduced by mechanical modes of the fiber taper.

4.4 Calibration: Accelerometer Sensitivity and Resolution

Now that we have characterized the optical and mechanical properties of our accelerometer and understand the noise sources of our measurement, we can calibrate its accelerometric performance. As previously mentioned, this calibration is done by driving a shear piezo, upon which our accelerometer and commercial sensors sit; see Fig. 4.4. Applying a sinusoidal voltage to the shear piezo results in a harmonic in-plane acceleration, $a(\omega)$, and thus modulation of the transmitted optical power. The optical power in the modulation sideband is given by Eq. (1.14) (cosmetically altered because we work on transmission in this experiment).

$$P_m(\omega) = P_{in}\eta\frac{dT}{d\Delta}g_{OM}|\chi(\omega)a(\omega)| \quad (4.28)$$

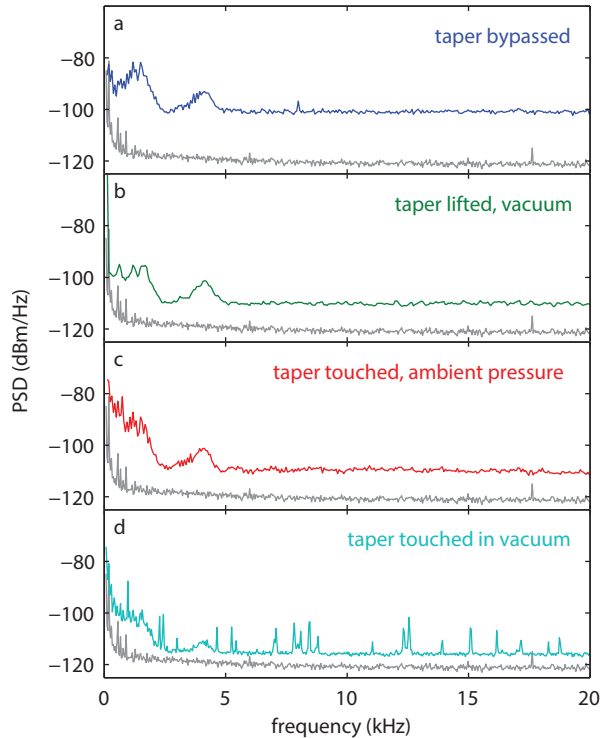


Figure 4.10: **Optical noise PSDs for different experimental configurations.** The blue curve is the noise PSD present in the detection system with the taper bypassed. The green curve shows the response with the taper in-line but far from the sample surface. The red curve shows the response with the taper touched down to the sample in ambient pressure, exhibiting an increased DC noise level. The cyan curve shows the response with the taper touched down in vacuum and the laser detuned from the optical resonance. Taken together, these curves suggest that the sharp resonances are due to mechanical modes of the taper whose Q-factors are enhanced in vacuum, and, the low frequency noise ($\lesssim 1$ kHz) is enhanced by the proximity of the taper to the substrate.

In Eq. (4.28), T is the normalized cavity transmission, the un-normalized cavity transmission for this experiment is plotted in Fig. 4.5. An example of such an applied acceleration tone is shown in Fig. 4.6. The narrow tone at 26 kHz (orange) arises from an applied root-mean square (rms) acceleration of $a_{rms} = 38.9$ mg, calibrated using the two commercial accelerometers mounted on the shake table. From the signal-to-noise ratio of this calibration tone, we estimate $a_{th} = 2.0 \mu g/\sqrt{Hz}$, comparable to the predicted theoretical value of $a_{th} = 1.4 \mu g/\sqrt{Hz}$. This confirms that the fundamental in-plane mechanical mode at 27.5 kHz is largely driven by room-temperature thermal noise.

Fig. 4.11a shows the demodulated photodiode signal (using the lock-in amplifier, see Fig. 4.4) normalized to the applied acceleration as a function of drive frequency, corresponding to the frequency-dependent acceleration sensitivity of the zipper cavity. The inset of Fig. 4.11a presents the data from the commercial accelerometers used to calibrate the applied acceleration. The dashed red line is the

theoretical calculation of the sensitivity without fit parameters and shows excellent agreement. The sharp, Fano-shaped features for lower frequencies can again be attributed to mechanical resonances of the fiber-taper waveguide. The broad region of apparent higher sensitivity around 15 kHz is due to an underestimate of the applied acceleration arising from an acoustic resonance of the shake table.

The calibrated frequency-dependent acceleration resolution, or noise-equivalent acceleration NEA, is shown in Fig. 4.11b. It was obtained by normalizing the PSD in Fig. 4.6 with the sensitivity curve in Fig. 4.11a. This is the same procedure as discussed for the tone at 26 kHz in Fig. 4.6. A known acceleration tone is applied and the noise floor is calibrated using the signal-to-noise ratio of this tone. Between 25 and 30 kHz, the resolution is limited by the thermal noise of the oscillator, and from 5 to 25 kHz, shot noise limits the resolution to $\sim 10 \mu\text{g}/\sqrt{\text{Hz}}$. For frequencies lower than 5 kHz, motion of the fiber-taper waveguide and the environment contribute extra noise. The sharp Fano-shaped feature at 27 kHz arises from interference with the fundamental out-of-plane mode of the test mass. The dashed red curve corresponds to a theoretical estimate of the NEA given shot noise and thermal noise, and shows good agreement. The dashed green line is the fundamental thermal noise sensing limit, a_{th} .

With a demonstrated acceleration resolution on the order of a few $\mu\text{g}/\sqrt{\text{Hz}}$ and a bandwidth above 25 kHz, the zipper cavity device presented here shows performance comparable to the best MEMs commercial sensors [104].

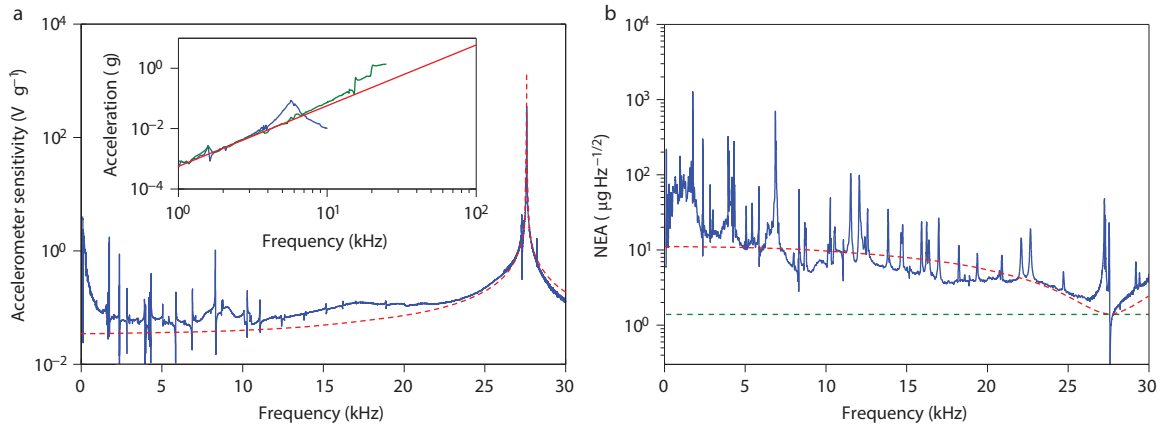


Figure 4.11: **Frequency-dependence of sensitivity and resolution.** (a) Sensitivity curve as a function of frequency, obtained by driving the shear piezo with a sinusoidal voltage and measuring the amplitude of the resulting voltage modulation of the BPD signal using a lock-in amplifier. The dashed red line corresponds to the theoretical expectation for the sensitivity without fit parameters. Inset: data from commercial accelerometers also attached to the shake table (blue and green curves), which were used for calibrating the applied acceleration (best-fit line, solid red curve). (b) Frequency-dependent NEA of the device, quantifying its broadband resolution. The plot is obtained by taking the PSD in Fig. 4.6 and normalizing it with the sensitivity in (a). The dashed red line depicts the theoretical expectation for the NEA given shot noise and thermal noise limitations. The green dashed curve corresponds to the thermal noise, a_{th} .

4.5 Moving Forward

Encouraged by the excellent acceleration resolution of our demonstrated optomechanical accelerometer, there several avenues of improvement for the device's performance and practicality. These avenues will be explored in the subsequent chapter. Fiber-coupled on-chip waveguides [12, 89] will enable convenient small form-factor packaging as well facilitating the removal of noise associated with the current fiber-taper coupling. These device also allow for the integration of electrostatic tuning capacitors [107], which allow dynamic tuning of the optical cavity resonance frequency. This allows for the replacement of expensive tunable lasers with cheaper and essentially fixed-wavelength laser sources, which can be fabricated on-chip [108].

Additionally, the thermal noise performance of our sensor can easily be enhanced by an order of magnitude by adding mass. Naively, adding mass would decrease the mechanical resonance frequency, thereby, sacrificing bandwidth. However, by increasing the number of nanostring tethers commensurate with the mass increase, the frequency can be held constant, see Fig. 4.12. Moreover, increasing the number of tethers to 140 does not greatly affect the mechanical quality factor, see Fig. 4.12. Furthermore, by increasing the mass by several orders of magnitude, the same a_{th} performance can be achieved with lower mechanical quality factor, see Eq. (4.3). Lower Q_{m} devices are more stable to shock inputs and can be operated in higher air pressure environments (see Fig. 4.7b), relaxing packaging constraints.

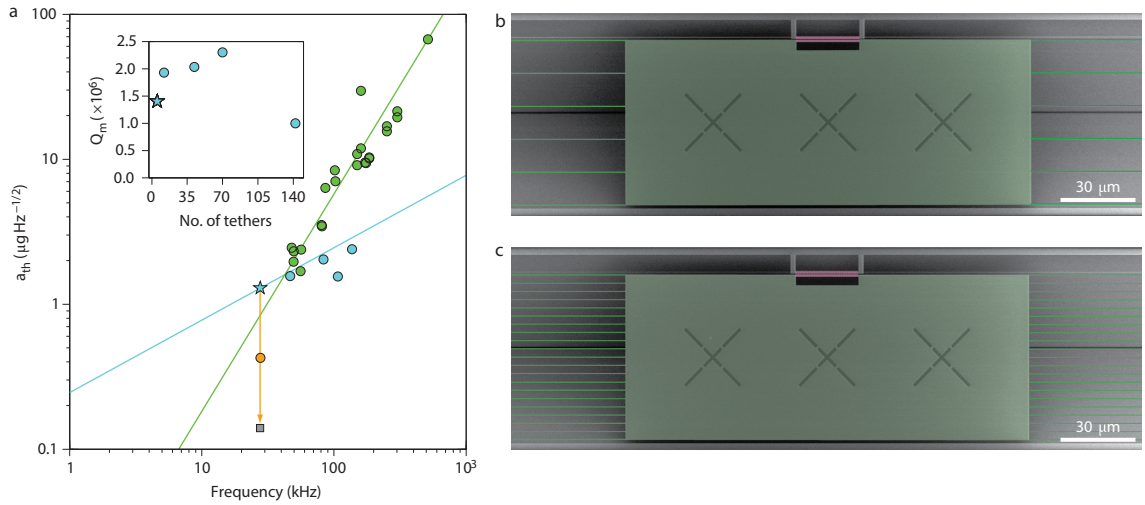


Figure 4.12: **Future Directions; adding mass and nanostrings.** (a) Thermal acceleration noise density of measured devices (green, cyan, and orange data points). The starred point represents the device discussed in this chapter. The green line is that traversed for adding mass with fixed Q_m and spring constant, k , and the cyan line is obtained for varying k while keeping Q_m and m fixed. Varying both m and k allows for independent control of bandwidth and resolution, for example along the orange line, where k/m is constant and Q_m is fixed. The grey point represents the theoretical device performance for the test mass increased by a factor of 100 over that in this chapter. Inset: Q_m for devices corresponding to the cyan circles in (a) versus the number of nanostring tethers attached to the test mass. (b)(c) False-color SEM images of devices with 12 (b) and 42 (c) nanostring tethers and $\omega_m = 2\pi \times 46$ kHz (b) and $\omega_m = 2\pi \times 83$ kHz (c), respectively.

Chapter 5

Improving the Performance and Practicality of the Optomechanical Accelerometer

The demonstration of an optomechanical accelerometer in Chapter 4 was an important proof of principle. However, there remains significant room for improvement. Firstly, the dimpled, tapered optical fiber coupling method was noisy (see Section 4.3.2 and Fig. 4.6) and completely impractical for a useful sensor. The method involves daintily placing the fiber onto the surface of the chip using a 3-axis set of nano-positioners. In Section 5.1, a much more robust coupling scheme is demonstrated using the V-groove coupling techniques first discussed in Section 2.2 and Fig. 2.11.

Secondly, the optical mode frequency so far has been lithographically defined with no means for active control. When dealing with relatively fixed wavelength laser sources and thermal drifts, it will be necessary to actively control the optical mode frequency. In Section 5.2, this is accomplished using capacitive wavelength tuning.

Thirdly, the eventual goal of this optomechanical accelerometer project would be to have a fully integrated and packaged sensor ready for practical applications. Perhaps the biggest hurdle to such a goal will be integration with on-chip lasers. In Section 5.3, we show a proof-of-principle that Intel's on-chip lasers can achieve the same acceleration sensing performance as our table-top tunable lasers.

Fourth, in Section 5.4, we discover and significantly reduce the source of important low frequency noise of our accelerometers, first clearly observed in Section 5.1.

Fifth, in Section 5.5, we use new fabrication techniques to increase the size of the test mass by approximately 4 orders of magnitude. This allows for a thermal noise resolution less than $100 \text{ ng}/\sqrt{\text{Hz}}$ even at atmospheric pressure.

5.1 V-groove Fiber Coupled Accelerometer

Example V-groove fiber coupled accelerometers as designed and studied in this thesis are shown in Fig. 5.1. The mechanical resonator component of the accelerometer is of identical design to that in Chapter 4. The V-groove optical coupling method is discussed in Section 2.2 and Fig. 2.11 and was designed in Ref. [12]. The on-chip waveguide can either take a 90-degree turn, Fig. 5.1f, or continue straight to the optical cavity, Fig. 5.1g. The data presented in this section were taken on devices similar to Fig. 5.1g.

The fabrication methods used to make these devices are discussed in Section 2.4 and Figs. 2.14 and 2.15, with one technical detail omitted. When fabricating devices of the design shown in Fig. 5.1g, the KOH release step was done in two parts, with the first KOH etch defining the V-groove and the second releasing the mechanical resonator and optical cavity. This was done to avoid the deleterious consequences of excessive etching of convex corners. Such a two step KOH release was accomplished by first spinning on a photosensitive protective coating for alkaline etches called Protek PSB by Brewer Science. The region of this coating covering the V-groove region was then exposed to UV radiation and removed upon development. The KOH etch to define the V-groove was then performed, then the remaining PSB was removed in a piranha solution, then the remaining structure was released in the second KOH etch, and then, finally, the structure was rinsed and critical-point dried.

Of particular importance to this section is the optical fiber in Fig. 5.1f. As one can see in this false-colored SEM image, the optical fiber is securely glued into the silicon V-groove. This is accomplished by slowly lowering the cleaved optical fiber into the V-groove using micrometer stages while monitoring with an optical microscope and then fixing the fiber with ultraviolet (UV) cure epoxy. Once secured, the fiber can sustain even moderate tugs by human hands without budging. By contrast, our standard dimpled, tapered optical fiber is attached to the surface only by van der waals forces and is known to jump after small bumps of the optical table upon which the testing setup sits. This means the V-groove coupling method is much more robust and useful for practical sensors. Moreover, the rigid connection of the fiber to the substrate suppresses its mechanical motion, shifting its mechanical modes to higher frequencies outside the range of interest.

That mechanical motion of the optical fiber is no longer a problem is shown by comparing Fig. 4.6 to Fig. 5.2. Fig. 5.2 is the optical power spectral density of light collected on reflection from the optical cavity with the laser locked half a linewidth red-detuned from the optical cavity. Note that all of the sharp fiber taper resonances seen in Fig. 4.6 are no longer present. This represents a significant improvement in the device performance, which is further highlighted by the noise equivalent acceleration (a.k.a. acceleration resolution) plotted in the inset of Fig. 5.2. This resolution was determined by assuming the fundamental in-plane mechanical mode was dominantly

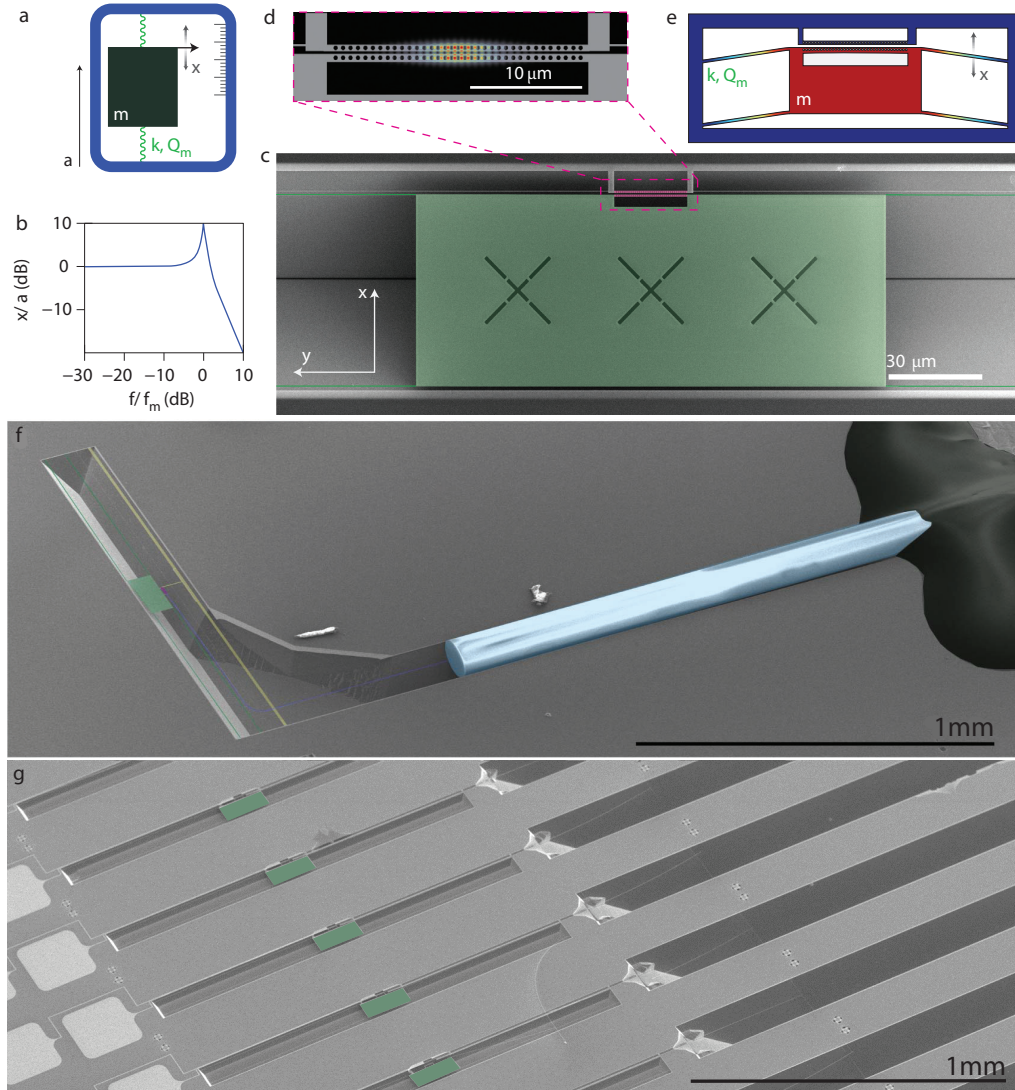


Figure 5.1: **V-groove Fiber Coupled Accelerometer**. (a) is the canonical accelerometer from Fig. 4.1 shown again. (b) shows a plot of the mechanical susceptibility, Eq. (1.34), for $Q_m = 10$. (c) zoom-in of an example test mass with the photonic crystal cavity attached. (d) zoom-in of the photonic crystal cavity region with the norm of the fundamental bonded electric field mode plotted. (e) finite-element simulation of the fundamental in-plane mechanical mode of the accelerometer (note: not to scale). (f) zoom-out showing an optical fiber securely glued into a silicon V-groove and coupling into an on-chip waveguide, which carries light to and from the accelerometer photonic crystal cavity. More detailed images of this coupling scheme are shown in Fig. 2.11. (g) This image shows a series of accelerometers coupled to V-grooves in a straight-line configuration. The data in Fig. 5.2 was taken on a device with this geometry.

driven by room-temperature thermal noise, an assumption supported by Section 4.4. Note that the source of the low-frequency noise roll-up is determined and significantly reduced in Section 5.4.

Using the autocorrelation technique described in Section 4.3, the intrinsic mechanical quality factor (i.e. at low enough optical power that back-action is insignificant) of the fundamental in-

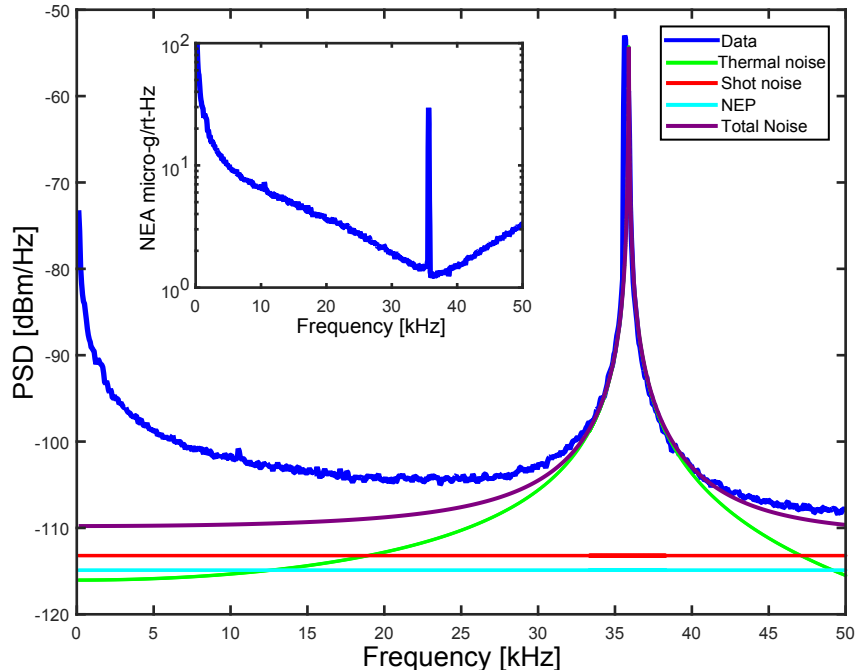


Figure 5.2: **V-groove Fiber Coupled PSD.** The main plot is the power spectral density of the photodiode signal with the laser locked half a linewidth red-detuned from the photonic crystal cavity resonance. The thermal noise of the fundamental in-plane mechanical mode is fit in green. The sharp peak near the fitted mechanical resonance is the fundamental out-of-plane mechanical resonance of the accelerometer. Note that it appears slightly better transduced than the fundamental in-plane mode because the in-plane mode is significantly cooled by the optomechanical damping caused by the laser. (inset) The acceleration resolution (noise equivalent acceleration, NEA) is plotted. It is calculated assuming the fundamental in-plane mechanical mode is dominantly driven by fundamental thermal noise Eq. (4.3). The spike near 35 kHz is again due to the fundamental out-of-plane mechanical mode.

plane mechanical mode is found to be, $Q_m \cong 2e6$. Once again, the reader will note the quality factor of the mode of interest in Fig. 5.2 is much less than $2e6$ and is in fact approximately 600. Once again this is due to thermo-opto-mechanical cooling, first described in Section 4.3.1. That is, the mode is both damped and cooled due to interactions with the laser light, leaving the fundamental thermal acceleration noise, Eq. (4.3), unchanged. A plot of the quality factor and effective mode temperature of the fundamental in-plane mechanical mode versus incident power in the optical fiber is shown in Fig. 5.3. Once again, the effective temperature is found using the integrated area of the mechanical mode in the PSD. Using Eqs. (1.15) and (1.36) this is seen to be proportional to temperature. For calibration we assume at low optical powers, where back-action is negligible, that the mode temperature is room-temperature: 295 K.

The optical mode used to measure the spectra and acceleration resolution of Fig. 5.2, is shown in Fig. 5.4. The fitted optical is $Q_o = 16,500$, using this and the assumption that at low enough optical power the mechanical mode is at room-temperature, the optomechanical coupling is calibrated from

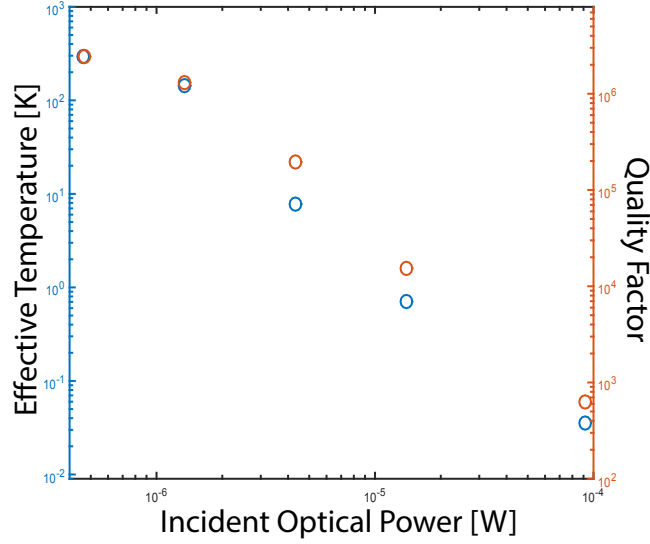


Figure 5.3: **Damping and Cooling.** The effective mode temperature (blue circles) and mechanical quality factor (orange circles) of the fundamental in-plane mechanical mode with the laser locked half a linewidth red-detuned is plotted versus incident optical power in the optical fiber. The highest power shown corresponds to the optical power used in Fig. 5.2.

the integrated mechanical motion to be $g_{\text{OM}} = 2\pi \times 6.4 \text{ GHz/nm}$. The series of fringes in the wide optical scan are interpreted to be Fabry-Pérot fringes. From the free spectral range of the fringes, $\Delta\lambda = 0.5 \text{ nm}$, the effective length of the Fabry-Pérot cavity can be inferred to be, $L_{\text{eff}} = \frac{\lambda^2}{2n_{\text{SiN}}\Delta\lambda} \cong 1.2 \text{ mm}$. This corresponds to the optical path length from the cleaved facet of the optical fiber to the photonic crystal cavity. We therefore conclude that the Fabry-Pérot cavity causing these fringes is resulting from reflections from the cleaved fiber facet and the end mirror of the photonic crystal cavity. While these fringes are an annoying side-effect of this coupling scheme, they do allow for calibration of the coupling losses, i.e. the amount of light lost between the cleaved fiber facet and the photonic crystal cavity. The system is modeled as a Fabry-Pérot cavity where the first mirror (the fiber facet) has a reflection coefficient, R_{fib} , and the second mirror (the mirror section of the photonic crystal) has unit reflection coefficient, and the system has a round-trip efficiency of η_{rt} . Note that $\sqrt{\eta_{\text{rt}}} = \eta_{\text{cpl}}$, where η_{cpl} is the single-sided coupling efficiency. By adding up the infinite series of reflections in this system and choosing the appropriate round-trip phase change to maximize and minimize the reflected signal, R , we can arrive at the following expression for the visibility, V , of the fringes (assuming we're far from the photonic crystal resonance) [12, 109, 110].

$$V = \frac{R_{\text{max}} - R_{\text{min}}}{R_{\text{max}} + R_{\text{min}}} = \frac{2\sqrt{R_{\text{fib}}}(1 - R_{\text{fib}})\eta_{\text{cpl}}(1 - \eta_{\text{cpl}}^2)}{R_{\text{fib}} + \eta_{\text{cpl}}^2 + R_{\text{fib}}\eta_{\text{cpl}}^2(R_{\text{fib}} + \eta_{\text{cpl}}^2 - 4)} \quad (5.1)$$

The reflection coefficient of the cleaved fiber face is found in finite difference time domain (FDTD) simulations to be, $R_{fib} = 0.035$ [109]. Using this parameter along with Eq. (5.1) and the measured visibilities in Fig. 5.4a allows us to back-out η_{cpl} . This coupling efficiency has been recorded as high as $\eta_{cpl} = 0.746$ [12]. Typical values for our accelerometers were $\eta_{cpl} = 0.5 - 0.6$. For the particular device whose data is shown in Fig. 5.4a and Fig. 5.2, the efficiency was worse, $\eta_{cpl} \cong 0.3$. These losses in efficiency come from a number of sources some of which are more fundamental than others. The fundamental sources are the theoretical mode overlap between the optical fiber mode and the on-chip waveguide mode, the finite adiabatic tapering length of the on-chip waveguide, scattering from support tethers for the on-chip waveguide, and scattering during the adiabatic transition from the waveguide to the photonic crystal cavity (see “end-coupling” Section 2.2). Together these more fundamental sources of loss limit the coupling efficiency to $\eta_{cpl} \cong 0.86$ [12]. The remaining sources of loss are due to fabrication non-idealities. These include particulates on the on-chip waveguide, making the waveguide width (especially its tip) the wrong size, and misalignment of the optical fiber and on-chip waveguide due to over-etching the V-groove. Due to the finite etch-rate in the $\langle 111 \rangle$ direction, the KOH etch of the V-groove must be carefully timed and temperature controlled.

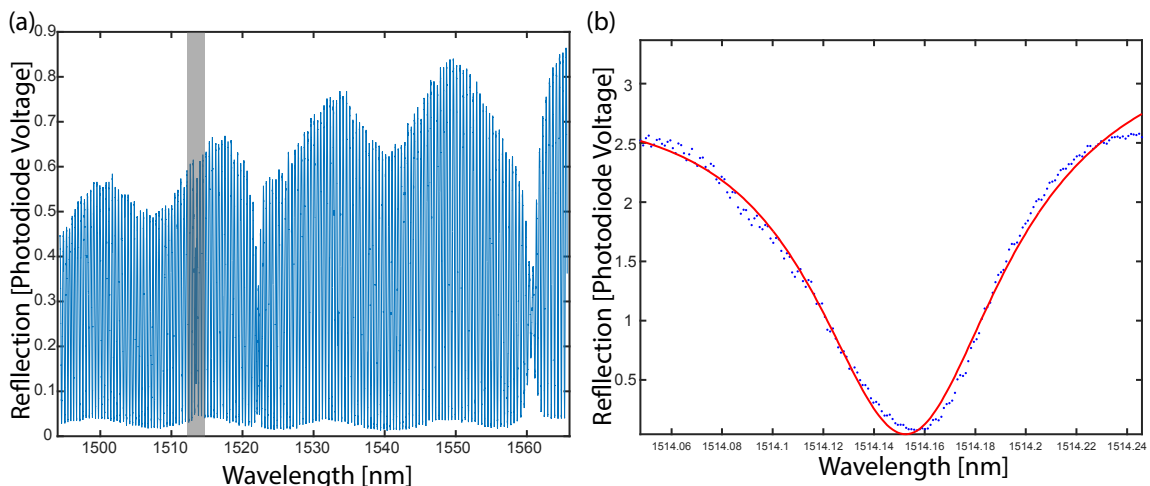


Figure 5.4: **V-groove Fiber Coupled Optical Scans.** (a) This is a 1500-band reflection spectrum (unnormalized) of the V-groove fiber-coupled device under test. The series of sharp fringes are due to a parasitic Fabry-Pérot cavity as discussed in the main text. The optical mode of interest is highlighted in grey. (b) A zoom-in of the optical mode of interest is shown along with a Lorentzian fit (red). The fitted optical Q is $Q_o = 16,500$. (note that the scans in (a) and (b) were taken at different detector gain and optical power settings).

5.2 Capacitive Wavelength Tuning

As stated in the introduction to this chapter, when dealing with relatively fixed wavelength, on-chip laser sources and thermal drifts, it will be necessary to actively control the optical mode frequency. To this end, we investigate capacitive wavelength tuning.

5.2.1 Working Principle of Capacitive Wavelength Tuning

The basic working principle behind capacitive wavelength tuning is quite simple. One side of a metal capacitor is placed on the rigid bulk of the chip. The other side is connected to a flexible side of the photonic crystal cavity. By applying a voltage, a capacitive force develops, which pulls the flexible side of the photonic crystal cavity away from the other. This increases the optical cavity slot gap and thereby changes the optical resonance frequency.

We can develop a simple mathematical model for this wavelength tuning method [107]. The simple geometry needed to understand this model is shown in Fig. 5.5. The energy stored in the capacitor and the corresponding force are given by the following equations.

$$E_{\text{cap}} = \frac{1}{2} C(x) V_a^2 \quad (5.2)$$

$$F_{\text{cap}} = -\frac{dE}{dx} = -\frac{1}{2} V_a^2 \frac{C(x)}{dx} \quad (5.3)$$

In Eqs. (5.2) and (5.3), V_a is the applied voltage across the capacitor, x is the position of the flexible side of the capacitor (see Fig. 5.5), and $C(x)$ is the capacitance as a function of x . For a canonical parallel plate capacitor $C(x) = A\epsilon_o/(w_g - x)$, where A is the cross-sectional area of the plates and ϵ_o is the permittivity of free space. For the on-chip capacitive wires we'll use, the parallel plate model isn't an accurate approximation because the wire thicknesses will be comparable to their separation and thus fringing fields will play a role. A realistic model for these on-chip wire capacitors including fringing effects is as follows.

$$C(x) = \frac{A\epsilon_o}{(w_g - x)^n} \quad (5.4)$$

In Eq. (5.4), n is some real number between 0 and 1. Typical parameter values for the wire capacitors in this work are $C(0) \sim 1fF$ and $n \cong 0.7$, calculated by finite element simulation in Comsol [107]. Eq. (5.4) leads to the following capacitive force.

$$F_{\text{cap}}(x) = \frac{nA\epsilon_o V_a^2}{2(w_g - x)^{n+1}} \quad (5.5)$$

This capacitive force will be balanced by the elastic restoring force of the flexible side, characterized by an effective spring constant, k_{eff} .

$$F_{\text{spring}} = -k_{\text{eff}}x \quad (5.6)$$

By approximating Eq. (5.5) to zeroth order for $x \ll w_g$ and equating it to Eq. (5.6), we arrive at the displacement caused by the capacitive force, δx .

$$\delta x = \frac{nA\epsilon_o V_a^2}{2k_{\text{eff}}w_g^{n+1}} \quad (5.7)$$

The corresponding wavelength shift of the optical mode is determined using the optomechanical coupling, g_{OM} .

$$\delta\lambda = \frac{g_{\text{OM}}}{2\pi} \frac{\lambda_o^2}{c} \delta x = \frac{g_{\text{OM}}}{2\pi} \frac{\lambda_o^2}{c} \frac{nA\epsilon_o V_a^2}{2k_{\text{eff}}w_g^{n+1}} \quad (5.8)$$

Therefore, the capacitive force leads to wavelength tuning that is proportional to V_a^2 and $w_g^{-(n+1)}$, thus emphasizing the benefit of small capacitive wire gaps.

5.2.2 On-Chip Capacitor Wire Fabrication

Now that we have an intuitive understanding of how on-chip capacitor wires can tune the wavelength of our photonic crystal cavities, how do we actually fabricate them? The metallized nanofabrication process flow is presented in Fig. 5.6.

The process flow begins identically to the standard process flow in Fig. 2.14. Then the first electron beam lithography step defines the capacitor wires along with a set of alignment markers in the electron beam resist. Metal is subsequently electron-beam deposited upon the developed resist pattern. Roughly speaking, electron beam deposition works by extracting a beam of electrons from a metallic source with high voltage in a vacuum environment and bending that beam in a magnetic field so that it strikes a crucible filled with evaporant material. The kinetic energy of the electrons heats the evaporant material until it melts and evaporates, coating everything by line of sight in the chamber (see Fig. 5.6d). Typically, we evaporate ~ 5 nm of chromium and ~ 200 nm of gold to

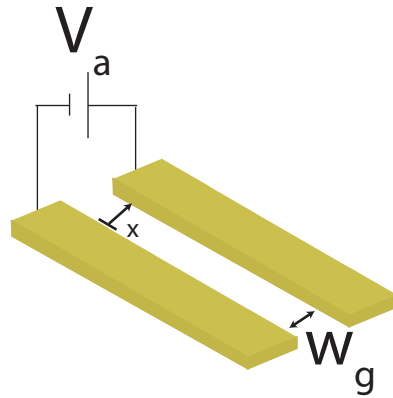


Figure 5.5: **Simple Capacitor Geometry.** The two rectangles represent gold wires. The static gap between the wire is w_g . The applied voltage between the wires is V_a . The right wire is considered rigidly fixed, and the left wire is flexible with a position given by x .

create the wires. The thin chromium layer simply acts as an adhesion layer, helping the gold stick to the surface. As long as the metal layer is approximately less than half the e-beam resist thickness, dissolving the e-beam resist in heated solvent such as Acetone removes the metal layer along with it, except where the resist was patterned (see Fig. 5.6e). Subsequently, a new layer of e-beam resist is spun on the chip and second e-beam lithography step is performed. The gold alignment markers can be imaged through the resist, which allows precise alignment of the second lithography pattern to the first. In this case, the gap between the electrodes is precisely written and, subsequently, dry-etched through the silicon nitride layer (see Fig. 5.6f-h). Finally, the chip is cleaned in piranha solution, KOH released, piranha cleaned again, and critical-point-dried (see Section 2.4 for more details). We are left with a chip with sections of the silicon nitride layer released from the silicon backside (the flexible regions) with gold capacitor wires with narrow gaps on top.

Now that we understand how the on-chip capacitors are fabricated, what's left to explain is how the voltage, V_a is applied to them. An image illustrating how this is done is shown in Fig. 5.7. Using standard equipment, one can easily apply voltages to wires on PCBs (printed circuit boards). From there one needs a means to connect those voltages to the wires on the chip. The wires on the PCB and the wires on the chip are terminated in small rectangular pads called “bond” pads. An arc of gold wire is then used to connect the bond pad on the PCB to the bond pad on the chip. The gold wire arc is attached using a specialized tool called a wire-bonder. It is a sophisticated piece of equipment that holds fine gauge metal wire in a tool bit. When the tool bit makes contact with the bond pad, it vibrates at ultrasonic frequencies with the possible application of heat. This locally melts the wire and bond pad together allowing for a secure electrical connection.

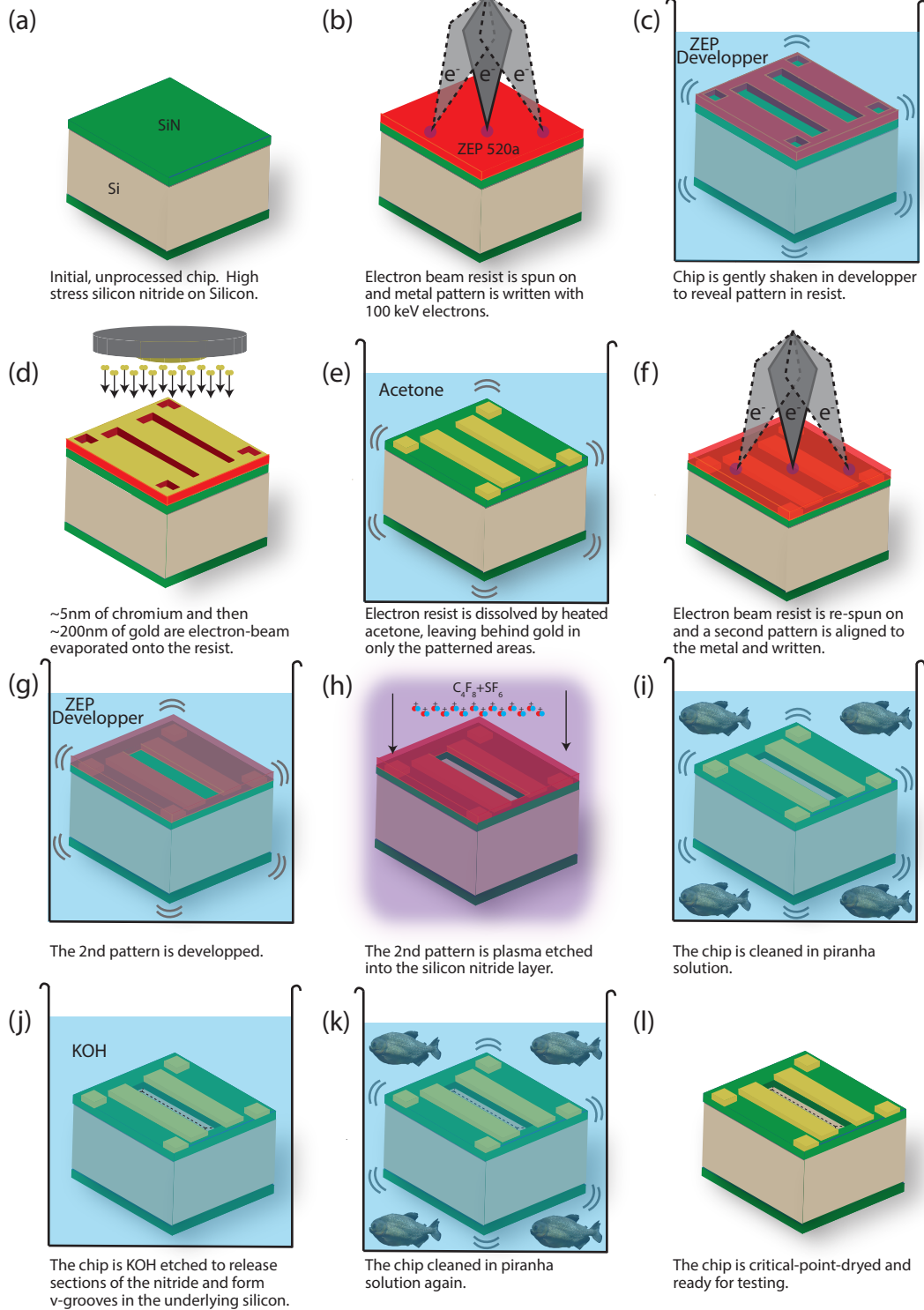


Figure 5.6: **Nano-fabrication process flow with metallization.** The processes are described in greater detail in the main text. Piranha photo was taken by Greg Hume.

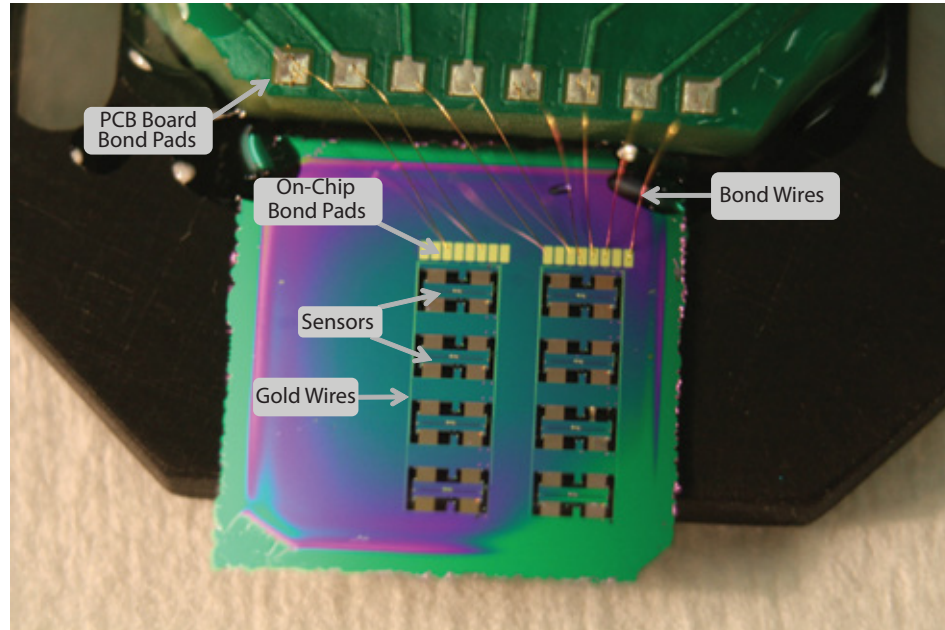


Figure 5.7: **Wire Bonding Example.** This figure shows an example of a wire bonded sensor chip. At the top of the figure is the PCB with its associated bond pads. From there bond wires connect the PCB bond pads to the on-chip bond pads. In this way voltages on the PCB are applied to the on-chip wire capacitors.

5.2.3 Silicon Wavelength Tuning [107]

Our first experience with capacitive wavelength tuning actually took place in a silicon, rather than silicon nitride, system [107]. The silicon devices are made from silicon-on-insulator chips purchased from the company SOITEC. The layers of the chips are a 220 nm thick silicon device layer then a 2 micron thick silicon dioxide glass layer then a 500 micron thick silicon handle wafer. The nanofabrication processing steps are extremely similar to those described for silicon nitride chips in Sections 2.4 and 5.2.2. The major differences are different parameters for the pseudo-Bosch $C_4F_8 - SF_6$ dry etch, and hydrofluoric acid, HF, is used to release the silicon device layer from the underlying silicon dioxide instead of the KOH used to release the silicon nitride layer from the underlying silicon. A more in-depth discussion of the specifics of our silicon nanofabrication techniques can be found in the following references [17, 107, 111].

The silicon device used for our first demonstration of capacitive wavelength tuning is shown in Fig. 5.8. The photonic crystal is comprised of a 2-dimensional triangular array of holes with a slot across the middle and, of course, a defect region in the center, which confines a series of optical modes (Fig. 5.8c-d). The design of this photonic crystal again requires solving Eq. (2.9), only this time in 2-D, and using the resulting band diagram to design defect region optical modes of high quality factor. In depth discussion of the design of this photonic crystal cavity can be found in Ref. [112] and similar

cavities without the slot are discussed in Refs. [113, 114]. The slot separates the photonic crystal into two mechanically compliant membranes that can move independently of one another. Relative motion of the two membranes changes the slot size and, through the optomechanical coupling, g_{OM} , of the structure, changes the optical mode frequencies. This is, of course, in perfect analogy to the 1-D zipper cavity discussed in depth in Section 2.1.1. Capacitor wires are placed on each membrane with one wire on the rigid bulk of the chip and the other on the compliant membrane. By applying a voltage across each capacitor, the membranes are electrostatically actuated and move apart according to the displacement profile shown in Fig. 5.8.

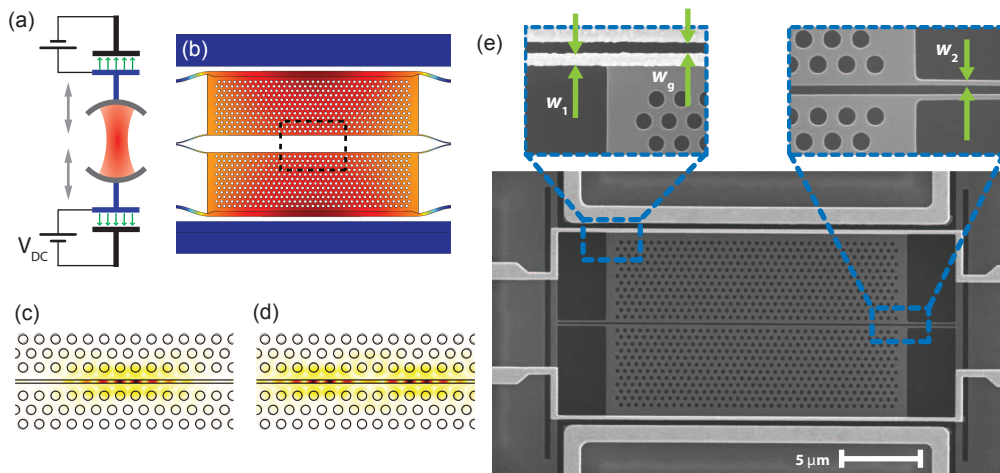


Figure 5.8: **Silicon Capacitive Tuning Device.** (a) This is a cartoon of a canonical electro-optomechanical system. Represented is a Fabry-Pérot optical cavity whose mirrors are connected to variable-gap capacitors, which can pull the mirrors apart, thereby, changing the resonant wavelengths of the cavity. (b) This is the displacement profile of the photonic crystal cavity due to electrostatic actuation. (c)-(d) A plot of the norm-squared electric field, $|\mathbf{E}(\mathbf{r})|^2$, for the fundamental and second order photonic crystal optical modes, respectively. (e) Scanning-electron microscope (SEM) image of the full device. The photonic crystal cavity is formed from a 2-D hexagonal array of holes suspended on narrow struts (see zoom-ins $w_1 = 250$ nm and $w_2 = 80$ nm). There is a slot and defect of the hole periodicity in the center to confine the optical modes. The slot allows each membrane of the photonic crystal to move independently, which changes the slot size and, thereby, the optical cavity frequency. On both the top and bottom membranes wire capacitors of thickness $\cong 200$ nm and gap $w_g \cong 200$ nm are in place to pull apart the membranes as shown in (b). This figure is reproduced from Ref. [107].

The first experiment performed with the device shown in Fig. 5.8, was to sweep the voltage and observe the change in the optical cavity frequency. The results are shown in Fig. 5.9. The optical transmission scans are obtained using a New Focus tunable external cavity diode laser and the dimpled, tapered optical fiber double-sided coupling technique described in Section 2.2. Both optical modes of the structure tune by approximately 19 nm for $V_a = 19$ V, which is very substantial (approximately 900 optical linewidths). We can define the tunability, α , as $\Delta\lambda = \alpha \cdot V_a^2$. For the

structure measured in Fig. 5.9, $w_1 \cong 250$ nm, $w_2 \cong 150$ nm, $w_g \cong 200$ nm, the measured tunability is $\alpha = 0.051\text{nm}/V^2$. This agrees to within a factor of two of the theoretical predictions of Eq. (5.8) combined with finite-element simulation [107]. The residual discrepancy likely stems from errors in determining the geometrical parameters of the structure.

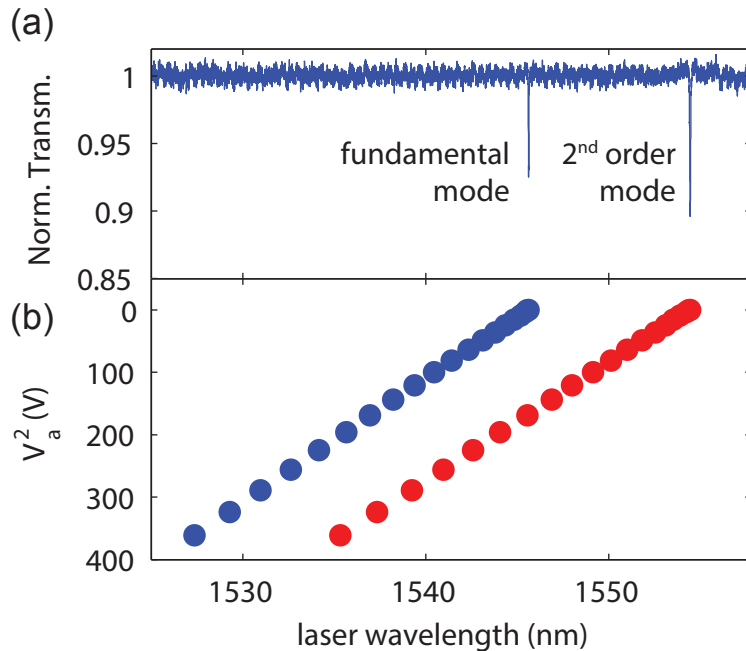


Figure 5.9: **Silicon Capacitive Tuning.** (a) Normalized transmission spectrum of a devices showing the fundamental and second order optical modes at zero applied volts. (b) Plot of the wavelength of the fundamental optical mode (blue) and the second order mode (red) as a function of V_a^2 . This figure is reproduced from Ref. [107].

Another important use of the tuning capacitors is to lock the optical cavity frequency to a fixed laser source, whereas the usual experimental configuration is the reverse. Fig. 5.10 shows an example power spectral density of the photodiode signal with the optical cavity locked half a linewidth detuned from the second order optical mode using the on-chip capacitors. The largest two peaks are interpreted to be the fundamental in-plane mechanical mode of each membrane (right inset Fig. 5.10), split by minor, unavoidable fabrication asymmetries. The other two features are due to hybridization with the nearly degenerate fundamental out-of-plane mode (left inset Fig. 5.10). Hybridization occurs because the gold wires on top of the membrane break the z-symmetry. The main takeaway from Fig. 5.10 is that these on-chip capacitors can be used to tune the optical cavity in-resonance with a fixed laser source and lock it at a fixed detuning for the purpose of detecting mechanical motion. Thus, this is an important proof of principle that will help integration of optomechanical sensors with on-chip, relatively fixed, laser sources.

One additional application of these electrostatic tuning methods is to electrically control the

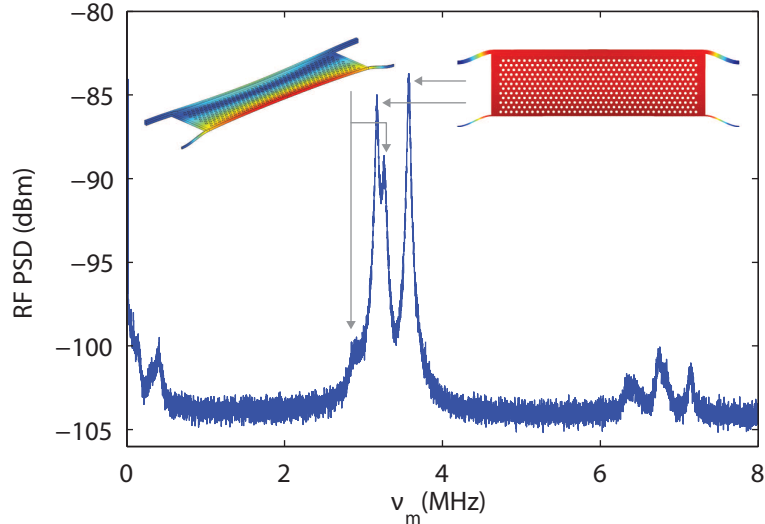


Figure 5.10: **Example Power Spectral Density.** Plot of the photodiode signal power spectral density from laser light transmitted through the second order optical cavity mode. The optical cavity is locked half a linewidth detuned from a fixed laser. The two best transduced modes are the fundamental in-plane modes of each membrane split by fabrication asymmetry (right inset). The other two modes are part in-plane, part out-of-plane modes (left inset) that have hybridized with the nearly degenerate fundamental out-of-plane mode. This figure is reproduced from Ref. [107].

optomechanical back-action. Fig. 5.11 shows a series of PSD spectra (each horizontal slice is a power spectral density like that shown in Fig. 5.10) each with a different voltage applied to the capacitors and each with $P = 25 \mu\text{W}$ incident at the cavity at a fixed frequency. As the voltage is changed so does the cavity-laser detuning and, thereby, the number of photons in the cavity (see Eq. (1.13)). As the detuning and intracavity photon number is changed so will the mechanical frequencies and amplitudes due to optomechanical dynamical back-action (see Section 1.5.1). In Fig. 5.11, when the cavity is red-detuned from the laser the mechanical modes are shifted to lower frequencies (spring softening) and their motion is cooled (damping) and vice-versa for blue-detuning. From the optomechanical spring shift for this device we can determine $g_{\text{OM}} = 2\pi \times 215 \text{ GHz/nm}$, in reasonable agreement with the theoretical value of $2\pi \times 152 \text{ GHz/nm}$. This is an interesting and potentially useful demonstration of electrically controlled back-action with a fixed frequency laser source.

5.2.4 Accelerometer Wavelength Tuning

Using the techniques and intuition developed previously in Section 5.2.3, we sought to make a proof-of-principle demonstration that on-chip capacitive tuning could be incorporated with our optomechanical accelerometers. Using the nanofabrication steps described in Section 5.2.2 and Fig. 5.6, we fabricated devices that incorporated both straight-line fiber v-groove coupling and capacitive

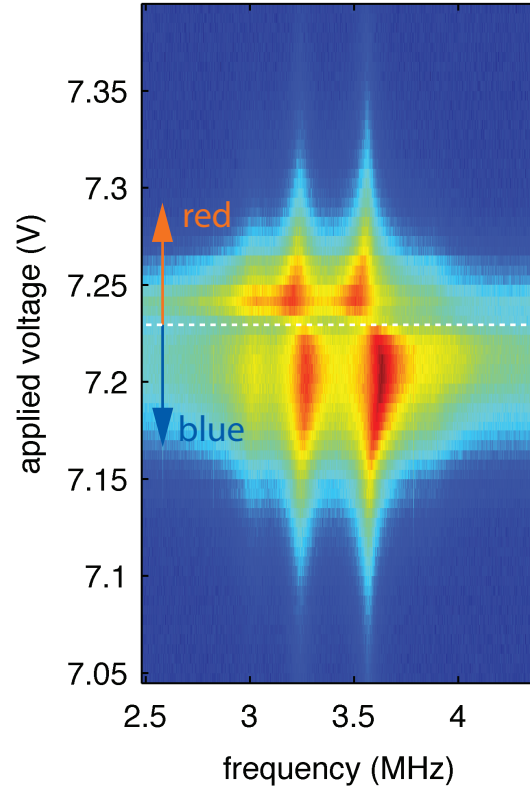


Figure 5.11: **Voltage-Controlled Dynamical Back-Action.** False-color plots of the power spectral density of laser light transmitted through the fundamental optical resonance as a function of V_a . For blue-detuning spring stiffening and amplification is observed and vice-versa for red-detuning. The dashed white line indicates the voltage where the laser is directly on resonance with the optical cavity. This figure is reproduced from Ref. [107].

tuning. The devices and results are shown in Fig. 5.12. The working principle is the same as that described in Section 5.2.1. As is shown in detail in Fig. 5.12, one side of the zipper cavity is, of course, connected to the test mass. The other side, instead of being rigidly connected to the bulk, is suspended on a flexible beam. Note that this flexible suspension is still designed to be much stiffer than the in-plane test-mass mode such that relative motion of zipper beams due to in-plane acceleration is still dominated by the test-mass mode. Otherwise, sensitivity to accelerations would be reduced. This flexible support beam is metallized with the other side of the capacitor being placed on the rigid bulk. Once again, voltages are applied to these capacitors by wire bonding the bond pads (left hand side of Fig. 5.12a) to a PCB board. Because we were simply shooting for a proof-of-principle demonstration, the effort was not made to minimize the capacitor gap size and it was simply designed at $1 \mu\text{m}$. The long length of the capacitor $\approx 600 \mu\text{m}$ compensated for this large gap to some degree. Nevertheless, Fig. 5.12b shows that we were able to achieve a substantial tuning of approximately 3.5 nm with an applied voltage of 15 V . Fabrication optimization could

certainly increase this tuning range, even by an order of magnitude, but we were satisfied with this proof of principle.

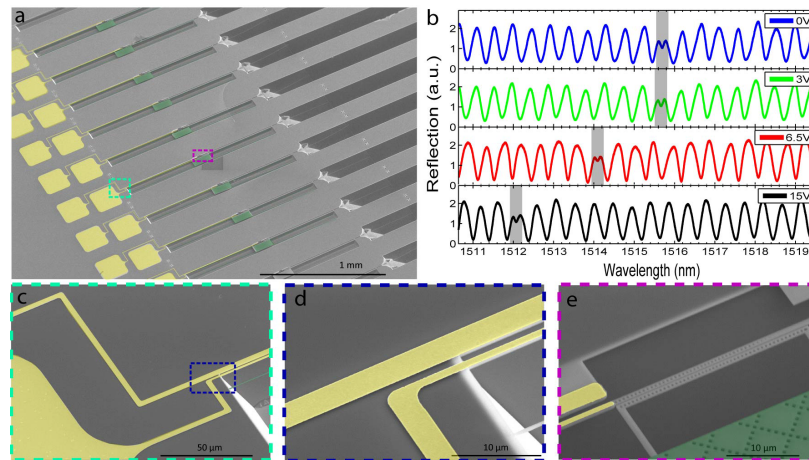


Figure 5.12: **Tunable Accelerometer.** (a) False color SEM showing a wide-field view of several capacitively tunable accelerometers. The gold metal is colored yellow and the large rectangles on the left hand side are the bond pads. The accelerometer test-masses are highlighted in solid green. A zoomed-in image of the regions demarcated by dashed colored rectangles will be shown in subsequent images (b) A series of laser reflection scans of a device. An optical mode is highlighted in grey and tracked as a function of voltage. The mode moves approximately 3.5 nm with 15 Volts applied. (c) A zoom-in of the dashed green rectangle in (a). This shows the edge of one bond pad and the wires running off of it. (d) A zoom-in of the blue dashed rectangle in (c). This shows the two wires running side by side as one wire (the thicker one on top) stays on the bulk of the chip and the other begins to run along the support beam of one side of the zipper cavity. (e) A zoom-in of the dashed magenta rectangle in (a). This shows the zipper cavity and the end of the wire capacitor. As one can clearly see, the bottom beam of the zipper cavity is connected to the accelerometer test-mass, while the top zipper beam is connected to a stiffer, yet flexible, support beam that is metallized, forming one side of a variable gap capacitor. By applying a voltage across these wires, the top zipper beam is pulled away from the bottom beam and the optical cavity frequency is changed (tuned).

5.3 Intel On-Chip Laser Testing

Practical use of our accelerometers in their V-groove coupled configuration without on-chip lasers is certainly possible. Oil fields on the ocean floor have been probed using arrays of optical accelerometers multiplexed into a remote tunable laser source [91]. These applications capitalize on light's ability to be transmitted over km scale distances with negligible loss. Nevertheless, the ultimate realization of our optomechanical accelerometer would be as a fully packaged and integrated sensor with both the laser source and photodetector on-chip. This would help make the accelerometer measurement system significantly cheaper and open up new applications such as, but certainly not limited to, guidance systems. To this end, we entered into a short-lived collaboration with Intel. Through a collaboration with John E. Bowers group at the University of California at Santa Bar-

bara (UCSB), Intel has developed and begun wafer-scale production of on-chip lasers and detectors. The lasers developed by John Bowers's group are shown in Fig. 5.13. They are electrically driven, multiple quantum well, separate confinement heterostructure, AlGaInAs-silicon evanescent lasers [108]. The III-V heterostructure is wafer bonded on top of the SOI wafer with the silicon waveguide defined. The silicon waveguide defines the laser cavity and 75% of the optical mode overlaps with the silicon waveguide while 3% overlaps with the quantum well gain medium. These lasers are not the first demonstration of III-V lasers integrated with silicon waveguides (called hybrid integration) [108]. However, previous demonstrations involved fabrication of individual laser die, which must be individually aligned to silicon waveguides, which is costly and difficult [108]. The lateral symmetry of the III-V material shown in Fig. 5.13a-b, means no alignment step is required during bonding and therein lies the promise of this laser architecture.

As previously stated, the ultimate goal would be to incorporate our accelerometer structures on Intel's laser chips. A couple factors prevented this route from being pursued. Firstly, our Intel collaborators lacked access to small test nanofabrication facilities necessary for an attempt to fabricate our devices on their wafers. Secondly, intellectual property concerns prevented Intel from allowing us to handle their chips in our cleanroom. Nevertheless, our Intel collaborators did visit our labs at Caltech and allowed us to couple light out of their laser chips for an important proof-of-principle experiment.

As shown in Figs. 4.11 and 5.2, our accelerometers have been able to achieve excellent acceleration resolution. However, this resolution has been achieved using expensive, shot-noise limited, table-top laser sources. Conceivably, Intel's on-chip lasers could have significantly worse noise properties, rendering sensitive optomechanical acceleration measurements impossible. Due to intellectual property concerns, Intel would not allow us to directly measure their lasers' amplitude or phase noise. However, they did allow us to measure the acceleration resolution of one of our devices using their laser.

For the experiment, we used one of our V-groove coupled accelerometers using the straight-line configuration shown in Fig. 5.1g. Intel's lasers operate in the 1300 nm band, so our zipper photonic crystals were redesigned so that their modes lay in this band. Light was coupled out of Intel's laser chip using an edge-coupling technique illustrated from topview in Fig. 5.13c and the actual experimental setup is shown in Fig. 5.13d. The laser chip is cleaved perpendicular to the silicon waveguide and, using a lensed optical fiber mounted on micrometer stages, the light emitted from the edge of the chip was collected. From there, the optical fiber was routed to a circulator, then glued into the on-chip fiber V-groove, then the reflected light was measured on a photodetector. The particular accelerometer chip tested did not have electrostatic tuning capability; however, several accelerometers were tested until one was found with an optical mode near the laser wavelength, 1310 nm. From there, the modest thermal and current tuning capability of the on-chip laser was

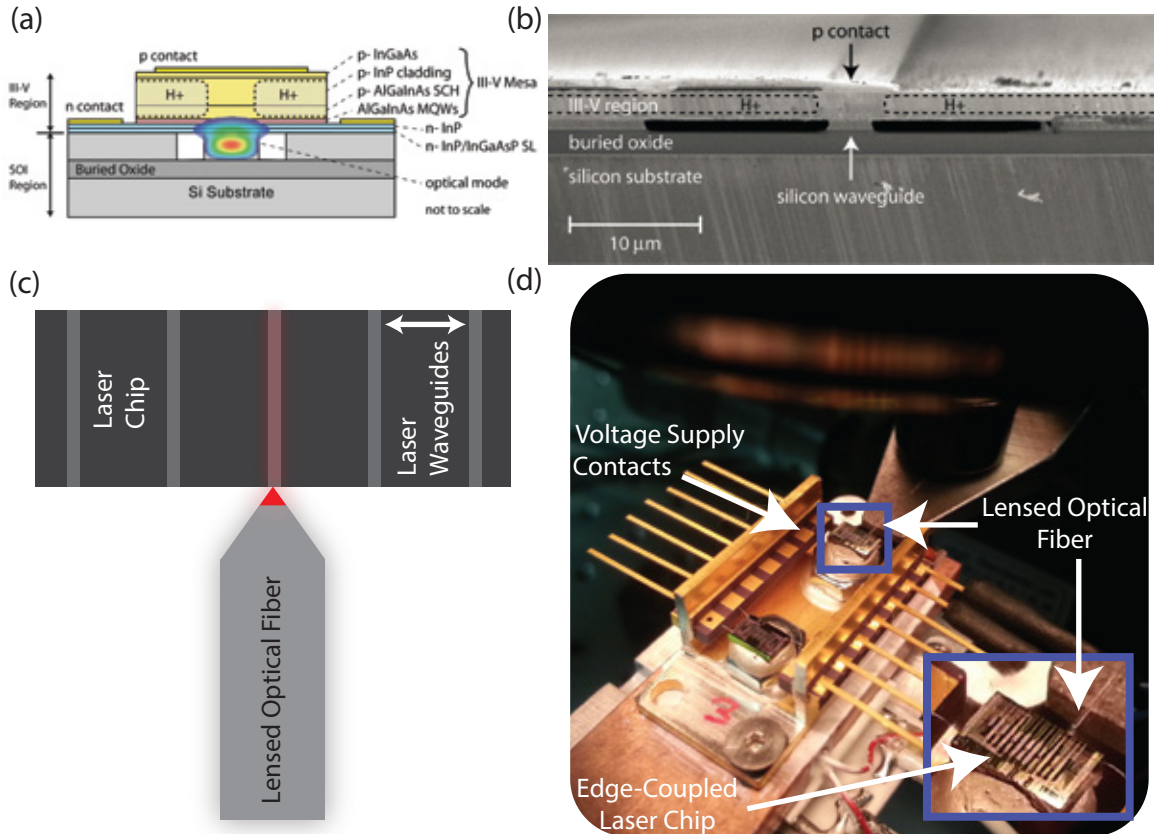


Figure 5.13: **Intel On-Chip Laser Coupling.** (a) This is a schematic drawing of the layer structure of the hybrid III-V silicon laser used in this experiment. This image is reproduced from Ref. [108]. (b) This is an SEM cross-sectional image of a fabricated laser. This image is reproduced from Ref. [108]. (c) Cartoon of the lensed fiber technique used to gather the light emitted from the on-chip waveguides at the edge of the chip. (d) This is an optical image of the experimental setup. The laser chip is mounted on a temperature-controlled stage. The outer packaging provides voltage supply bond pads and pins so the electrical pump can be supplied to the on-chip lasers. A lensed optical fiber mounted on micrometer stages can be finely positioned to efficiently collect light that is edge-emitted from the on-chip waveguides.

used to tune the laser approximately half a linewidth detuned from the optical resonance. The results of this acceleration resolution measurement are shown in Fig. 5.14. The data from Intel's on-chip laser is the blue curve and the data from our New Focus Velocity tunable external cavity diode laser is the red curve. The two curves were taken at the same laser power input to the optical cavity of $330 \mu\text{W}$, and the dashed lines of the same color are the corresponding laser shot noises for each experiment. There is discrepancy in the shot noise levels due to slightly different laser detunings for each experiment (achieving a precise detuning with the intel laser was difficult in our experimental setup). As can be seen in Fig. 5.14, the acceleration noise floors are limited primarily by shot noise and a low frequency noise roll-up (whose source we will investigate in the subsequent sections). Regardless, the two curves lie directly on top of each other, meaning Intel's

on-chip lasers are capable of achieving comparable noise performance to our table-top lasers with our accelerometers. This is an important proof of principle that shows excellent performance can be expected if our accelerometers are successfully integrated with Intel’s on-chip lasers.

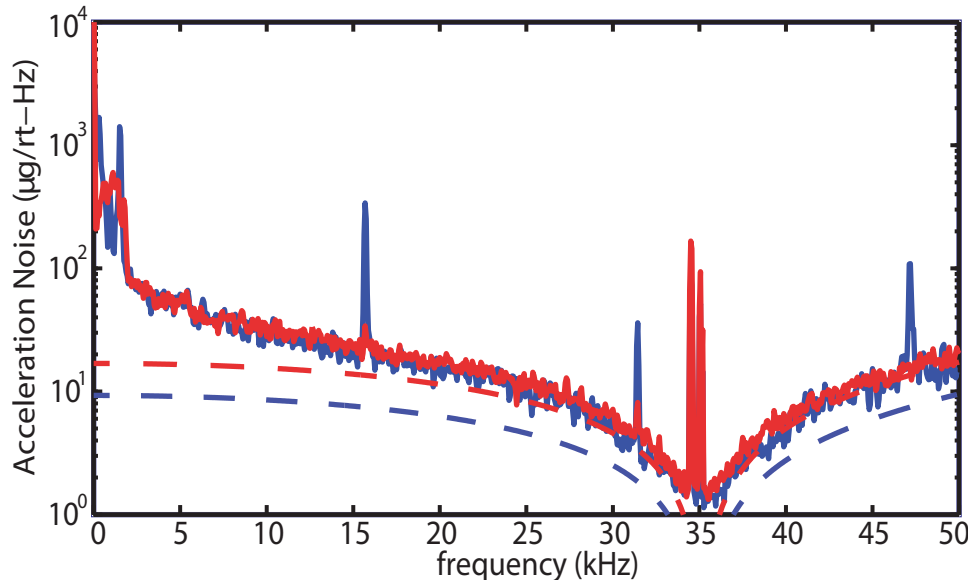


Figure 5.14: **Intel Laser Acceleration Resolution.** The acceleration resolution of a V-groove coupled accelerometer using Intel’s on-chip laser (blue curve) and a New Focus velocity table-top laser (red curve). The dashed lines of the same color are the corresponding shot noise floors for each experiment. The low frequency rollup of the acceleration noise is present again, as it was in the inset Fig. 5.2. The source of this noise will be discussed in Section 5.4.

5.4 Reduction of Low-Frequency Noise

In Section 5.1 and Fig. 5.2, we noted the presence of a low-frequency increase, or “roll-up”, in the electronic PSD of our accelerometer. This is an important noise source because it dramatically limits the low frequency performance of our devices. It turns out this noise originates from fluctuations of the optical cavity frequency. In this section, we will characterize this noise, argue for its noise source, model it, and eliminate it as best we can.

A close-up, log-log plot of the roll-up noise is shown in Fig. 5.15. The blue data is taken on an accelerometer device of the type shown in Fig. 5.22. The red data is taken on a “test” cavity of the same geometry as the device in Fig. 2.10. The PSDs for each curve are normalized by the optical transduction factor (the pre-factor on S_{xx} in Eq. (1.15)) to make direct comparison meaningful. The roll-up noise follows an approximate $\omega^{-1.5}$ frequency dependence until very low frequencies of 10-20 Hz (the black line in Fig. 5.15 is the fitted frequency slope which is -1.52). Moreover, to within a factor of two, the roll-up on the two devices is the same. The two mechanical structures of these

devices could scarcely be more different. The accelerometer structure has a fundamental resonance frequency at ~ 10 kHz, and the test cavity's fundamental mechanical frequency is ~ 10 MHz. It is inconceivable, therefore, that the noise source could be mechanical or vibratory in nature.

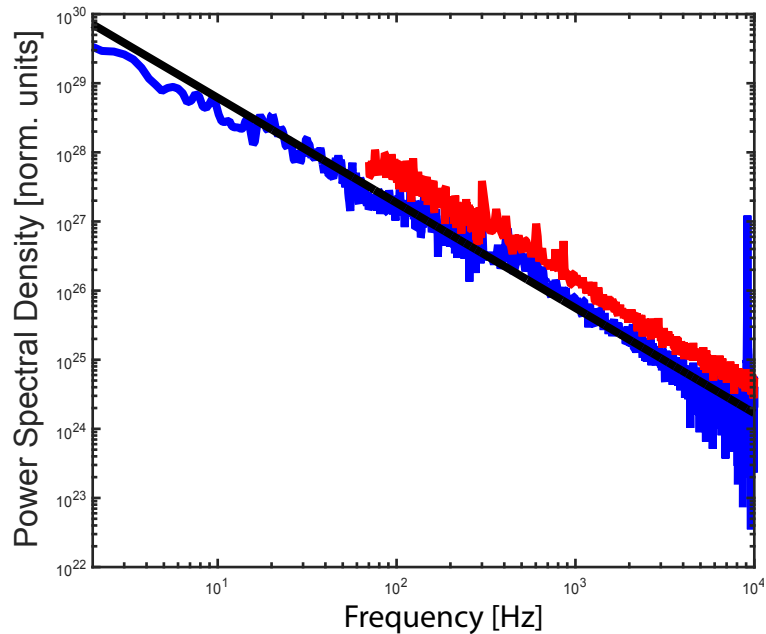


Figure 5.15: **Roll-up Noise Characterization.** This is a log-log plot of the electronic power spectral density normalized by the optical transduction coefficient. The flat noise floor consisting of NEP and shot noise has been subtracted. The blue curve is data for an accelerometer of the same design as shown in Fig. 5.22. The red curve is data from a test optical cavity of the same design as the device in Fig. 2.10. The black line is a fitted slope to the blue data and its value is -1.52 .

It is also relatively simple to rule out classical laser noise as the source of the roll-up. By putting the output of our laser directly onto our photodetector we can see that the amplitude noise of our laser is shot noise limited at powers relevant to our experiment. This is neither the same magnitude nor the same shape as the observed roll-up. Similarly, by putting our laser through a Mach-Zehnder interferometer and locking it to the side of a fringe (lock frequency < 100 Hz), we can see the phase noise of the laser is neither the right magnitude nor the right shape.

Moreover, there is an elegant experiment we can do that simultaneously rules out mechanical motion and laser noise as the sources of the roll-up. As discussed in Section 2.1.1, our zipper photonic structure hosts a series of optical modes. Of interest here is the fundamental bonded and anti-bonded modes. If the roll-up noise is the same when collecting light reflected from either of these modes then by probing both modes at the same time and subtracting their photocurrents on a balanced photodetector (BPD) (like the one shown in Fig. 4.4), the noise can be cancelled. The experimental setup was quite simple. Light from two separate lasers was sent to two respective attenuators to independently control their power. Then the two lasers were mixed into a single fiber

using a 50-50 coupler. This fiber was then sent to the 1st port of a circulator. Port 2 of the circulator led to the device under test and port 3 lead to a de-multiplexer. Using the de-multiplexer the two laser frequencies were again separated and each laser is sent to an optical switch and then to one of the ports of the balanced photodetector. The switches allow us to turn the cancellation on or off, by switching one of the lasers away from the detector. Using this experimental setup, we could set each laser approximately half a linewidth red-detuned, one from the fundamental bonded mode and the other from the fundamental anti-bonded mode. By fine tuning the optical power in each mode, the roll-ups were made to match each other in magnitude and then were subtracted on the balanced photodetector. The results of the experiment are shown in Fig. 5.16.

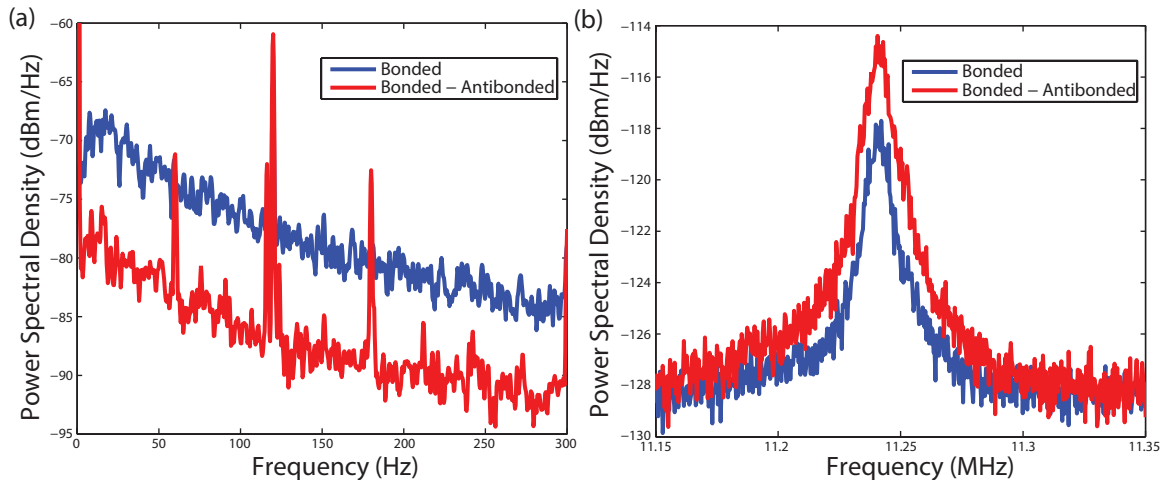


Figure 5.16: **Roll-up Noise 2 Laser Cancellation.** (a) Shows the cancellation of the roll-up noise between 0 and 300 Hz. The blue data is obtained when only laser light reflected from the bonded optical mode hits the balanced photodetector. The red data is obtained when both light reflected from the bonded and anti-bonded modes hits the balanced photodetector and the signals are subtracted. (b) This data is the same as (a) except the frequency span is confined to a narrow band around the fundamental mechanical resonance. Note how subtraction of the bonded and antibonded modes leads to an increase in mechanical signal (this is discussed in the main text). Also note that this mechanical data was taken using a different balanced photodetector than the data in (a), so strict comparison of the y-axis is not meaningful.

As can be seen in Fig. 5.16a, the 2 laser cancellation scheme reduces the low-frequency roll-up noise by 9 dB. The two lasers used were independent of each other and, in fact, the laser cavities were located in different laboratories. Therefore, it is unreasonable to propose that their classical noise would be correlated and, thus, this cancellation shows that the source of the roll-up noise can not be classical laser noise. Additionally, in Fig. 5.16b, we see that when the two laser signals are subtracted the mechanical transduction actually increases by approximately 3.5 dB. This is because the bonded and anti-bonded optical modes, due to their different symmetry about the zipper slot gap, actually have optomechanical couplings, g_{OM} , that differ in sign. Thus, when the two lasers are subtracted (with the same sign for their detuning), mechanical motion is actually added together.

This, in turn, implies the low frequency roll-up can not be mechanical motion.

If the roll-up is not caused by laser noise or mechanical motion, the remaining reasonable source is fluctuations of the optical cavity frequency. The roll-up does have a definite dependence on the laser's detuning from the optical resonance. That is, the noise disappears when the laser is directly on resonance with the optical cavity or very far-detuned (several linewidths). This is consistent with a noise source that causes frequency fluctuations of the optical cavity frequency.

There are several such noise sources for micro-resonators and the most common and best understood sources are described in great detail in Refs. [115, 116]. However, none of these well-understood noise sources accurately describes our noise source. Frequency noise from a Kerr nonlinearity, ponderomotive fluctuations, and photothermal noise are not good descriptions because those transduced noises increase nonlinearly with optical power while our noise increases linearly. Thermo-elastic (a.k.a thermo-mechanical) noise involves temperature fluctuations causing thermal expansions or mechanical vibrations of the cavity. We have already discussed that this can not be the source. Moreover, the expected frequency spectrum would look like the mechanical susceptibility (Eq. (1.34)) and not the $\omega^{-1.5}$ we observe. Elasto-optic noise involves temperature fluctuations, causing mechanical motion fluctuations which induce stress and thereby shift the optical resonance via the photoelastic effect [116]. For many reasons, elasto-optic noise is not a good description of the observed roll-up, the easiest reason for this is again it predicts the wrong frequency spectrum (it should follow the mechanical susceptibility). Moreover, the fundamental mechanical frequencies of these structures are ~ 10 kHz for the accelerometer and ~ 10 MHz for the test cavities, yet the roll-up has significant frequency dependence all the way down to at least the 1 Hz range. Finally, thermo-refractive noise, which is fluctuations of the refractive index due to fundamental temperature fluctuations, is also not a good model for our noise. The theoretical prediction for the magnitude of thermo-refractive fluctuations (see Refs. [115, 117]) is about a factor of 100 smaller than the magnitude of the roll-up we observe. Moreover, the frequency spectrum for thermo-refractive noise should be essentially flat below the frequency of the lowest thermal eigenmode [117]. Yet, we find that for the test cavity structure the lowest thermal eigenmode is ~ 2700 Hz assuming a thermal conductivity of 3.2 W/mK [23, 118], and we still have significant frequency dependence of our roll-up at the single Hz range.

5.4.1 Adsorbed Water Diffusion Model

If none of the well-known optical cavity frequency noise sources is a good description of our observed noise, we are left to develop an alternative reasonable explanation. In a paper from the Roukes group at Caltech on their nanomechanical mass sensors, mechanical frequency noise was observed and attributed to surface diffusion of adsorbates on their mechanical beams [119]. On our devices, as we'll discuss more later, we do expect the presence of adsorbed water molecules. In this section, we will develop a model for the effect the diffusion of adsorbed water molecules would have on the

frequency of our optical cavities.

We will assume that these adsorbed water molecules primarily affect the optical frequency by changing the local refractive index. From Ref. [117], the relative shift of the optical frequency due to a index of refraction change δn is given by the following.

$$\frac{\delta\omega}{\omega_0} = -\frac{\int |\mathbf{E}_0|^2 \delta n dV}{\int n |\mathbf{E}_0|^2 dV} \quad (5.9)$$

In Eq. (5.9), n is the index of refraction of the photonic crystal, \mathbf{E}_0 is the unperturbed optical mode of interest, and δn is the refractive index change induced by the adsorbed water molecules. For simplicity, we will model the photonic crystal beams and this system as a 1-dimensional problem. We will assume a fluctuating density per unit length of adsorbed water molecules on the surface of the beams given by $C(x, t)$. Using $C(x, t)$, we can rewrite Eq. (5.9) as follows.

$$\frac{\delta\omega}{\omega_0} = -V_{\text{water}} \frac{\int |\mathbf{E}_0(x, y_0, z_0)|^2 (n_{\text{water}} - 1) C(x, t) dx}{\int n |\mathbf{E}_0|^2 dV} \quad (5.10)$$

In Eq. (5.10), V_{water} is the volume of a water molecule, n_{water} is the index of refraction of water, and $\mathbf{E}_0(x, y_0, z_0)$ is the value of the electric field at the surface of the beams. Note that the top integral in Eq. (5.10) will be broken into 8 parts, one for each surface of the two beams (many of them will be the same from symmetry). Simplifying Eq. (5.10) yields the following.

$$\frac{\delta\omega}{\omega_0} = A \int |\mathbf{E}_0(x, y_0, z_0)|^2 C(x, t) dx \quad (5.11)$$

$$A \equiv \frac{-(n_{\text{water}} - 1) V_{\text{water}}}{\int n |\mathbf{E}_0|^2 dV} \quad (5.12)$$

The subsequent derivation borrows heavily from Ref. [119]. Our ultimate goal will be to obtain the power spectral density of the optical frequency. The power spectral density of a variable is the Fourier transform of its autocorrelation (see appendix A). Therefore, our first step will be to calculate the autocorrelation, $G(\tau)$, of the frequency fluctuations.

$$G(\tau) = \frac{\langle \omega(t) \omega(t + \tau) \rangle}{\omega_0^2} = A^2 \int dx \int |\mathbf{E}_0(x, y_0, z_0)|^2 |\mathbf{E}_0(x', y_0, z_0)|^2 \langle C(x, t + \tau) C(x', t) \rangle dx' \quad (5.13)$$

In order to move forward with Eq. (5.13), we'll need to find $\phi(x, x', t) \equiv \langle C(x, t + \tau) C(x', t) \rangle$.

We can do this by recognizing that $C(x, t)$ must satisfy a diffusion equation as follows.

$$\frac{\partial C(x, t)}{\partial t} = D \frac{\partial^2 C(x, t)}{\partial x^2} \quad (5.14)$$

$$\frac{\partial C[k, t]}{\partial t} = -Dk^2 C[k, t] \quad (5.15)$$

$$C[k, t] = e^{-Dk^2 t} C[k, 0] \quad (5.16)$$

Between Eqs. (5.14) and (5.15), we performed a Fourier transform with respect to the x-coordinate and denoted this as, $C[k, t]$. Using Eq. (5.16), and standard Fourier transform results for Gaussians, we can find $\phi(x, x', t)$.

$$\phi(x, x', t) = \frac{N}{L} \frac{1}{2\sqrt{\pi D\tau}} e^{-\frac{(x-x')^2}{4D\tau}} \quad (5.17)$$

The normalization constant out in front in Eq. (5.17) contains N, the total number of adsorbed water molecules on the particular surface of the beam, and L, the relevant length of the beam (relevance set by optical mode size). In order to obtain a reasonable analytic expression for the integral in Eq. (5.13), we fit the optical mode to a gaussian on each surface of the beam.

$$|\mathbf{E}_0(x, y_0, z_0)|^2 = |\mathbf{E}_a|^2 e^{-\left(\frac{x}{L}\right)^2} \quad (5.18)$$

In Eq. (5.18), \mathbf{E}_a is the electric field amplitude for the gaussian fit and L is the fitted length scale for the optical mode (same L as the one found in Eq. (5.17)). Putting Eqs. (5.17) and (5.18) into Eq. (5.13) and performing the integral yields the following.

$$G(\tau) = |\mathbf{E}_a|^4 \frac{A^2 N \sqrt{\pi}}{\sqrt{2}} \frac{1}{\sqrt{1 + \frac{\tau}{\tau_D}}} \quad (5.19)$$

$$\tau_D \equiv \frac{L^2}{2D} \quad (5.20)$$

Now we are in a position to calculate the power spectral density for the relative optical frequency fluctuations, $y = \frac{\delta\omega}{\omega_0}$.

$$\begin{aligned}
S_{yy} &= \int_{-\infty}^{\infty} G(\tau) e^{-i\omega\tau} d\tau = 2 |\mathbf{E}_a|^4 A^2 N \sqrt{\frac{\pi}{2}} \int_0^{\infty} \frac{\cos(\omega\tau)}{\sqrt{1 + \frac{\tau}{\tau_D}}} d\tau \\
&= \frac{|\mathbf{E}_a|^4 A^2 N \pi \tau_D}{\sqrt{\omega \tau_D}} (\cos(\omega\tau_D) + \sin(\omega\tau_D) - 2C_1(\sqrt{\omega\tau_D}) \cos(\omega\tau_D) - 2S_1(\sqrt{\omega\tau_D}) \sin(\omega\tau_D))
\end{aligned} \tag{5.21}$$

In Eq. (5.21), C_1 and S_1 are the first Fresnel cosine function and the first Fresnel sine function, respectively. Once again, there will be 8 contributions of Eq. (5.21) to the total noise, one for each surface of the optical beams. The gaussian fit to the optical mode along the top surface of the optical beam is shown in Fig. 5.17. The value of the norm-squared of the electric field was found in COMSOL simulation in the middle between consecutive holes (black circles in Fig. 5.17a) and fit to a gaussian (red line in Fig. 5.17a). The fitted gaussian width, parameterized by L in Eq. (5.18), is $2.35 \mu\text{m}$ and the fitted magnitude is $|\mathbf{E}_a| = 1.06 \times 10^8 \text{ V/m}$. The gaussian fits for the other sides of the optical beam were very similar.

The remaining parameters needed in Eq. (5.21) are the number of adsorbed water molecules, N , and the diffusion coefficient, D (note that D determines τ_D through Eq. (5.20)). Silicon nitride, when exposed to the oxidizing piranha solution [120] or simply ambient air [121], will oxidize forming a thin layer of silicon dioxide. From Refs. [122–124], silicon dioxide is hydrophilic because water easily hydrogen bonds to surface hydroxyl (OH) groups. Furthermore, at room temperature silicon dioxide will develop approximately 2-4 monolayers of water when exposed to atmosphere with relative humidity between 20% and 70% [122]. The surface diffusion coefficient, D , for water on a hydrophilic silicon dioxide surface can be modeled using molecular dynamics simulations [124]. The lateral (in-plane) diffusion coefficient is found to be between $0.99 \times 10^{-9} \text{ m}^2/\text{s}$ and $1.18 \times 10^{-9} \text{ m}^2/\text{s}$ for the first monolayer, between $2.18 \times 10^{-9} \text{ m}^2/\text{s}$ and $2.34 \times 10^{-9} \text{ m}^2/\text{s}$ for the second monolayer, and approximately $3 \times 10^{-9} \text{ m}^2/\text{s}$ for the remaining bulk water layers. These numbers give us a great idea of the reasonable values for the diffusion coefficient and the number of monolayers of water on our structures.

Briefly, before proceeding further with fitting our measured roll-up noise to the form in Eq. (5.21), we note that the molecular dynamics simulation results for the diffusion coefficient do not account for interactions with air molecules at atmospheric pressure. Therefore, we'll fit using data taken at vacuum pressure ($\sim 1 \times 10^{-5} \text{ mbar}$). The character of the roll-up noise does change slightly in vacuum versus atmospheric pressure and a comparison plot is shown in Fig. 5.18.

Fig. 5.19 shows the best fit (using least squares optimization) of Eq. (5.21) (including the contributions from all 8 surfaces) to the low-frequency roll-up noise measured on the fundamental bonded mode of an optical cavity of the same geometry as Fig. 2.10 in vacuum. As one can readily see, the

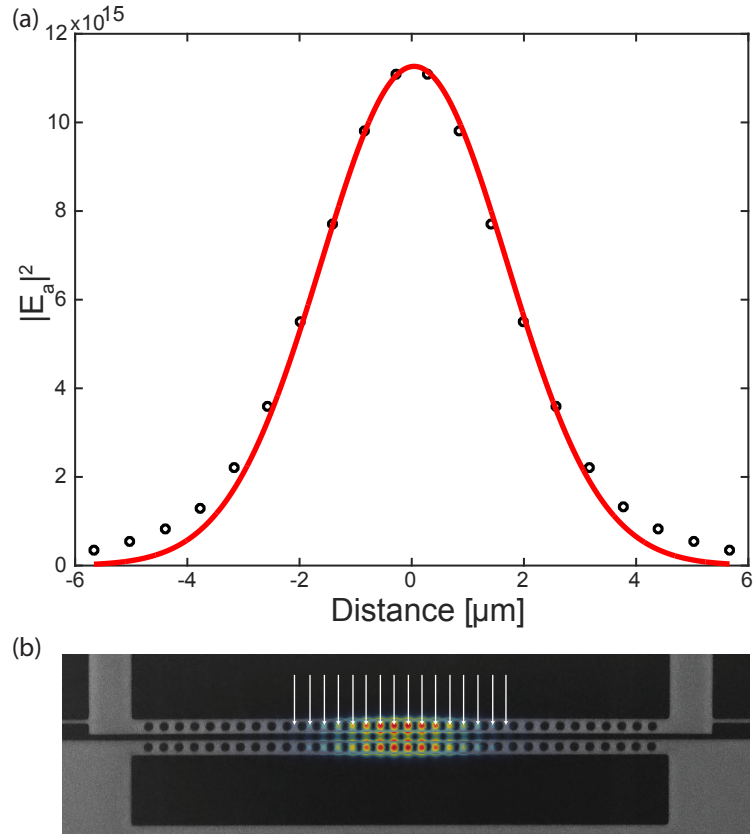


Figure 5.17: **Optical Mode Gaussian Fit.** (a) Gaussian fit to the norm-squared of the fundamental bonded optical mode. The black circles are the value of the norm-squared electric field at the top surface of the optical beam at the middle point between optical holes (see white arrows in (b)). The red line is the gaussian fit with fitted width, L (see Eq. (5.18)), of approximately $2.35 \mu\text{m}$. (b) Plot of the norm of the electric field overlaid on the optical beams. The white arrows indicate the points where the electric field was sampled on the top surface for the gaussian fit.

fit is excellent. As discussed earlier, there are really only two fit parameters: the number of water molecules (or equivalently the number of water monolayers) and the surface diffusion coefficient. The best fit shown in Fig. 5.19 occurs when $D = 1.3 \times 10^{-9} \text{ m}^2/\text{s}$ and the number of monolayers is 2.3. As discussed previously, this is in very good agreement with the values expected from the literature [122, 124].

5.4.2 Removing Diffusion Noise Through Surface Treatment

As shown in Fig. 5.19, the adsorbed water diffusion model (Eq. (5.21)) appears to predict the low frequency roll-up very well. Nevertheless, an experiment on a device with a reduced amount of adsorbed water, which showed a reduction in this noise would increase our confidence in the model. The water layers cannot be removed simply by going to vacuum (as is consistent with our data) and instead have to be subjected to a bake-out procedure much like ultra high vacuum systems [125].

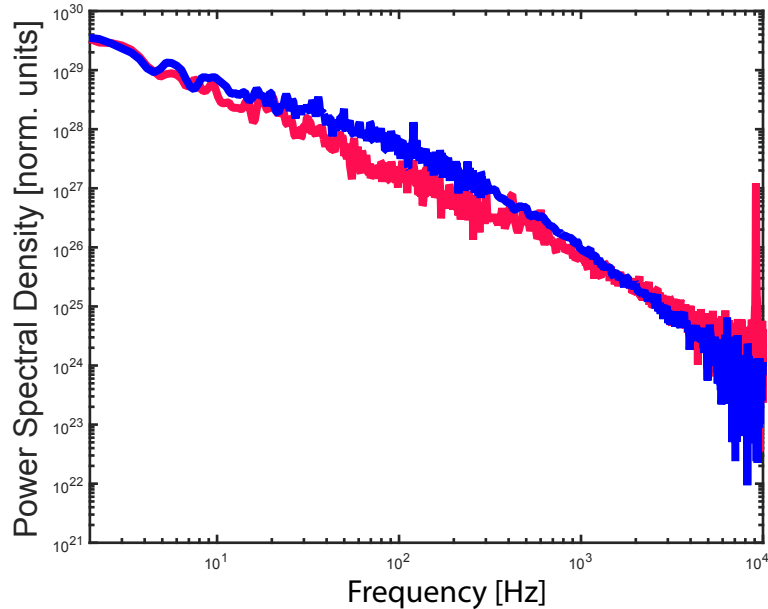


Figure 5.18: **Compare Roll-Up Noise in Vacuum and Atmospheric Pressure.** This is a log-log plot of the electronic power spectral density normalized by the optical transduction coefficient (see discussion of Fig. 5.15). The flat noise floor consisting of NEP and shot noise has been subtracted. The blue curve is data taken in vacuum ($\sim 1 \times 10^{-5}$ mbar) and the red curve is data taken at atmospheric pressure.

However, we decided to implement a more permanent solution by using a surface treatment of the silicon nitride devices that makes them highly hydrophobic and, thereby, less susceptible to water adsorption. Both theoretical Monte Carlo simulations and experimental work have shown the lack of water adsorption on hydrophobic surfaces [125, 126].

The main idea is to conformally cover our released structures with a hydrophobic monolayer of material that takes the place of the water monolayers. Furthermore, this hydrophobic monolayer should be rigidly (covalently) bonded to the surface to prevent its own diffusion like the hydrogen bonded water molecules.

More specifically, we used alkyltrichlorosilane based self-assembled monolayer (SAM) techniques that are excellently described in Refs. [120, 127–130]. Broadly speaking, this SAM method works as follows. The alkyl-trichlorosilane (RSiCl_3) precursor molecules (R is a hydrocarbon chain and SiCl_3 is trichlorosilane) are placed in a suitable solution with the oxidized chip. The trichlorosilane head groups hydrolyze into three silanols (SiOH), if the solution used is anhydrous this occurs at the water layer on the device surface. These silanols then condense with both hydroxyl groups on the oxidized device surface and silanol groups on other precursor molecules. These reactions replace the water layer with an extremely hydrophobic monolayer of covalently bonded siloxane (Si-O-Si) crosslinks, see Fig. 5.20 adapted from Ref. [127].

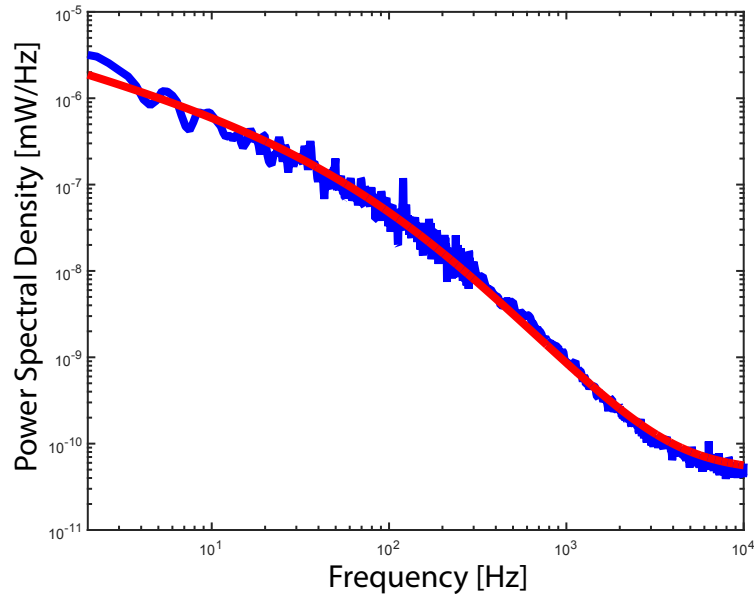


Figure 5.19: **Adsorbed Water Diffusion Model Fit.** The blue curve is the electronic power spectral density of light reflected approximately half a linewidth red-detuned from the fundamental bonded optical mode of a photonic crystal of geometry shown in Fig. 2.10, at a vacuum pressure of 1×10^{-5} mbar. The flat noise floor consisting of NEP and shot noise has not been subtracted. The red curve is the best fit of this data to Eq. (5.21). The best fit has $D = 1.3 \times 10^{-9}$ m²/s and 2.3 monolayers of water.

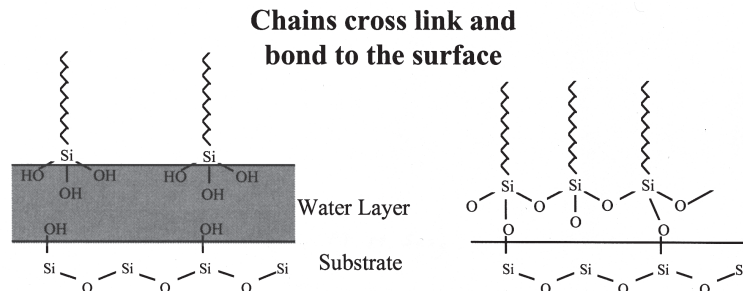


Figure 5.20: **SAM Siloxane Crosslinking.** This figure illustrates the silanols from the precursor molecules reacting with surface hydroxyl groups to form a crosslinked siloxane layer as discussed in the main text. This figure is adapted from Ref. [127].

The nanofabrication of our devices with SAM coatings was done following exactly the steps shown in Figs. 2.14 and 2.17, except, before the final critical-point dry, the processes in table 5.1 were performed. The SAM coating is formed from 1H, 1H, 2H, 2H-perfluorodecyltrichlorosilane (FDTS). The FDTS mixture mentioned in table 5.1 is a 1 mM (milliMolar) solution of FDTS in anhydrous iso-octane. The entire SAM process technique is taken Ref. [130], with a slight modification to the hydrofluoric acid (HF) dip step. In Ref. [130], the HF dip step is used to undercut a sacrificial layer, which is not necessary here. In order to deviate as minimally as possible from the prescribed

process, we incorporated a short, low concentration, HF dip, which Ref. [56] states may slightly increase Q_m by removing the thin top layer of nitride that may have been damaged by the dry etch. During all steps and rinses the chip was carried in the teflon holder shown in Fig. 2.16, to avoid deleterious surface tension forces. Also, we note that the critical-point dry step in table 5.1 may well be unnecessary, but we included it as a precaution. Because the water does not wet the SAM coated nitride surface, the devices can be simply lifted out of the last rinse step without fear of stiction for they will be dry. In fact, this SAM procedure reduces the work of adhesion by approximately four orders of magnitude when compared to the standard oxide coating [128, 130]. Therefore, the SAM coating, from our point of view, doubles as a useful fabrication technique for low-frequency mechanical structures (in fact, this is the real reason why they were developed).

SAM Process Sequence		Approximate Time
Surface Preparation Step	1:10 HF to H ₂ O Dip	1.5 min.
Surface Oxidization	H ₂ O Rinse	10 min.
	H ₂ O ₂ Rinse	15 min.
	H ₂ O Rinse	5 min.
SAM Formation	Isopropanol Rinse	5 min.
	Iso-octane Rinse	5 min.
	Iso-octane Rinse	5 min.
	FDTs mixture	10 min.
	Iso-octane Rinse	5 min.
	Iso-octane Rinse	5 min.
	Isopropanol Rinse	5 min.
Rinse and Dry	Isopropanol Rinse	5 min.
	H ₂ O Rinse	5 min.
	Critical-Point Dry	

Table 5.1: **SAM Procedure.** Procedure taken from Ref. [130].

Finally, in Fig. 5.21 we show the result of coating our structures with this SAM layer. Both data sets (red and blue) are taken on the same optical mode and device at atmospheric pressure. The device geometry is the same as that shown in Fig. 2.10. The red data was taken before the device was coated with the SAM layer and the blue data afterward. As one can readily see, there is a dramatic 15 dB reduction in the low-frequency roll-up noise. This adds another excellent piece of evidence that the low-frequency noise is really due to adsorbed water diffusion on the surface of the optical beams.

There is still low-frequency noise remaining after SAM treatment. This could be due to step imperfections in the SAM layer, which can act as sites for water adsorption and can lead to water surface coverage of approximately 10% [131]. Water on hydrophobic SAM layers does not form a uniform layer but instead forms microspheres (much like what happens on the macro-scale) [131, 132]. Perhaps these sources could be mitigated by refining our techniques for the SAM coating process. Ref. [129] states that the FDTs mixture and coating step may be improved by using a nitrogen dry

box (to avoid contact with moisture in the air) and that was not done in this work. Additionally, the two laser cancellation scheme could be used to provide further cancellation. As it currently stands we have a very good understanding of the noise source and the 15 dB suppression will provide nearly a factor of 6 improvement in acceleration resolution.

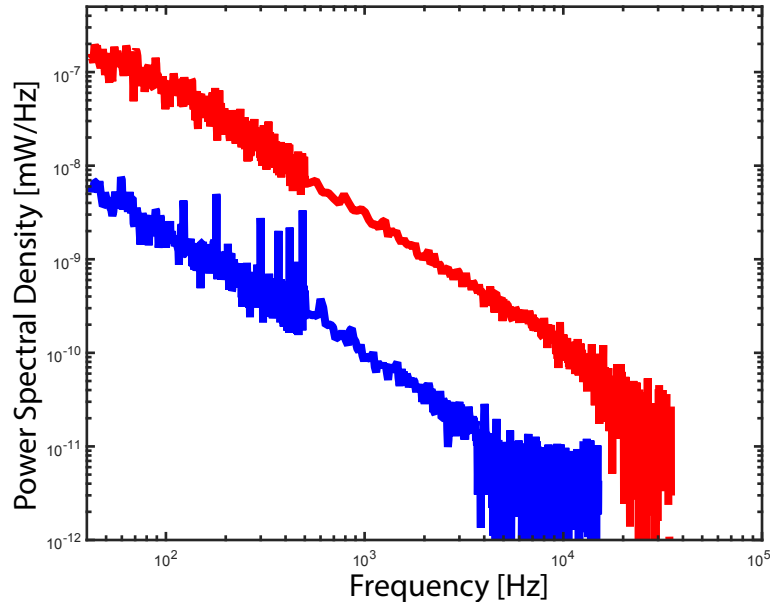


Figure 5.21: **SAM Suppression of Low-Frequency Roll-Up.** This is a plot of the electronic power spectral density of light reflected approximately half a linewidth red-detuned from an optical mode of a photonic crystal of geometry shown in Fig. 2.10. The flat noise floor consisting of NEP and shot noise has been subtracted. The red curve is taken before SAM coating and the blue curve afterward. The blue curve is adjusted by approximately 0.1 dB to account for changes in the optical transduction coefficient (Eq. (1.15)) between experiments. Both data sets are taken at atmospheric pressure. The dB difference between the two curves is 15 dB.

5.5 Heavy Mass Accelerometers

A further improvement to the performance and practicality of the accelerometer can be achieved by greatly increasing the test mass size. By releasing entire sections of the 200 μm thick chip, the test mass size can be increased by a factor greater than 10,000. This significantly reduces the fundamental acceleration thermal noise, Eq. (4.3). Furthermore, it allows the use of a lower mechanical quality factor while still achieving excellent thermal noise resolution. This means devices can be operated at room (atmospheric) pressure, which alleviates long-term low pressure packaging complications. Additionally, risk of failure due to resonant response from a large, broadband, shock input is greatly reduced when using lower mechanical Q .

The nanofabrication techniques used to release entire sections of the chip are discussed in Sec-

tion 2.4.1 and Fig. 2.17. The real strength of these techniques is their simplicity, i.e. the processing techniques are not fundamentally different from those used for our single-sided lithography (see Section 2.4). The same test mass and nanostring pattern is written on the top and bottom side of the chip. If the patterns are well-aligned and the openings etched in the silicon nitride are wide enough, the KOH+IPA liquid etch can etch all the way through the chip (see Fig. 2.15). Moreover, due to the anisotropic nature of the KOH etch, the silicon underneath the rectangular test mass defined in the nitride layer remains (see Fig. 5.22). Again, we should note that these fully released devices are floppy and the ~ 200 nm photonic crystal slot gaps are liable to collapse during fabrication if great care is not taken. As noted at the end of Section 2.4, during all wet etches and rinses the samples must not be lifted out of liquid or else surface tension will cause collapse. These techniques are described in great detail in Ref. [38]. Also, the device studied in this section has been coated in a SAM layer as described in Section 5.4.2 to reduce the low-frequency roll-up.

Scanning electron microscope (SEM) images of an example heavy mass accelerometer are shown in Fig. 5.22. It is essentially the same as our initial accelerometer design (shown in Fig. 4.3) except at a much larger scale. That is, a rectangular test mass with a photonic crystal on one side. This time, however, there are several thousand tethers to maintain frequencies of ~ 10 kHz with this much larger test mass (see Section 4.5 for our first discussion of this technique). Light is coupled into the photonic crystal using the adiabatic on-chip waveguide (see Fig. 5.22a,e) and end-coupling techniques first discussed in Section 2.2. The adiabatic coupler is placed at a point after the coupling waveguide has been pinned to the bulk (Fig. 5.22e) to help mitigate the presence of taper modes (see Section 4.3.2), although, as we'll see, their effect is not completely eliminated. If the fiber taper is placed on the coupling waveguide before it is pinned to the bulk, taper motion can cause motion of the waveguide and the taper modes are much more pronounced.

5.5.1 Testing at Atmospheric Pressure

This heavy mass accelerometer was first characterized at atmospheric pressure in order to highlight its excellent acceleration resolution at these high pressures. Data characterizing the device, including an electronic power spectral density of the reflected laser light, is shown in Fig. 5.23. The optical mode used was the fundamental bonded mode (see Section 2.1.1) and its quality factor was $Q_o = 9600$, see Fig. 5.23c. The mechanical quality factor at air pressure was found by fitting the power spectral density to be $Q_m = 5500$, see Fig. 5.23d. The electronic power spectral densities shown in Fig. 5.23a-b, were obtained from the photodetector signal of laser light reflected from the optical cavity with the laser approximately half a linewidth red-detuned from the optical cavity. Both Fig. 5.23a and Fig. 5.23b plot the same electronic power spectral density, but the difference is (a) uses linear axes while (b) is plotted on a logarithmic scale. Using the fiber taper and on-chip adiabatic waveguide end-coupled into the photonic crystal (see Section 2.2), the total detection

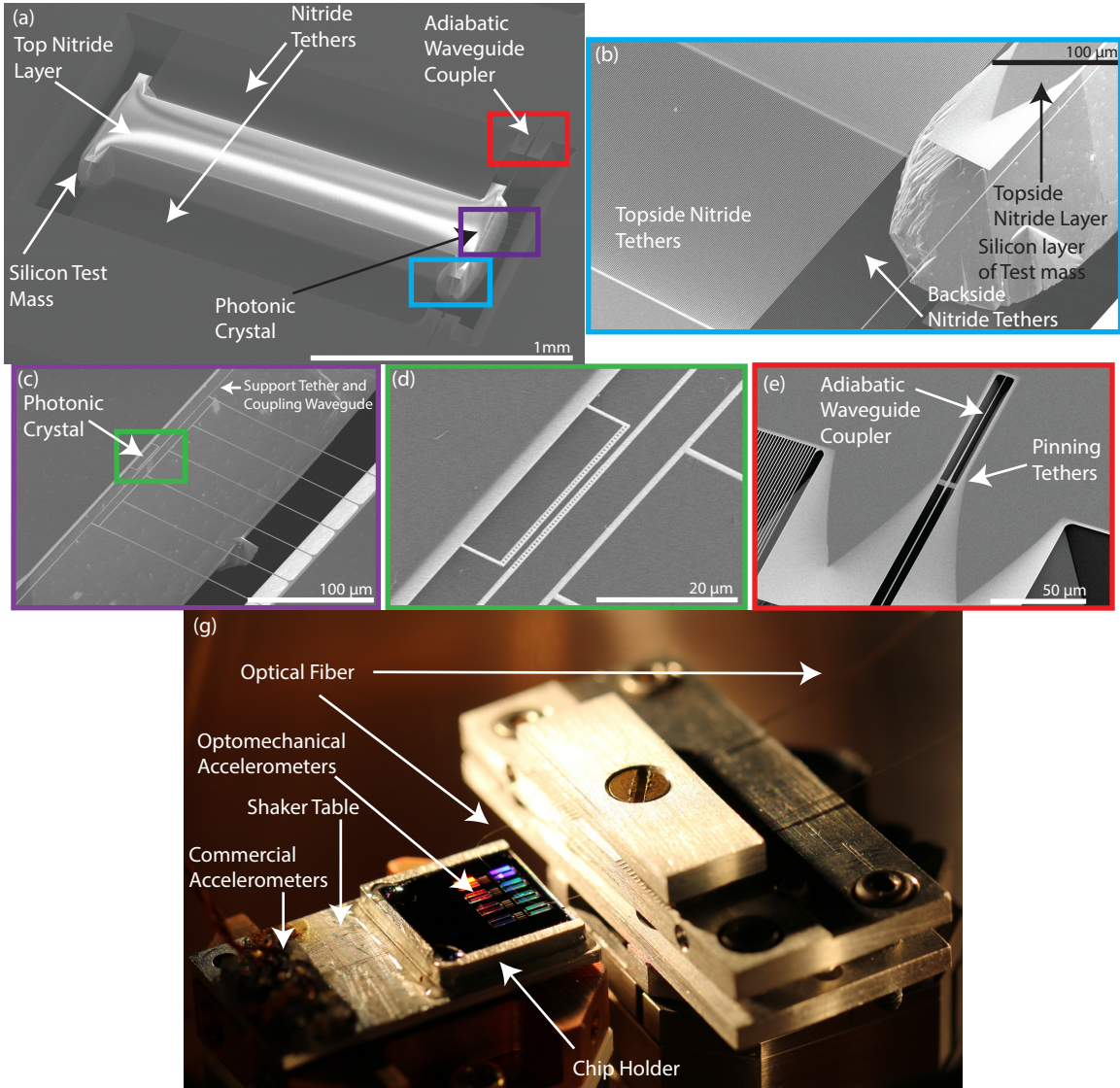


Figure 5.22: **Heavy Mass Accelerometer.** (a) SEM image showing a heavy mass accelerometer. The large rectangle in the middle is the test mass, which is supported by ~ 3000 nanostring tethers. The photonic crystal cavity is located on the right hand side (purple rectangle). Light enters the cavity via an adiabatic coupler and on-chip waveguide (red rectangle). The small rectangles added to the corners of the test mass and where the adiabatic waveguide is pinned to the bulk protect those regions from the KOH etching of convex corners. (b) This is a zoom-in of the side of the test mass (cyan rectangle in (a)). Here one can see individual nanostring tethers on both the topside and backside and the silicon layer of the test mass. (c) Zoom-in of the photonic crystal region. One side is attached to the test mass while the other side is attached to the bulk via a long parallel tether (which doubles as an input waveguide) and several perpendicular tethers. (d) Further zoom-in of the photonic crystal. Here one can resolve that the cavity is end-coupled to the input waveguide. (e) zoom-in of the adiabatic on-chip waveguide coupling region. (g) Optical image of the test setup.

efficiency of light in the cavity to the detector was $\eta_{tot} \cong 0.24$. The optical power used at the photonic crystal cavity was $P = 12.4 \mu W$, limited by a thermo-optic bistability [133]. Using these

optical loss and power calibrations, and assuming the main mechanical peak in Fig. 5.23a is driven by room-temperature thermal noise (an assumption which will be validated later), we can fit an optomechanical coupling to this mechanical mode of $g_{\text{OM}} = 2\pi \times 10 \text{ GHz/nm}$.

In both Fig. 5.23a-b, the noise contributions of shot noise, detector NEP, and intrinsic mechanical thermal noise are shown. However, these cannot account for the mostly noise floor seen best in Fig. 5.23a. The cause of this noise floor is a rather simple and tractable one: it is the result of extraneous mechanical modes of the “stiff” side of the photonic crystal cavity, which are shown in the inset of Fig. 5.23a. The “stiff” side of the photonic crystal cavity is best illustrated in Fig. 5.22a,c,d. One side of the zipper cavity is attached to test-mass whose fundamental frequency is $\omega_{\text{m}} \cong 2\pi \times 11.48 \text{ kHz}$. The other side is tethered to the bulk in such a way that KOH etchant can get through to release the test-mass, yet its mechanical frequencies are still much greater than that of the test-mass $\omega_{\text{m}} \gtrsim 100 \text{ kHz}$ (see inset of Fig. 5.23a). As the fundamental frequencies of the “stiff” side are at least 10 times greater than the fundamental frequency of the test-mass, this means the “stiff” side’s response to applied in-plane accelerations will be at least 100 times less than that of the test-mass (see Eq. (1.34) and Fig. 1.8b). Therefore, the response of our entire accelerometer structure is dominated by the response of the test-mass and accelerations are efficiently sensed. If both sides of the photonic crystal had the same mechanical resonance frequency, their DC response to applied accelerations would be the same and no relative motion could be sensed. Even though the “stiff” side was correctly engineered to have much higher frequency modes, the combination of the much lower mass and much lower room-pressure Q’s of these modes causes their thermal noise to be pushed above our other noise sources in Fig. 5.23a. The fix is simple, however, by going to vacuum the mechanical Q’s of these modes will greatly increase and, consequently, their thermal noise will decrease and become negligible. We’ll see this shortly.

The acceleration resolution of the heavy mass accelerometer at room pressure is shown in Fig. 5.24. For those not familiar with our calibration scheme in general, see Sections 4.3 and 4.4 and Fig. 4.4. To measure the acceleration resolution the device was mounted on a shear piezo “shake table” just as shown Fig. 4.4 and Fig. 5.22g. As one can see in Fig. 5.24, we utilized two different ways to calibrate the acceleration resolution of this device and they agree extremely well above $\sim 500 \text{ Hz}$ and diverge below that frequency. The “driven response” calibration simply involves shaking (driving) the device with a tone (whose strength is calibrated by commercial accelerometers) at each frequency, measuring the response, and comparing that to the noise spectrum. In other words, it is the same measurement technique as that used for Fig. 4.11b. The “assumed response” calibration involves shaking the device with a calibrated tone at one frequency where the test-mass response is known to dominate, i.e. very near the fundamental in-plane resonance frequency of the test-mass. This calibrates the acceleration noise of the mechanical mode in Fig. 5.23a, and then the standard mechanical response is assumed for all other frequencies (see Eq. (1.34) and Fig. 1.8). In

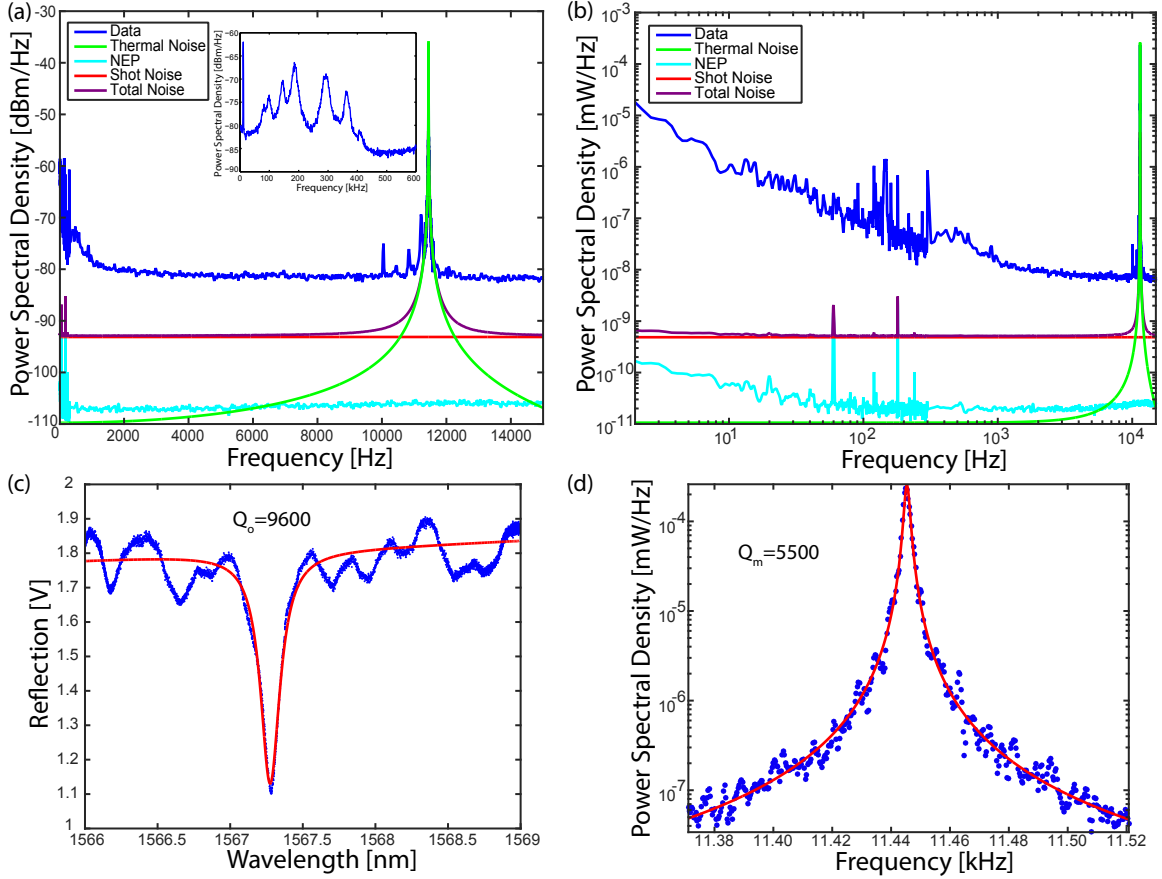


Figure 5.23: **Heavy Mass Accelerometer Room Pressure Characterization.** (a) Electronic power spectral density of laser light reflected from the optical cavity with the laser approximately half a linewidth red-detuned from the optical resonance. The noise floor is set by the “DC” tail of mechanical modes of the “rigid” side of the optical cavity. inset: electronic PSD showing the “rigid” side mechanical modes. (b) same as (a) except with logarithmic scaling on both axes. (c) The un-normalized reflected laser light at the photodetector is shown in blue. In red is the fit of the optical resonance to a lorentzian lineshape with a $Q_o = 9600$. (d) A zoom-in of the electronic PSD centered around the main mechanical resonance is shown in blue. In red, a theoretical fit to the mechanical resonance showing a $Q_m = 5500$.

other words, the “assumed response” method involves calibrating the acceleration noise of the green mechanical response curve in Fig. 5.23a-b and then using the signal-to-noise ratio of the measured power spectral density and the green mechanical response curve to obtain the broadband acceleration resolution of the device. The result of applying these calibration techniques are shown in Fig. 5.24.

Both of these methods obviously agree at the mechanical resonance, the lowest point on both resolution curves, with a resolution of $\approx 100 \text{ ng}/\sqrt{\text{Hz}}$. This agrees very well with theoretical thermal acceleration noise, Eq. (4.3), $a_{\text{th}} = \sqrt{\frac{4k_B T \omega_m}{m Q_m}} \cong 92 \text{ ng}/\sqrt{\text{Hz}}$. Here we have used $\omega_m = 2\pi \times 11.48 \text{ kHz}$, $Q_m = 5500$, $T = 300 \text{ K}$, and $m = 267 \text{ nKg}$. The mass was calculated using the well-known density of silicon and the physical dimensions of the test mass as shown in Fig. 5.22a.

This confirms, once again, that the mechanical motion observed in our measured electronic PSDs is indeed due to room-temperature thermal noise of the fundamental in-plane mechanical mode of the test mass.

These two methods obviously diverge at frequencies below ~ 500 Hz. This is due to a low-lying resonance of the fiber taper. This same phenomenon was observed in our first demonstration of an optomechanical accelerometer, see Section 4.3.2 and Fig. 4.9. This low-lying taper mode causes a spurious increase in response at low frequencies and a corresponding decrease in the noise equivalent acceleration (a.k.a. resolution), this was also observed previously in Fig. 4.11. We say spurious because any final integrated and robustly packaged device cannot rely on such a taper mode to provide added response. Such a low-lying taper mode is again observed when testing this heavy-mass accelerometer as shown in Fig. 5.25, where the driven response is shown normalized by the strength of the drive. The red curve in this figure shows the expected response due solely to the fundamental in-plane mechanical mode of the test mass. This is a good fit to the measured response curve until ≈ 500 Hz, where the response rises like $\omega^{-1.7}$. This is reasonably close to the ω^{-2} behavior we'd expect if approaching a low-lying mechanical resonance. Furthermore, this behavior is observed even if the laser is far-detuned from the optical cavity (inset of Fig. 5.25) and an increase in response is not observed on the commercial accelerometers. All of this evidence taken together makes us confident this spurious increased response at low frequency is due to a low-frequency taper mode (again see Section 4.3.2 for more discussion). Therefore, for low frequencies, we rely on the “assumed response” calibration shown in Fig. 5.24.

5.5.2 Testing in Vacuum

These measurements were repeated in vacuum (pressure $\approx 10^{-5}$ mbar), in order to eliminate the relevance of the mechanical modes of the “stiff” side of the optical cavity. The electronic PSD of the measurement is shown in Fig. 5.26, again with (a) plotted on a linear scale and (b) on a log-log scale. It must be noted that this vacuum data was taken with 8 dB less optical power incident at the optical cavity than the room pressure data. This, again, is due to the thermo-optic bistability. In vacuum, the device is less able to conduct heat from absorbed photons away from optical cavity and the thermo-optic bistability sets in at a lower optical power. In air, mechanical noise from the “rigid” side of the optical cavity was ~ 12 dB above shot noise (see Fig. 5.23a). Therefore, even at this 8 dB lower power, we'd expect this mechanical noise to be 4 dB above shot noise, if not reduced. However, in Fig. 5.26a, we see that the noise floor is set predominantly by shot noise of the laser light, meaning the mechanical noise of the “rigid” side has been reduced by going to vacuum and increasing the Q_m of those modes. The inset of Fig. 5.26a plots the autocorrelation of the amplitude of the fundamental in-plane mechanical mode of the test mass, which yields $Q_m = 75,000$ (see Section 4.3 and Fig. 4.7 for more information on this technique).

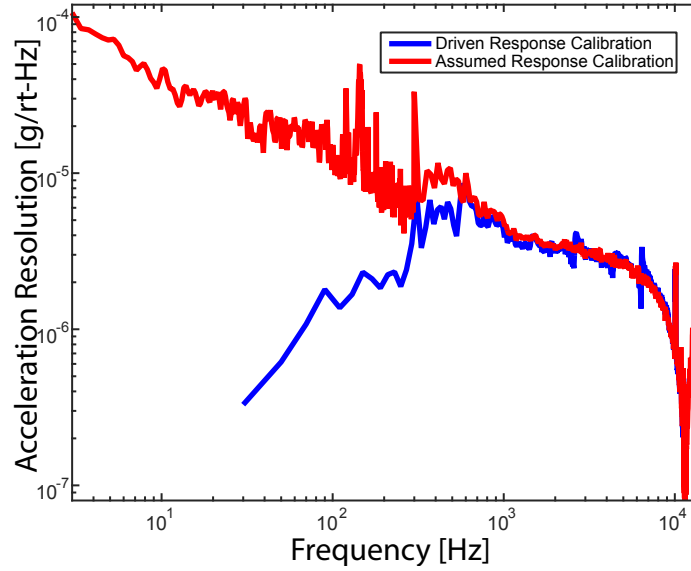


Figure 5.24: **Heavy Mass Accelerometer Room Pressure Resolution.** Plotted here is the acceleration resolution (a.k.a. noise equivalent acceleration) of the heavy-mass accelerometer at atmospheric (air) pressure. A description of the two techniques used to calibrate the resolution, “driven response” and “assumed response”, can be found in the main text.

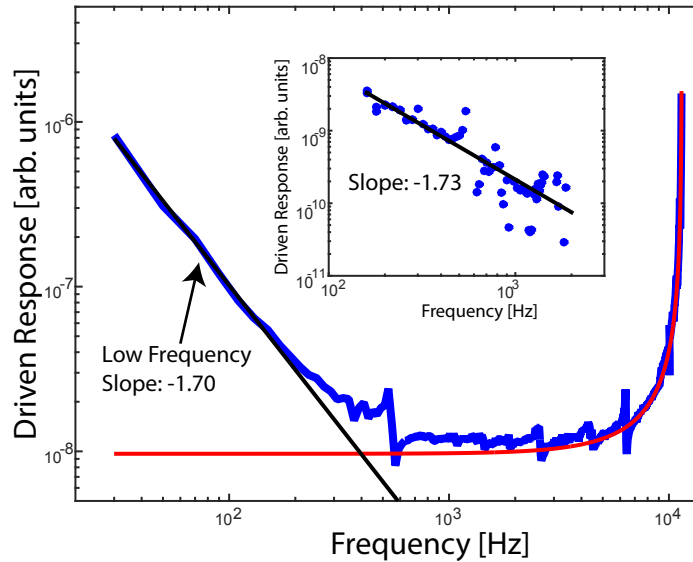


Figure 5.25: **Heavy Mass Accelerometer Normalized Driven Response.** This is a plot (in arb. units) of the response of the heavy mass accelerometer with the laser approximately half a linewidth red-detuned from the optical resonance, normalized by the drive strength. The red line is the expected response based solely on the susceptibility of the mechanical mode at $\omega_m = 2\pi \times 11.48$ kHz, which is in excellent agreement down to several hundred Hz. At low frequency the response increases as $\omega^{-1.7}$ and this behavior is repeated even when the laser is far-detuned from the optical resonance (inset). This reasonably agrees with the ω^{-2} response expected for a low-lying taper mode.

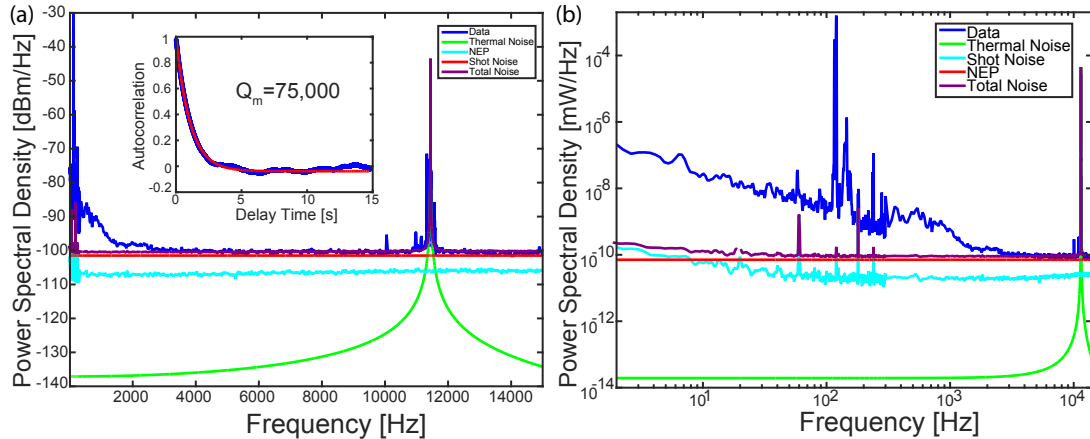


Figure 5.26: **Heavy Mass Accelerometer Vacuum Characterization.** (a) Electronic power spectral density of laser light reflected from the optical cavity with the laser approximately half a linewidth red-detuned from the optical resonance in vacuum. (b) same as (a) but on a log-log scale.

The resolution of the heavy mass accelerometer in vacuum is shown in Fig. 5.27. We plot both the “driven response” calibration and the “assumed response” calibration. Once again, the presence of a low-frequency taper mode is inferred from the driven data, and therefore at low-frequency we trust the “assumed response” calibration. The resolution in vacuum from approximately 1 kHz to 10 kHz, is approximately 1.5 times lower than the resolution in air (Fig. 5.24). This makes sense given the additional 4 dB of signal to noise we have in our vacuum measurement (this 4 dB is argued for in the previous paragraph), note that $\sqrt{10^{4/10}} \approx 1.5$. Note also that the minimum of the acceleration resolution occurs near the mechanical resonance frequency and its value is $\approx 25 \text{ ng}/\sqrt{\text{Hz}}$, in agreement with what we expect theoretically for a_{th} given the increase in Q_m , so the test mass can still be considered driven by room-temperature thermal noise.

Note that in Fig. 5.26b we can still see the low frequency noise roll-up, but this device was given a SAM treatment, so this noise is much lower than what it would have been otherwise. If this noise could be further reduced by another 10 dB, using the two laser cancellation technique or refining our SAM treatment techniques, and the g_{OM} of the structure was increased to 200 GHz/nm (demonstrated in Ref. [1]), the resolution would be $\lesssim 1 \mu\text{g}$ over the entire bandwidth shown (ignoring the couple taper modes, which can be eliminated with V-groove coupling).

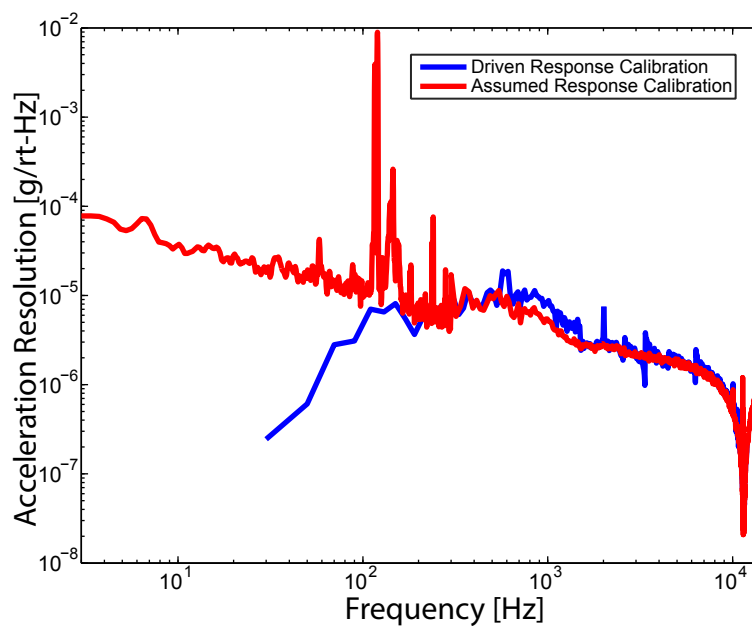


Figure 5.27: **Heavy Mass Accelerometer Vacuum Resolution.** Plotted here is the acceleration resolution (a.k.a. noise equivalent acceleration) of the heavy-mass accelerometer in vacuum. A description of the two techniques used to calibrate the resolution, “driven response” and “assumed response”, can be found in the main text.

Chapter 6

Progress Towards an Optomechanical Gyroscope

After exploring and developing an optomechanical accelerometer, it is natural to consider what other types of sensors could benefit from optomechanical displacement sensing. Micromachined vibratory gyroscopes, which sense rates of rotation, are the obvious candidate. Their use has increased greatly in recent years with applications ranging from inertial navigation (when paired with accelerometers) to automotive ride-stabilization to video recording stabilization and the video game industry [79]. In this chapter, we'll explore the working principle of micromachined vibratory gyroscopes and the progress we made towards developing an optomechanical version.

6.1 Introduction

The first question to answer is how micromachined vibratory gyroscopes sense rotation. Imagine that you wanted to prove to a child that the earth is indeed spinning, how would you do so? One popular and conceptually easy proof of the earth's rotation is the dynamics of a Foucault pendulum. The plane in which the pendulum swings precesses due to the coriolis force, a force unique to rotating reference frames. In a similar vein, micromachined gyroscopes leverage the coriolis force by monitoring how it causes vibrational motion in one mechanical resonance to be transferred into another orthogonal mechanical resonance. For reference, the form of the coriolis force, \mathbf{F}_c , is provided below, where m is the mass of the test mass, $\boldsymbol{\Omega}$ is the angular velocity of the test mass's reference frame, \mathbf{v} is the velocity of the test mass, and \times represents the cross-product.

$$\mathbf{F}_c = -2m\boldsymbol{\Omega} \times \mathbf{v} \quad (6.1)$$

A cartoon of a z-axis canonical vibratory gyroscope is shown in Fig. 6.1. It is obviously based off of the cartoon for a canonical accelerometer shown in Fig. 4.1. However, instead of just a single

mechanical mode for sensing with stiffness $k_{\text{sense}} = m\omega_{\text{sense}}^2$, and quality factor, Q_{sense} , the test mass is now engineered to have a second orthogonal mechanical mode, called the “drive” mode with stiffness $k_{\text{drive}} = m\omega_{\text{drive}}^2$, and quality factor, Q_{drive} . The idea is to purposefully ring-up (drive) motion in the aptly named “drive” mode and then observe the amplitude of motion in the sense mode and, from that, infer the magnitude of the angular velocity, Ω . Walking through a general example, let’s suppose the drive mode is rung-up to an amplitude A , its velocity will then be $v = A\omega_{\text{drive}}\sin(\omega_{\text{drive}}t)$ (in the y -direction, using the reference frame of Fig. 6.1), if there is a constant angular rotational velocity of magnitude, Ω , in the z -direction, the coriolis acceleration will be in the sense (x) direction and its magnitude is

$$a_c = 2A\omega_{\text{drive}}\sin(\omega_{\text{drive}}t)\Omega. \quad (6.2)$$

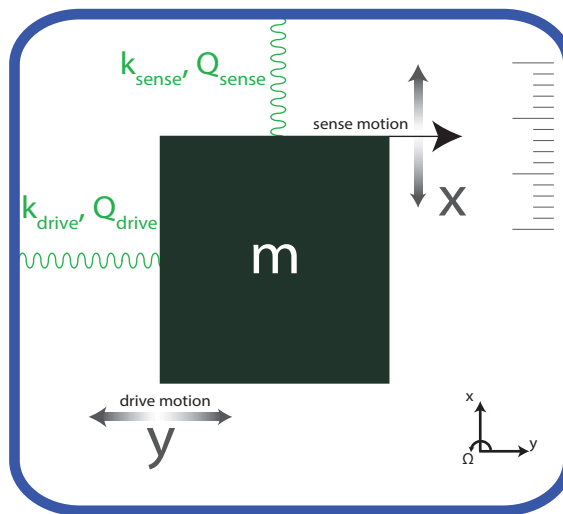


Figure 6.1: **Canonical Gyroscope.** This is a cartoon of a canonical vibratory gyroscope. It is adapted from the canonical accelerometer shown in Fig. 4.1. In much the same way as the accelerometer, there is a “sense” mechanical mode with stiffness $k_{\text{sense}} = m\omega_{\text{sense}}^2$ and quality factor, Q_{sense} , which is used to sense mechanical motion. Now, there is also a “drive” mechanical mode, with stiffness $k_{\text{drive}} = m\omega_{\text{drive}}^2$, and quality factor, Q_{drive} , which allows the test mass to move in a direction orthogonal to the sense mode. If the test mass is rotating about the z -axis and moving in the drive mode the resulting coriolis force will cause a displacement in the sense mode, which can be read-out and used to infer the rotational velocity.

A fundamental sensing limit for such a vibratory gyroscope, similar to the accelerometer, comes from the fundamental thermal motion of the test mass in the sense mode. This thermal motion of the sense mode will be indistinguishable from the motion caused by rotations that we wish to detect. From Eq. (4.3) we know the noise equivalent acceleration of the test mass in the sense mode

due to fundamental thermal noise. Furthermore, from Eq. (6.2), we know the acceleration expected in the sense mode for angular velocity of magnitude Ω . Combining Eq. (4.3) and the amplitude of Eq. (6.2) allows us to write the fundamental thermal noise limited noise equivalent rotation for a vibratory gyroscope as follows [134, 135].

$$\Omega_{\text{th}} = \sqrt{\frac{k_{\text{B}}T\omega_{\text{sense}}}{mQ_{\text{sense}}\omega_{\text{drive}}^2A^2}} \quad (6.3)$$

Into Eq. (6.3) we can plug in the parameters of our demonstrated accelerometers, assuming we have also engineered a drive mode of comparable frequency, and integrate electrostatic drive capacitors on-chip (like those discussed in Section 5.2). Assuming the parameters of the device presented in Chapter 4 and a drive amplitude of $1 \mu\text{m}$ results in $\Omega_{\text{th}} \approx 10 \text{ }^\circ / (h\sqrt{Hz})$, and with a drive of $10 \mu\text{m}$, $\Omega_{\text{th}} \approx 1 \text{ }^\circ / (h\sqrt{Hz})$. In the units of Ω_{th} , $^\circ$ represents degrees and h represents hours. If instead we assume the device parameters of the heavy accelerometer from Section 5.5 in vacuum, assuming a drive amplitude of $1 \mu\text{m}$ results in $\Omega_{\text{th}} \approx 0.3 \text{ }^\circ / (h\sqrt{Hz})$, and with a drive of $10 \mu\text{m}$, $\Omega_{\text{th}} \approx 0.03 \text{ }^\circ / (h\sqrt{Hz})$. In the field, the noise-equivalent rotation is called the angular random walk (obviously, not necessarily set by thermal noise of the sense mode), and its value for several devices from the literature is shown in Fig. 6.2 (this figure is adapted from Ref. [135]). Our projected thermal noise numbers are shown as red stars in Fig. 6.2. Given these numbers, we decided to pursue fabricating an optomechanical gyroscope.

6.2 Device Presentation, Fabrication, and Characterization

As discussed in Section 6.1, the easiest way to construct a gyroscope is to take the accelerometer we've already developed (see Chapter 4) and engineer the structure to have a de-coupled, orthogonal drive mode as well. The simplest way to achieve this is to attach the accelerometer to a "frame", which is in turn suspended from the bulk in the orthogonal direction. A Comsol simulation of an example configuration is shown in Fig. 6.3.

One must take care, however, when attempting to implement this method. The frame (rectangular annulus) cannot simply be made from the silicon nitride device layer (as the accelerometer from Chapter 4 was). The reason being, if this frame of nitride is released from the underlying silicon, all of its internal stress will be released. This, in turn, will cause the stress to disappear from the nano-strings supporting the enclosed accelerometer. All of the great advantages that high-stress silicon nitride provides (notably high mechanical frequencies and quality factors) will be lost. We must design the frame in such a way that the stress is maintained, which means leaving the silicon layer on the backside of the frame. In this way, the silicon will hold the nitride in place, preventing

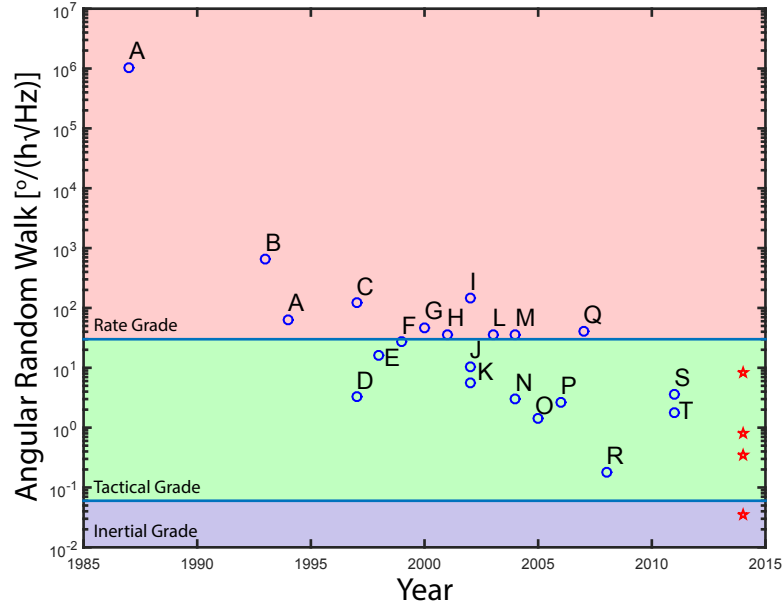


Figure 6.2: **ARW of Micromachined Gyroscopes.** This figure is adapted from Ref. [135]. A is Ref. [136]. B is Ref. [137]. C is Ref. [138]. D is Ref. [139]. E is Ref. [140]. F is Ref. [141]. G is Ref. [142]. H is Ref. [143]. I is Ref. [144]. J is Ref. [145]. K is Ref. [146]. L is Ref. [147]. M is Ref. [148]. N is Ref. [149]. O is Ref. [150]. P is Ref. [151]. Q is Ref. [152]. R is Ref. [153]. S is Ref. [154]. T is Ref. [155]. The thermal noise limited angular random walk of our proposed devices are shown as red stars. The regions for rate, tactical, and inertial grade gyroscopes are taken from Ref. [79].

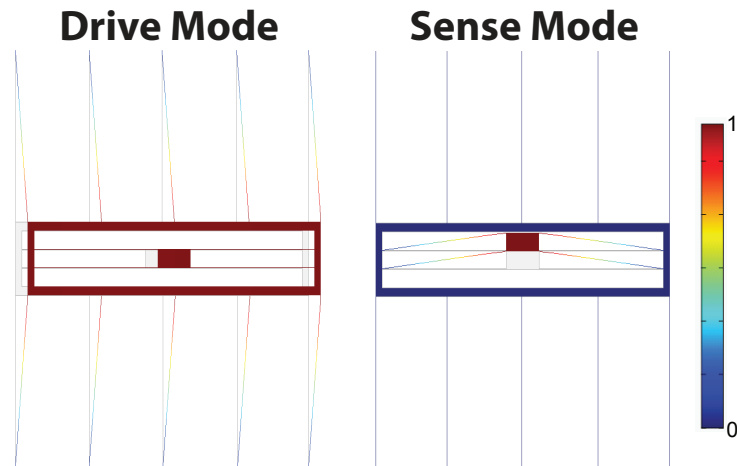


Figure 6.3: **Comsol Simulation of Drive and Sense Modes.** Comsol eigenmode mechanical simulation illustrating both the sense and drive modes of the example gyroscope structure. Color indicates displacement with blue indicating zero and red indicating 1 on a normalized scale.

it from contracting and releasing its stress. Comsol mechanical simulations illustrating these results are shown in Fig. 6.4.

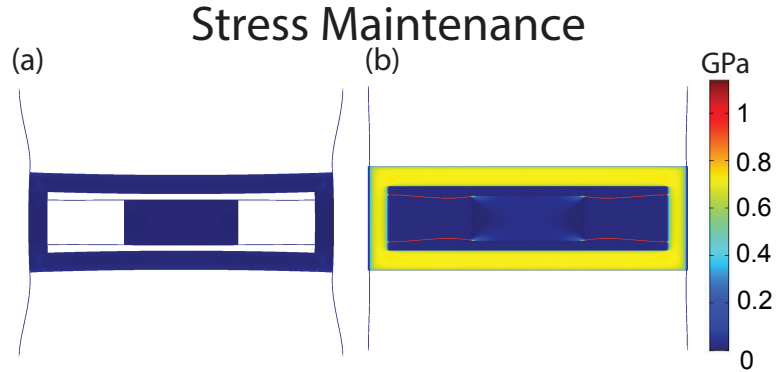


Figure 6.4: **Consol Simulation Stress in Gyro Designs.** This is a plot of the x-axis (along the length of the sense tethers) stress in the example gyroscope structure using Consol. (a) The case of no silicon on the backside of frame. All of the stress in the nitride film is released, including, most importantly, in the sense mode tethers. (b) In this case, $\sim 200 \mu\text{m}$ of Silicon is left attached to the underside of the frame. The frame is unable to contract to release its tension, and the sense mode tethers maintain their $\sim 1 \text{ GPa}$ stress.

The way to design the gyroscope, therefore, is to take the heavy-mass accelerometer (shown in Fig. 5.22 and discussed in Section 5.5) and add the accelerometer from Chapter 4 to the center of the large test mass and add electrostatic driving capacitors. Optical microscope images of a fabricated prototype of an optomechanical gyroscope is shown in Fig. 6.5. As can be seen by comparing Fig. 6.5 to Fig. 5.22, the structures are qualitatively similar with the device in Fig. 6.5 having some added features. The large rectangle in the center of the image is the “frame” and it is fully suspended by thousands of nanostring drive mode support tethers. There is a large gap opened up in the middle of the support tethers where an optical cavity is made. One of the zipper optical beams is placed on a support tether and the other is connected to a rigid platform protruding from the bulk (see Fig. 6.5c). The optical cavity is end-coupled to on-chip optical waveguide with adiabatic coupler (see Section 2.2). This is called the drive mode optical cavity and is simply used to characterize and monitor the drive mode motion.

In the center of the frame is the sense mechanics, comprised of an accelerometer of the same mechanical design as that studied in Chapter 4 and shown in Fig. 4.3. One side of the zipper optical cavity is connected to the sense mode test mass (see Fig. 6.5d), the rigid side of the cavity is connected to the frame by its own nanostring tether, and laser light is side-coupled (see Section 2.2) into the optical cavity using an on-chip waveguide. Crucially, the light in this waveguide must make it out of the frame. This can be done with a dimpled, tapered optical fiber, but, as already discussed (see Section 5.1), this is far from ideal for a practical sensor. Therefore, we showed, as of proof of principle, that a gap can be opened in the frame, which allows the coupling waveguide to pass through and connect to the bulk. In more advanced designs, this coupling waveguide could be used in a V-groove coupling scheme as in Section 5.1. In the device shown in Fig. 6.5, we are only

concerned with the proof of principle and the coupling waveguide has an adiabatic coupler region shortly after exiting the frame, upon which a dimpled, tapered fiber is set. The main idea of this waveguide is to couple light into the sense mode optical cavity without disturbing or sensing the drive motion.

Fabricating these devices requires 4 lithography steps (3 electron and 1 optical). The nanofabrication process flow is a straightforward combination of the metalization process flow shown in Fig. 5.6 and Section 5.2.2 and the double-sided lithography process flow shown in Fig. 2.17 and Section 2.4.1. First the metal pattern is written, chrome-gold layer evaporated, and then the topside gyro pattern aligned to the gold pattern and written following steps (a)-(i) of Fig. 5.6. The topside gyro pattern contains alignment marks to align the backside pattern and, utilizing these, steps (e)-(l) are carried out from Fig. 2.17. The end result is the device in Fig. 6.5.

The most important fundamental properties of the gyroscope will be the mechanical quality factors of the sense and drive modes. As shown in Eq. (6.3), Q_{sense} sets the thermal noise resolution, and Q_{drive} will set the amplitude of the drive mode when the device is driven on resonance. Therefore, it is important to characterize these devices by measuring their mechanical quality factors. The mechanical quality factor of the drive mode in vacuum of a device similar to that shown in Fig. 6.5 was found to be $Q_{\text{drive}} = 70,000$, consistent with the Q-factor of the heavy mass accelerometer in vacuum (see Section 5.5.2), which is obviously what one would expect. The mechanical quality factor of the sense mode in vacuum of a device similar to that shown in Fig. 6.5 was found to be $Q_{\text{sense}} = 3.7 \times 10^6$. This data is shown in Fig. 6.6.

Electrostatic actuation of drive mode is accomplished using interdigitated capacitors on one side of the frame (see Fig. 6.5a-b). Interdigitated capacitors are necessary as opposed to parallel wire capacitors (as discussed in Section 5.2.1) because of the large amplitude of motion desired. For $1 \mu\text{m}$ motion, a parallel plate capacitor would need a gap of $3 \mu\text{m}$ to avoid stiction, which makes its applied force relatively tiny. Interdigitated capacitors capitalize on small gaps between the fingers (here designed to be 300 nm). The capacitance and applied force for an interdigitated capacitor are given below (assuming, for simplicity, parallel plate capacitance between the wires).

$$C_{id} = \frac{2(L-x)\epsilon_0 t}{d} N \quad (6.4)$$

$$F_{id} = \frac{1}{2} V_a^2 \frac{2\epsilon_0 t}{d} N \quad (6.5)$$

In Eqs. (6.4) and (6.5), t is the thickness of the wires, N is the number of interdigitations, V_a is the applied voltage, and the rest of the geometry is shown in Fig. 6.7. For our device geometry, F_{id} is predicted to be approximately 25 times greater than that for a parallel wire capacitor with a gap of $3 \mu\text{m}$. Using the mechanical susceptibility from Eq. (1.34), and interdigitated capacitor force from

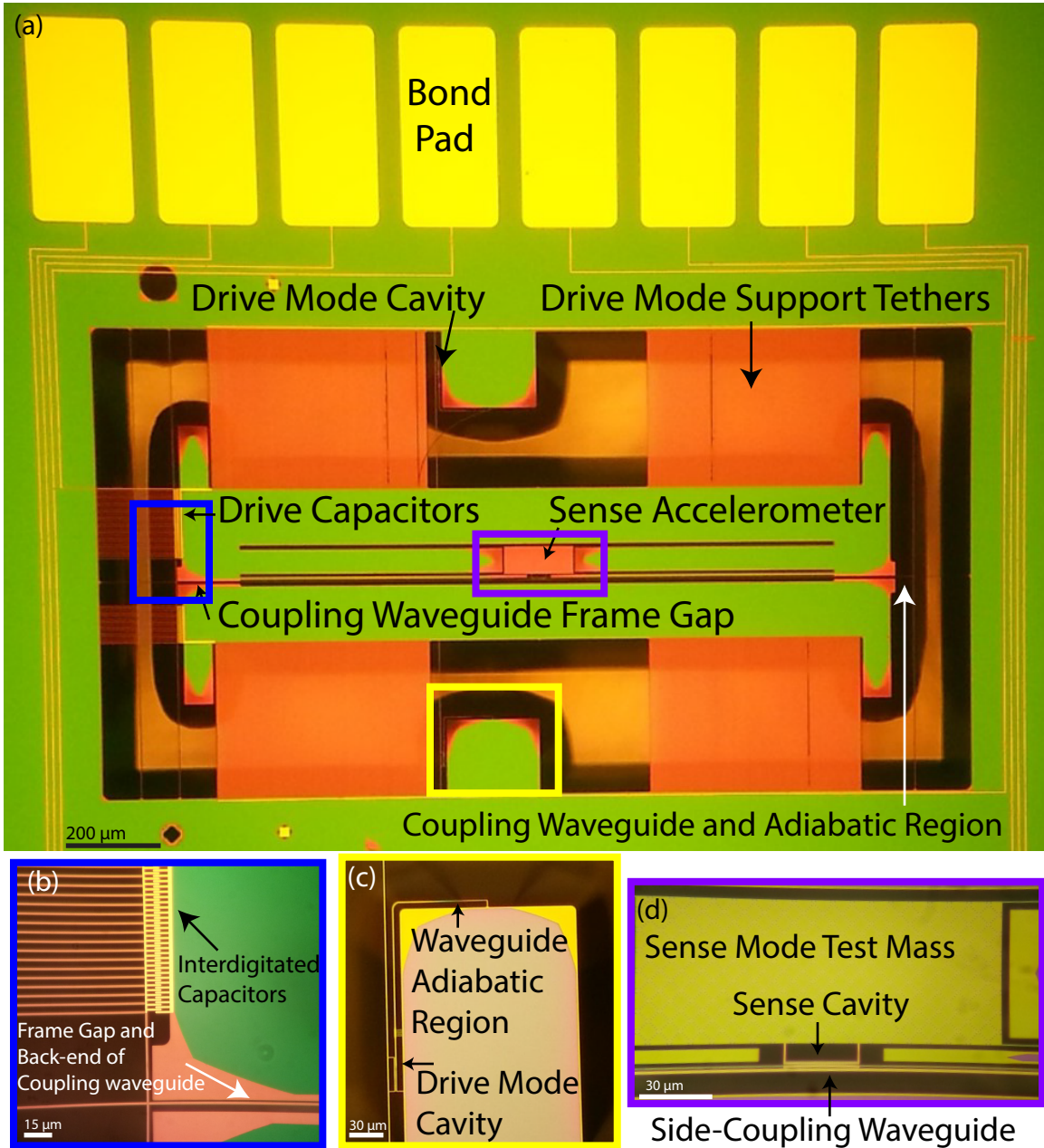


Figure 6.5: **Prototype Optomechanical Gyroscope.** These are a series of annotated optical microscope images of a prototype optomechanical gyroscope device. It is qualitatively similar to the heavy-mass accelerometer shown in Fig. 5.22 with some additional features. (a) Shows an overview of one whole gyroscope device complete with bond pads (only 2 bond pads are used for this devices, the remaining are for other devices on the chip). (b) This image shows a zoom-in of the interdigitated capacitor region and the gap in the frame for the coupling waveguide. (c) Zoom-in of of the drive mode optical cavity, showing the optical cavity and its coupling waveguide. (d) Zoom-in of the sense mode test mass with its associated optical cavity and the coupling waveguide.

Eq. (6.5), we can obtain the expected drive amplitude, A .

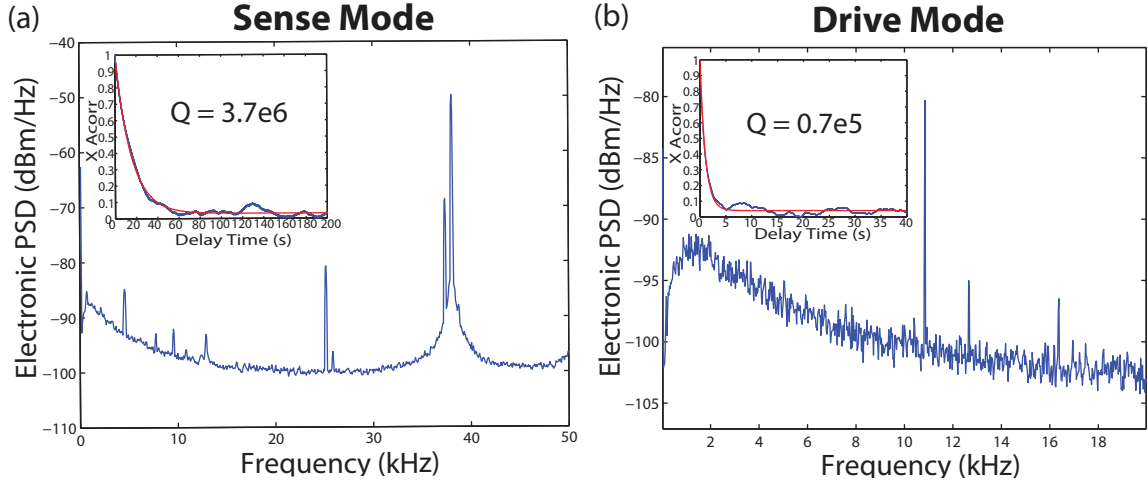


Figure 6.6: **Measured Drive and Sense Mode Quality Factors.** (a) Electronic power spectral density of laser light reflected from the sense optical mode. The sense mode is the best transduced feature at approximately 38 kHz. inset: autocorrelation of the sense mode amplitude signal, showing $Q_{\text{sense}} = 3.7 \times 10^6$. (b) Electronic power spectral density of laser light reflected from the drive optical mode. The drive mode is the best transduced feature at approximately 11 kHz. inset: autocorrelation of the drive mode amplitude signal, showing $Q_{\text{drive}} = 70,000$. The specific devices used to obtain this data were similar to the device shown in Fig. 6.5, but did not have the metallized capacitors nor the backside frame tethers. Neither of these should significantly affect the mechanical quality factors.

$$A = \frac{1}{2} V_a^2 \frac{2\epsilon_0 t}{d} N \frac{Q_{\text{drive}}}{m_{\text{frame}} \omega_{\text{drive}}^2} \quad (6.6)$$

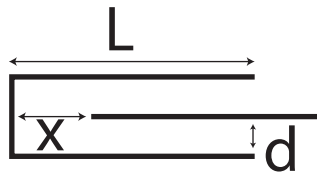


Figure 6.7: **Interdigitated Capacitor Geometry.** This is a parameterized geometry for one section of an interdigitated capacitor. The length of each finger (or digit) is L , the spacing between them in the lateral direction is d , and the distance between the tip of one finger and the back line is x . When a voltage is applied there will be a resulting force along the x -direction.

In Fig. 6.8, we present a calibration of a drive tone applied to the interdigitated capacitors of a device very similar to the one shown in Fig. 6.5 (except without the sense-mode coupling waveguide). The mechanical frequency and quality factor of the drive mode were calibrated in vacuum to be $Q_{\text{drive}} = 21,000$ and $\omega_m = 2\pi \times 11.165$ kHz. The red curve shows the electronic power spectral density of laser light reflected from the drive optical cavity with the capacitive drive off, and hence this is

the thermal noise of the drive mode. The blue curve is the electronic PSD with 1 Volt applied to the interdigitated capacitors at the half-frequency of the drive mechanical mode (because $F_{id} \sim V_a^2$, one must drive at the half-frequency). Using Eq. (1.36) to obtain the theoretical value for the mechanical displacement due to thermal noise, and comparing the driven tone height to the measured thermal noise height, allows us to calibrate the driven tone height to be an amplitude of 4 nm. This is comparable to the prediction of Eq. (6.6), $A = 6.8$ nm, using the measured parameters of $V_a = 1$, $t = 200$ nm, $d = 300$ nm, $N = 78$, $Q_{\text{drive}} = 21000$, $m = 290$ nKg, and $\omega_m = 2\pi \times 11.165$ kHz. Unfortunately, we cannot calibrate drive mode amplitudes significantly larger than this because the optical transduction scheme becomes non-linear (mechanical displacements shift the optical cavity frequency by an amount comparable to or greater than its linewidth). However, we can successfully apply 10 Volts to the capacitors and, extrapolating this calibration, this corresponds to a drive amplitude of $0.4 \mu\text{m}$, on the order of the drive amplitudes we were hoping for in Section 6.1.

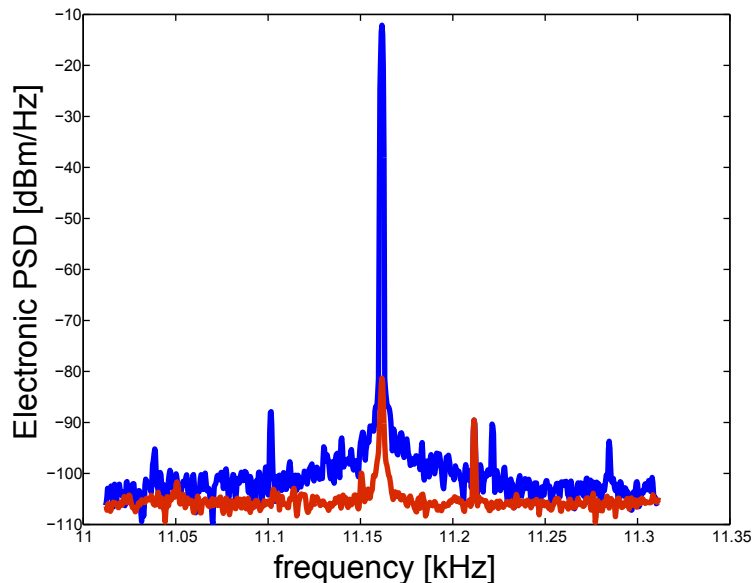


Figure 6.8: **Calibration of Gyroscope Drive Amplitude.** This is a comparison of the electronic power spectral density of laser light reflected from the drive optical mode with the interdigitated capacitor drive on (blue curve) and off (red curve). The capacitors are driven with 1 Volt at the half-frequency of the mechanical mode. By comparing the height of the driven tone (blue) to the thermal noise curve (red) we can calibrate the drive amplitude to be 4 nm.

To conclude this section, we have made progress towards the development of an optomechanical gyroscope. We have measured high mechanical quality factors on both the drive and sense mechanical modes. We have also driven amplitudes in the drive mechanical mode that are approaching the micron level (using an extrapolated calibration) that is necessary for competitive performance. Going forward, fabrication reliability needs to be improved so that all of these capabilities can be found in a single device. Calibration will need to be done to see if cross-talk between the drive mode amplitude

and the sense mode is a problem. Additionally, a test setup capable of applying and calibrating rotations will need to be developed to test the fabricated gyroscopes.

6.3 Vibration Isolation Introduction

The prototype gyroscope discussed in the last section and shown in Fig. 6.5 has the drawback that it is sensitive to linear accelerations as well as rotations. If a vibration (linear acceleration) struck the device along the sense axis, the sense mode would respond and produce an output. This is non-ideal. Ideally, when the gyroscope produces an output near the drive frequency the user should be confident the sensor is measuring a rotation and not a linear acceleration.

This is a well-known problem in micromachined gyroscopes and for an excellent introduction to the design of gyroscopes with vibration immunity see chapter 1 of Ref. [135]. One solution is to use symmetry to cancel out linear accelerations. Dual mass [153] and even quad-mass [154, 156] gyroscopes have been developed, which utilize symmetry between the coupled masses to gain immunity from linear accelerations. The main idea of designs such as these is to engineer a drive mode where the identical masses move completely out-of-phase with one another. Then the coriolis force on each mass will be of equal magnitude, but opposite direction, thus driving the out-of-phase sense mode. Linear accelerations, on the other hand, will force the identical masses in the same direction. This allows one to distinguish between linear acceleration and rotations by designing your sense electrodes to reject common motion and sense differential motion. Another solution to vibration sensitivity is a degenerate mode disk gyroscope (see Ref. [152] for an example). Here two ideally degenerate internal flexural modes of a disk are used as the drive and sense modes. Since these modes have zero net momentum, they can not be excited by linear accelerations.

The provided examples [152–154] are certainly highly impressive. However, the dual mass and quad mass designs Refs. [153, 154, 156] have considerable design complexity, the need for very precise and robust nanofabrication so that the masses are as close to identical as possible, and control electronics to counter fabrication imperfections for optimal performance. The disk gyroscope [152] is elegant even if it does have small drive mode displacements given the high frequencies of the mechanical mode. Additionally, the design does not work well with our silicon nitride structures because all of the stress (and the benefits it provides) is released in such designs.

An alternative to defeating linear acceleration sensitivity with symmetry is to implement passive low-pass mechanical filters (a.k.a. vibration isolation stages) to prevent vibrations and linear acceleration from reaching your device. These techniques are known to the gyroscope community and a good introduction is provided by chapter 3 of Ref. [157]. A prominent example of a passive vibration isolation stage in the literature is a vacuum packaging system complete with isolation suspensions and an isolation platform to which the MEMS device is bonded [158–160]. Another example is a

chip-scale vibration isolation platform that is fabricated separately from the sensor and to which the sensor is later bonded [161]. These results, while certainly impressive, add a great deal of complexity to the fabrication and design process. We sought a simple solution to vibration isolation that would require no additional fabrication steps or processes.

This can be achieved by connecting the gyroscope to another frame that has a low resonance frequency (100's of Hz to a few kHz). This can be viewed as a continuation of the structure we've already shown in Fig. 6.5. Just as the inner accelerometer is connected to the frame which is also suspended, we can suspend this entire gyro structure on yet another frame with a low resonance frequency that will damp out high-frequency vibrations. This method requires no extra fabrication steps or techniques and is trivial to incorporate into our existing fabrication methods. We will discuss the design in much more detail, but first we will describe the working principle of this passive mechanical isolation scheme.

6.3.1 Passive Mechanical Isolation Working Principle

Prima facie, this passive mechanical isolation scheme may seem counter-intuitive, as in, we will reduce our signal as much as our noise and thereby gain nothing. The key point to remember is that signals in a vibratory gyroscope will be mixed up to the drive frequency, as dictated by Eq. (6.2). For example, a constant rotation will appear at the drive frequency. What becomes important, therefore, is our confidence that output signal from the gyroscope in some specified bandwidth around the drive frequency is due to rotations and not linear accelerations. Thus, we can design a low-pass passive mechanical filter that allows our low-frequency signals to pass through, and greatly damps linear vibrations at/near the drive frequency.

This is simply accomplished by attaching our gyroscope to a mechanical structure with a low frequency resonance (say around 1 kHz). Vibrations much below 1 kHz will pass unfettered, while vibrations much above 1 kHz will be attenuated because the low frequency mechanical resonance will not be able to significantly respond at those frequencies. To be more exact, we can write down a mathematical model for this vibration isolation. Suppose we shake the entire chip with some amplitude, x_{chip} , and at a variable frequency, ω . The motion of the low frequency mechanical resonance, hereafter called the frame, relative to the chip, $x_{\text{frame,rel}}$, is simply given by the following.

$$x_{\text{frame,rel}} = x_{\text{chip}}\omega^2\chi(\omega) \quad (6.7)$$

In Eq. (6.7), $\chi(\omega)$ is the mechanical susceptibility to accelerations as first defined in Eq. (1.34). Therefore, the absolute motion of the frame, x_{frame} , is given by the following.

$$|x_{\text{frame}}| = |x_{\text{chip}} + x_{\text{chip}}\omega^2\chi(\omega)| \quad (6.8)$$

$$\left| \frac{x_{\text{frame}}}{x_{\text{chip}}} \right| = |1 + \omega^2\chi(\omega)| \quad (6.9)$$

Eq. (6.9) is plotted in Fig. 6.9 using two different frame resonators both with $\omega_m = 2\pi \times 500$ Hz and one with $Q_m = 5000$ (solid red curve) and the other with $Q_m = 10$ (dashed blue curve). For both resonators, $|x_{\text{frame}}/x_{\text{chip}}| = 1$ for frequencies below the resonance frequency of the frame. As one can see in Fig. 6.9, for frequencies above the frequency of the frame, $|x_{\text{frame}}/x_{\text{chip}}|$ falls off like $(\omega/\omega_m)^{-2}$ (as long as the Q_m is reasonably high, for low Q_m the suppression is not as large). That is, $|x_{\text{frame}}/x_{\text{chip}}| = 10^{-2}$ for $\omega/\omega_m = 10$ and $|x_{\text{frame}}/x_{\text{chip}}| = 10^{-4}$ for $\omega/\omega_m = 100$ (for the case that $Q_m \gtrsim 5000$). In this way, incoming vibrations at low frequency are allowed to pass while those at high frequency are greatly suppressed. This is the type of behavior we expect to observe in the next section.

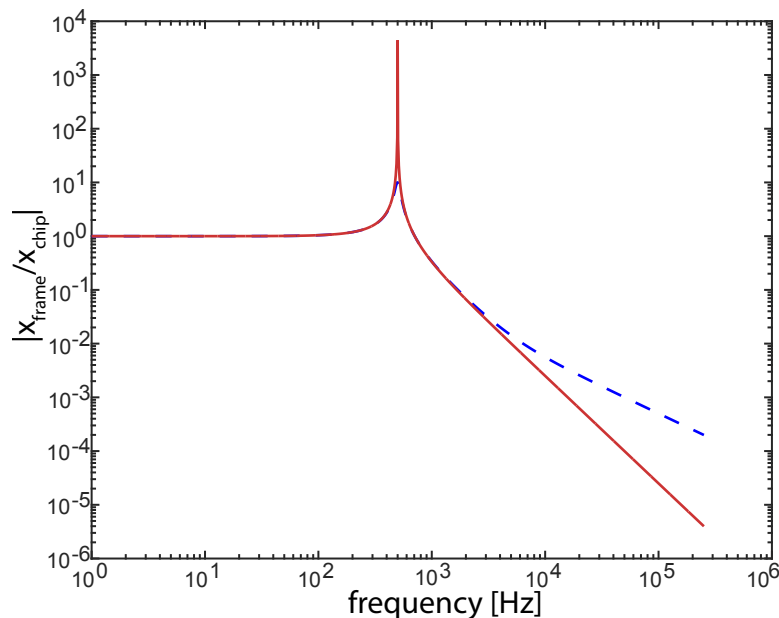


Figure 6.9: **Passive Mechanical Isolation Theory.** This is a plot of Eq. (6.9) for the case of $\omega_m = 2\pi \times 500$ Hz and $Q_m = 5000$ (solid red curve) and $Q_m = 10$ (dashed blue curve).

6.3.2 Frame Isolation Results

The device used for passive mechanical isolation using concatenated frames surrounding the sensor is shown in an optical image in Fig. 6.10. A more basic schematic of the device is shown in Fig. 6.11. In these images, a gyroscope very similar to the one shown in Fig. 6.5, instead of being mounted to

the bulk of the chip, is mounted to a frame. This frame is suspended by the same nanostring tethers as the gyroscope drive mode, there's just far fewer of them (10's or 100's of tethers instead of 1000's for the gyroscope drive mode). This gives the first frame a low frequency, fundamental in-plane mechanical resonance in the drive direction. This first frame is mounted to a second frame that is suspended by nanostring tethers in the orthogonal direction. This gives the second frame a low frequency, mechanical resonance in the sense mode direction. Combined, these two frames should provide isolation from linear accelerations in both the x and y directions. These frames should also provide attenuation for z-axis vibrations because the frames also have fundamental out-of-plane mechanical modes at nearly degenerate frequencies to the fundamental in-plane mode (as seen first in Fig. 4.6), although this will not be tested. These devices are fabricated using the exact same double-sided lithography methods used previously in this thesis (see Fig. 2.17).

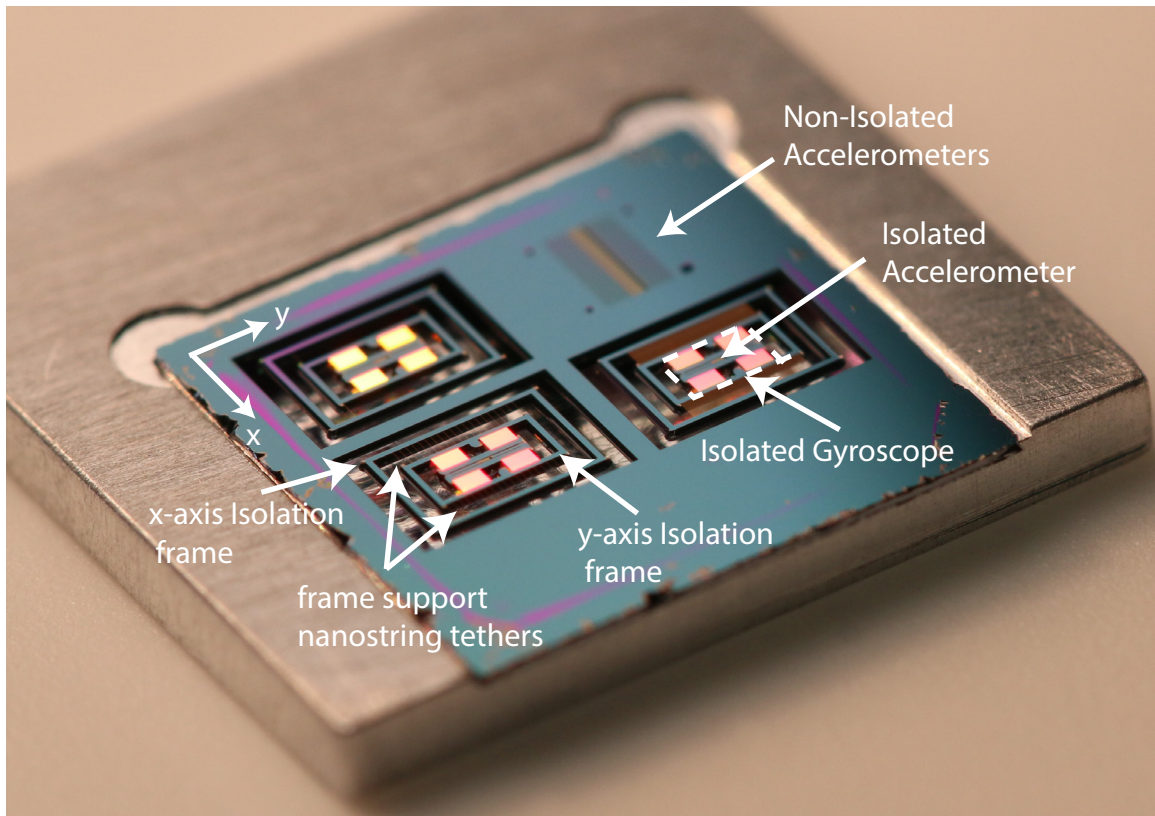


Figure 6.10: **Vibration Isolation Device Optical Image.** This is an annotated image showing the frame structures for vibration isolation. The gyroscope and accelerometer are located at the center of each set of nested frames. The first frame (moving outwards from the center) is suspended such that it suppresses vibration in the drive-mode direction and vice-versa for the second frame. In the upper right-hand corner there is a field of non-isolated accelerometers, used for calibration.

In order to confirm that the frames do indeed provide vibration isolation, we subjected the chip to shaker table tests (the shaker table was first described in Fig. 4.4). Included on the chip was a

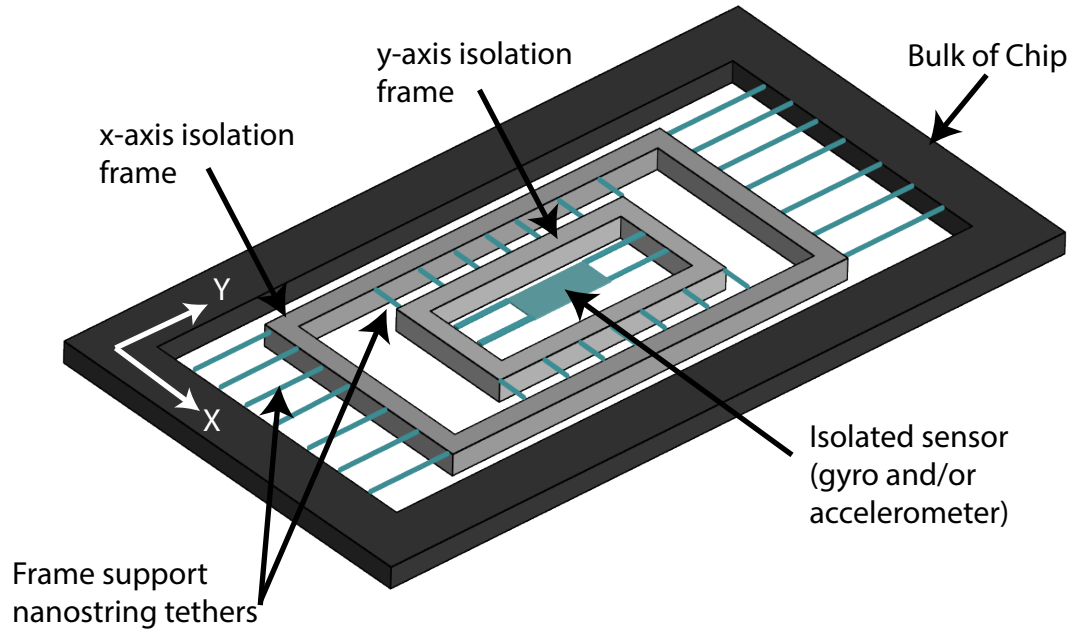


Figure 6.11: **Vibration Isolation Device Schematic.** This is a simplified schematic version of Fig. 6.10. At the center of the nested frames we did not draw the full gyroscope structure, but a simple sensor for clarity.

field of non-isolated accelerometers (see Fig. 6.10), which were used as a baseline. Accelerations were applied to the chip, observed by the optomechanical accelerometer, and compared to the intrinsic thermal noise of the fundamental in-plane mechanical mode. These shaker tests were repeated with two of the isolated accelerometers, again comparing the transduced tone to the intrinsic thermal noise for an absolute calibration. Light was coupled into the structures using the dimpled, tapered optical fiber and on-chip adiabatic waveguide couplers. The data is presented in Fig. 6.12.

Fig. 6.12a shows the results of shaking the non-isolated accelerometers, Fig. 6.12b shows data for shaking an accelerometer isolated by a set of x-y frame isolators each with 180 nanotethers on a side, and Fig. 6.12c shows data for shaking an accelerometer isolated by a set of x-y frame isolators each with 19 nanotethers on a side. It must be noted that that the applied acceleration tones in Fig. 6.12 have been normalized such that they all correspond to the same voltage applied to shear piezo. This was done to allow the reader to easily observe the diminishing tone heights with increased isolation. In practice, the non-isolated accelerometers must be shaken with much smaller amplitudes than the isolated accelerometers, or else transduction will become non-linear. The intrinsic thermal noise for each device is plotted in red in Fig. 6.12. The intrinsic mechanical quality factors of each device were within 10% of 3×10^6 , and the shake measurements were taken at optical powers where optomechanical back-action was insignificant. By comparing each applied acceleration tone (blue) to the intrinsic thermal noise of each device (red) we obtain the inferred

acceleration for each device. Then we compare each device to the bare (non-isolated) accelerometer to obtain the amount of vibration isolation. For the frame isolation device in Fig. 6.12b, with 180 nanotethers on each side of the frames, the average vibration suppression is 22 dB. For the frame isolation device in Fig. 6.12c, with 19 nanotethers on each side of the frames, the average vibration suppression is 32 dB. This implies a corresponding fundamental in-plane mechanical mode of approximately 3.1 kHz and 950 Hz, respectively.

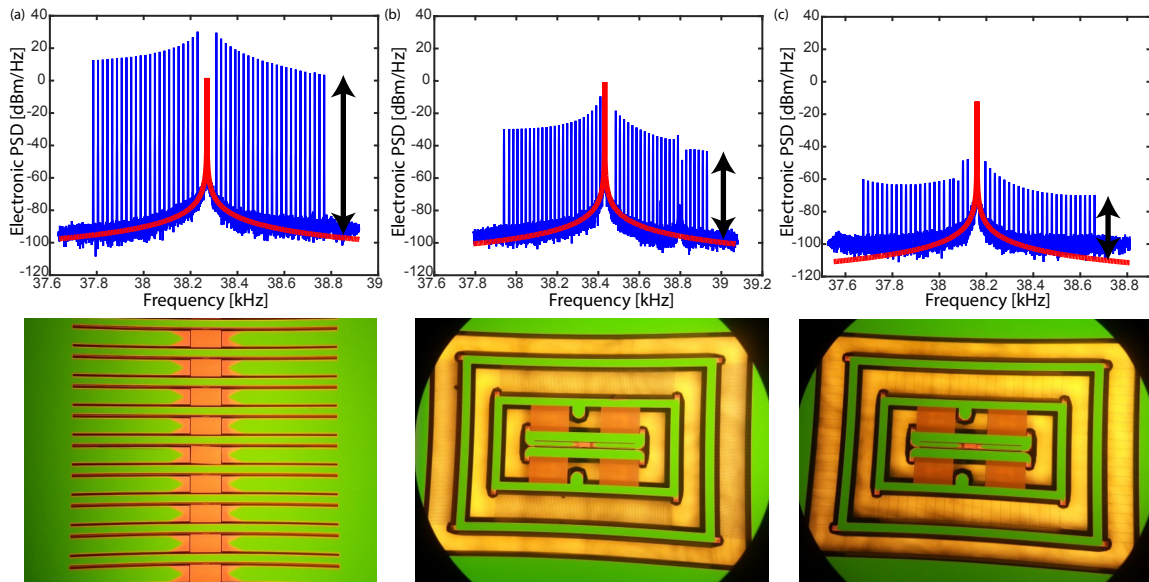


Figure 6.12: **Vibration Isolation Results.** (a) shows the electronic power spectral density of light reflected from a non-isolated accelerometer’s optical resonance. The blue spikes are accelerations due to applying a tone at that frequency to the shaker table. Their heights have been normalized to correspond to the drive strengths used for the isolated device in (c). Absolute acceleration calibration is obtained by comparing the blue tone heights to the fitted intrinsic thermal noise of the device. Below the plot is an optical microscope image of example non-isolated optomechanical accelerometers. (b) same as (a) except the internal accelerometer is isolated from the environment using a set of x-y isolator frames each suspended by 180 nanotethers on a side. (c) same as (b) except the device now has frames suspended by 19 nanotethers on a side.

6.4 Conclusions

In this chapter we have developed several of the pieces needed to demonstrate an optomechanical gyroscope. That is, high mechanical quality factors on both the drive and sense modes, reasonable drive amplitudes for improved resolution, and a simple method to isolate our devices from unwanted linear accelerations. If the demonstrated vibration isolation is insufficient for a given application, the results can, in theory, be significantly improved by chaining on additional isolation frames. Such vibration isolation may be useful for a wide range of practical sensors, including improving cross-axis sensitivity in accelerometers.

Appendix A

Mathematical Definitions

At several points in this thesis we make use of the mathematical operation called the Fourier transform. The Fourier transform of some integrable function of time, $f(t)$, is denoted by, $f[\omega]$, and is defined below. We also provide the definition of the inverse Fourier transform which takes us from $f[\omega]$ to $f(t)$.

$$f[\omega] = \int_{-\infty}^{\infty} f(t) e^{-i\omega t} dt \quad (\text{A.1})$$

$$f(t) = \int_{-\infty}^{\infty} f[\omega] e^{-i\omega t} \frac{d\omega}{2\pi} \quad (\text{A.2})$$

A simple consequence of this definition is that the Fourier transform of derivatives of $f(t)$, $\frac{d^n f(t)}{dt^n}$, are simply given by, $(i\omega)^n f[\omega]$. This property means that certain differential equations turn into easier algebraic equations under Fourier transform. We have used this property several times in this thesis.

We also use the power spectral density repeatedly throughout the text. It tells us how the power of signal is distributed in frequency space. In the case where there is no physical power associated with the signal, we simply mean the square of the signal. For a signal $x(t)$, the power spectral density is denoted $S_{xx}(\omega)$ and defined below.

$$S_{xx}(\omega) = \int_{-\infty}^{\infty} \langle x(t) x^*(t + \tau) \rangle e^{-i\omega\tau} d\tau \quad (\text{A.3})$$

That is, it is the Fourier transform of the autocorrelation of $x(t)$. If $x(t)$ is real, then $S_{xx}(\omega)$ is even, and we can use the simplified single-sided power spectral density, as defined below.

$$S_{xx}(\omega) = 2 \int_0^{\infty} \langle x(t) x^*(t + \tau) \rangle e^{-i\omega\tau} d\tau \quad (\text{A.4})$$

In this thesis, we almost exclusively use the single-sided power spectral density.

Appendix B

Publications

1. A. G. Krause, T. D. Blasius, and O. Painter, “Optical feedback cooling of a photonic crystal optomechanical resonator,” *arXiv:1506.01249 [physics, physics:quant-ph]*. (2015)
2. A. G. Krause, M. Winger, T. D. Blasius, Q. Lin, and O. Painter, “A high-resolution microchip optomechanical accelerometer,” *Nature Photonics* **6**, 768–772 (2012).
3. M. Winger, T. D. Blasius, T. P. Mayer Alegre, A. H. Safavi-Naeini, S. Meenehan, J. Cohen, S. Stobbe, and O. Painter, “A chip-scale integrated cavity-electro-optomechanics platform,” *Optics Express* **19**, 24905 (2011).

Bibliography

- [1] M. Eichenfield, R. Camacho, J. Chan, K. J. Vahala, and O. Painter, “A picogram- and nanometre-scale photonic-crystal optomechanical cavity,” *Nature* **459**, 550–555 (2009).
- [2] A. G. Krause, T. D. Blasius, and O. Painter, “Optical read out and feedback cooling of a nanostring optomechanical cavity,” *arXiv:1506.01249 [physics, physics:quant-ph]* (2015).
- [3] J. Chan, T. P. M. Alegre, A. H. Safavi-Naeini, J. T. Hill, A. Krause, S. Grblacher, M. Aspelmeyer, and O. Painter, “Laser cooling of a nanomechanical oscillator into its quantum ground state,” *Nature* **478**, 89–92 (2011).
- [4] J. D. Teufel, T. Donner, D. Li, J. W. Harlow, M. S. Allman, K. Cicak, A. J. Sirois, J. D. Whittaker, K. W. Lehnert, and R. W. Simmonds, “Sideband cooling of micromechanical motion to the quantum ground state,” *Nature* **475**, 359–363 (2011).
- [5] K. Srinivasan, *Semiconductor optical microcavities for chip-based cavity QED*, phd, California Institute of Technology (2006).
- [6] H.-A. Bachor and C. T. Ralph, *A Guide to Experiments in Quantum Optics* (Wiley-VCH, Weinheim, 2004), 2nd edition.
- [7] S. Grblacher, *Quantum opto-mechanics with micromirrors*, phd, University of Vienna (2010).
- [8] A. G. White, *Classical and quantum dynamics of optical frequency conversion*, phd, Australian National University (1997).
- [9] A. A. Clerk, M. H. Devoret, S. M. Girvin, F. Marquardt, and R. J. Schoelkopf, “Introduction to quantum noise, measurement, and amplification,” *Reviews of Modern Physics* **82**, 1155–1208 (2010).
- [10] T. J. Kippenberg and K. J. Vahala, “Cavity Opto-Mechanics,” *Optics Express* **15**, 17172–17205 (2007).
- [11] J. D. Teufel, T. Donner, M. A. Castellanos-Beltran, J. W. Harlow, and K. W. Lehnert, “Nanomechanical motion measured with an imprecision below that at the standard quantum limit,” *Nature Nanotechnology* **4**, 820–823 (2009).

- [12] J. D. Cohen, S. M. Meenehan, and O. Painter, “Optical coupling to nanoscale optomechanical cavities for near quantum-limited motion transduction,” *Optics Express* **21**, 11227–11236 (2013).
- [13] J. D. Joannopoulos, S. G. Johnson, J. N. Winn, and R. D. Meade, *Photonic Crystals: Molding the Flow of Light* (Princeton University Press, 2008), 2nd edition.
- [14] “COMSOL Multiphysics,” .
<http://www.comsol.com/products/multiphysics/>
- [15] S. G. Johnson, “MIT Photonic-Bands,” .
http://ab-initio.mit.edu/wiki/index.php/MIT_Photonic_Bands
- [16] J. Chan, M. Eichenfield, R. Camacho, and O. Painter, “Optical and mechanical design of a zipper photonic crystal optomechanical cavity,” *Optics Express* **17**, 3802 (2009).
- [17] J. Chan, *Laser cooling of an optomechanical crystal resonator to its quantum ground state of motion*, phd, California Institute of Technology (2012).
- [18] M. Eichenfield, J. Chan, R. M. Camacho, K. J. Vahala, and O. Painter, “Optomechanical crystals,” *Nature* **462**, 78–82 (2009).
- [19] S. G. Johnson, M. Ibanescu, M. A. Skorobogatiy, O. Weisberg, J. D. Joannopoulos, and Y. Fink, “Perturbation theory for Maxwell’s equations with shifting material boundaries,” *Physical Review E* **65**, 066611 (2002).
- [20] J. Chan, A. H. Safavi-Naeini, J. T. Hill, S. Meenehan, and O. Painter, “Optimized optomechanical crystal cavity with acoustic radiation shield,” *Applied Physics Letters* **101**, 081115 (2012).
- [21] C. P. Michael, M. Borselli, T. J. Johnson, C. Chrystal, and O. Painter, “An optical fiber-taper probe for wafer-scale microphotonic device characterization,” *Optics Express* **15**, 4745 (2007).
- [22] S. Groblacher, J. T. Hill, A. H. Safavi-Naeini, J. Chan, and O. Painter, “Highly efficient coupling from an optical fiber to a nanoscale silicon optomechanical cavity,” *Applied Physics Letters* **103**, 181104 (2013).
- [23] S. S. Verbridge, J. M. Parpia, R. B. Reichenbach, L. M. Bellan, and H. G. Craighead, “High quality factor resonance at room temperature with nanostrings under high tensile stress,” *Journal of Applied Physics* **99**, 124304 (2006).
- [24] D. R. Southworth, R. A. Barton, S. S. Verbridge, B. Ilic, A. D. Fefferman, H. G. Craighead, and J. M. Parpia, “Stress and Silicon Nitride: A Crack in the Universal Dissipation of Glasses,” *Physical Review Letters* **102**, 225503 (2009).

- [25] Q. P. Unterreithmeier, T. Faust, and J. P. Kotthaus, “Damping of Nanomechanical Resonators,” *Physical Review Letters* **105**, 027205 (2010).
- [26] T. Faust, J. Rieger, M. J. Seitner, J. P. Kotthaus, and E. M. Weig, “Signatures of two-level defects in the temperature-dependent damping of nanomechanical silicon nitride resonators,” *Physical Review B* **89**, 100102 (2014).
- [27] S. Schmid, K. D. Jensen, K. H. Nielsen, and A. Boisen, “Damping mechanisms in high- Q micro and nanomechanical string resonators,” *Physical Review B* **84**, 165307 (2011).
- [28] A. G. Noskov, E. B. Gorokhov, G. A. Sokolova, E. M. Trukhanov, and S. I. Stenin, “Correlation between stress and structure in chemically vapour deposited silicon nitride films,” *Thin Solid Films* **162**, 129–143 (1988).
- [29] M. D. Henry, *ICP etching of silicon for micro and nanoscale devices*, phd, California Institute of Technology (2010).
- [30] H. Rhee, H. Kwon, C.-K. Kim, H. Kim, J. Yoo, and Y. W. Kim, “Comparison of deep silicon etching using SF₆/C₄F₈ and SF₆/C₄F₆ plasmas in the Bosch process,” *Journal of Vacuum Science & Technology B* **26**, 576–581 (2008).
- [31] J. T. Hill, *Nonlinear optics and wavelength translation via cavity-optomechanics*, phd, California Institute of Technology (2013).
- [32] R. P. Donovan, *Contamination-Free Manufacturing for Semiconductors and Other Precision Products* (CRC Press, 2001).
- [33] B. Ashe, C. Giacomini, G. Myhre, and A. W. Schmid, “Optimizing a cleaning process for multilayer dielectric (MLD) diffraction gratings,” *Proc. SPIE 6720, Laser-Induced Damage in Optical Materials* (2007).
- [34] K. Bean and K. Bean, “Anisotropic etching of silicon,” *IEEE Transactions on Electron Devices* **25**, 1185–1193 (1978).
- [35] H. Seidel, L. Csepregi, A. Heuberger, and H. Baumgrtel, “Anisotropic Etching of Crystalline Silicon in Alkaline Solutions I. Orientation Dependence and Behavior of Passivation Layers,” *Journal of The Electrochemical Society* **137**, 3612–3626 (1990).
- [36] R. Hull, *Properties of Crystalline Silicon* (IET, 1999).
- [37] D. L. Kendall, “A new theory for the anisotropic etching of silicon and some underdeveloped chemical micromachining concepts,” *Journal of Vacuum Science & Technology A* **8**, 3598–3605 (1990).

- [38] R. A. Norte, *Nanofabrication for On-Chip Optical Levitation, Atom-Trapping, and Superconducting Quantum Circuits*, phd, California Institute of Technology (2015).
- [39] Inductiveload, “Wikipedia,” https://commons.wikimedia.org/wiki/File:Anisotropic_wet_etching.svg.
- [40] C. Monroe, D. M. Meekhof, B. E. King, S. R. Jefferts, W. M. Itano, D. J. Wineland, and P. Gould, “Resolved-Sideband Raman Cooling of a Bound Atom to the 3D Zero-Point Energy,” *Physical Review Letters* **75**, 4011–4014 (1995).
- [41] S. Mancini, D. Vitali, and P. Tombesi, “Optomechanical Cooling of a Macroscopic Oscillator by Homodyne Feedback,” *Physical Review Letters* **80**, 688–691 (1998).
- [42] C. Genes, D. Vitali, P. Tombesi, S. Gigan, and M. Aspelmeyer, “Ground-state cooling of a micromechanical oscillator: Comparing cold damping and cavity-assisted cooling schemes,” *Physical Review A* **77**, 033804 (2008).
- [43] J.-M. Courty, A. Heidmann, and M. Pinard, “Quantum limits of cold damping with optomechanical coupling,” *The European Physical Journal D - Atomic, Molecular, Optical and Plasma Physics* **17**, 399–408 (2001).
- [44] P. F. Cohadon, A. Heidmann, and M. Pinard, “Cooling of a Mirror by Radiation Pressure,” *Physical Review Letters* **83**, 3174–3177 (1999).
- [45] D. Kleckner and D. Bouwmeester, “Sub-kelvin optical cooling of a micromechanical resonator,” *Nature* **444**, 75–78 (2006).
- [46] T. Li, S. Kheifets, and M. G. Raizen, “Millikelvin cooling of an optically trapped microsphere in vacuum,” *Nature Physics* **7**, 527–530 (2011).
- [47] J. Gieseler, B. Deutsch, R. Quidant, and L. Novotny, “Subkelvin Parametric Feedback Cooling of a Laser-Trapped Nanoparticle,” *Physical Review Letters* **109**, 103603 (2012).
- [48] B. Abbott et al., “Observation of a kilogram-scale oscillator near its quantum ground state,” *New Journal of Physics* **11**, 073032 (2009).
- [49] D. J. Wilson, *Cavity optomechanics with high-stress silicon nitride films*, phd, California Institute of Technology (2012).
- [50] T. Corbitt, C. Wipf, T. Bodiya, D. Ottaway, D. Sigg, N. Smith, S. Whitcomb, and N. Mavalvala, “Optical Dilution and Feedback Cooling of a Gram-Scale Oscillator to 6.9 mK,” *Physical Review Letters* **99**, 160801 (2007).

- [51] M. Poggio, C. L. Degen, H. J. Mamin, and D. Rugar, “Feedback Cooling of a Cantilever’s Fundamental Mode below 5 mK,” *Physical Review Letters* **99**, 017201 (2007).
- [52] P. Bushev, D. Rotter, A. Wilson, F. Dubin, C. Becher, J. Eschner, R. Blatt, V. Steixner, P. Rabl, and P. Zoller, “Feedback Cooling of a Single Trapped Ion,” *Physical Review Letters* **96**, 043003 (2006).
- [53] D. J. Wilson, V. Sudhir, N. Piro, R. Schilling, A. Ghadimi, and T. J. Kippenberg, “Measurement-based control of a mechanical oscillator at its thermal decoherence rate,” *Nature* **524**, 325–329 (2015).
- [54] A. H. Safavi-Naeini, S. Grblacher, J. T. Hill, J. Chan, M. Aspelmeyer, and O. Painter, “Squeezed light from a silicon micromechanical resonator,” *Nature* **500**, 185–189 (2013).
- [55] T. P. Purdy, R. W. Peterson, and C. A. Regal, “Observation of Radiation Pressure Shot Noise on a Macroscopic Object,” *Science* **339**, 801–804 (2013).
- [56] R. Zhang, C. Ti, M. I. Davano, Y. Ren, V. Aksyuk, Y. Liu, and K. Srinivasan, “Integrated tuning fork nanocavity optomechanical transducers with high fMQM product and stress-engineered frequency tuning,” *Applied Physics Letters* **107**, 131110 (2015).
- [57] B. C. Stipe, H. J. Mamin, T. D. Stowe, T. W. Kenny, and D. Rugar, “Noncontact Friction and Force Fluctuations between Closely Spaced Bodies,” *Physical Review Letters* **87**, 096801 (2001).
- [58] W. B. Davenport and W. L. Root, *An introduction to the theory of random signals and noise* (McGraw-Hill, 1958).
- [59] P.-L. Yu, T. P. Purdy, and C. A. Regal, “Control of Material Damping in High-Q Membrane Microresonators,” *Physical Review Letters* **108**, 083603 (2012).
- [60] R. M. Camacho, J. Chan, M. Eichenfield, and O. Painter, “Characterization of radiation pressure and thermal effects in a nanoscale optomechanical cavity,” *Optics Express* **17**, 15726 (2009).
- [61] H. Miao, S. Danilishin, H. Mller-Ebhardt, and Y. Chen, “Achieving ground state and enhancing optomechanical entanglement by recovering information,” *New Journal of Physics* **12**, 083032 (2010).
- [62] H. M. Wiseman, “Quantum theory of continuous feedback,” *Physical Review A* **49**, 2133–2150 (1994).

- [63] H. M. Wiseman, “Using feedback to eliminate back-action in quantum measurements,” *Physical Review A* **51**, 2459–2468 (1995).
- [64] A. C. Doherty and K. Jacobs, “Feedback control of quantum systems using continuous state estimation,” *Physical Review A* **60**, 2700–2711 (1999).
- [65] A. A. Clerk, F. Marquardt, and K. Jacobs, “Back-action evasion and squeezing of a mechanical resonator using a cavity detector,” *New Journal of Physics* **10**, 095010 (2008).
- [66] M. R. Vanner, “Selective Linear or Quadratic Optomechanical Coupling via Measurement,” *Physical Review X* **1**, 021011 (2011).
- [67] Y. Chen, “Macroscopic quantum mechanics: theory and experimental concepts of optomechanics,” *Journal of Physics B: Atomic, Molecular and Optical Physics* **46**, 104001 (2013).
- [68] A. Szorkovszky, G. A. Brawley, A. C. Doherty, and W. P. Bowen, “Strong Thermomechanical Squeezing via Weak Measurement,” *Physical Review Letters* **110**, 184301 (2013).
- [69] G. A. Brawley, M. R. Vanner, P. E. Larsen, S. Schmid, A. Boisen, and W. P. Bowen, “Non-linear optomechanical measurement of mechanical motion,” *arXiv:1404.5746 [cond-mat, physics:physics, physics:quant-ph]* (2014), arXiv: 1404.5746.
- [70] J. J. Gorman and B. Shapiroeds., *Feedback Control of MEMS to Atoms* (Springer US, Boston, MA, 2012).
- [71] H. Miao, K. Srinivasan, and V. Aksyuk, “A microelectromechanically controlled cavity optomechanical sensing system,” *New Journal of Physics* **14**, 075015 (2012).
- [72] K. Srinivasan, H. Miao, M. T. Rakher, M. Davano, and V. Aksyuk, “Optomechanical Transduction of an Integrated Silicon Cantilever Probe Using a Microdisk Resonator,” *Nano Letters* **11**, 791–797 (2011).
- [73] J. L. Garbini, K. J. Bruland, W. M. Dougherty, and J. A. Sidles, “Optimal control of force microscope cantilevers. I. Controller design,” *Journal of Applied Physics* **80**, 1951–1958 (1996).
- [74] T. Ando, T. Uchihashi, and T. Fukuma, “High-speed atomic force microscopy for nano-visualization of dynamic biomolecular processes,” *Progress in Surface Science* **83**, 337–437 (2008).
- [75] A. G. Krause, M. Winger, T. D. Blasius, Q. Lin, and O. Painter, “A high-resolution microchip optomechanical accelerometer,” *Nature Photonics* **6**, 768–772 (2012).
- [76] G. M. Harry and the LIGO Scientific Collaboration, “Advanced LIGO: the next generation of gravitational wave detectors,” *Classical and Quantum Gravity* **27**, 084006 (2010).

- [77] J. Aasi and the LIGO Scientific Collaboration, “Characterization of the LIGO detectors during their sixth science run,” *Classical and Quantum Gravity* **32**, 115012 (2015).
- [78] G. Krishnan, C. U. Kshirsagar, G. K. Ananthasuresh, and N. Bhat, “Micromachined High-Resolution Accelerometers,” *Journal of the Indian Institute of Science* **87**, 333 (2012).
- [79] N. Yazdi, F. Ayazi, and K. Najafi, “Micromachined inertial sensors,” *Proceedings of the IEEE* **86**, 1640–1659 (1998).
- [80] P. Zwahlen, A. M. Nguyen, Y. Dong, F. Rudolf, M. Pastre, and H. Schmid, “Navigation grade MEMS accelerometer,” in *2010 IEEE 23rd International Conference on Micro Electro Mechanical Systems (MEMS)* pp. 631–634 (2010).
- [81] “Accelerometer Selection Based on Applications,” Tech. rep., Endevco (2006).
http://www.endevco.com/news/archivednews/2006/2006_08/2006_08_f4.pdf
- [82] C. Acar and A. M. Shkel, “Experimental evaluation and comparative analysis of commercial variable-capacitance MEMS accelerometers,” *Journal of Micromechanics and Microengineering* **13**, 634 (2003).
- [83] H. Kulah, J. Chae, N. Yazdi, and K. Najafi, “Noise analysis and characterization of a sigma-delta capacitive microaccelerometer,” *IEEE Journal of Solid-State Circuits* **41**, 352–361 (2006).
- [84] S. Tadigadapa and K. Mateti, “Piezoelectric MEMS sensors: state-of-the-art and perspectives,” *Measurement Science and Technology* **20**, 092001 (2009).
- [85] A. Partridge, J. Reynolds, B. Chui, E. Chow, A. Fitzgerald, L. Zhang, N. I. Maluf, and T. Kenny, “A high-performance planar piezoresistive accelerometer,” *Journal of Microelectromechanical Systems* **9**, 58–66 (2000).
- [86] C.-H. Liu, A. Barzilai, J. Reynolds, A. Partridge, T. Kenny, J. Grade, and H. Rockstad, “Characterization of a high-sensitivity micromachined tunneling accelerometer with micro-g resolution,” *Journal of Microelectromechanical Systems* **7**, 235–244 (1998).
- [87] R. H. O. U. Krishnamoorthy, “In-plane MEMS-based nano-g accelerometer with sub-wavelength optical resonant sensor,” *Sensors and Actuators A: Physical* **145**, 283–290 (2008).
- [88] K. Zandi, B. Wong, J. Zou, R. V. Kruzelecky, W. Jamroz, and Y. A. Peter, “In-plane silicon-on-insulator optical MEMS accelerometer using waveguide fabry-perot microcavity with silicon/air bragg mirrors,” in *2010 IEEE 23rd International Conference on Micro Electro Mechanical Systems (MEMS)* pp. 839–842 (2010).

- [89] W. Noell, P.-A. Clerc, L. Dellmann, B. Guldemann, H.-P. Herzig, O. Manzardo, C. Marxer, K. Weible, R. Dandliker, and N. de Rooij, "Applications of SOI-based optical MEMS," *IEEE Journal of Selected Topics in Quantum Electronics* **8**, 148–154 (2002).
- [90] T. Berkoff and A. Kersey, "Experimental demonstration of a fiber Bragg grating accelerometer," *IEEE Photonics Technology Letters* **8**, 1677–1679 (1996).
- [91] H. Nakstad and J. T. Kringlebotn, "Oil and gas applications: Probing oil fields," *Nature Photonics* **2**, 147–149 (2008).
- [92] X. Jiang, F. Wang, M. Kraft, and B. E. Boser, "An Integrated Surface Micromachined Capacitive Lateral Accelerometer with 2 $\mu\text{G}/\text{rt-Hz}$ resolution," *Solid-State Sensor, Actuator and Microsystems Workshop, Hilton Head Island* **2**, 2–6 (2002).
- [93] A. Salian, H. Kulah, N. Yazdi, G. He, and K. Najafi, "A High-Performance Hybrid CMOS Microaccelerometer," *Technical Digest. Solid-State Sensor and Actuator Workshop, Hilton Head Island, SC* (2000).
- [94] H. Luo, G. Fedder, and L. Carley, "A 1 mG lateral CMOS-MEMS accelerometer," in *The Thirteenth Annual International Conference on Micro Electro Mechanical Systems, 2000. MEMS 2000* pp. 502–507 (2000).
- [95] C. Yeh and K. Najafi, "A low-voltage tunneling-based silicon microaccelerometer," *IEEE Transactions on Electron Devices* **44**, 1875–1882 (1997).
- [96] H. Rockstad, J. Reynolds, T. Tang, T. Kenny, W. Kaiser, and T. Gabrielson, "A Miniature, High-sensitivity, Electron Tunneling Accelerometer," in *The 8th International Conference on Solid-State Sensors and Actuators, 1995 and Eurosensors IX.. Transducers '95* **2**, 675–678 (1995).
- [97] "GURALP CMG-PEPP," .
<http://www.guralp.com/>
- [98] M. Lemkin and B. E. Boser, "A three-axis micromachined accelerometer with a CMOS position-sense interface and digital offset-trim electronics," *IEEE Journal of Solid-State Circuits* **34**, 456–468 (1999).
- [99] "ADXL05 datasheet," .
<http://www.analog.com>
- [100] C.-H. Liu and T. Kenny, "A high-precision, wide-bandwidth micromachined tunneling accelerometer," *Journal of Microelectromechanical Systems* **10**, 425–433 (2001).

- [101] J. Bernstein, R. Miller, W. Kelley, and P. Ward, “Low-noise MEMS vibration sensor for geophysical applications,” *Journal of Microelectromechanical Systems* **8**, 433–438 (1999).
- [102] “ADXL105 datasheet,” .
<http://www.analog.com>
- [103] R. Kubena, G. Atkinson, W. Robinson, and F. Stratton, “A new miniaturized surface micro-machined tunneling accelerometer,” *IEEE Electron Device Letters* **17**, 306–308 (1996).
- [104] “Endevco, Model 752A13 accelerometer,” .
<http://www.endevco.com/datasheets/752A1.pdf>
- [105] Y. Li, S. Lee, and H. Pastan, “Air Damped Capacitance Accelerometers and Velocimeters,” *IEEE Transactions on Industrial Electronics and Control Instrumentation* **IECI-17**, 44–48 (1970).
- [106] H. V. Allen, S. C. Terry, and D. W. De Bruin, “Accelerometer systems with self-testable features,” *Sensors and Actuators* **20**, 153–161 (1989).
- [107] M. Winger, T. D. Blasius, T. P. Mayer Alegre, A. H. Safavi-Naeini, S. Meenehan, J. Cohen, S. Stobbe, and O. Painter, “A chip-scale integrated cavity-electro-optomechanics platform,” *Optics Express* **19**, 24905 (2011).
- [108] A. W. Fang, H. Park, O. Cohen, R. Jones, M. J. Paniccia, and J. E. Bowers, “Electrically pumped hybrid AlGaInAs-silicon evanescent laser,” *Optics Express* **14**, 9203 (2006).
- [109] S. M. Meenehan, *Cavity Optomechanics at Millikelvin Temperatures*, phd, California Institute of Technology (2015).
- [110] A. Yariv and P. Yeh, *Photonics: Optical Electronics in Modern Communications* (Oxford University Press, 2007).
- [111] M. Eichenfield, *Cavity optomechanics in photonic and phononic crystals: engineering the interaction of light and sound at the nanoscale*, phd, California Institute of Technology (2010).
- [112] A. H. Safavi-Naeini, T. P. M. Alegre, M. Winger, and O. Painter, “Optomechanics in an ultrahigh-Q two-dimensional photonic crystal cavity,” *Applied Physics Letters* **97**, 181106 (2010).
- [113] S. G. Johnson, P. R. Villeneuve, S. Fan, and J. D. Joannopoulos, “Linear waveguides in photonic-crystal slabs,” *Physical Review B* **62**, 8212–8222 (2000).
- [114] A. Chutinan and S. Noda, “Waveguides and waveguide bends in two-dimensional photonic crystal slabs,” *Physical Review B* **62**, 4488–4492 (2000).

- [115] A. B. Matsko, A. A. Savchenkov, N. Yu, and L. Maleki, “Whispering-gallery-mode resonators as frequency references. I. Fundamental limitations,” *Journal of the Optical Society of America B* **24**, 1324 (2007).
- [116] A. Chijioko, Q.-F. Chen, A. Y. Nevsky, and S. Schiller, “Thermal noise of whispering-gallery resonators,” *Physical Review A* **85**, 053814 (2012).
- [117] M. L. Gorodetsky and I. S. Grudinin, “Fundamental thermal fluctuations in microspheres,” *Journal of the Optical Society of America B* **21**, 697 (2004).
- [118] K. Yasumura, T. Stowe, E. Chow, T. Pfafman, T. Kenny, B. Stipe, and D. Rugar, “Quality factors in micron- and submicron-thick cantilevers,” *Journal of Microelectromechanical Systems* **9**, 117–125 (2000).
- [119] Y. T. Yang, C. Callegari, X. L. Feng, and M. L. Roukes, “Surface Adsorbate Fluctuations and Noise in Nanoelectromechanical Systems,” *Nano Letters* **11**, 1753–1759 (2011).
- [120] M. Girons i Nogu, *Inorganic and polymeric microsieves : strategies to reduce fouling*, info:eu-repo/semantics/doctoralThesis, University of Twente, Enschede (2005).
- [121] S. I. Raider, R. Flitsch, J. A. Aboaf, and W. A. Pliskin, “Surface Oxidation of Silicon Nitride Films,” *Journal of The Electrochemical Society* **123**, 560–565 (1976).
- [122] D. B. Asay and S. H. Kim, “Evolution of the Adsorbed Water Layer Structure on Silicon Oxide at Room Temperature,” *The Journal of Physical Chemistry B* **109**, 16760–16763 (2005).
- [123] M. A. Henderson, “The interaction of water with solid surfaces: fundamental aspects revisited,” *Surface Science Reports* **46**, 1–308 (2002).
- [124] S. H. Lee and P. J. Rossky, “A comparison of the structure and dynamics of liquid water at hydrophobic and hydrophilic surfacesa molecular dynamics simulation study,” *The Journal of Chemical Physics* **100**, 3334–3345 (1994).
- [125] M. James, T. A. Darwish, S. Ciampi, S. O. Sylvester, Z. Zhang, A. Ng, J. J. Gooding, and T. L. Hanley, “Nanoscale condensation of water on self-assembled monolayers,” *Soft Matter* **7**, 5309–5318 (2011).
- [126] M. Szri, P. Jedlovsky, and M. Roeselov, “Water adsorption on hydrophilic and hydrophobic self-assembled monolayers as proxies for atmospheric surfaces. A grand canonical Monte Carlo simulation study,” *Physical Chemistry Chemical Physics* **12**, 4604–4616 (2010).
- [127] M. M. Sung, G. J. Kluth, and R. Maboudian, “Formation of alkylsiloxane self-assembled monolayers on Si₃N₄,” *Journal of Vacuum Science & Technology A* **17**, 540–544 (1999).

- [128] U. Srinivasan, M. Houston, R. Rowe, and R. Maboudian, "Self-assembled fluorocarbon films for enhanced stiction reduction," in , *1997 International Conference on Solid State Sensors and Actuators, 1997. TRANSDUCERS '97 Chicago* **2**, 1399–1402 vol.2 (1997).
- [129] R. Maboudian, W. R. Ashurst, and C. Carraro, "Self-assembled monolayers as anti-stiction coatings for MEMS: characteristics and recent developments," *Sensors and Actuators A: Physical* **82**, 219–223 (2000).
- [130] U. Srinivasan, M. Houston, R. Howe, and R. Maboudian, "Alkyltrichlorosilane-based self-assembled monolayer films for stiction reduction in silicon micromachines," *Journal of Microelectromechanical Systems* **7**, 252–260 (1998).
- [131] Y. Rudich, I. Benjamin, R. Naaman, E. Thomas, S. Trakhtenberg, and R. Ussyshkin, "Wetting of Hydrophobic Organic Surfaces and Its Implications to Organic Aerosols in the Atmosphere," *The Journal of Physical Chemistry A* **104**, 5238–5245 (2000).
- [132] J. Hautman and M. L. Klein, "Microscopic wetting phenomena," *Physical Review Letters* **67**, 1763–1766 (1991).
- [133] H. M. Gibbs, *Optical Bistability: Controlling Light with Light* (Academic Press, 1985).
- [134] H. Xie and G. Fedder, "Integrated Microelectromechanical Gyroscopes," *Journal of Aerospace Engineering* **16**, 65–75 (2003).
- [135] J. Y. Cho, *High-Performance Micromachined Vibratory Rate- and Rate-Integrating Gyroscopes*, phd, University of Michigan (2012).
- [136] A. Kourepenis, J. Borenstein, J. Connelly, R. Elliott, P. Ward, and M. Weinberg, "Performance of MEMS inertial sensors," in *Position Location and Navigation Symposium, IEEE 1998* pp. 1–8 (1998).
- [137] J. Bernstein, S. Cho, A. King, A. Kourepenis, P. Maciel, and M. Weinberg, "A micromachined comb-drive tuning fork rate gyroscope," in *Micro Electro Mechanical Systems, 1993, MEMS '93, Proceedings An Investigation of Micro Structures, Sensors, Actuators, Machines and Systems. IEEE*. pp. 143–148 (1993).
- [138] T. Juneau, A. Pisano, and J. Smith, "Dual axis operation of a micromachined rate gyroscope," in , *1997 International Conference on Solid State Sensors and Actuators, 1997. TRANSDUCERS '97 Chicago* **2**, 883–886 vol.2 (1997).
- [139] M. Weinberg, J. Connelly, A. Kourepenis, and D. Sargent, "Microelectromechanical instrument and systems development at the Charles Stark Draper Laboratory, Inc," in , *AIAA/IEEE Digital Avionics Systems Conference, 1997. 16th DASC* **2**, 8.5–33–8.5–40 vol.2 (1997).

- [140] W. Geiger, B. Folkmer, J. Merz, H. Sandmaier, and W. Lang, "A new silicon rate gyroscope," in , *The Eleventh Annual International Workshop on Micro Electro Mechanical Systems, 1998. MEMS 98. Proceedings* pp. 615–620 (1998).
- [141] R. L. Kubena, D. J. Vickers-Kirby, R. J. Joyce, and F. P. Stratton, "New miniaturized tunneling-based gyro for inertial measurement applications," *Journal of Vacuum Science & Technology B* **17**, 2948–2952 (1999).
- [142] H. Song, Y. Oh, I. Song, S. Kang, S. Choi, H. Kim, B. Ha, S. Baek, and C. Song, "Wafer level vacuum packaged de-coupled vertical gyroscope by a new fabrication process," in *The Thirteenth Annual International Conference on Micro Electro Mechanical Systems, 2000. MEMS 2000* pp. 520–524 (2000).
- [143] S. Kim, B. Lee, J. Lee, and K. Chun, "A gyroscope array with linked-beam structure," in *The 14th IEEE International Conference on Micro Electro Mechanical Systems, 2001. MEMS 2001* pp. 30–33 (2001).
- [144] "Analog Devices ADXRS614 Data Sheet," .
www.analog.com/static/imported-files/data_sheets/ADXRS614.pdf
- [145] G. He and K. Najafi, "A single-crystal silicon vibrating ring gyroscope," in *The Fifteenth IEEE International Conference on Micro Electro Mechanical Systems, 2002* pp. 718–721 (2002).
- [146] S. Y. Bae, K. J. Hayworth, K. Y. Yee, K. Shcheglov, and D. V. Wiberg, "High-performance MEMS microgyroscope," **4755**, 316–324 (2002).
- [147] M. Palaniapan, R. Howe, and J. Yasaitis, "Performance comparison of integrated z-axis frame microgyroscopes," in *IEEE The Sixteenth Annual International Conference on Micro Electro Mechanical Systems, 2003. MEMS-03 Kyoto* pp. 482–485 (2003).
- [148] J. Kim, S. Park, D. Kwak, H. Ko, and D.-I. D. Cho, "A planar, x-axis, single-crystalline silicon gyroscope fabricated using the extended SBM process," in *Micro Electro Mechanical Systems, 2004. 17th IEEE International Conference on. (MEMS)* pp. 556–559 (2004).
- [149] D. Karnick, G. Ballas, L. Koland, M. Secord, T. Braman, and T. Kourepenis, "Honeywell gun-hard inertial measurement unit (IMU) development," in *Position Location and Navigation Symposium, 2004. PLANS 2004* pp. 49–55 (2004).
- [150] J.-Y. Lee, S.-H. Jeon, H.-K. Jung, H.-K. Chang, and Y.-K. Kim, "Vacuum packaged low noise gyroscope with sub mdeg/s/ radic;Hz resolution," in *18th IEEE International Conference on Micro Electro Mechanical Systems, 2005. MEMS 2005* pp. 359–362 (2005).

- [151] M. Zaman, A. Sharma, and F. Ayazi, "High Performance Matched-Mode Tuning Fork Gyroscope," in *19th IEEE International Conference on Micro Electro Mechanical Systems, 2006. MEMS 2006 Istanbul* pp. 66–69 (2006).
- [152] H. Johari and F. Ayazi, "High-frequency capacitive disk gyroscopes in (100) and (111) silicon," in *IEEE 20th International Conference on Micro Electro Mechanical Systems, 2007. MEMS* pp. 47–50 (2007).
- [153] A. Sharma, M. Zaman, M. Zucher, and F. Ayazi, "A 0.1 deg/Hr bias drift electronically matched tuning fork microgyroscope," in *IEEE 21st International Conference on Micro Electro Mechanical Systems, 2008. MEMS 2008* pp. 6–9 (2008).
- [154] I. Prikhodko, S. Zotov, A. Trusov, and A. Shkel, "Sub-degree-per-hour silicon MEMS rate sensor with 1 million Q-factor," in *Solid-State Sensors, Actuators and Microsystems Conference (TRANSDUCERS), 2011 16th International* pp. 2809–2812 (2011).
- [155] E. Sahin, S. Alper, and T. Akin, "Experimental evaluation of alternative drive-mode control electronics developed for high-performance MEMS gyroscopes," in *Solid-State Sensors, Actuators and Microsystems Conference (TRANSDUCERS), 2011 16th International* pp. 2817–2820 (2011).
- [156] I. P. Prikhodko, S. A. Zotov, A. A. Trusov, and A. M. Shkel, "Foucault pendulum on a chip: Rate integrating silicon MEMS gyroscope," *Sensors and Actuators A: Physical* **177**, 67–78 (2012).
- [157] S. W. Yoon, *Vibration Isolation and Shock Protection for MEMS.*, phd, University of Michigan (2009).
- [158] S.-H. Lee, S. Lee, and K. Najafi, "A Generic Environment-Resistant Packaging Technology for MEMS," in *Solid-State Sensors, Actuators and Microsystems Conference, 2007. TRANSDUCERS 2007. International* pp. 335–338 (2007).
- [159] S.-H. Lee, J. Cho, S. Lee, M. Zaman, F. Ayazi, and K. Najafi, "A Low-Power Oven-Controlled Vacuum Package Technology for High-Performance MEMS," in *IEEE 22nd International Conference on Micro Electro Mechanical Systems, 2009. MEMS 2009* pp. 753–756 (2009).
- [160] S.-H. Lee, *Wafer-Level Packaging for Environment-Resistant Microinstruments.*, phd, University of Michigan (2009).
- [161] J. Reid, V. Bright, and J. Kosinski, "A micromachined vibration isolation system for reducing the vibration sensitivity of surface transverse wave resonators," *IEEE Transactions on Ultrasonics, Ferroelectrics, and Frequency Control* **45**, 528–534 (1998).